Defect chemistry of methylammonium lead iodide

THÈSE N^{O} 7292 (2018)

PRÉSENTÉE LE 17 DÉCEMBRE 2018

À LA FACULTÉ DES SCIENCES DE BASE
LABORATOIRE DE PHOTONIQUE ET INTERFACES
PROGRAMME DOCTORAL EN CHIMIE ET GÉNIE CHIMIQUE

ÉCOLE POLYTECHNIQUE FÉDÉRALE DE LAUSANNE

POUR L'OBTENTION DU GRADE DE DOCTEUR ÈS SCIENCES

PAR

Alessandro SENOCRATE

acceptée sur proposition du jury:

Prof. S. Gerber, présidente du jury
Prof. J. Maier, Prof. M. Graetzel, directeurs de thèse
Prof. J. Fleig, rapporteur
Prof. A. Walsh, rapporteur
Prof. A. Fontcuberta i Morral, rapporteuse

ÉCOLE POLYTECHNIQUE
FÉDÉRALE DE LAUSANNE

Suisse
2018

ACKNOWLEDGMENTS

As it always happens when wrapping up several years of work, one claims as his own many things that have actually been carried out collaboratively. Science is, more often than not, a collective effort, where many different sorts of expertise (not only scientific) end up merging. I particularly enjoyed these interactions at the Max Planck Institute in Stuttgart, especially at the personal level.

First of all, I'd like to thank Prof. Maier for his supervision, for his willingness and passion in teaching me and also for raising the bar always a little higher (as frustrating as that was sometimes, it made me a better scientist). I'm also indebted to Prof. Grätzel for the fruitful collaboration and precious suggestions.

I am very grateful to Gee Yeong for all the fantastic (and fun) work we have done together. It has been great to have someone so nice to share the hardships of this project with. Thanks to Igor, for introducing me to one of the coolest techniques ever invented, and for his "Sure, why not?" attitude; thanks for investing so much time and resources in the project, but also in me.

Special thanks go to Florian for building many of the contraptions I had in mind (without which I would have achieved absolutely nothing) while also teaching me lots about practical stuff. Who knows, maybe I'll become a technician when I grow up. Thanks to Udo for the great help, und auch für die Geduld, mit der er mir Deutsch beigebracht hat.

Thanks to Sofia, for always having a smile ready and for the silent (but very noticeable) constant support. Infinite thanks must go to Rotraut for her (virtually) infinite availability and willingness to help me. In some moments, this has been absolutely priceless. Thanks to Rob for the can-do attitude and precious suggestions. Thanks to Giuliano and to Tae-Youl, for supervising me and teaching me lots of stuff at the beginning of the project. To both of them I'm also grateful for keeping in touch.

Thanks to all my fellow PhD students (special mention to Pinar, Maryam, Simon, Torben, Reihaneh, Marco, Federico, Elisa and Norman), for making this path we walked down together very pleasant. Thanks to my friends here in Stuttgart, in particular to Matteo, Joel, Daniel for providing me with a much-needed venting valve.

A great, big thanks to Helga, to Tolga, to Gisela Siegle and Reinhard Kremer, for all the time and effort they spent measuring my samples. Thanks to Eugene

for all the great suggestions. Thanks also to Uwe, Armin, Annette and Babsie for all the help.

Heartfelt thanks go to my parents, for being patient, and for being proud of me. I might not have shown it, but that has kept me going since the beginning. (Un enorme grazie, dal profondo del cuore, va ai miei genitori, per essere stati pazienti e fieri di me. Anche se forse non l'ho dato a vedere, il loro supporto è stato necessario fin dall'inizio.) Last, but most definitely not least, sincere thanks go to my girlfriend. For being there for me, for getting angry in my place and for all the beautiful things that we shared. I'm sorry this period was so hard on us, but I truly look forward to the rest of our journey together.

Stuttgart, November 6, 2018

Alessandro

ABSTRACT

The present work deals with the defect chemistry and charge transport properties in halide perovskites, and in particular in the archetypal methylammonium lead iodide ($MAPbI_3$). These materials are extensively researched due to their very promising application as light-harvesters in solar cells and in other optoelectronic devices.

Notwithstanding the numerous studies dealing with these materials (especially with their optical and electronic properties, and with device application), a significant portion of the underlying physics and chemistry is still poorly understood. Indeed, the physico-chemical features behind their exceptional photoelectrochemical properties are still largely unknown. Moreover, these materials suffer from severe degradation processes presently impeding their practical application. In addition, the charge transport in these materials is not purely electronic, but rather shows a significant ionic portion due to mobile ionic defects. The nature of such ion conduction, alongside its effect on the photoelectrochemical properties and on the materials stability, has never been systematically investigated. The study of these aspects is the aim of this thesis, where:

- At first, we study the charge transport properties of $MAPbI_3$, with particular attention to the ionic contribution, and we perform a defect chemical study of the compound. We show how the ionic conductivity, in equilibrium conditions, can be unambiguously assigned to mobile iodine vacancies, with an electronic contribution due to electron holes or conduction electron depending on the iodine activity.

- Secondly, we investigate the light effect on the charge transport previously characterized. Alongside an expected increase of the electronic contribution, we observe a striking enhancement of ionic conductivity in $MAPbI_3$ upon illumination. This remarkable observation is of fundamental relevance for both photovoltaics and solid state ionics fields. Here we also discuss a mechanism for such photo-enhanced ion conduction that relies on electron-ion interaction.

- Subsequently, we analyze $MAPbI_3$ and other hybrid halide perovskites under oxygen exposure, both in the dark and under illumination. We show

that light strongly affects the kinetics of oxygen interaction, so much so that under illumination $MAPbI_3$ completely degrades, while it is metastable in the dark. The oxygen, when incorporated in a sufficient amount in the lattice, also acts as acceptor dopant, greatly varying the ionic and electronic conductivities.

- We then investigate stability of several halide perovskites with respect to temperature, oxygen, and illumination through thermodynamic considerations. Here we show how many of these processes are expected to be extremely severe for some of the compounds, underlining an important -and intrinsic- bottleneck for the application of these materials.

- At last, we investigate the short-range ion dynamics in $MAPbI_3$, since these are linked to stability and electronic transport properties. Here, we show that methylammonium dynamics conforms well to a fast bi-axial rotation becoming isotropic in the cubic phase. In the inorganic lattice, a strong nuclear coupling between Pb and I is present, alongside highly active iodine dynamics.

Keywords: *Ionic conductivity; defect chemistry; charge transport; solar cells; halide perovskites; methylammonium lead iodide*

SINOPSI

Il presente lavoro di ricerca intende investigare la chimica dei difetti e il trasporto elettrico nelle perovskiti ibride a base alogenurica, in particolare nello ioduro di piombo e metilammonio ($MAPbI_3$). Questi materiali sono attualmente di grande rilevanza in quanto promettenti semiconduttori da impiegare in celle solari ad alta efficienza ed in altre applicazioni optoelettroniche.

Nonostante vi siano già numerosi studi recenti che trattano questa famiglia di composti (soprattutto le loro proprietà ottiche, elettroniche ed il loro utilizzo in dispositivi), molti aspetti della fisica e della chimica sottostante rimangono ancora ignoti. In particolare, non si conoscono le caratteristiche fondanti delle loro eccezionali proprietà di semiconduzione. Inoltre, questi materiali presentano una significativa instabilità chimica e strutturale, che ne impedisce al momento l'applicazione. Infine, in questi composti, il trasporto elettrico (fondamentale per il funzionamento di qualunque dispositivo) non è solamente di natura elettronica, ma presenta una sostanziale porzione ionica, dovuta a difetti ionici mobili. La natura di questa conducibilità ionica, insieme ai suoi effetti sulla stabilità e sulle proprietà funzionali, non è mai stata investigata sistematicamente. Lo studio di questi aspetti è lo scopo primario di questa tesi:

- Inizialmente si discutono le proprietà di trasporto elettrico in $MAPbI_3$, con particolare attenzione al contributo ionico, insieme ad uno studio completo della chimica dei difetti del composto. Qui si mostra che la conducibilità ionica, in condizioni di equilibrio, è riconducibile chiaramente alle vacanze di iodio presenti.

- Come secondo punto, si discutono gli effetti dell'illuminazione sulle proprietà di trasporto trattate precedentemente. Se da un lato, in queste condizioni, si osserva un normale aumento della conducibilità elettronica, la luce incrementa sostanzialmente anche il trasporto ionico in $MAPbI_3$. Questa sorprendente osservazione è di fondamentale rilevanza sia per il campo del fotovoltaico che per quello della chimica dello stato solido. Infine, viene proposto e discusso un meccanismo per questo fenomeno.

- Successivamente, $MAPbI_3$ ed altre perovskiti ibride vengono analizzate durante l'esposizione ad ossigeno, sia in condizioni d'equilibrio che sotto illuminazione. Qui si mostra come l'ossigeno sia un forte agente degradante

per questi materiali, e che la cinetica di interazione è accellerata dalla luce. Allo stesso tempo, l'ossigeno influenza le proprietà elettriche quando viene introdotto in quantità sufficienti all'interno del materiale, agendo da drogante.

- In seguito, si calcola la stabilità termodinamica di questi materiali, sia rispetto alla temperatura che ad altri agenti degradanti quali acqua, ossigeno e luce. Qui si mostra come molte perovskiti ibride, tra cui $MAPbI_3$, siano soggette a diversi meccanismi di decomposizione, alcuni dei quali estremamente severi.

- Infine, l'ultimo capitolo è dedicato allo studio delle dinamiche molecolari che coinvolgono i cationi di metilammonio ed il reticolo inorganico in $MAPbI_3$, di grande importanza poichè collegate alla stabilità strutturale ed al trasporto elettronico. Si osserva che i cationi di metilammonio sono coinvolti in una rapida rotazione bi-assiale, mentre nel reticolo inorganico è presente una forte interazione nucleare tra atomi di piombo e iodio.

Parole chiave: *Conducibilità ionica; chimica dei difetti; trasporto elettrico; celle solari; perovskiti ibride; ioduro di piombo e metilammonio*

CONTENTS

LIST OF FIGURES

LIST OF TABLES

INTRODUCTION

1

INTRODUCTORY REMARKS

1.1 MOTIVATION AND AIM

The fundamental study of functional solids is key to both science and technology of energy-related materials. On one hand, compounds that can be used for environmental friendly energy conversion (e.g. in solar cell or fuel cell devices) and storage (e.g. metal-ion batteries or supercapacitors) are of great importance due to the necessity of quickly reducing humanity's carbon footprint and the related disastrous environmental effects. On the other hand, many fundamental processes underlying energy conversion and storage are still poorly understood, ultimately limiting our ability to exploit and improve them.

The study presented in this thesis focuses on a class of semiconductor materials (hybrid organic-inorganic halide perovskites, or HOIHPs) that has shown such exceptional photo-electrochemical properties as to rapidly become one of the most heavily researched material classes. Their functional properties make them ideal primarily as light-harvesters for solar cell devices,[1–3] but other potential applications include optoelectronics,[4,5] transistors,[6,7] and even lasing[8,9] and X-ray detection.[10] For these compounds, the underlying physics and chemistry are presently largely unknown, however their remarkable properties make a fundamental study potentially highly rewarding. In addition, there is a great need to improve these materials' stability and charge transport properties before practical application. This thesis intends to contribute in these directions, by studying in particular defect chemistry and charge transport properties in these compounds.

1.2 HALIDE PEROVSKITE MATERIALS AND DEVICES

Hybrid organic-inorganic halide perovskites are a family of compounds of general formula ABX_3, composed of a large organic A cation (typically methylammonium, MA = $CH_3NH_3^+$ or formamidinium, FA = $CH(NH_2)_2^+$), an inorganic

B cation (commonly Pb^{2+} or Sn^{2+}) and an halide X anion (I^-, Br^- or Cl^-).[11] The archetypal -and most studied- compound of the family is methylammonium lead iodide ($MAPbI_3$), and its structure is represented in **Fig. 1.1a**. As mentioned previously, the main point of interest of HOIHPs is their photo-electrochemical properties, such as their high absorption coefficients, low exciton binding energies ($\sim$ 20-40 meV),[12,13] long electron-hole diffusion lengths ($> 1\mu$m)[14,15] and slow ($\sim$ 100 ps) cooling of high energy (hot) carriers.[16–18] As a further advantage, these compounds can be fabricated through low temperature methods, and this makes them very attractive from an industrial point of view, as it could potentially allow for low-cost, large-scale production through coating or printing techniques (e.g. roll-to-roll).

All these features make the materials ideal for many semiconducting applications (given in **§ 1.1**), even though the vast majority of the efforts has focused on their use as light-harvester in solar cells.[1] These devices have shown an astonishing rate of improvement, going from solar-to-electric power conversion efficiencies (PCEs) of 3.8% in their first application[1] to a striking 22.7% in approximately 8 years.[19] As shown in **Fig. 1.1b**, these photovoltaic devices (called perovskite solar cells, PSCs) have partially inherited the dye-sensitized solar cell[20] architecture, and are now typically composed of a mesoscopic TiO_2 layer acting as electron transport materials (ETM), and a solid organic hole transport material (HTM, such as Spiro-OMeTAD, PCBM, PTAA, etc.).[1–3] Inorganic HTMs are also receiving increasing attention due to the fact that they can enhance device stability.[21,22]

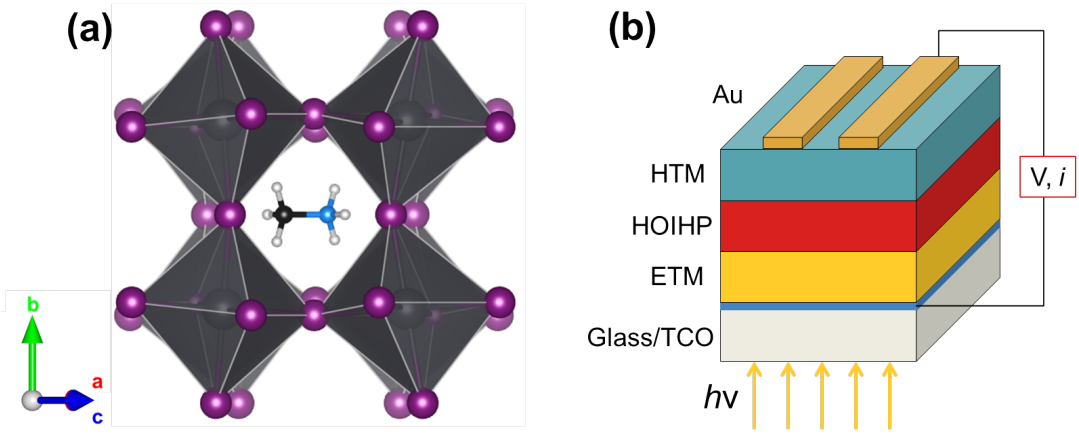

Figure 1.1. **(a)** Structure of the tetragonal phase (T < 327 K) of $MAPbI_3$, drawn with Vesta.[23] **(b)** Schematics of a PSC architecture, with a transparent conducting oxide (TCO) deposited on top of a glass substrate, an electron transport material (ETM, commonly mesoporous TiO_2), infiltrated or top-contacted with the HOIHP and with on top a hole transport material (HTM, typically Spiro-OMeTAD) and a current collector (Au).

Interestingly, a great degree of chemical tunability in HOIHPs can be achieved by mixing different A cations (also with inorganic Cs^+, Rb^+), B cations or even different halides, forming solid solutions. As an example, a typical state-of-the-art perovskite composition used in PSCs contains 4 A-cations and 2 halide anions and reads as follows: $\{Rb_{0.05}[Cs_{0.05}(MA_{0.17}, FA_{0.83})_{0.95}]_{0.95}\}Pb(I_{0.83}, Br_{0.17})_3$.[24] Many other A and B cations are presently under investigation, further broadening the chemical space available. In this respect, the need to replace A cations is part of an effort to improve stability and performance,[25,26] while alternative B cations are being investigated mostly in order to avoid the toxicity of Pb.[27] An alternative approach has also emerged in recent years and consists in reducing the perovskite dimensionality to 2D, to improve both stability and functional properties.[28,29]

As far as their electrical transport properties are concerned, these materials have been shown to be mixed ionic-electronic conductors.[30,31] The substantial ionic contribution to the conductivity has been linked to degradation processes[32–34] and also gives rise to significant and anomalous polarisation phenomena in devices under operation.[35,36]

In addition, HOIHPs presents several other major disadvantages, which hinder their development into a commercial reality. First and foremost, HOIHPs and related devices are plagued by important degradation issues, which can be activated by temperature,[37–45] water or humidity,[39,46–52] oxygen exposure[53–62] and also high intensity illumination.[45,63–68] Secondly, the solution-based fabrication processing suffers from a lack of reproducibility and a large standard deviation of functional properties, likely attributable to the challenges of accurately controlling stoichiometry during synthesis. This is hardly surprising, as the variation of properties obtained in a compound upon changing its stoichiometry (and thus its defect concentrations) is often larger than what can be achieved by changing the compound itself.

1.3 THESIS OUTLINE

The present thesis concentrates on $MAPbI_3$ (the archetypal HOIHP) and addresses fundamental questions concerning stoichiometry, stability and degradation from the point of view of defect chemistry. It is organized in the following chapters:

- **The nature of ion conduction in $MAPbI_3$. (§ 2)**
  Since HOIHPs are mixed ionic-electronic conductors, any study of electrical and electrochemical properties must also consider ion transport pro-

cesses. In this respect, it becomes of great significance to determine the nature of this ion transport. Thus, in this chapter we study $MAPbI_3$, with the aim of identifying its dominant mobile ions. Applying a multitude of techniques, we unambiguously attribute the significant ionic conductivity observed under equilibrium conditions to mobile iodine ions, simultaneously also ruling out any significant cation diffusion.

- **Defect chemical study of $MAPbI_3$ (§ 3).**
  Here we investigate the defect chemistry of $MAPbI_3$ in order to identify its dominant ionic and electronic charge carriers. By applying defect chemical modeling and conductivity experiments as a function of stoichiometry and doping content, we find iodine vacancies and electron holes as dominant ionic and electronic charge carriers in $MAPbI_3$ under equilibrium. Conduction electrons also come into play, but only at very low iodine activities. We also show how such stoichiometry variations lead to a purposeful and significant tuning of the ionic and electronic conductivities. The information extracted in these first two chapters lays the foundation for all the subsequent investigations.

- **Light effects on ion transport. (§ 4)**
  In this chapter we discuss a completely novel aspect in both photovoltaics and solid state ionics fields, i.e. the interaction of light and ion transport. By building on the situation under equilibrium, we identify the dominant ionic and electronic charge carriers in $MAPbI_3$ under illumination, that are still electron holes and iodine vacancies. Subsequently we show that, strikingly, the ionic conductivity in this material is greatly enhanced upon illumination. The characterization of such a remarkable effect leads us to the proposal of a mechanism for the photo-enhanced ion conduction which relies on electron-ion interaction.

- **Interaction of oxygen with halide perovskites (§ 5).**
  Here we study stability and charge transport properties of various HOIHP compositions under oxygen exposure, both in the dark and under illumination. Thermodynamic considerations show some of these compounds, such as $MAPbI_3$, to be unstable against oxygen. Nevertheless, the kinetics of oxygen interaction is so much affected by illumination that, in the dark, the materials are metastable. In addition, we show that by incorporating oxygen in the $MAPbI_3$ lattice we induce significant changes (analogous to acceptor doping) in both electronic and ionic conductivity.

- **Thermodynamic stability of halide perovskites (§ 6).**
  In this chapter we discuss the thermodynamics of several degradation processes involving HOIHPs, specifically those activated by temperature, oxygen and light. These thermodynamic considerations show that many HOIHP formulations have a large tendency to degrade, even under relatively mild conditions, in agreement with literature experimental observations. This aspect is particularly critical for $MAPbI_3$, and is a serious intrinsic bottleneck for potential applications.

- **Short-range ion dynamics in $MAPbI_3$ (§ 7).**
  Here we study the short-range ion dynamics involving MA cations, as well as the Pb-I framework in $MAPbI_3$. In this compound, short-range dynamics have been linked to structural stability and extended carrier lifetimes and are thus of great significance. We resolve the type and rate of the molecular motion involving MA, showing that it conforms well to an extremely fast bi-axial rotation becoming isotropic in the cubic phase. As for the inorganic lattice, we observe a strong nuclear coupling between Pb and I, along with highly active I-dynamics in the forms of oscillations about Pb atoms.

RESULTS AND DISCUSSION

2

THE NATURE OF ION CONDUCTION IN $MAPbI_3$

Abstract. *In this chapter, we study the nature of ion conduction in $MAPbI_3$ under equilibrium conditions. This is realized by performing several electrical and electrochemical characterizations (d.c. galvanostatic measurements, a.c. impedance, emf and Faradaic cell experiments), tracer diffusion experiments and by applying nuclear magnetic techniques (^1H, ^{14}N, ^{207}Pb NMR). We will show that, under equilibrium conditions, $MAPbI_3$ is a mixed ionic-electronic conductor with a substantial ionic conductivity due to iodine motion. In parallel, no significant diffusion of the cations is observed.*
We acknowledge Dr. Igor Moudrakovski for performing the NMR measurements and the related data evaluation.

Publications. *This study has been published in Ref.[69].*

2.1 INTRODUCTION

Despite the exceptional semiconducting properties of HOIHPs[14–17,70] and the high solar-to-electric power conversion efficiencies that can be achieved in related photovoltaic devices,[1–3,71] many aspects of the underlying physics and chemistry are still unknown. As a notable example, sizable and peculiar polarisation phenomena influencing charge transport have been reported in devices under operation (at long times or low a.c. frequencies). Specifically, an anomalous hysteretic behavior in i-V curves has been observed,[35] along with a high apparent dielectric constant that increases upon illumination.[36] Moreover, these polarisation phenomena lead to a field-switchable photovoltaic effects under load.[72] All the above-mentioned behaviors can be explained by taking into account the ion conduction processes happening in the halide perovskite layer of the photovoltaic device.

Indeed, as shown in this chapter for the specific case of $MAPbI_3$, these materials are mixed ionic-electronic conductors, with a significant portion of the conductivity carried by mobile ions under equilibrium conditions. Unsurpris-

ingly, many previously studied halide perovskites (both hybrid and inorganic) have been already known to be mixed conductors.[30,73–76] It is therefore necessary to take into account this ion conductivity whenever discussing charge transport, both in the bulk of the perovskite materials but also at the interfaces with electrodes or selective contacts that are present in devices.

Regarding bulk transport, one should note that materials showing both ionic and electronic conductivity, whenever charged by a current while in contact with neighboring phases that are blocking for one of the carriers, must undergo a significant stoichiometric polarisation.[77–79] This process is described in detail in the Appendix (**§ 10.1.2**). Here it suffices to say that it affects the stoichiometry of the material in a spatially-dependent way, comprising the entire bulk (from one electrode to the other), and involving necessarily both ionic and electronic charge carriers. This situation is expected to happen in all perovskite-based solar cell devices because of the ion-blocking nature of electron- and hole-transport materials normally used.[31]

Focusing now on the interface with the contacts, here space charge polarisation will occur, but on a completely different length scale.[80,81] In materials with high concentration of mobile ionic defects, as it is the case for $MAPbI_3$, the space charge potentials are expected to be heavily influenced (or even entirely driven) by ionic charge carriers.[82] It is therefore extremely likely that the ionic transport in HOIHPs greatly affects charge transport and charge transfer in related solar cell devices. In addition, ion conduction has been linked to degradation kinetics[32,33] and electrode reaction[34] that severely shorten the lifetime of these devices.

Being of such importance, we have dedicated a thorough study to the nature of ion conduction in $MAPbI_3$, that here we take as a model material for the HOIHP family. The aim of this chapter is to clarify the nature of the mobile ions in $MAPbI_3$, considering that both iodine[31,83–91] and methylammonium[90–95] ions have been claimed to be mobile in this material. We will try to solve this controversy[96,97] by applying a multitude of techniques to the study of ion conduction in $MAPbI_3$. This topic is not only relevant for the understanding of materials and for the performance of devices, but also for the purposeful conditioning of the material properties that could be realized upon doping or stoichiometry variations (see **§ 3.3**).

2.2 THE MIXED CONDUCTING NATURE OF $MAPbI_3$

This work follows a previous study carried out in our group,[31] where $MAPbI_3$ was directly shown for the first time to be a mixed conductor, with a significant portion of the conductivity carried by mobile ions. We revisited some of the experiments in Ref.[31] with the intent of fully confirming these findings.

In this respect, electrical characterizations already strongly indicate this compound to be a mixed conductor. Indeed, as shown in **Fig. 2.1a,b**, when using ion-blocking electrodes, d.c. galvanostatic polarisation experiments yields a significant voltage transient, while through a.c. impedance we observe an increasing capacitance at low frequencies. Both these experiments indicate that a stoichiometric polarisation is taking place in the bulk of the samples (details in Appendix § **10.1.2**). However, the decisive experiment to unambiguously confirm the mixed conducting nature of $MAPbI_3$ is the measurement of the emf voltage of a battery cell using this material as an electrolyte phase (**Fig. 2.1c**).

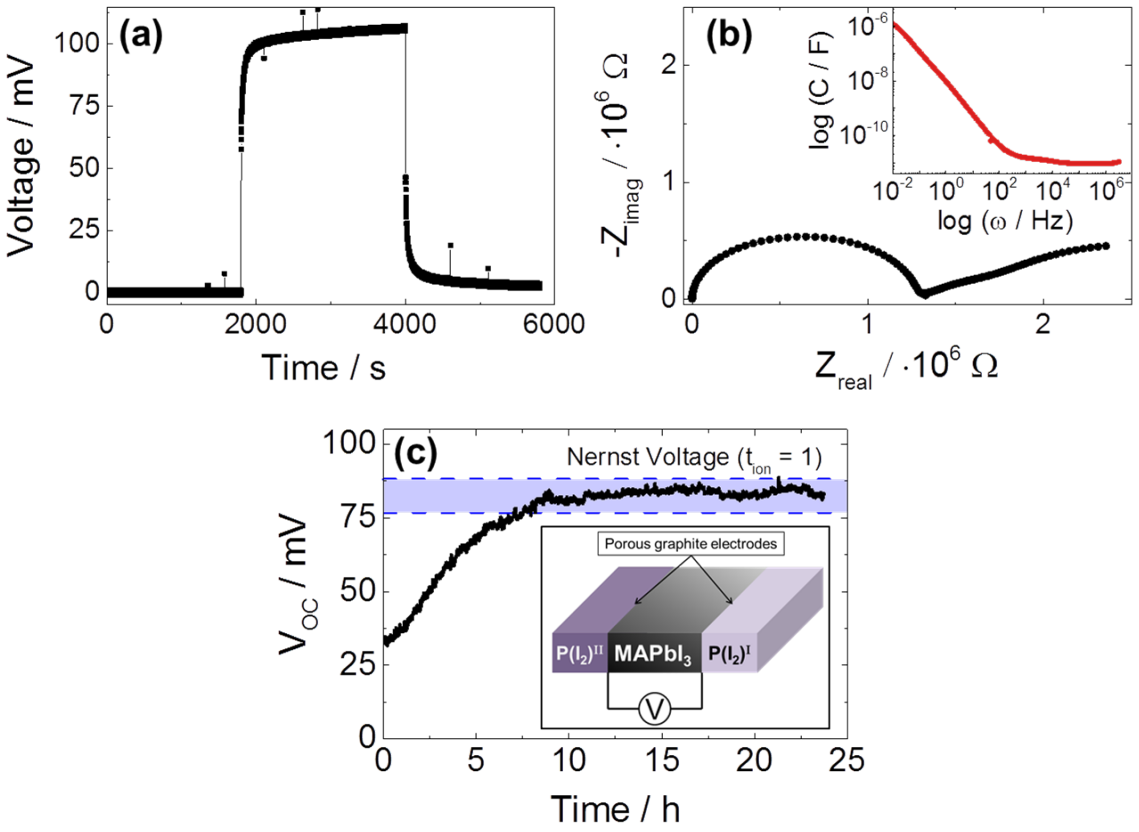

Figure 2.1. Electrical responses of a $MAPbI_3$ pellet with ion-blocking carbon electrodes, measured at 343 K under Ar with **(a)** d.c. galvanostatic polarisation (I = 150 nA/cm^2) and **(b)** a.c. impedance (50 mV of perturbation voltage). **(c)** Voltage of an emf cell obtained applying two different $P(I_2)$ ($1.7 \cdot 10^{-7}$ and $1.5 \cdot 10^{-5}$ bar) on the sides of a $MAPbI_3$ pellet kept at 403 K. Inset shows the schematics of the experiment.

As schematized in the inset of **Fig. 2.1c**, this is achieved by exposing the two sides of a sample to different iodine activities, in order to establish a chemical potential gradient across the sample.

Under these conditions, mixed ionic-electronic conductors yield an emf voltage response that depends both on the thermodynamic Nernst voltage (which is a function of the ratio of the iodine activities used) and on their portion of ionic conductivity:[98]

$$E_{emf} = E_{Nernst} \cdot t_{ion} \tag{2.1}$$

This thermodynamic voltage can be theoretically predicted by applying Nernst equation:

$$E_{Nernst} = -\frac{RT}{2F} \ln \frac{P(I_2)^{I}}{P(I_2)^{II}} \tag{2.2}$$

The portion of ionic conductivity, instead, is described by the ionic transport number:

$$t_{ion} = \frac{\sigma_{ion}}{\sigma_{ion} + \sigma_{eon}} \tag{2.3}$$

It follows that when using a purely ionic conductor ($t_{ion} = 1$), the related emf cell will theoretically show the full Nernst voltage. On the other hand, for a purely electronic conductor ($t_{ion} = 0$), such a cell would yield a short-circuit battery voltage of 0 V. As shown in **Fig. 2.1c**, a emf cell with $MAPbI_3$ as electrolyte phase gives a substantial voltage, from which we can clearly conclude that $MAPbI_3$ is a mixed ionic-electronic conductor. The t_{ion} value observed (~ 1) indicate a predominantly ionic conductor under the measurement conditions, a behavior that is -given the high temperature used- consistent with d.c. polarisation data.

D.c. polarisation, a.c. impedance, emf measurement

$MAPbI_3$ is a mixed ionic-electronic conductor under dark conditions.

2.3 WHICH ION IS MOBILE?

After obtaining the above confirmation, it is necessary to clarify the nature of the moving ion under equilibrium conditions. As mentioned in the introduction, there is much confusion in the literature regarding this very aspect,[31,83–97] making such unambiguous clarification a matter of utmost importance for the understanding of this material. A powerful experiment in this respect is the analysis of a Faradaic reaction cell.[31] As shown in **Fig. 2.2**, by flowing a current through a cell of type $+M|MAPbI_3|AgI|Ag-$ (M=Cu or Pb), we consistently observe the formation of MI (at the expenses of the metal) at the $M/MAPbI_3$ contact.

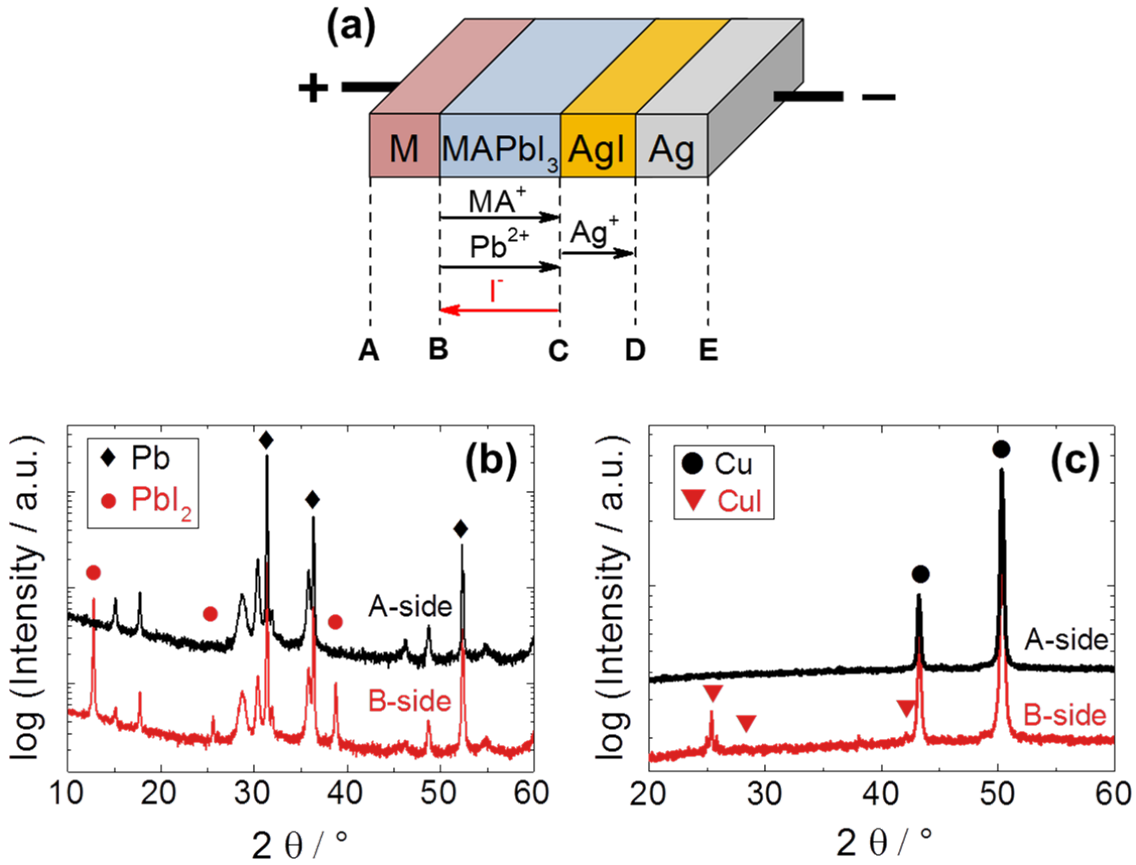

Figure 2.2. **(a)** Schematics of the Faradaic cells used (+M|$MAPbI_3$|AgI|Ag−, with M=Cu or Pb). **(b)** XRD analysis of the interfaces of a Pb reaction cell, exposed to Ar atmosphere at 343 K under 50 nA/cm^2 current. On the B side, formation of PbI_2 can be observed. Unmarked peaks belong to a PbO phase already present in the Pb powders used. **(c)** XRD analysis of the interfaces of a Cu reaction cell, exposed to Ar atmosphere at 323 K while flowing 25 nA/cm^2. On the B side, formation of CuI can be observed.

No morphological changes or secondary phase formations are detected at any of the other interfaces. This experiment clearly indicates that iodine ions are mobile in $MAPbI_3$, while the absence of secondary phases at the $MAPbI_3$/AgI interface suggests no significant motion of the cations. To confirm that the formation of the iodide MI is not due to a chemical reaction between $MAPbI_3$ and metal contact, we performed a control experiment on identical cells without applying current. No formation of MI is detected (see Appendix **§ 10.1.3**), in line with the expected thermodynamic stability of the metals used against $MAPbI_3$.

Faradaic reaction cell
Significant I^- motion is detected.

2.4 DIFFUSION OF MA CATIONS

Albeit clear in showing prevailing I^- motion, the Faradaic cell experiment does not allow us to rule out a possible minor diffusion of the cations. Since MA migration was previously observed,[92–95] and also in the interest of estimating diffusion coefficients for all the potentially mobile species in $MAPbI_3$, we performed several solid-state NMR experiments. NMR is a powerful tool for evaluating solid-state diffusion and it is widely used in materials science for the study of dynamic processes.[99–102] To characterize $MAPbI_3$, we performed NMR on all of its nuclei. In this section, we will only discuss the ones yielding useful information for the study of solid-state diffusion processes, that are ^1H, ^{14}N and ^{207}Pb. The rest will be presented in a later chapter (**§ 7**).
Let us start by discussing ^{14}N spectra. As ^{14}N is a quadrupolar nucleus (I = 1), it has an electric quadrupole moment that strongly interacts with the internal electric field of the sample. While in liquids this interactions is entirely averaged by fast isotropic tumbling, in solids it can give rise to a characteristic splitting of the signals in multiplets.[103,104] As shown in **Fig. 2.3**, this behavior is observed in the tetragonal phase of $MAPbI_3$ and disappears when moving to the cubic phase ($T > 327$ K). In a similar way as for liquids, isotropic motion in solids result in the averaging of the quadrupolar interactions and subsequent disappearance of the related splitting. We can thus conclude that, in the tetragonal phase, no isotropic motion (be it short- or long-range) of ^{14}N (and thus of MA) is taking place, in contrast with the cubic phase. As solid-state diffusion is intrinsically isotropic, we can safely rule out any significant MA long-range motion in $MAPbI_3$, at least in the tetragonal phase. Analysis of ^1H spectra will show that such a conclusion holds for the cubic phase as well.

As shown in **Fig. 2.3b**, the linewidth of the proton signal (composed by both C- and N-bound protons) is almost unvaried in a very large range of temperatures (200 - 500 K). This linewidth is comprised of several contributions, such as homo and heteronuclear dipole-dipole interactions, both intra- and inter-molecular, which are differently averaged by the motions involving the methylammonium cation (details are discussed in **§ 7**). While intra-molecular interactions are already significantly averaged in the cubic phase (due to fast short-range MA reorientation, see **§ 7**), the same is not true for inter-molecular interactions. The latter remains nearly constant as long as the MA cation does not leave the confined space formed by the eight PbI_6 octahedra. If we encountered the activation of significant solid-state diffusion, the inter-molecular interactions would be averaged and, as a consequence, the linewidth would severely narrow

around the diffusion activation temperature. Since we see no evidence of such behavior in the entire temperature range probed (**Fig. 2.3c**), we can conclude that no significant long-range motion of MA is present. Assuming that a substantial diffusion process is indeed becoming active above the highest temperature probed (500 K), we can extract an upper limit for the diffusion coefficient of MA in $MAPbI_3$ using reported procedures.[105] We found these limit values to be $4 \cdot 10^{-15}$ $cm^2 \cdot s^{-1}$ at 343 K and $6 \cdot 10^{-13}$ $cm^2 \cdot s^{-1}$ at 378 K.

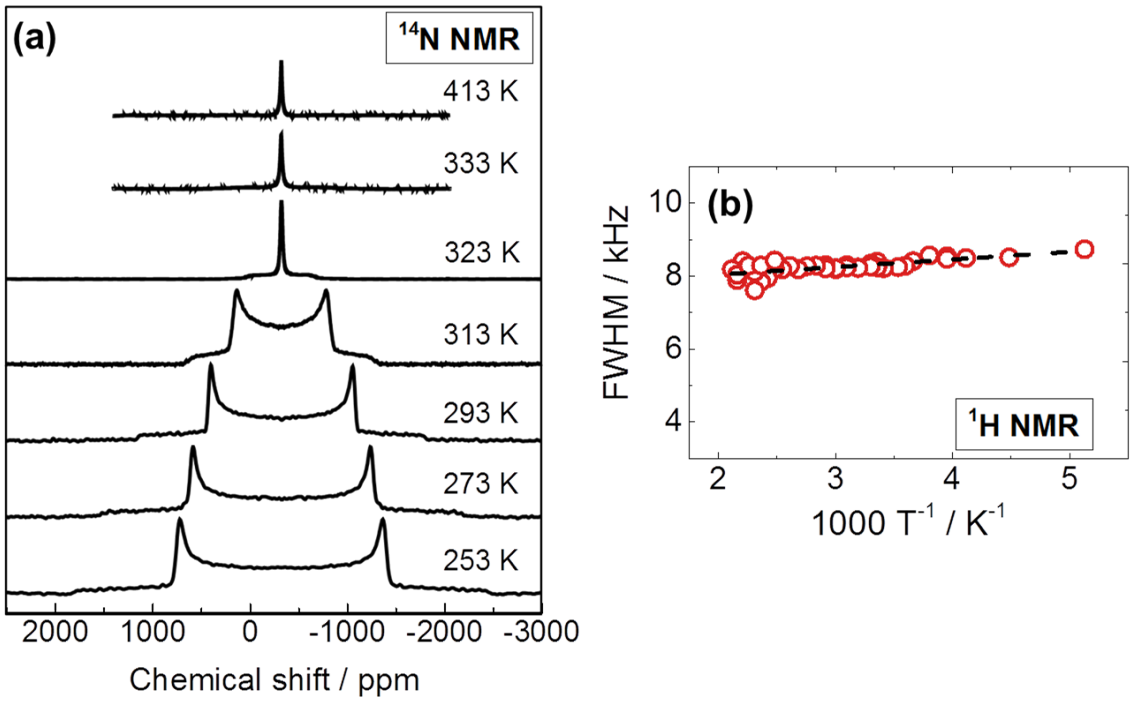

Figure 2.3. (a) ^{14}N NMR spectra of $MAPbI_3$, recorded as a function of temperature. In the tetragonal phase ($T < 327$ K), the sample show a characteristic quadrupolar splitting. **(b)** Full Width Half Maximum (FWHM) of the ^{1}H NMR signal as a function of temperature.

In an attempt to obtain a more precise quantification of the MA diffusion coefficient, and also to confirm the above results, we performed tracer diffusion experiments with ^{13}C. As shown in **Fig. 2.4**, by using an enriched $MAPbI_3$ pellet as a source of the isotope, and contacting it with a pure (i.e., containing ^{13}C at natural abundance) sample, we can probe the diffusion of ^{13}C as a function of the distance from the contact surface using Time of Flight Secondary Ions Mass Spectroscopy (ToF-SIMS). As shown in **Fig. 2.4b**, this yields a direct measurements of the fraction of different isotopes as a function of depth from the sample surface, that in our case also represents the source of enriched isotopes. These signals can be used to calculate the isotope ratio $^{13}C/C_{tot}$, i.e. $c(x,t)$, which can then be

normalized with respect to the isotope background natural abundance (c_{bg}) and enrichment of the source used (c_s), according to:

$$c_{norm}(x,t) = \frac{c(x,t) - c_{bg}}{c_s - c_{bg}} \tag{2.4}$$

The normalized value is then used to build a diffusion profile as a function of depth (**Fig. 2.4c**), that can be fitted in order to extract the values of diffusion coefficient (D^*) and surface rate constant (k^*). This is performed by using the following equation, which represents diffusion in a semi-infinite medium:[106]

$$c_{norm}(x,t) = erfc(\frac{x}{\sqrt{D^*t}}) - [exp(\frac{k^*x}{D^*} + \frac{k^{*2}t}{D^*}) \cdot erfc(\frac{x}{\sqrt{D^*t}} + k^*\sqrt{\frac{t}{D^*}})] \tag{2.5}$$

As shown in **Fig. 2.4c** we observe only a weak diffusion profile of ^{13}C (and, thus, of MA) in $MAPbI_3$. This indicates that, albeit only slightly, a diffusion process involving MA cations indeed takes place in $MAPbI_3$, in agreement with literature reports.[92–95]

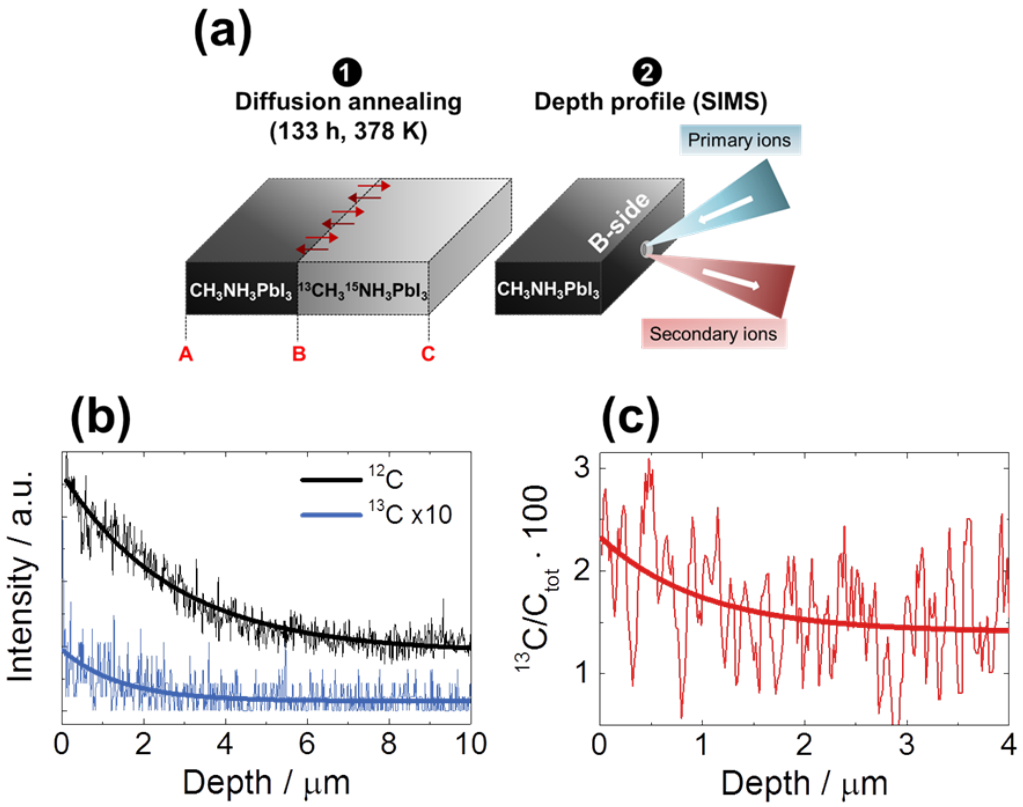

Figure 2.4. (a) Schematic representation of the tracer diffusion experiment. **(b)** Amount of ^{13}C and ^{12}C as a function of depth in a pure (i.e., natural abundance) $MAPbI_3$ pellet, induced by diffusion annealing in contact with a (^{13}C,^{15}N)-enriched $MAPbI_3$ sample (20 % abundance). **(c)** Ratio of $^{13}C/C_{tot}$ extracted from the curves of panel b, showing a weak diffusion profile quickly decaying after $\sim 2\ \mu m$.

Using the aforementioned procedure, we can extract from the diffusion profile $D^*_{MA} = 9 \cdot 10^{-14}$ cm$^2 \cdot$ s^{-1} and $k^*_{MA} = 2 \cdot 10^{-11}$ cm $\cdot$ s^{-1} at 378 K. We also performed similar tracer experiments on thin films, with the aim of comparing the diffusion process in the dark and under light. The results of these analysis is given and discussed in **§ 4.4**. The diffusion coefficients under equilibrium obtained here conform rather nicely with the upper limit values extracted previously from ^{1}H NMR. A direct comparison between the various diffusion coefficients found for different mobile ions will be discussed in detail later (**§ 3.5**). Here it suffices to say that the diffusion process involving MA cations is of little significance compared to the considerable iodine motion detected in $MAPbI_3$. We note, nevertheless, that the observed minor MA diffusion could still be relevant for other phenomena such as cation exchange reactions in nanocrystals[107] or decomposition processes, even though it is negligible from the point of view of the ionic charge transport.

^{13}C tracer, ^{1}H and ^{14}N NMR

No significant long-range diffusion of $CH_3NH_3^+$ in $MAPbI_3$ observed.

2.5 DIFFUSION OF Pb CATIONS

Due to its high polarizability, Pb cations are mobile in a variety of lead compounds such as PbI_2[108] or Pb-$\beta-Al_2O_3$.[109] We have therefore considered this ion as a possible candidate for solid-state diffusion in $MAPbI_3$. We note that several computational studies reported high formation energy of Pb defects or high activation energy for their motion.[83,84,110] In contrast, other reports indicated much more favorable values for Pb defect formation and migration.[111,112]

We therefore experimentally study the possible diffusion of Pb cations in $MAPbI_3$ using ^{207}Pb NMR. As shown in **Fig. 2.5**, the linewidth of ^{207}Pb signal is almost constant in the entire temperature range probed (200 - 500 K), in a similar manner as the ^{1}H NMR signal discussed previously (**Fig. 2.3b**). ^{207}Pb has the same nuclear spin as ^{1}H (I = $\frac{1}{2}$), therefore we can apply the same reasoning used previously for the proton case. As a consequence, the absence of any change in ^{207}Pb linewidth as a function of temperature can be related to the absence of any significant long-range diffusion processes involving Pb in $MAPbI_3$.

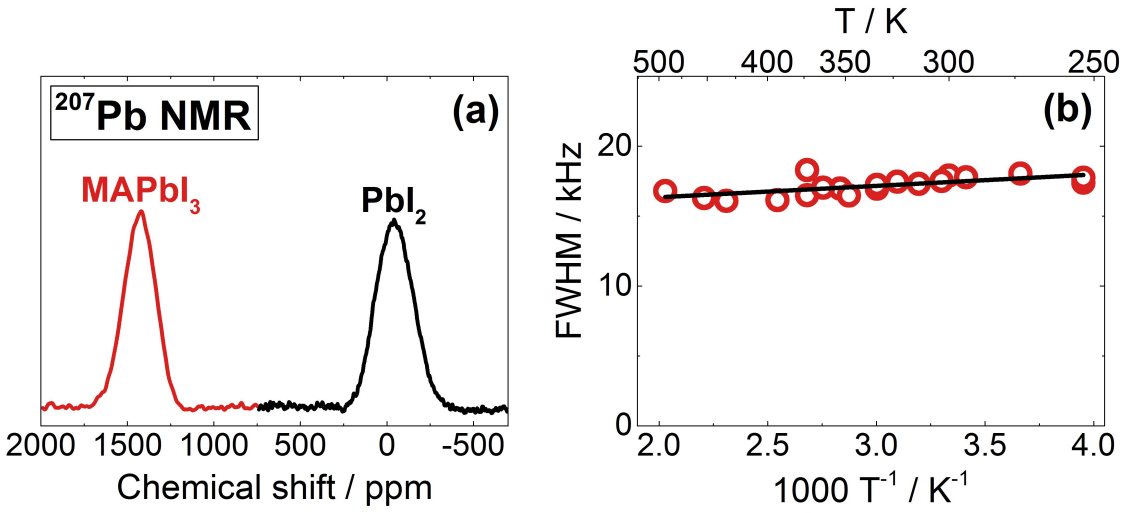

Figure 2.5. **(a)** ^{207}Pb NMR spectra of $MAPbI_3$ and PbI_2, showing the great sensitivity of this nucleus chemical shift to its environment. **(b)** ^{207}Pb Full Width Half Maximum (FWHM) as a function of temperature. Line is only to guide the eye.

Also here, we can estimate upper limits for the diffusion coefficient of Pb^{2+} in $MAPbI_3$, that are $4 \cdot 10^{-15}$ $cm^2 \cdot s^{-1}$ at 343 K and $6 \cdot 10^{-13}$ $cm^2 \cdot s^{-1}$ at 378 K. In addition, as it will be discussed in detail later on (§ 7), we observe various evidences of a strong quadrupolar coupling between ^{207}Pb and ^{127}I. This behavior also indicates an immobile nature of the Pb cations in the $MAPbI_3$ structure.

^{207}Pb NMR

No significant long-range diffusion of Pb in $MAPbI_3$ is observed.

2.6 CONCLUSIONS

In this chapter, we analyzed the nature of ion conduction in $MAPbI_3$ with the intent of identifying the majority mobile ionic species under equilibrium conditions. Major findings are:

- Under equilibrium, $MAPbI_3$ is a mixed ionic-electronic conductor.
- Electrochemical experiments show substantial iodine migration.
- No significant MA^+ diffusion observed by NMR and tracer diffusion.
- No significant Pb^{2+} diffusion observed by NMR.

3

DEFECT CHEMICAL STUDY OF $MAPbI_3$

Abstract. *In this chapter, we explore the defect chemistry of $MAPbI_3$, with particular attention to the nature of the relevant ionic and electronic charge carriers under equilibrium conditions. Defect chemical modeling is heavily used to predict the material behavior, and is compared with electrical measurements carried out under conditions where the intrinsic defect concentrations can be purposefully altered (i.e., through stoichiometry variation and doping). Ultimately, these analyses allowed us to show that, under equilibrium conditions, iodine vacancies are the dominant charge carriers for ionic (and electron holes for electronic) transport.*

Publications. *This study has been published in Ref.[113].*

3.1 INTRODUCTION

We observed through a multitude of techniques that $MAPbI_3$ presents substantial I^- conductivity, while not having a significant Pb^{2+} and/or MA diffusion (§ **2**, also Ref.[69]). However, the important question concerning the nature of the mobile defect responsible for such I^- transport remains still to be answered. For this purpose, we applied standard solid state ionics techniques normally used for the defect chemical study of binary oxides and oxide perovskites.[98,114,115] Among these, varying oxygen partial pressure (and therefore stoichiometry and point defect concentrations) and recording the so-induced changes in conductivity is most powerful. These techniques can be adapted to $MAPbI_3$ (and to other halide perovskites) by varying the halogen partial pressure instead. Another widely used method is the introduction of a dopant in the lattice, followed by the analysis of the corresponding conductivity changes. Both the effects of doping and of stoichiometry variations on the defect concentrations can be modeled, therefore we will compare the experimental observation with the defect chemical modeling results.

3.2 DEFECT CHEMICAL MODEL

In any given compound, the effects of doping and of stoichiometry variations on the point defect concentrations can be modeled. Thus, before carrying out the related experiments, we performed defect chemical modeling on $MAPbI_3$ on the level of mass action laws. For simplicity, only part of the procedure will be reported here, but details can be easily found in the literature.[98,114,115] It is important to note that, due to its nature, the model relies on the establishment of a thermodynamic equilibrium among randomly distributed point defects, and between these point defects and the surrounding atmosphere. For this reason, the model well represents only of the situation in the dark, thus all the experiments presented in this section have been carried out in these conditions. Nonetheless, as it is discussed in detail in a later chapter (**§ 4**), under certain assumptions the qualitative conclusions of the model can still hold under illumination.

Let us now start by discussing the assumptions and simplifications under which the model is built. Note that here the point defects are written in the so-called Kröger-Vink notation, where positive and negative effective charges (with respect to the original lattice sites they occupy) are represented by the superscript $^{\bullet}$ and $^{\prime}$ respectively (full explanation about the notation is given in Appendix **§ 10.1.1**). Due to the dense lattice, perovskites intrinsically prefer to form vacancies rather than interstitial defects, therefore we do not explicitly consider in the model the occurrence of interstitials (i.e., we assume their concentrations not to be dominant). Some computational works, however, showed rather low formation energies for iodine interstitials ($I_i^{\prime}$) in $MAPbI_3$.[111,116] It is worth noting that several other computational works have reported low formation energies and migration barriers for iodine vacancies ($V_I^{\bullet}$), and higher -but still comparatively low- values for methylammonium vacancies ($V_{MA}^{\prime}$).[83,84,117] Nevertheless, even if we do not explicitly consider $I_i^{\prime}$ while building the defect model, we will still discuss its possible occurrence below, and show that this defect cannot be a relevant charge carrier in $MAPbI_3$. In addition, we expect lead vacancies ($V_{Pb}^{\prime\prime}$) to have high migration energies (due to the double charge, in agreement with Ref.[83,84]), therefore we will treat them as frozen dopants (constant concentration). Again, we note that the presence of $V_{Pb}^{\prime\prime}$ (or of any other defects that is not explicitly considered) does not affect the model conclusions as long as their concentrations are not dominant.

At first we model the stoichiometry change, i.e. the effect obtained upon iodine exposure. Based on the previous assumptions, the intrinsic defect situation

in $MAPbI_3$ is described by a partial Schottky reaction and by its corresponding mass action law:

$$MA^x_{MA} + I^x_I \rightleftharpoons V'_{MA} + V^\bullet_I + MAI \qquad K_S = [V^\bullet_I][V'_{MA}] \tag{3.1}$$

Iodine exposure results in incorporation and subsequent decrease of the intrinsic iodine-deficiency, according to:

$$\frac{1}{2}I_2 + V'_I \rightleftharpoons I^x_I + h^\bullet \qquad K_I = \frac{[h^\bullet]}{[V^\bullet_I]P^{1/2}_{I_2}} \tag{3.2}$$

From the mass action laws of the defect reactions one can obtain defect concentrations as a function of the pressure of the exchangeable component (in this case I_2). These concentrations are usually plotted schematically in a so-called Kröger-Vink diagram. Using the above defect chemical reactions and applying the electroneutrality condition, the diagram representing the effects of stoichiometry variations in $MAPbI_3$ is obtained by assuming different regions (N, I, P) where the iodine activity (a_{I_2}) is:

Low a_{I_2} (N). [R. 3.3.2] shifted to the left. $V^\bullet_I$ and e' are the dominant defects.

Intermediate a_{I_2} (I). Intrinsic disorder ([R. 3.3.1]) prevails. $V^\bullet_I$, V'_{MA} dominate.

High a_{I_2} (P). [R. 3.3.2] shifted to the right. V'_{MA} and $h^\bullet$ dominate.

The obtained diagram is reported in **Fig. 3.1a**. As intuitively expected, increasing iodine partial pressure decreases $V^\bullet_I$ concentration while enhancing $[V'_{MA}]$. As a consequence of **(Eq. 3.2)**, $h^\bullet$ concentration is also increased, while e' concentration is naturally suppressed.

We can now apply the same procedure for doping, assuming an arbitrary acceptor (A') or donor ($D^\bullet$) dopant of single effective positive or negative charge. Note that, for the model, it is irrelevant which lattice site the dopant occupies, as long as it introduces an effective positive (or negative) charge. The resulting Kröger-Vink diagram is given in **Fig. 3.1b**. Acceptor doping (effectively negatively charged) increases the concentration of all positive defects while a donor dopant naturally behaves oppositely. We can also calculate the stoichiometry dependence of the defect concentrations for an acceptor- or donor-doped $MAPbI_3$, assuming a fixed dopant concentration.

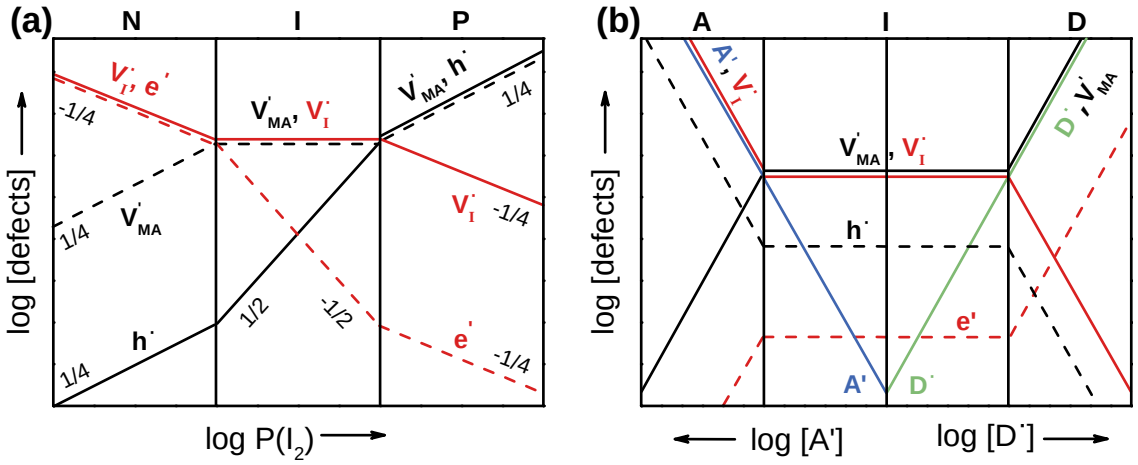

Figure 3.1. Kröger-Vink diagram representing the defect concentrations in $MAPbI_3$ as a function of **(a)** iodine partial pressure and **(b)** doping content. Calculated slopes are reported on the figure; note that, for the doping diagram, all slopes are $= 1$.

In the example of acceptor doping, the diagram is again obtained by assuming different regions (A_1, A_2, P) where the iodine activity is:

Low a_{I_2} (A_1). Intrinsically, $[V_I^{\bullet}]$ dominates. $V_I^{\bullet}$ compensates $A^{'}$.

Intermediate a_{I_2} (A_2). $[h^{\bullet}] \gg [V_I^{\bullet}]$. $h^{\bullet}$ compensates $A^{'}$. $V_I^{\bullet}$ depleted.

High a_{I_2} (P). $[V_{MA}^{'}]$ dominates over $[A^{'}]$. Analogous to I_2-excess in pure $MAPbI_3$.

The resulting diagram is displayed in **Fig. 3.2**, along with the one obtained for donor doping using an analogous procedure.

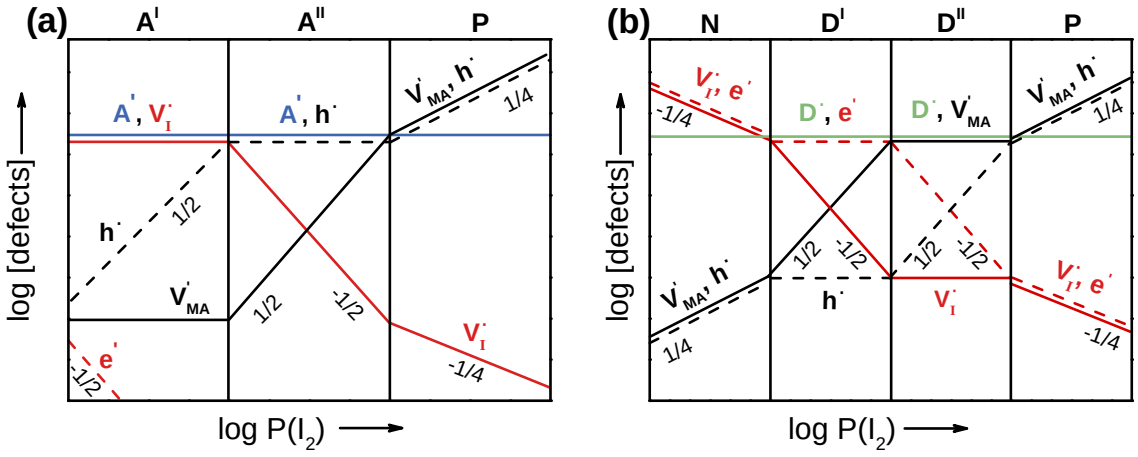

Figure 3.2. Kröger-Vink diagram representing the defect concentrations as a function of iodine partial pressure (stoichiometry) in **(a)** acceptor- and **(b)** donor-doped $MAPbI_3$. Slopes are given on the figure.

We note that, for both dopants, the iodine activity required to surpass the doping level and establish the P region is naturally dependent on the dopant concentration, and correspondingly greater than the one needed for pure, undoped $MAPbI_3$.

Defect chemical model

Charge carrier chemistry in $MAPbI_3$ predicted by defect modeling.

3.3 CONDUCTIVITY VS STOICHIOMETRY

Having set out the trends expected for defect concentrations as a function of iodine partial pressure, we are now armed to discuss the experimental results. As mentioned previously, it is possible to measure conductivity (ionic and electronic) as a function of iodine partial pressure (stoichiometry). Under the assumption that the charge carrier mobilities do not change with $P(I_2)$, we can directly compare the measured conductivity trends with the calculated defect concentration trend given in the previous diagrams. The assumption of a constant mobility holds as long as the temperature is fixed and the defect concentrations are low with respect to the original lattice constituents (dilute limit). Above such limit, defect associations (e.g., clustering of native defects or trapping by the dopant) plays a significant role and greatly complicates the interpretation of the results.[98,118] We note that this situation usually happens only for severe non-stoichiometry (e.g. high doping levels introduced), that is not the case for our pure samples. We can thus compare the defect diagram with the conductivity curves reported in **Fig. 3.3**. As shown in **Fig. 3.3a**, varying $P(I_2)$ induces important changes in the ionic and electronic conductivity of $MAPbI_3$. Qualitatively, one observes that the electronic conductivity is enhanced by iodine treatment, while the ionic contribution is decreased. A simple comparison with **Fig. 3.1a** shows that this is expected for an ionic conductivity carried by $V_I^{\bullet}$, and an electronic conductivity due to $h^{\bullet}$. We thus conclude that these are the majority ionic and electronic charge carriers in $MAPbI_3$.

However, we also note that the observed slopes lie in between the expected value for the intrinsic (I) region and the P-region of the relevant defect diagram (**Fig. 3.1a**), a behavior that is not completely in agreement with previous considerations. Indeed, based on literature computational data,[117] we would expect a much larger concentration of ionic defects with respect to electronic in $MAPbI_3$ under equilibrium.

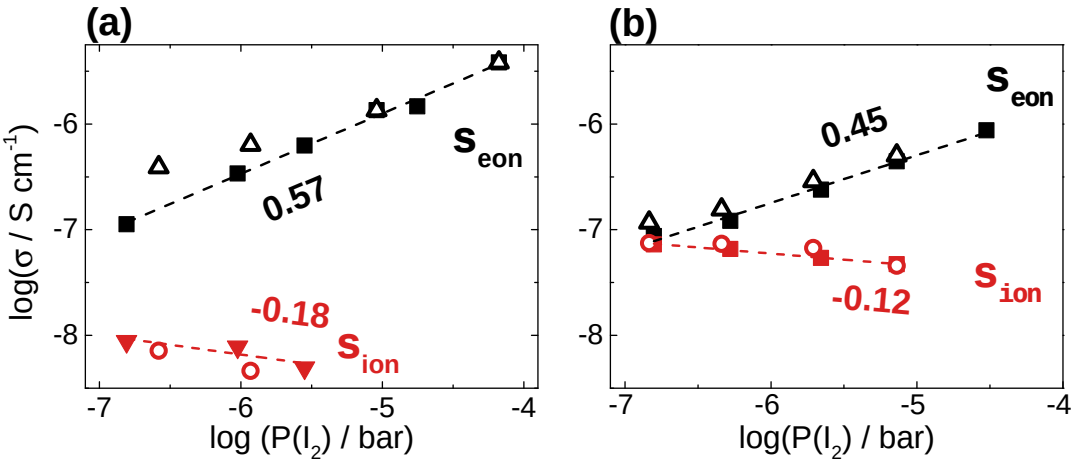

Figure 3.3. Ionic and electronic conductivity of two $MAPbI_3$ pellets as a function of $P(I_2)$, measured at **(a)** 343 K and **(b)** 378 K. Open symbols represent the points taken decreasing $P(I_2)$, to observe reversibility. Slopes of the linear fits are given on the figure.

In this scenario, $P(I_2)$ would only affect the electronic transport, as long as the induced stoichiometry change does not exceed the intrinsic ionic disorder (I-region of **Fig.3.1a**). This is supported by electrical measurements under Ar atmosphere showing comparable values of the ionic and electronic conductivity (see e.g. **§ 2.2**). Since electronic carriers are expected to have much higher mobilities with respect to ionic carriers, the comparable conductivities reflect a large discrepancy in the concentrations. For a much larger concentration of $V_I^{\bullet}$ than of $h^{\bullet}$ one would ideally expect a zero dependence in the double logarithmic plots. This, however, is not completely in line with the experimental observation that the logarithm of the ionic conductivity changes with $\log P(I_2)$ (**Fig. 3.3a**), though much less than what expected for $\log [V_I^{\bullet}]$ (**Fig.3.1a**).

The observed behavior could be explained by imagining that the probed $P(I_2)$-range falls into a transition between I and P regions. For this to be realistic, the ionic and electronic defect concentrations would have to differ not more than 1-2 orders of magnitude, and based on mobility data for ionic ($10^{-9} cm^2 \cdot s^{-1}$ [91], also **§ 3.5**) and electronic carriers (10-100 $cm^2 \cdot s^{-1}$ under illumination[15,119]), the expected discrepancy in the carrier concentrations is much higher. To reconcile this difference, one could imagine that in the dark, the electronic carrier mobility is much lower than under illumination, as it is unexpected for the low temperatures used in our measurement. It is also adequate to question the accuracy of the ionic mobility measurements of Ref.[91].

As of now, no direct measurements (e.g. by tracer diffusion) of mobilities/diffusion coefficients of the mobile iodine species have been reported for $MAPbI_3$. In addition, no Hall effect measurements (that could give electronic mobilities and concentrations) in the dark have been successful. In the absence

of such characterizations, the situation remains unfortunately still partially unclear. Be it as it may, these uncertainties do not affect our qualitative conclusions regarding the nature of the ionic and electronic charge carriers in $MAPbI_3$.

Stoichiometric variations

Dominant charge carriers in $MAPbI_3$ are $h^\bullet$ and $V_I^\bullet$.

3.4 CONDUCTIVITY VS DOPANT CONTENT

Similarly to the analysis of the stoichiometric variations, we can measure conductivity as a function of doping content and compare it with the defect diagram previously calculated. Again, under the assumption that the mobility does not change with dopant content, we can directly compare conductivity trends with defect concentration slopes obtained from the model. This experiment can confirm or discard the hypothesis that $V_I^\bullet$ and $h^\bullet$ are the dominant charge carriers in $MAPbI_3$.

Here, we incorporate Na in the perovskite lattice where, due to its compatible ionic radius with Pb (116 pm and 133 pm, respectively)[120], we expect it to occupy a Pb-site, and thus to form a substitutional defect of effective negative charge (Na'_{Pb}). This corresponds to acceptor doping, and the relevant defect diagram (**Fig. 3.1b**) predicts that Na must enhance the concentration of all positive defects, both ionic and electronic ($V_I^\bullet$, $h^\bullet$), while simultaneously suppressing the concentration of negative ones (V'_{MA}, e'). As shown in **Fig. 3.4a**, when comparing conductivities of pure and Na-doped samples, we observe a parallel increase in both ionic and electronic conductivities of ~ 1 order of magnitude.

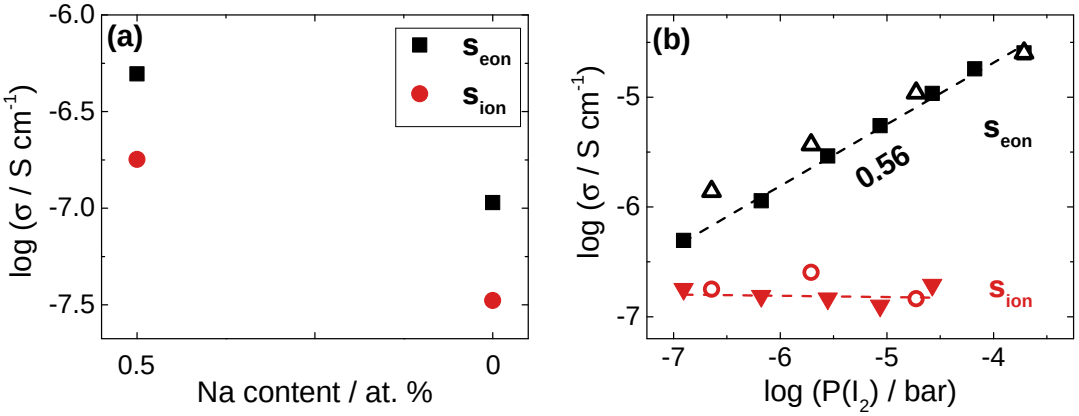

Figure 3.4. (a) Ionic and electronic contributions to the conductivity of a $MAPbI_3$ pellet as a function of Na content, measured at 343 K under identical conditions ($P(I_2) = 2 \cdot 10^{-7}$ bar, $P(O_2) = 5 \cdot 10^{-5}$ bar). **(b)** Conductivity as a function of $P(I_2)$ for a Na-doped $MAPbI_3$ sample (0.5 % at. Na), measured at 343 K.

This behavior is fully in agreement with the defect chemical modeling and clearly confirms $V_I^{\bullet}$ and $h^{\bullet}$ to be the dominant charge carriers in $MAPbI_3$. We can also obtain further confirmation of the successful doping of our sample by measuring its $P(I_2)$ dependence of the conductivity. As shown in **Fig. 3.4b**, we observe a clear difference from the $P(I_2)$ dependence collected on a pure sample (**Fig. 3.3**), in that the ionic conductivity here does not vary with $P(I_2)$. This occurrence is indeed expected from the defect model (see the diagram of **Fig. 3.2a**, in particular the I-region), since as stated previously the $P(I_2)$ necessary to reach the P-region for an acceptor doped sample must be greater than the one required to do the same on a pure sample. We have therefore obtained a clear confirmation that the dominant charge carriers in $MAPbI_3$ are $V_I^{\bullet}$ and $h^{\bullet}$.

Doping experiment

Dominant charge carriers confirmed to be $V_I^{\bullet}$ and $h^{\bullet}$.

3.5 ESTIMATING IONIC MOBILITY

In addition to conclusions on the nature of the dominant charge carriers in $MAPbI_3$, the doping experiment also allows us to estimate mobility values for the dominant defects based on conductivity data, provided we know the dopant concentration. When a defect situation is dominated intrinsically by ionic defects, these will directly compensate the dopant: in our specific case, $V_I^{\bullet}$ are expected to compensate Na'_{Pb} (**Fig. 3.1b**). Thus, by quantifying Na we obtain the concentration of iodine vacancies in the doped sample. We can assess the Na content of the doped $MAPbI_3$ sample to be 0.5 % at. with respect to Pb by using quantitative ^{23}Na NMR (Appendix **§ 10.2.1**). In addition, we measure its ionic conductivity (at 378 K) to be $2 \cdot 10^{-7}$ S cm^{-1}. Using the vacancy concentration value ($c_{V_I^{\bullet}} = 0.5$ at. $\% = 2 \cdot 10^{-19}$ cm^{-3}) in the conductivity expression ($\sigma = u_{V_I^{\bullet}} \cdot c_{V_I^{\bullet}} \cdot q$), we obtain a value for the mobility of $u_{V_I^{\bullet}} = 5 \cdot 10^{-8}$ cm^2 V^{-1}s^{-1}, consistent with previous reports.[91] It is important to note that the mobility value extracted here represents only a lower limit, due to the fact that not all Na atoms incorporated might be effectively acting as dopant. In addition, generating high carrier concentrations at such low temperatures could result in a large degree of defect association, which would further limit the effective conductivity enhancement given by the dopant. As a last step, we can use this limit value to extract a diffusion coefficient through the Nernst-Einstein relationship ($D_{V_I^{\bullet}} = u_{V_I^{\bullet}} \cdot \frac{k_B T}{q}$), obtaining $D_{V_I^{\bullet}} = 2 \cdot 10^{-9}$ cm^2 s^{-1}. We can now compare this value with the one calculated if V'_{MA} would be the

fastest moving ionic defect. Under the assumption that Schottky disorder is the dominant defect reaction in undoped $MAPbI_3$ ($[V'_{MA}]=[V_I^\bullet]$), and using the diffusion data previously obtained for MA ions (**§ 2.4**), we calculate a diffusion coefficient for methylammonium vacancies ($D_{V'_{MA}}$) of $3 \cdot 10^{-12}$ cm^2 s^{-1}. This value is 2-3 orders of magnitude too low to account for the measured ionic conductivity. This occurrence confirms that, under equilibrium conditions, $V_I^\bullet$ motion gives the only relevant contribution to the ionic conductivity of $MAPbI_3$.

Ionic mobility estimate

$V_I^\bullet$ only relevant contribution to ion transport; $u_{V_I} \geq 5 \cdot 10^{-8}$ cm^2 V^{-1} s^{-1}

3.6 CONCLUSIONS

Aim of this chapter was to identify the majority charge carriers in the mixed-conducting perovskite $MAPbI_3$ under equilibrium conditions. The most relevant conclusions of our analysis are:

- Defect chemical modeling is successfully used to predict defect concentration changes as a function of stoichiometry and doping.
- Electrical measurements, together with defect chemical modeling, show that dominant ionic and electronic carriers are $V_I^\bullet$ and $h^\bullet$.
- The only relevant contribution to ionic charge transport is due to $V_I^\bullet$.
- Stoichiometry change and/or doping allow us to achieve a large degree of tunability of the electrical properties of $MAPbI_3$.

4

LIGHT EFFECTS ON IONIC TRANSPORT

Abstract. *This chapter focuses on the study of ionic conductivity in $MAPbI_3$ under illumination. Using multiple techniques (d.c. galvanostatic polarisation, permeation cell experiments, emf measurements, I_2-excorporation rate analysis and Hall effect measurements) we show that, in $MAPbI_3$, the mixed-conducting nature of the conductivity is preserved under light, due to a large photo-induced enhancement of the ionic contribution. We propose a mechanism for this surprising finding based on the interaction between photo-generated carriers and lattice ions.*
This work was performed in close collaboration with Dr. Gee Yeong Kim who performed the majority of the electrical and electrochemical experiments.

Publications. *This study has been published in Ref.[121,122].*

4.1 INTRODUCTION

Anomalous hysteresis in i-V sweeps has been reported in PSCs under operation, indicating that HOIHPs exhibit a substantial ionic conductivity even under illumination.[35,123,124] In addition, light has been reported to induce an enhancement of the apparent dielectric constant in these materials,[36,125] likely caused by an increased chemical capacitance.[31,96] The topic is still heavily debated in the community, even though many reports have directly linked ion conductivity with these phenomena.[31,94,126–129] These observations, however, raise an important question: if these materials are mixed conductors under equilibrium, and their semiconducting properties allow for a massive concentration of electronic carriers to be photo-generated, why is the ionic contribution still relevant under illumination, and not simply overwhelmed? We will show in this chapter that the reason lies in an enormous -and rather surprising- increase of ionic conductivity upon illumination, which takes place in $MAPbI_3$ alongside the expected increase in the electronic contribution.

A few reports have previously suggested a light-induced increase of ionic

conductivity, but on a completely speculative level.[130,131] Indications are also found by using d.c. galvanostatic polarisation measurements,[31,132] that however do not provide sufficient proof if not backed up by additional experiments. This is already the case in the dark (i.e. under equilibrium conditions), but is even more relevant under illumination, where the high concentration of electronic carriers and the absence of a thermodynamic equilibrium substantially complicate the picture. For this reason, we performed several further experiments in order to unambiguously show that, in $MAPbI_3$, the ionic conductivity is indeed massively increased upon illumination. These characterizations are:

- **emf measurements** under illumination, where an electrochemical voltage is generated by applying two different I_2 activities over a sample.
- **permeation cell experiments**, where we applied an high $P(I_2)$ on one side of a $MAPbI_3$ film as I_2-source, while using Cu on the other side as I_2-sink and then comparing the induced permeation rate in the dark and under illumination.
- analysis of the **rate of I_2-excorporation** from $MAPbI_3$ films immersed in toluene, comparing the situation with and without illumination.

All these characterizations are clear in showing a photo-induced enhancement of ionic conductivity in $MAPbI_3$. Even more importantly, they give us for the first time evidences that such striking effects can take place in solids.
As a follow-up, we collected information on the nature of the moving ion under illumination, by:

- **^{13}C tracer diffusion** experiments under light.
- **^{1}H and ^{13}C NMR** on $MAPbI_3$ thin films with and without illumination.
- analysis of the conductivity under light as a function of **stoichiometry**.

The results clearly indicate that iodine is the mobile ion also under illumination (most probably through a vacancy-assisted conduction mechanism). As a final step, we propose a model for the photo-induced enhancement of ion conduction that relies on the well-known (for alkali halides) self-trapping of electron holes on halide lattice sites. This process could make a site exchange between regular and interstitial sites energetically accessible, ultimately yielding an increased halide vacancy concentration and, as a consequence, an enhanced ionic conductivity.

4.2 INDICATIONS OF LIGHT-ENHANCED ION CONDUCTION

First indications of light-enhanced ionic conductivity were provided by Yang *et al.*[31] using d.c. galvanostatic polarisation measurements on $MAPbI_3$ pellets. We provide here an analogous experiment on $MAPbI_3$ thin films, in which we can achieve a uniform illumination of the samples. As shown in **Fig. 4.1a**, a significant voltage transient is still visible under illumination, with a slightly shorter time scale with respect to dark conditions. The analysis of these transient, given in **Fig. 4.1b**, shows how both ionic and electronic conductivities increase, almost of the same amount, as a function of light intensity. We will discuss this parallel increase more in detail below. Here it should be noticed that even at low light intensity (1 mW/cm^2), the measured enhancement is already very large ($\sim$ 100-fold).

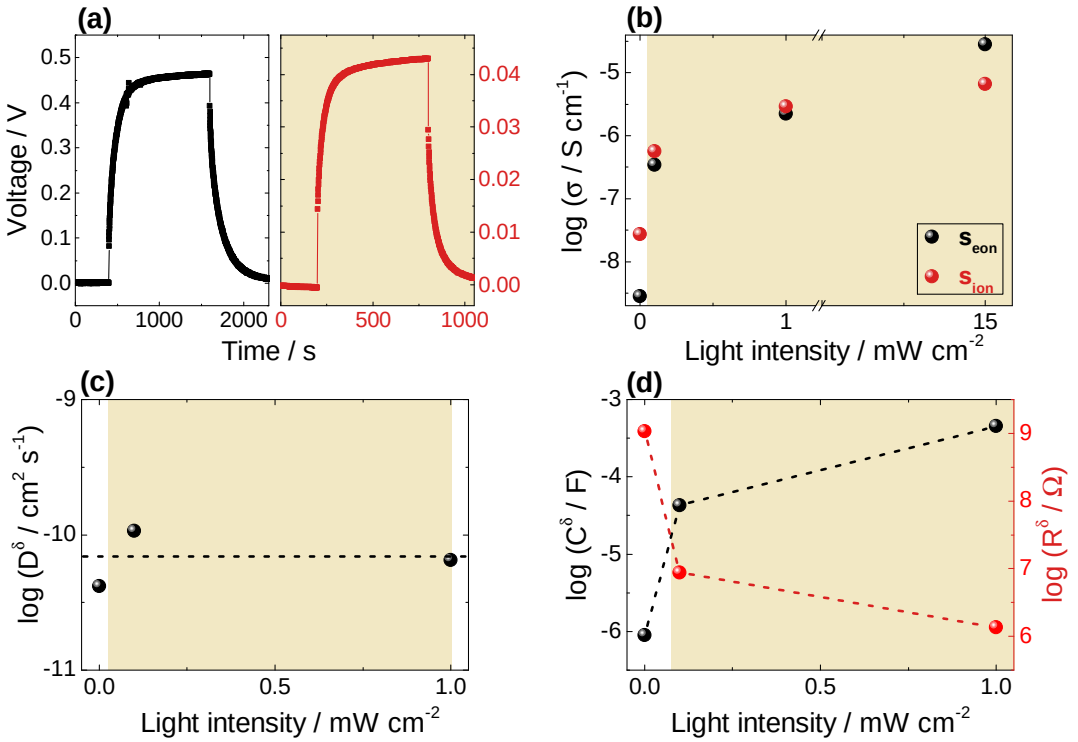

Figure 4.1. **(a)** D.c. galvanostatic polarisation in $MAPbI_3$ thin films, recorded at 333 K and Ar atmosphere (10 nA current), in the dark dark (left) and under 0.5 mW/cm^2 illumination (right, yellow region). Note different y-axis scales. **(b)** Ionic and electronic conductivity, **(c)** chemical diffusion coefficient (D^δ), **(d)** chemical capacitance (C^δ) and chemical resistance (R^δ) as a function of light intensity. All data are extracted from d.c. polarization curves as the ones given in panel (a) collected at 313 K under Ar.

As mentioned previously, the d.c. galvanostatic experiments are not sufficient to decisively confirm the presence of ionic conductivity. Nevertheless, they provide a clear indication that this process is indeed taking place. In particular, a

thorough analysis of the voltage transient under illumination shows how this, similarly as in the dark situation, conforms rather nicely to a chemical diffusion process (Appendix § **10.3.1**). Furthermore, from the polarization time scale (τ^{δ}) we can extract a chemical diffusion coefficient (D^{δ}) that is insensitive to light intensity, in contrast to the behavior observed in the conductivities (**Fig. 4.1c**). This occurrence is theoretically expected for a stoichiometric polarization, since τ^{δ} is the product of a chemical capacitance and a chemical resistance ($\tau^{\delta} = R^{\delta}C^{\delta}$) varying in opposite ways as a function of light intensity (**Fig. 4.1d**). These results provide consistent indications that a substantial ionic conduction is indeed present in $MAPbI_3$ under illumination.

D.c. polarisation experiments under light

Steady state and transient indicate significant ion contribution to the conductivity also under light.

4.3 CONFIRMING THE PRESENCE OF ION CONDUCTIVITY UNDER LIGHT

Unambiguous confirmation of the above mentioned indications come from a series of different electrical and electrochemical experiments, i.e. emf voltage measurements, permeation cell experiments and analysis of the I_2-excorporation rate upon immersing $MAPbI_3$ in toluene.

Let us start by discussing the emf experiments, that are conceptually analogous to what was presented for the equilibrium situation (§ **2.2**). Again, the experiment consists in applying different iodine activities over a $MAPbI_3$ sample, thus yielding a battery cell with $MAPbI_3$ as electrolyte, in which the electromotive force (emf) can be measured in the form of voltage. For a purely electronic conductor, such a cell yields 0 V, while a pure ionic conductor gives the full Nernst voltage determined by the difference in the iodine activities applied (details in § **2.2**).

As schematized in **Fig. 4.2a**, here we control the iodine activities by using two metal/metal-iodide mixtures, one Pb-based and one Ag-based. Thermodynamically, the expected voltage is given by the Gibbs free energy of reaction:

$$Pb + 2AgI \rightleftharpoons 2Ag + PbI_2$$

multiplied by the mean ionic transport number ($t_{ion} = \sigma_{ion}/\sigma_{tot}$), averaged over the partial pressure range applied.[77,133] As show in **Fig. 4.2b**, the emf voltage is substantial under dark, and decreases only slightly upon illumination. The extracted t_{ion} values under different light intensities (0.7 in the dark, 0.6 under

0.3 mW/cm^2 and 0.5 under 3 mW/cm^2 light) indicate that a significant ionic conductivity is still present under light, and that its increase upon illumination must be in the order of the electronic enhancement. This observation is in semi-quantitative agreement with d.c. galvanostatic polarisation experiments presented above (**Fig. 4.1c**). We note, however, that the used mixtures are expected to establish a very low iodine activity over the $MAPbI_3$ sample, that could potentially be below the *p-n* transition (see the defect diagram of **Fig. 3.1**, in particular the N region). Since t_{ion} is naturally dependent on the stoichiometry, and since we do not have d.c. galvanostatic data at such low iodine activities, we cannot directly compare this t_{ion} values with the ones extracted from the previous experiments. Nevertheless, this experiment gives us clear evidences that a substantial ionic conduction is present under illumination, since, as already mentioned, a emf voltage of ~ 0 would be measured if only electronic conduction would be enhanced by light.

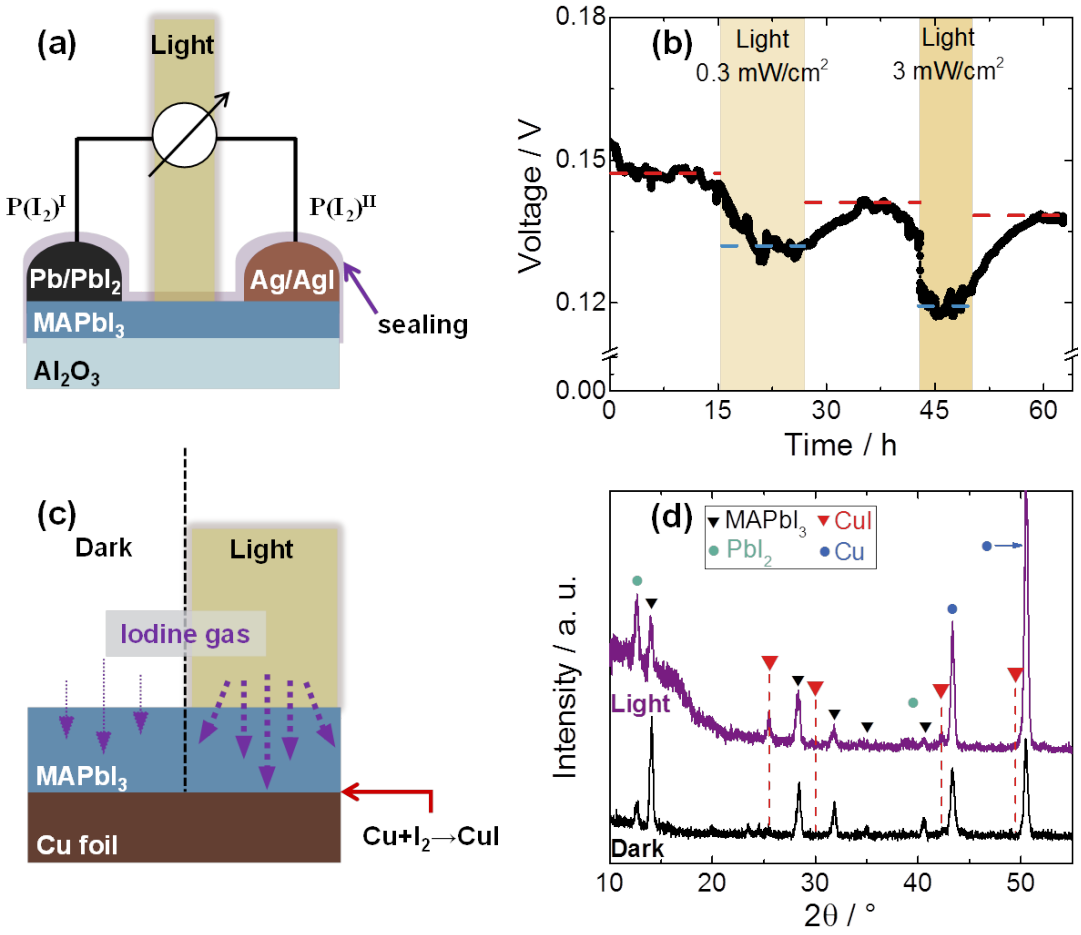

Figure 4.2. **(a)** Schematics of the emf experiment. **(b)** Voltage measured across the emf cell of (a), with and without illumination at different intensities. **(c)** Schematics of the permeation cell experiment. **(d)** XRD analysis of the permeation cell after exposure to iodine, with and without light.

Another important experiment that can prove the increased ionic conductivity upon illumination is the permeation cell schematized in **Fig. 4.2c**. In this experiment, a $MAPbI_3$ thin film is grown on a Cu substrate, and later exposed to a fixed $P(I_2)$; part of the sample is illuminated, in order to induce the enhanced ionic conduction. This is expected to significantly enhance the I_2 permeation rate through $MAPbI_3$, thus allowing larger quantities of I_2 to reach the Cu side at a given time, where they can react and form CuI. The driving force for this mass transport is given by the difference in iodine activity between the $I_2/MAPbI_3$ interface (high activity, I_2-source) and the $Cu/MAPbI_3$ interface (low activity, I_2-sink). The permeation rate is then represented by the quantity of CuI that is ultimately formed at the latter interface. As shown in **Fig. 4.2d**, XRD analysis show formation of CuI under illumination, while in the dark no CuI reflections are visible. This observation is in agreement with the expected increase of the permeation rate upon illumination, that is calculated as ~ 1 order of magnitude (Appendix § **10.3.2**). It should however be noted that the permeation rate of I_2 through the newly-formed CuI film can also greatly affect the final CuI quantity, especially when the film becomes thick. This would lead to an underestimation of the ionic conductivity enhancement. In addition, we note that if only electronic conductivity was enhanced, the permeation flux would also increase, but to a substantially lesser degree (Appendix § **10.3.2**).

The final experiment we performed in order to unambiguously confirm the photo-enhancement of ionic conduction is schematized in **Fig. 4.3a**. Here, we immerse $MAPbI_3$ films in toluene (that is a solvent for I_2) and record the I_2-excorporation rate by measuring *in-situ* the I_2 absorption with UV-Vis spectroscopy.

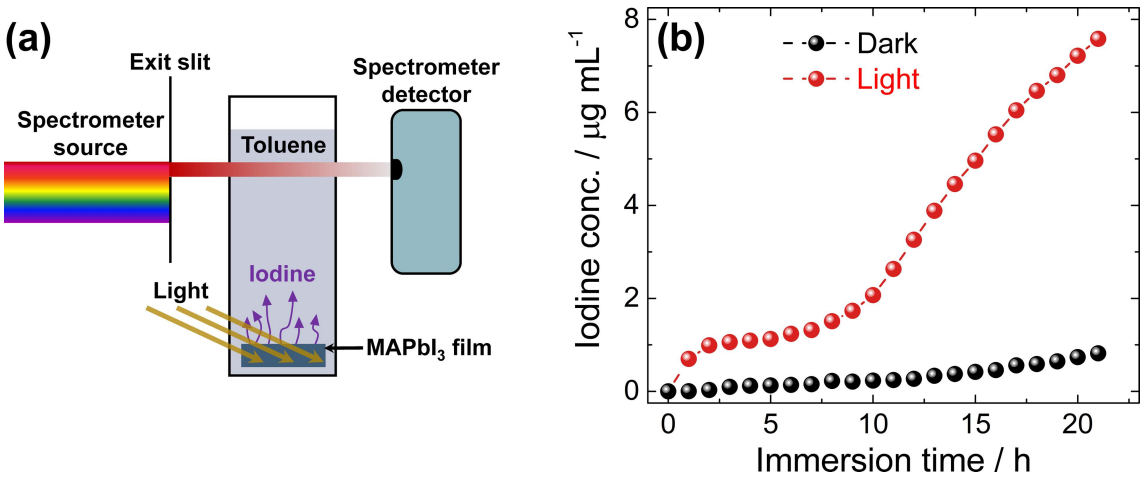

Figure 4.3. **(a)** Schematics of the toluene immersion experiment. **(b)** Rate of I_2 removal from $MAPbI_3$ thin films immersed in toluene in the dark and under illumination (1 mW/cm^2).

The detailed evaluation of the excorporation process is not trivial, and it is given in Appendix § **10.3.3**. Here we simply state that, for low I_2 amounts in toluene, the iodine outflux into toluene (and thus the final I_2 content) is expected to be proportional to the ionic charge carrier concentration in $MAPbI_3$. We thus record the I_2-excorporation rate with and without light (**Fig. 4.3b**), clearly observing an excorporation rate that is greatly accelerated by illumination ($\sim$ 10 times), consistently with the expected ionic conductivity enhancement. This observation does not only confirm the enhanced ionic conduction under light, but also indicates that this process stems from a photo-induced increase in ionic carrier concentration rather than from mobility effects. As discussed below in § **4.5**, in this respect our experiments indicate that under illumination the dominant ionic charge carriers are $V_I^{\bullet}$, analogously as in the dark.

Light enhancement of ion conduction

All experiments confirm the surprising phenomenon of huge ion conduction increase upon illumination.

4.4 MA CATION DIFFUSION UNDER LIGHT

Having confirmed that $MAPbI_3$ is a mixed conductor also under illumination, it becomes of importance to investigate the nature of the ionic conductivity also under these conditions. Analogously to the situation in the dark (§ **2.1**), the two most probable candidates for solid-state diffusion are MA and I ions. The experiments presented above (I_2-excorporation and Cu permeation cell in § **4.3**) clearly indicate significant iodine conductivity, while direct evidences of minor contributions due to MA motion have not yet been given. In this section we focus therefore on the organic cation.

At first, we perform ^{13}C tracer diffusion experiments (as previously carried out on pellets under equilibrium conditions in § **2.4**) on $MAPbI_3$ thin films. A schematic of the experimental setup is given in **Fig. 4.4a**. As shown in **Fig. 4.4b**, no difference is visible in the ^{13}C diffusion profiles with and without light, ruling out substantial MA diffusion in $MAPbI_3$ also under these conditions. Nevertheless, we note that a MA diffusion process, albeit very sluggish, still takes place in $MAPbI_3$, consistently with what we observed in pellet samples under equilibrium conditions (§ **2.4**). The difference here is that the annealing process resulted in an increase of the ^{13}C content across the entire sample, likely due to the finite nature of the thin films. However, we note that a single diffusion process in a finite medium cannot emulate the experimental data.[98,106] On the other hand,

the flat tail visible in the profile speaks for the presence of two distinct processes. This is not surprising considering that a film-to-film mechanical contact such as the one established here for the isotope treatment (§ **9** and **Fig. 4.4a**) can easily be non-uniform. As shown in **Fig. 4.4b**, we can satisfactorily simulate our profiles by assuming two distinct processes with the same surface rate constant (k^*_{MA} = $2 \cdot 10^{-11}$ cm/s) but having different diffusion coefficients ($D^*_{MA,1}$ = $1 \cdot 10^{-13}$ cm^2/s, $D^*_{MA,2}$ = $3 \cdot 10^{-17}$ cm^2/s). Details on the simulation can be found in the Appendix (§ **10.3.4**).

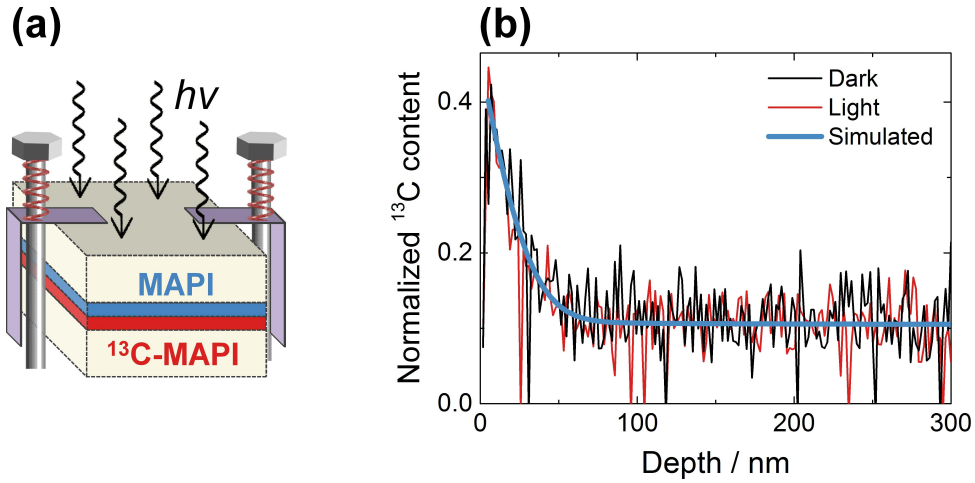

Figure 4.4. ^{13}C tracer diffusion experiments on $MAPbI_3$ thin films. **(a)** Schematics of the experiment. **(b)** ^{13}C tracer diffusion profiles obtained at 333 K in the dark and under 1 mW/cm^2 illumination. Annealing time was 40 hours. The profile was fitted with two separate diffusion processes in a finite medium, with the same k^*_{MA} (=$2 \cdot 10^{-11}$ cm/s) but with separate D's ($D^*_{MA,1}$ = $1 \cdot 10^{-13}$ cm^2/s, $D^*_{MA,2}$ = $3 \cdot 10^{-17}$ cm^2/s).

The fast diffusion coefficient extracted here represents only a lower limit, as this process is surface controlled (Appendix § **10.3.4**). While presently direct experimental evidences to identify these processes are lacking, we recognize that this situation is consistent with a comparatively fast grain boundary diffusion taking place with a comparatively sluggish bulk diffusion (providing the distance between the grain boundaries is sufficiently large). Note that, for both A- and B-site cations in oxide perovskites, a grain boundary diffusion significantly faster than the bulk one is a rather common occurrence.[134–138] Consistently with this hypothesis, the slow diffusion coefficient extracted here is in agreement with the upper limit value previously measured on bulk samples ($9 \cdot 10^{-15}$ cm^2/s at 333 K, see § **2.4**), while the fast coefficient exceeds it. Also, the fact that no second, fast, diffusion process is visible in the case of bulk samples (**Fig. 2.4**), which show much larger grain sizes (and thus fewer grain boundaries) supports the above claim. We recognize that the comparison between the diffusion coefficients obtained for bulk and thin film samples can only be qualitative, due to

the different defect concentrations and microstructures involved.

To confirm these results, we also carried out ^{1}H and ^{13}C NMR measurements. Albeit rather challenging from a practical point of view (details in § 9, see also **Fig. 4.5a**), it is possible to collect NMR signals from both ^{1}H and ^{13}C in $MAPbI_3$ thin films, and obtain NMR data under illuminated conditions. **Fig. 4.5** shows the NMR signals obtained at different temperatures on ^{1}H and ^{13}C, in the dark and under illumination.

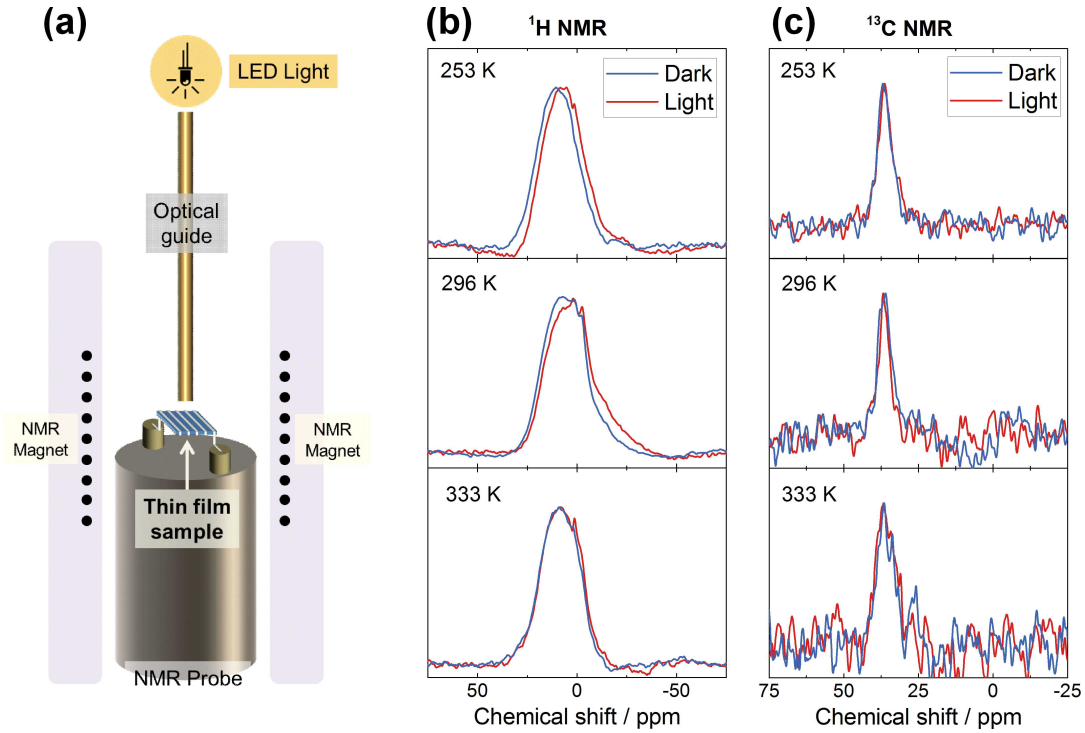

Figure 4.5. (a) Schematics of the NMR experiment with *in-situ* illumination. **(b)** ^{1}H and **(c)** ^{13}C NMR collected at different temperatures on $MAPbI_3$ films in the dark and under 10 mW/cm^2 illumination. Minor changes in the chemical shift can be due to phasing issues in the in-house built flat coil.

In the dark, even though the temperature range spans 80 K, there is no visible changes in the linewidth of the two signals, in agreement with what we observed on bulk samples (§ 2.4, **Fig. 2.3**). This indicates, unsurprisingly, the absence of significant long-range motion of MA cations also in thin film samples. More interestingly, the same behavior is present under illumination. In addition, at any temperature studied, there is no change in the signal linewidth or shape upon illumination, indicating that the conclusions drawn in the dark regarding the absence of solid state MA diffusion in $MAPbI_3$ are also valid under illumination.

MA cation diffusion under illumination

No changes from the dark situation. No significant MA diffusion.

4.5 PREDOMINANT MOBILE DEFECTS UNDER LIGHT

All the experiment reported in § **4.3** give clear evidences of iodine transport, while ^{13}C tracer diffusion and NMR under light rule out any significant methylammonium diffusion (§ **4.4**). In this respect, the situation is similar to equilibrium conditions. Nevertheless, we find it important to definitely assess the nature of the mobile ionic charge carriers also under illumination. To achieve this, we can measure the $MAPbI_3$ conductivity as a function of stoichiometry ($P(I_2)$), as previously done under equilibrium conditions. As shown in **Fig. 4.6a**, the behavior of $MAPbI_3$ films in the dark is completely in agreement with the one observed in the case of pellets (**Fig. 3.3**), where the dominant carriers were identified as $h^\bullet$ and $V_I^\bullet$.

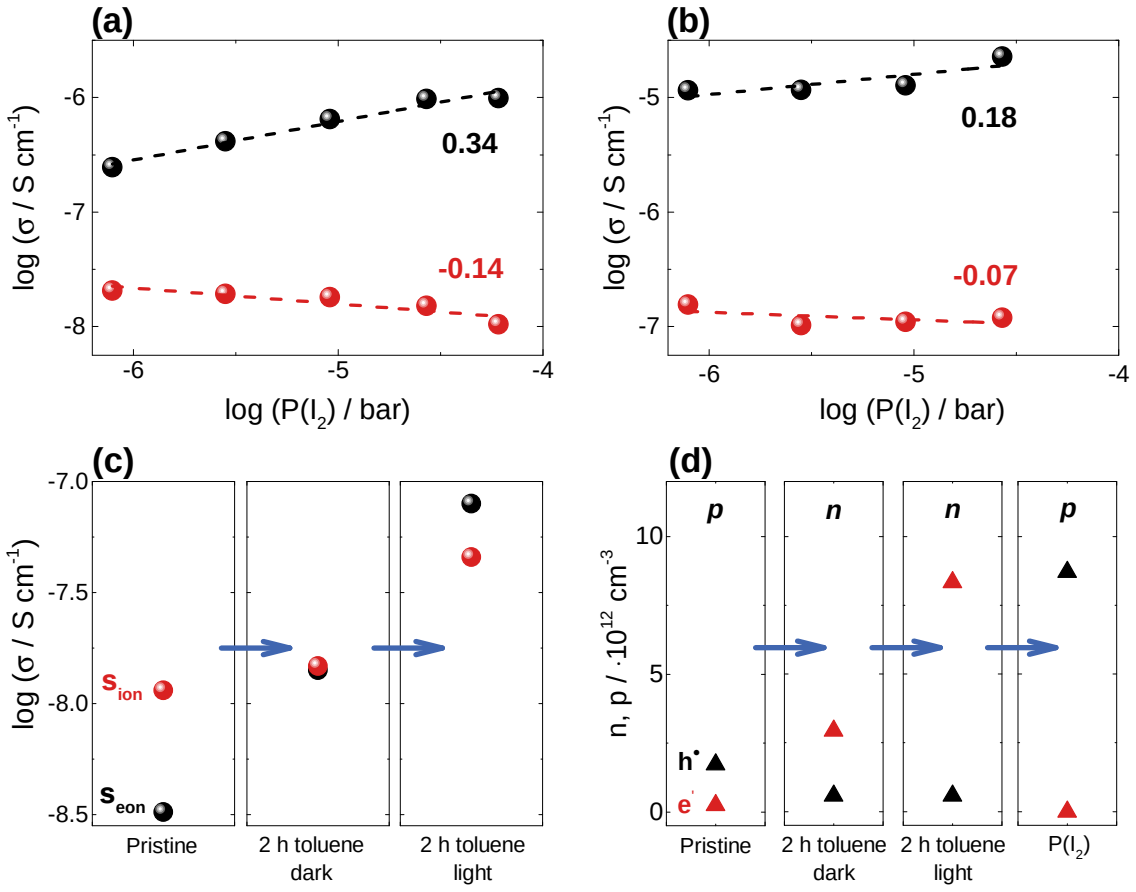

Figure 4.6. (a), (b) Conductivity as a function of iodine partial pressure (a) in the dark and (b) under 1 mW/cm^2 illumination. **(c), (d)** Conductivity variations upon immersing a $MAPbI_3$ thin film in toluene, initially for 2 h in the dark, then for 2 h under illumination. The conductivity changes after the various treatment steps are measured by (c) d.c. galvanostatic polarisation in the dark and (d) by Hall effect measurements under 1 mW/cm^2 illumination. In this last measurement, after the toluene treatment, a $P(I_2)= 3.6 \cdot 10^{-6}$ bar is applied to observe reversibility to *p*-type conduction.

Interestingly, upon illumination, a qualitatively similar situation is observed in the stoichiometry dependence (**Fig. 4.6b**). Here, the electronic conductivity still increases with $P(I_2)$, albeit with a smaller slope than in the dark. We note that under light this dependence can also be attributed to changes in the recombination center (or deep trap) density upon $P(I_2)$ exposure. Regarding ionic conductivity, this slightly decreases with $P(I_2)$, even though the slope falls between the error margin of our characterization. This overall observation is expected, since smaller slopes (for both ionic and electronic charge carriers) under illumination are a direct consequence of a higher carrier concentration and the resulting partial insensitivity to stoichiometry changes. These observations therefore suggest that $h^\bullet$ and $V_I^\bullet$ are the majority electronic and ionic charge carriers in $MAPbI_3$ also under light.

Another interesting observation regarding the dominant charge carriers in $MAPbI_3$ comes from conductivity and Hall effect measurements performed after immersing $MAPbI_3$ in toluene. As stated in **§ 4.3**, toluene is expected to remove I_2 from $MAPbI_3$ and thus enhance its $V_I^\bullet$ concentration. This is expected to happen in parallel to a decrease in $h^\bullet$ concentration (see **(Eq. 3.2)**). Being an I_2-sink, toluene effectively behaves similarly to the application of a low $P(I_2)$. Interestingly, as shown in **Fig. 4.6c**, the ionic conductivity indeed increases upon toluene treatment, both when the treatment is carried out in the dark and much more so when illuminating (accelerated excorporation). Interestingly, the electronic conductivity also increases, in contrast to the expected behavior for a *p*-type conductor. This occurrence finds its explanation in the fact that, if the effective $P(I_2)$ established by toluene is low enough, one must reckon with a *p* to *n* transition. As shown in **Fig. 4.6d**, Hall effect measurements indeed confirm that a pristine *p*-type sample turns to *n*-type after toluene treatment. The transition, as expected, can be reverted by applying $P(I_2)$ to the sample. Interestingly, we observe no electronic mobility changes upon these treatments ($u \approx 5 - 10\ cm^2V^{-1}s^{-1}$), indicating variation only in the carrier concentrations. These characterizations give us another evidence of the large degree of tunability of the electrical transport properties that is achieved in $MAPbI_3$ by modifying its stoichiometry, extending the potentially affected region also under illumination.

From all the above experiments we thus conclude that $h^\bullet$ are clearly the dominant electronic charge carriers in $MAPbI_3$ under illumination, both in pristine samples and under relatively high $P(I_2)$. As expected, under relatively low $P(I_2)$ conduction electrons become the dominant electronic charge carriers. Concerning the nature of the ionic charge carriers, we recognize that the same degree of

confidence cannot be achieved. Nevertheless, all the above findings are consistent with $V_I^\bullet$ being the dominant ionic charge carrier also under illumination.

Predominant mobile defects under light

Similarly to dark, $h^\bullet$ and $V_I^\bullet$ are likely the dominant charge carriers. At very low iodine activities, conduction electrons come into play.

4.6 MECHANISM OF THE PHOTO-INDUCED ENHANCEMENT

We have now sufficient information on the photo-induced enhancement of ion conduction to speculate about the underlying mechanism. Let us first review the main findings concerning this remarkable effect:

- Ionic conduction is enhanced by orders of magnitude upon illumination.
- The predominantly mobile ion is iodine, likely with $V_I^\bullet$ as dominant ionic defect.
- Experiments indicate concentration effects rather than mobility.

Based on these considerations, our proposed mechanism is sketched in **Fig. 4.7**. Light generates electron-hole pairs, corresponding to an electron transfer between I atoms and Pb atoms. This is so because, in $MAPbI_3$, the valence band maximum is essentially composed by occupied I *p* orbitals (possible hybridized with Pb-antibonding orbitals), while the conduction band minimum by unoccupied Pb *p* orbitals (with negligible coupling to I).[111,139,140] We can therefore recognize that the photo-generated electron holes could rapidly form neutral iodine atoms sitting on regular iodine sites ($I_I^x + h^\bullet \rightleftharpoons I_I^\bullet$ in defect notation). This process is sketched in **Fig. 4.7b**. Notably, the size of a iodide ion (r_{I^-} = 2.1 Å) is greatly reduced when coupling with an electron hole (r_{I^0} = 1.5 Å). This makes it possible for the neutral species to move into a neighboring interstitial site, while iodide ions are unlikely to fit interstitially in the dense perovskite structure. This process yield a vacant iodine site that can act as ionic charge carrier and thus cause the enhanced ion conduction. In addition, this newly formed interstitial particle (I_i^x) can be stabilized even further by subsequent structural relaxations resulting from the large polarizability and tendency to form covalent bonds of the iodide ions. As schematized in **Fig. 4.7c**, this process is expected to involve the immediate I-environment in forming dumbbells or similar complex aggregates (I_2^-, I_3^{2-}, etc.). In alkali halides, these aggregates are a rather common occurrence; also, in these compounds the interaction between halide sites

and electron holes ordinarily takes place and is referred to as self-trapping of electron holes.[141–145] Even more relevantly, self-trapped holes and complex aggregates have also been computationally predicted for $MAPbI_3$,[146–148] and very recently the presence of neutral interstitial was even experimentally observed through structural analysis.[149] It seems therefore quite plausible that such a site-exchange between regular and interstitial iodine lattice sites could rapidly take place under illumination.

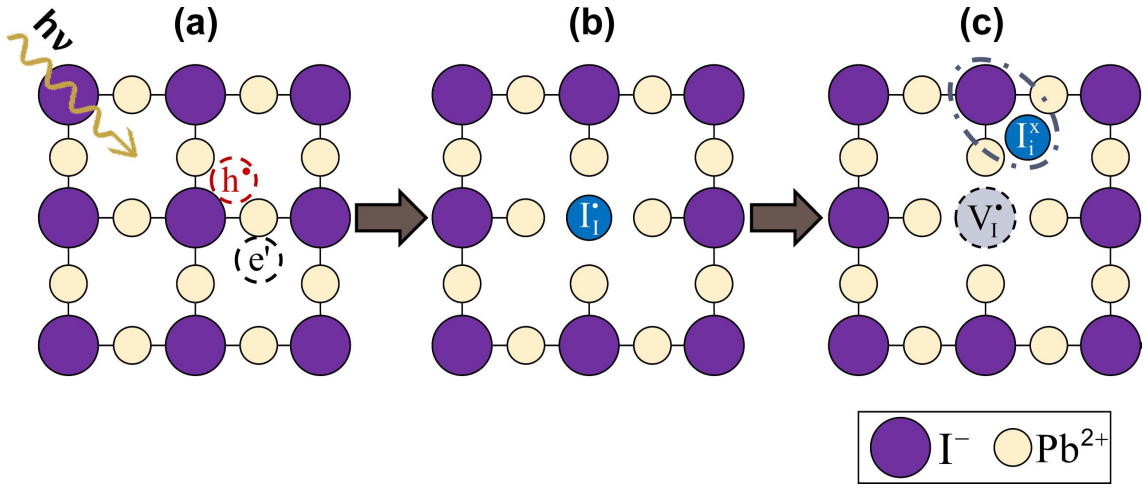

Figure 4.7. Schematic of the proposed mechanism for the photo-induced ion conduction. **(a)** Light induces electron-hole pairs, and holes are quick to react with iodide ions on regular lattice sites. **(b)** Iodide ions become neutral, shrinking considerably. In defect notation, this correspond to an effectively positively charged defect ($I_I^\bullet$). **(c)** This neutral and small specie can now move to a close-by interstitial site (I_i^x), and even form aggregates (e.g. I_2^-, I_3^{2-}) with other iodide ions as the one depicted here.

The above-mentioned electron-ion interaction can be written, in defect notation (Appendix § **10.1.1**), as:

$$I_I^x + h^\bullet \rightleftharpoons I_i^x + V_I^\bullet \tag{4.1}$$

and the result is an effectively increased $V_I^\bullet$ concentration upon removal of iodine ions from lattice sites. This can directly explain the photo-induced increase of ion conduction. In the extreme case, we can assume **(Eq. 4.1)** to be in equilibrium, with the mass action law dictating a fixed ratio of $[h^\bullet]/[V_I^\bullet]$. This is consistent with the observed almost parallel increase of ionic and electronic conductivity obtained upon illumination (**Fig. 4.1**).

Some more details concerning this model have to be discussed:

(i) The assumption of a fixed ratio between $[h^\bullet]$ and $[V_I^\bullet]$ (**(Eq. 4.1)**) assumes a constant activity of the neutral iodine interstitial, which is only fulfilled in equilibrium with a gas phase of constant iodine activity. However, illumination

increases the concentration of neutral interstitials, and hence enhances their activity. This is expected to lead to a weaker increase of ionic conductivity when compared to the electronic one upon $P(I_2)$ variations, which is indeed observed (**Fig. 4.1**).

(ii) The substantial ionic conduction increase observed requires a very large number of $V_I^\bullet$ to be generated; this implies a strongly reduced concentration of $h^\bullet$ through **(Eq. 4.1)**. For the material to be still *p*-type (**Fig. 4.6d**), substantial trapping of e' through a different mechanism is required. While we presently have no direct experimental evidence on this process, we could imagine Pb atoms to partially or fully neutralize by coupling with e'. We note that the formation of Pb^0 has been extensively observed in the literature,[38,55,150,151] and in some cases even found to be reversible. This occurrence would also be consistent with our proposed photo-decomposition mechanism (discussed in **§ 6.5**) that happens as a consequence of the photo-induced increase of $V_I^\bullet$.

(iii) The neutral interstitials might be mobile themselves. Then, the evaluation of the ambipolar conductivity in these conditions must take into account shuttle effects.[152] If this motion would be the only relevant ion migration under illumination it could still explain part of our experimental results (e.g. the toluene excorporation), but it would be in contrast with the observation of a significant voltage transient in d.c. galvanostatic polarisation measurements, for which an ionic charge carrier motion is necessary.[152] $V_I^\bullet$ could also undergo a coupled motion with the neutral interstitial, but if this would be the dominant mechanism it would result into a zero net mass transport, and be equivalent to the transport of the self-trapped hole.

(iv) The short distance between regular sites and interstitial sites allow the aforementioned exchange to be quick. On a long run, the enhanced iodine activity given by the formation of neutral interstitials is expected to decrease in favor of an increased outer $P(I_2)$.

We now briefly discuss the implications of this model for the photo-induced decomposition of $MAPbI_3$ and other halide perovskites (details will be given in a later chapter, i.e. **§ 6.5**). The generation of a high number of neutral iodine atoms as a consequence of illumination is only reversible if these remain in the lattice. This is the situation taking place in our normal d.c. polarisation experiments, where complete reversibility is commonly observed. However, if I_2 is extracted by a sink (e.g. toluene, vacuum, ambient gas phase, etc.), the homogeneity range of the $MAPbI_3$ phase may be greatly exceeded and eventually decomposition will take place. We expect the non-stoichiometry level induced by illumination

to be able to exceed the homogeneity range of the $MAPbI_3$ phase and thus surpass the equilibrium stability limit, ultimately leading to decomposition (**§ 6.5**).

Mechanism of photo-induced ionic conduction

Localization of $h^\bullet$ transforms I^- into I^0. The neutral atom can fit in an interstitial site, leaving behind an iodine vacancy.

4.7 CONCLUSIONS

In this chapter we have reported the analysis of the electrical properties of $MAPbI_3$ under illuminated conditions. The major findings can be summarized as follows:

- $MAPbI_3$ is still a mixed conductor under illumination, with a significant portion of ionic conductivity.
- Majority carriers are $h^\bullet$ and $V_I^\bullet$ in pristine samples under light.
- Ion conduction is enhanced by orders of magnitude upon illumination, alongside the expected increase in electronic conduction.
- The proposed mechanism for the ionic conductivity enhancement involves redistribution of iodide ions by localizing $h^\bullet$, followed by site exchange of the shrunk neutral iodine atoms into interstitial site, creating $V_I^\bullet$.
- This process also opens an important photo-decomposition pathway.

5

INTERACTION OF OXYGEN WITH HALIDE PEROVSKITES

Abstract. *In this chapter, we explore the effect of O_2 exposure on $MAPbI_3$ and other halide perovskites. By applying many different techniques (^{18}O incorporation experiments, electrical characterizations, thermodynamic considerations and degradation studies monitored by UV-Vis spectrometry and XRD), we show that $MAPbI_3$ is, as thermodynamically expected, unstable against O_2 under light, but kinetically metastable in the dark. Incorporation of oxygen in the lattice is also sluggish in the dark and is significantly accelerated by illumination. This leads to substantial changes in the electrical (ionic and electronic) transport properties of $MAPbI_3$ analogous to acceptor doping.*
Here we acknowledge the precious help of Tolga Acartürk for the ToF-SIMS measurements and of Dr. Helga Hoier for the XRD characterizations.

Publications. *This study has been published in Ref.[153].*

5.1 INTRODUCTION

The interaction of oxygen with HOIHPs deserves a thorough characterization since it can simultaneously lead to strong improvements in their photoluminescence,[154–156] as well as causing severe degradation to materials and devices.[53–62] The strong photoluminescence enhancement corresponds to a reversible increase in both emission intensity and lifetime, and has been attributed to a reduced density of trap states present after oxygen exposure.[154–156] Curiously, this effect takes place by treating the samples with oxygen under illumination, while there is no significant improvement when treating them in the dark. The time scale in which this enhancement takes place (hundreds of seconds)[154–156] indicate that the reaction is probably not limited to the sample surface, but that chemical diffusion of species also takes place.[154] Considering the degradation processes, formation of superoxide species has been observed when exposing HOIHPs simultaneously to O_2 and light,[53,58,61] and it was attributed to a charge transfer process involving the photo-excited halide perovskite and

the oxygen molecules.[54,56,57] These so-formed superoxide species are then expected to deprotonate methylammonium cations, forming water and volatile methylamine, inducing a complete degradation of the perovskite layer. It is worth noting that the aforementioned studies have been carried out in solar cell devices containing the halide perovskite.[53–58,60,61] However, many selective transport materials ordinarily used in solar cells undergo photo-oxidation or degradation processes when exposed simultaneously to O_2 and light.[157–161] This processes can easily alter the transport properties of the selective contacts and thus heavily weaken the final cell performance, without having to directly affect the halide perovskite layer. For this reason, all characterizations given in this chapter are performed on pure HOIHPs.

Specifically, here we aim at studying their interaction with oxygen both from a thermodynamic and kinetic point of view, again with a special focus on $MAPbI_3$. Under conditions that precede degradation, we expect a certain solubility of O_2 in the $MAPbI_3$ lattice, with the incorporated O-defects potentially acting as dopants. We start by describing this situation through defect modeling. Experimentally, we observe incorporation of O_2 using an ^{18}O tracer, both in the dark, where the incorporation is modest, and under illumination, where it is substantially accelerated. This incorporation, when significant, indeed leads to great variations in the electronic and ionic transport properties of $MAPbI_3$, in a manner that conforms to acceptor doping. In addition, we show through thermodynamic considerations that O_2 is ultimately expected to degrade $MAPbI_3$, but this reaction is only experimentally observed under illumination, since in the dark the sluggish kinetics makes the material metastable. As a last analysis, we study the stability of mixed-halide (Br, I) and mixed-cation (MA, FA) perovskites, as these state-of-the-art device compositions are expected to show a higher stability against oxygen than $MAPbI_3$.

5.2 DEFECT CHEMICAL MODEL OF O_2 INCORPORATION

Let us start by considering oxygen dissolution in the $MAPbI_3$ lattice. In the same way as done in **§ 3** for I_2, the incorporation of O_2 in the $MAPbI_3$ lattice and the corresponding changes in the defect concentrations can be modeled through defect chemical considerations. Since oxygen is an impurity in $MAPbI_3$, it can be treated as a dopant. Due to size considerations, we could expect oxygen to either occupy an iodine vacancy (forming $O_I^{'}$), i.e. substituting iodine, or to sit in an empty interstitial site (yielding $O_i^{''}$). For the following treatment, we will consider the occupation of an iodine vacancy, but we will show later that the

resulting defect diagrams are qualitatively identical in the interstitial case.

The incorporation of oxygen in the $MAPbI_3$ lattice and the corresponding mass action law can be written in the following form:

$$\frac{1}{2}O_2 + I_I^x \rightleftharpoons O_I^{'} + h^{\bullet} + \frac{1}{2}I_2 \qquad K_O = \frac{[O_I^{'}][h^{\bullet}]P(I_2)^{1/2}}{P(O_2)^{1/2}} \tag{5.1}$$

We note that the oxygen incorporation can equivalently be formulated as $\frac{1}{2}O_2 + V_I^{\bullet} \rightleftharpoons O_I^{'} + 2h^{\bullet}$, through the coupling with the iodine non-stoichiometry reaction given previously in **(Eq. 3.2)**, which we repeat here for simplicity:

$$\frac{1}{2}I_2 + V_I^{\bullet} \rightleftharpoons I_I^x + h^{\bullet} \qquad K_I = \frac{[h^{\bullet}]}{[V_I^{\bullet}]P_{I_2}^{1/2}} \tag{5.2}$$

The intrinsic defect situation in the HOIHP structure is again described by a partial Schottky defect equilibrium (**§ 3.2**):

$$MA_{MA}^x + I_I^x \rightleftharpoons V_{MA}^{'} + V_I^{\bullet} \qquad K_S = [V_I^{\bullet}][V_{MA}^{'}] \tag{5.3}$$

From the mass action laws of these defect reactions -together with the electroneutrality condition- we can obtain the defect concentrations as a function of $P(O_2)$, by taking $P(I_2)$ constant and by assuming different regions (I, O) where the oxygen activity is:

Low a_{O_2} (I). Materials behave intrinsically, **(Eq. 5.3)** dominates.

High a_{O_2} (O). (Eq. 5.1) shifted to the right, $[V_I^{\bullet}]$,$[h^{\bullet}]$ increase, $[V_{MA}^{'}]$,$[e^{'}]$ decrease.

The resulting defect diagram is given in **Fig. 5.1a**, which shows that when the O-defect exceeds the intrinsic defect level, all the other defect concentrations are correspondingly affected (O-region). The incorporation of oxygen as an effectively negatively charged species is analogous to the insertion of a metal ion acceptor dopant, such as Na, in the $MAPbI_3$ lattice (compare with **Fig. 3.1b** and **Fig. 3.4a**). The main difference is that the O-impurity ($O_I^{'}$) can be practically inserted post-synthesis, provided it has a perceptible diffusion coefficient to migrate in the lattice. As shown in the next section (**§ 5.3**), this is indeed observed, and it also allows for the O-doping process to be reversible. Since oxygen is ubiquitous, we find it worth to recalculate the previously obtained intrinsic defect diagram of $MAPbI_3$ as a function of $P(I_2)$, this time allowing for a certain concentration of O-defects. The diagram is depicted in **Fig. 5.1b**, and the only

difference with the one previously given in **Fig. 3.1a** is the presence of a extra region (O) dominated by O-defects at very low $P(I_2)$.

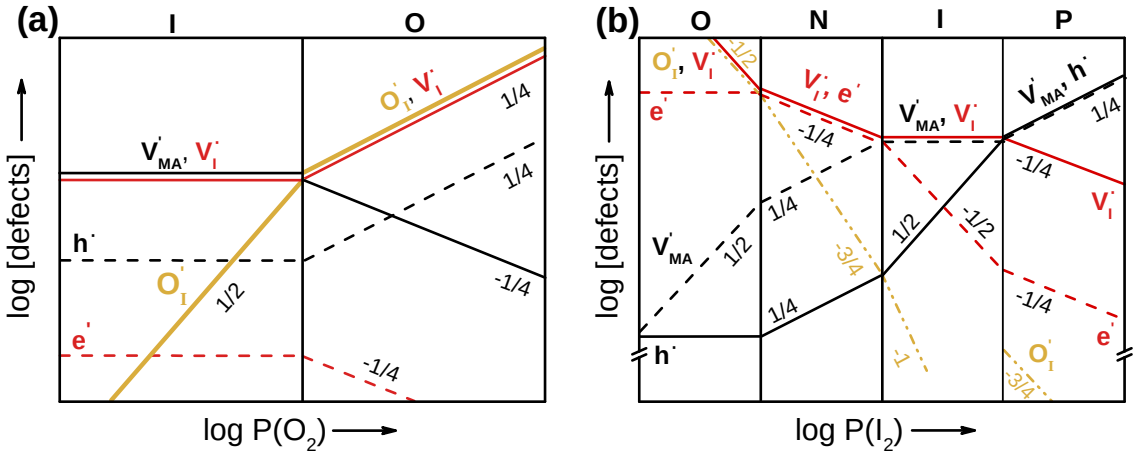

Figure 5.1. Kröger-Vink diagram depicting defect concentrations in $MAPbI_3$ as a function of **(a)** oxygen partial pressure and **(b)** iodine partial pressure including a fixed concentration of O-defects. Calculated slopes are given on the figure.

As previously done for $P(I_2)$we give, for completeness, the defect diagrams of acceptor- and donor-doped $MAPbI_3$ as a function of $P(O_2)$ in **Fig. 5.2**.

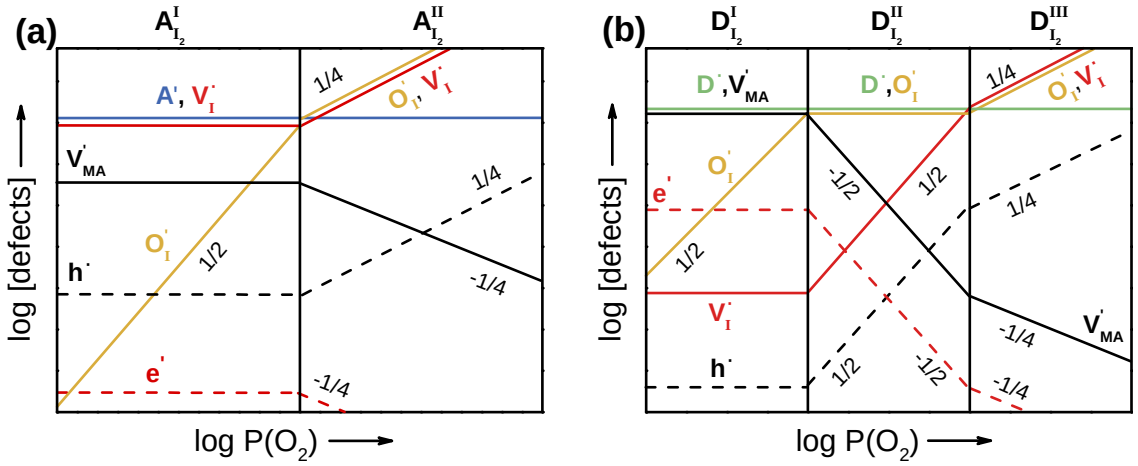

Figure 5.2. Kröger-Vink diagram representing defect concentrations as a function of oxygen partial pressure for **(a)** acceptor- and **(b)** donor-doped $MAPbI_3$. Calculated slopes are given on the figure.

As mentioned previously, we can also perform the defect chemical modeling considering an interstitial oxygen defects (O_i'') instead. In oxide perovskites, this is a rather unlikely occurrence due to the high density of the structure. However, in $MAPbI_3$, the ionic radius of oxide ions is significantly smaller than that of iodide ions (140 and 210 pm, respectively) and this might make an interstitial

oxygen defect energetically accessible. Unsurprisingly, the calculated defect diagram is qualitatively identical to what we obtained for $O_I^{'}$, apart from different slopes due to the double effective charge (see Appendix **§ 10.4.1**, **Fig. 10.11**).

Defect chemical model of O_2 incorporation

When the concentration of O-defects surpasses the intrinsic disorder, it acts as efficient acceptor dopant.

5.3 ^{18}O INCORPORATION EXPERIMENTS

It is of considerable interest to come up with a direct experimental evidence of oxygen solubility and diffusion in $MAPbI_3$. For this purpose, we performed incorporation experiments using an ^{18}O tracer on $MAPbI_3$ thin films, and compared dark and illuminated conditions. The reason for the choice of an oxygen tracer lies in the need to avoid contributions from other oxygen sources (e.g. solvents such as DMSO). In this experiments, the films are exposed to a fixed ^{18}O pressure, at a constant temperature and under different illumination intensities. By measuring the ^{18}O content as a function of depth (using ToF-SIMS), we can reconstruct a diffusion profile of ^{18}O, from which diffusion coefficients and surface rate constants can be extracted, according to Ref.[106]. The treatment is analogous to the one reported previously for the tracer experiments with ^{13}C (**§ 2**). Nevertheless, it is important to note that, due to the nature of this experiment, the process probed here is not a proper tracer diffusion, but rather a chemical diffusion process.

As shown in **Fig. 5.3**, incorporation of oxygen is negligible for $MAPbI_3$ films in the dark, but becomes substantial under illumination, where it increases with light intensity. By performing the same experiment on a $MAPbI_3$ pellet exposed to O_2 at higher temperatures and for longer times, we can confirm that there is clearly oxygen incorporation also in the dark, albeit generally rather modest (**Fig. 5.3d**). A more thorough analysis of the diffusion profiles allows us to extract a chemical diffusion coefficient (D_O^{δ}) and a surface rate constant (k_O^{δ}) for the oxygen impurity incorporated in $MAPbI_3$. As shown in **Fig. 5.3c**, illumination only significantly enhances k_O^{δ}, while D_O^{δ} appears unvaried. The increasing k_O^{δ} with light intensity can be attributed to a faster reduction of O_2 from the gas phase due to the presence of photo-generated electrons. We note that this occurrence was also reported for the perovskite $SrTiO_3$.[162] Considering instead the unvaried D_O^{δ}, we note that -as presented in **§ 4**- light enhances the concentration of iodine vacancies in $MAPbI_3$, and this could therefore affect the $O_I^{'}$ diffusion

coefficient. However, there are several explanation for this behavior, the simplest of which being the occupation of an interstitial site by the incorporated oxygen (O_i'', as mentioned previously), that would naturally give a D_O^δ that is independent on the $V_I^\bullet$ concentration.

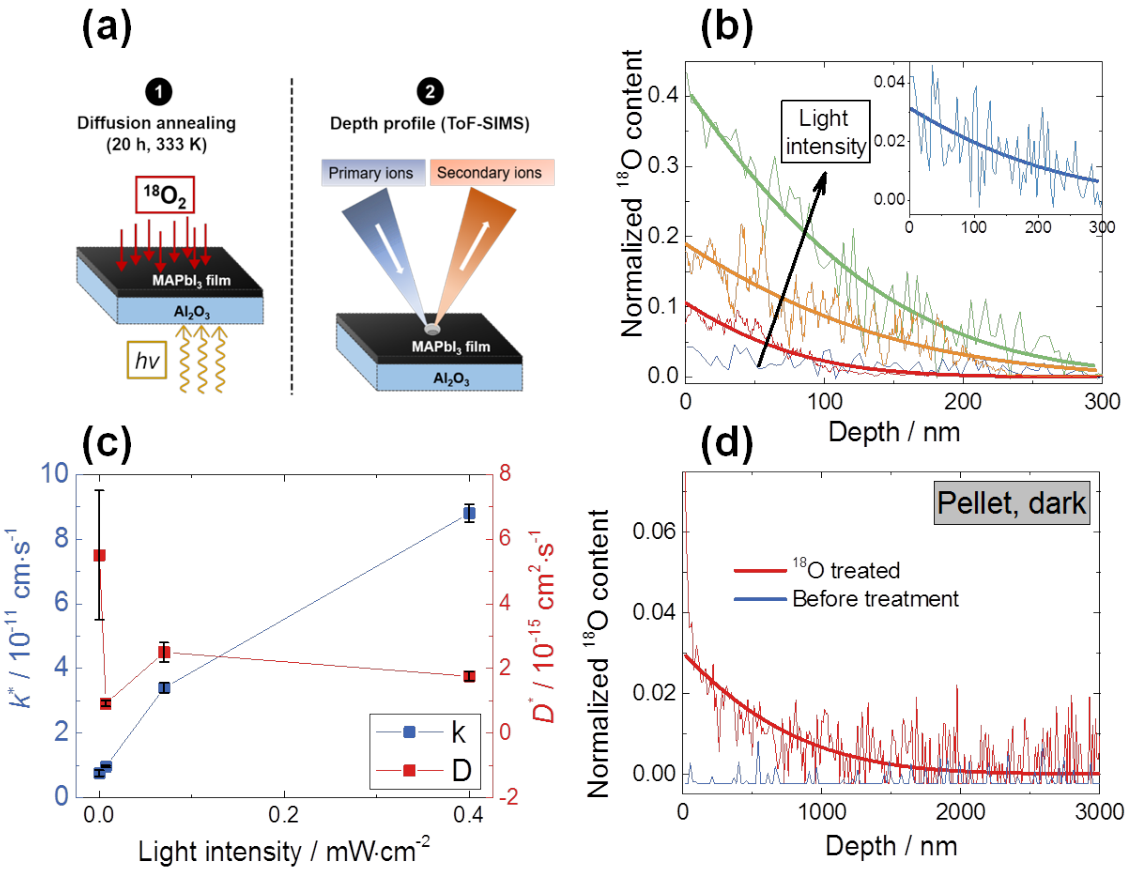

Figure 5.3. **(a)** Schematic of the ^{18}O incorporation experiment. **(b)** ^{18}O diffusion profiles of $MAPbI_3$ thin films measured by ToF-SIMS. During the $^{18}O_2$ treatment (20 h at 333 K), different light intensities were used, namely 0 (—), 0.015 (—), 0.3 (—) and 1 (—) mW/cm². Inset shows a magnification of the dark profile. **(c)** Chemical diffusion coefficients (D_O^δ) and surface rate constants (k_O^δ) for the oxygen impurity extracted from the curves of panel (b). **(d)** ^{18}O diffusion profiles collected on a $MAPbI_3$ pellet before and after treatment with $^{18}O_2$ at 378 K for 46 h ($D^\delta_{O,pellet} = 3 \cdot 10^{-14}$ cm^2/s, $k^\delta_{O,pellet} = 1.2 \cdot 10^{-11}$ cm/s).

A further possibility is a coupled motion of the substitutional oxygen defect (O_I') with the locally generated $V_I^\bullet$. As presented in detail in Appendix § **10.4.3**, this coupling is rather expected for low temperatures and leads to an impurity motion that does not involve any extra iodine vacancies to take place, making it independent on the inherent $V_I^\bullet$ concentration.

^{18}O incorporation experiments

Light accelerates surface reaction and enhances oxygen incorporation.

5.4 INFLUENCE ON THE TRANSPORT PROPERTIES

As detailed in **§ 5.2**, oxygen incorporation is expected to lead to acceptor doping, providing that the concentration of oxygen defects surpasses the concentration of dominant intrinsic defects. This would increase the concentrations of $h^{\bullet}$ and $V_I^{\bullet}$, that are the majority electronic and ionic carriers in $MAPbI_3$ (see **§ 2** and **§ 3**), thus directly affecting its electrical transport properties. We can verify the defect model by simply measuring the conductivities as a function of $P(O_2)$, under the assumption that mobility values are constant. In order to be able to perform the analysis both in the dark and under uniform illumination, here we investigate thin film samples.

As shown in **Fig. 5.4b**, we indeed observe a doping effect at higher $P(O_2)$ values ($> 10^{-2}$ bar) under illumination. In this region, highlighted in blue, both ionic and electronic conductivities are strongly increased by oxygen incorporation, in complete agreement with what is expected by a doping effect (see O-region of defect diagram of **Fig. 5.4c**). The same behavior is observed at higher light intensities (Appendix **§ 10.4.4**).

In contrast, at lower $P(O_2)$ values ($< 10^{-2}$ bar) the ionic conductivity is unvaried by $P(O_2)$, while the electronic conductivity still increases, albeit rather modestly. This behavior is analogous to what is observed in the dark (**Fig. 5.4a**), and it deserves some more detailed comments. As seen with ^{18}O incorporation experiments, O_2 incorporation the dark is rather sluggish, therefore we would not expect a significant influence of O_2 on the transport properties under these conditions. However, while this is true for the ionic conductivity, it is not the case for the electronic conductivity, that is clearly enhanced by O_2 exposure (**Fig. 5.4a**). The same observation comes from the analysis of the effect of O_2 in $MAPbI_3$ pellets (**Fig. 5.5**). We note that this oxygen-induced behavior does also not conform with the expected doping effect, in which both ionic and electronic conductivities must increase. Rather, the effect is qualitatively comparable to what is obtained by exposing $MAPbI_3$ to different $P(I_2)$ (**Fig. 3.3**). In addition, as shown in **Fig. 5.4d**, by measuring the $P(O_2)$ dependence of the conductivity in $MAPbI_3$ thin films (or pellets, **Fig. 5.5b**) under a constant iodine activity, we obtain ionic and electronic conductivities that are invariant to $P(O_2)$. This indicate that, under these latter conditions, the material behaves intrinsically as the concentration of O-defects is smaller than the intrinsic disorder (left region of **Fig. 5.1** or of **Fig. 5.4c**). These observations are consistent with an oxygen effect that is initially limited to the surface, where O_2 oxidizes iodide ions to iodine, ultimately resulting in an enhanced iodine activity over the sample.

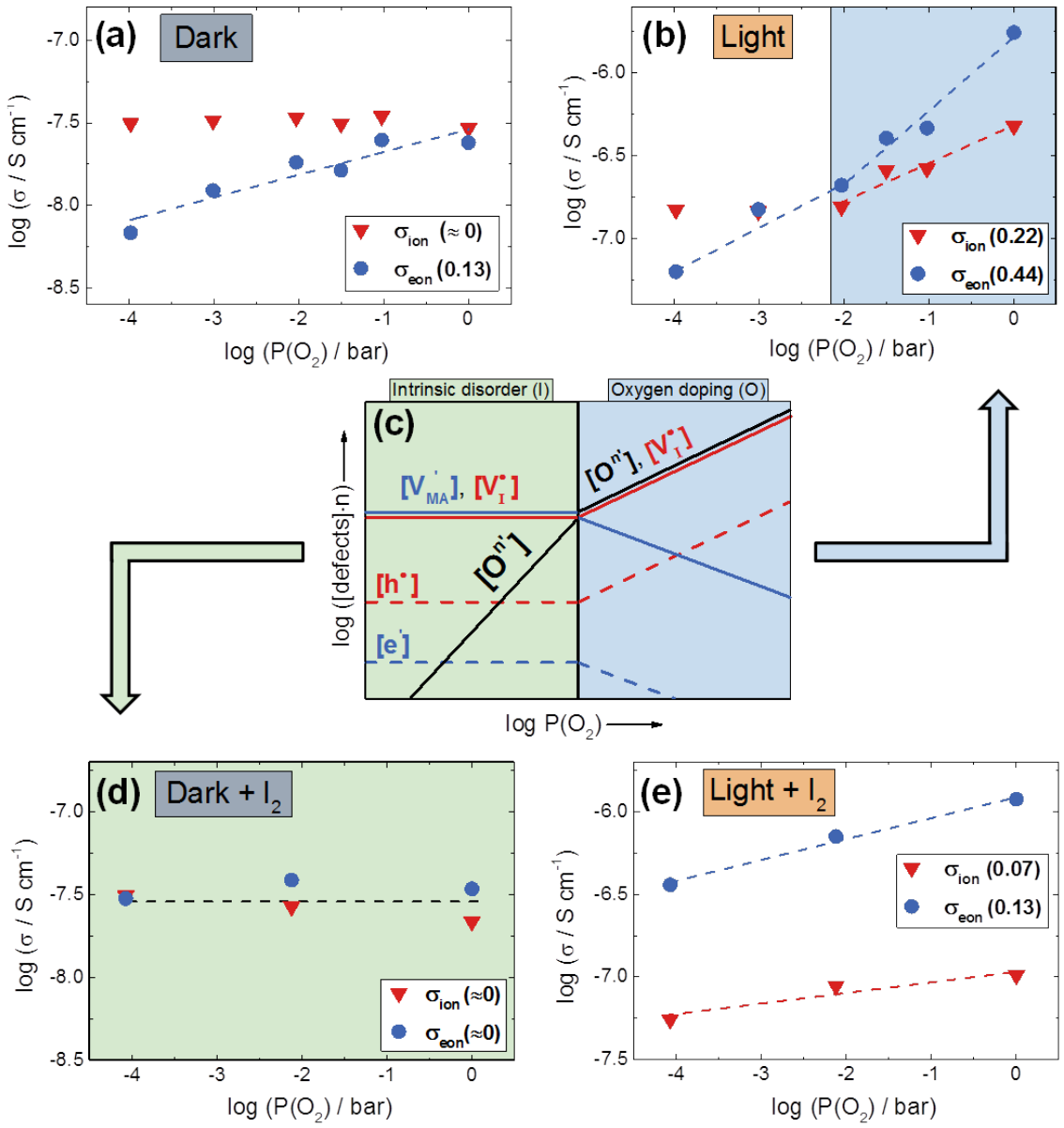

Figure 5.4. Conductivity of $MAPbI_3$ thin films as a function of oxygen partial pressure, recorded at 333 K **(a)** in the dark, **(b)** under 0.5 mW/cm^2 illumination **(d)** in the dark with iodine exposure ($P(I_2) = 1.4 \cdot 10^{-6}$ bar) **(e)** under 0.5 mW/cm^2 illumination with iodine exposure ($P(I_2) = 1.4 \cdot 10^{-6}$ bar). **(c)** Defect concentrations as a function of $P(O_2)$ (as in **Fig. 5.1**), with a generic oxygen defect of charge n represented.

In contrast to the sluggish kinetics of O_2 incorporation, previous experimental evidences show that the exchange of I_2 with the $MAPbI_3$ lattice is rather quick (see for example § 3). This can thus explain the observed immediate influence on the transport properties given by oxygen exposure. Thermodynamic considerations presented in the next section (§ 5.5) will show that this conversion reaction yielding iodine is indeed expected.

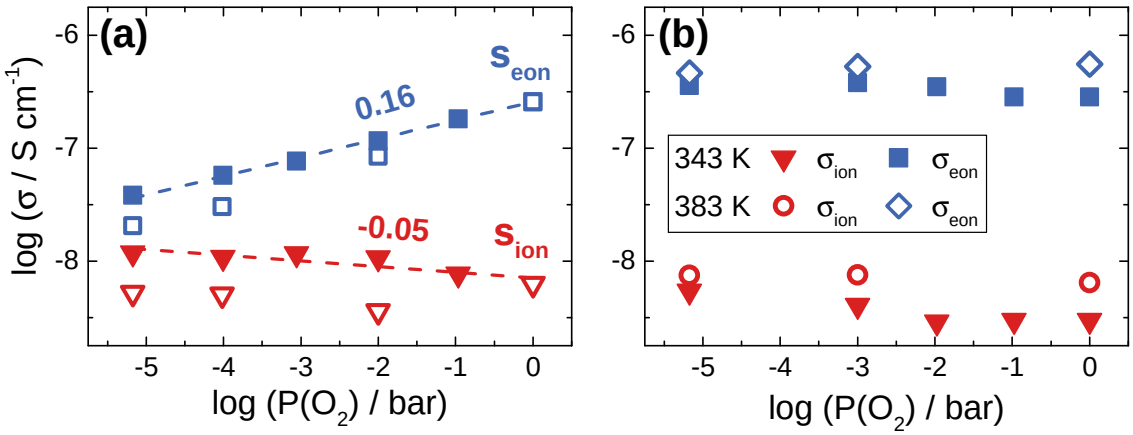

Figure 5.5. Conductivity as a function of oxygen partial pressure in $MAPbI_3$ pellets. **(a)** Argon as carrier gas, 343 K. Open symbols are points collected from high to low $P(O_2)$ to test reversibility. **(b)** Ar as carrier gas with constant $P(I_2)$ ($= 5 \cdot 10^{-6}$ bar), measured at 343 K (closed symbols) and 383 K (open symbols).

As shown in **Fig. 5.4e**, the simultaneous exposure of $MAPbI_3$ to iodine and oxygen severely weakens the O_2 effect also under illumination. This is in complete agreement with the expected oxygen incorporation reaction (**(Eq. 5.1)**), where an enhanced I_2 activity can reduce iodine excorporation and, as a consequence, impede O_2 insertion into the lattice and thus prevent oxygen doping.

As a last point, it is worth noting that, for all the above electrical experiments, the observed O_2 effect is fully reversible, both in the dark and under illumination (**Fig. 5.6**).

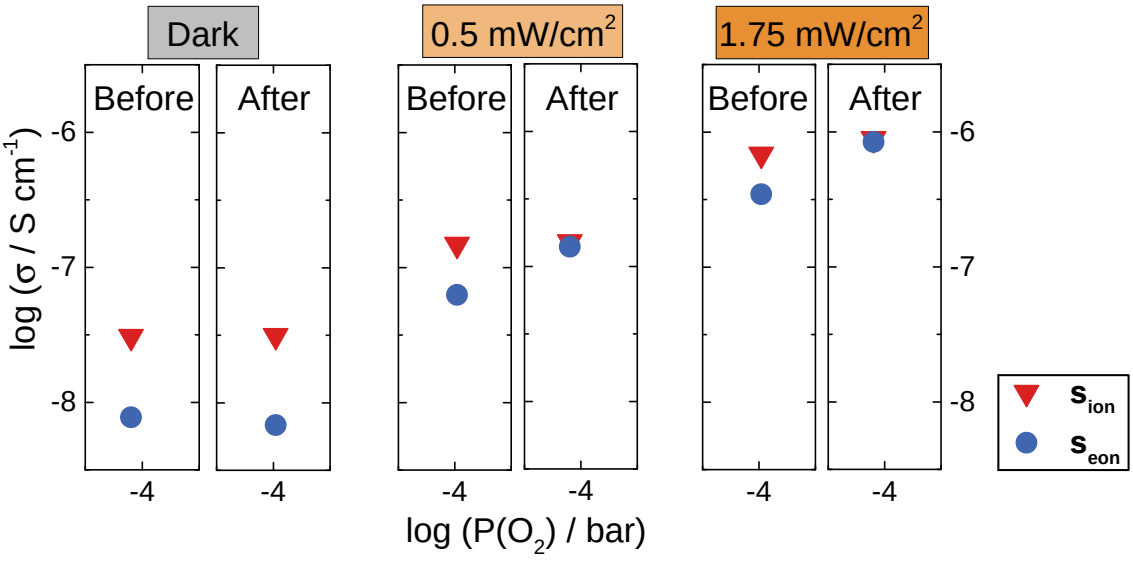

Figure 5.6. Conductivity of $MAPbI_3$ films before and after being exposed to several $P(O_2)$ values to collect the curves of **Fig. 5.4**. Total measurement time was > 500 h.

This indicates that, upon oxygen exposure, iodine is not excorporated into the gas phase, but it is likely accumulated at higher dimensional defect or possibly even in the interstitial lattice (as also proposed for the light effects on ion transport presented in **§ 4.6**).

O_2 effect on transport properties

- **Dark:** O_2 effect limited to the surface, where it affects I_2 activity.
- **Illumination:** O_2 acts as reversible acceptor dopant.

5.5 THERMODYNAMICS OF O_2-INDUCED DEGRADATION

As mentioned in the introduction, oxygen exposure can cause severe degradation of HOIHPs.[53,56,58] A degradation reaction is expected to happen whenever the incorporated oxygen content in the halide perovskite lattice exceeds the solubility limit. We can calculate the standard Gibbs energies for the relevant degradation reaction using tabulated data and standard formation enthalpy and entropy values for different HOIHPs. This procedure will be discussed in detail in a later chapter (**§ 6.6**). Here it suffices to state that the degradation of $MAPbI_3$ involving O_2 is expected to take place as follows:

$$CH_3NH_3PbI_3 + \frac{1}{4}O_2 \rightarrow \frac{1}{2}H_2O + CH_3NH_2 + PbI_2 + \frac{1}{2}I_2 \tag{5.4}$$

This reaction shows a weakly positive standard Gibbs energy of degradation ($\Delta_r G^0 = 5.3$ kJ/mol), indicating minor stability, which is however easily turned to a negative value whenever the products are far from standard conditions. This effect will largely dominate under real operative conditions, thus yielding a strongly negative Gibbs energy for the oxygen degradation reaction (see **§ 6.6** for details). We thus conclude that, without a complete exclusion of oxygen, $MAPbI_3$ is expected to degrade upon O_2 exposure, producing PbI_2, CH_3NH_2 and I_2. We note that water formation *in-situ* can also offer a further degradation pathway,[39,46–52] and this can also happen upon illumination (see **§ 6.5**).[45,63–68]

For this reason, we have also investigated whether other HOIHPs could have a better thermodynamic stability against O_2 degradation. The analogous decomposition reactions for $MAPbBr_3$ and $MAPbCl_3$ have a much more positive $\Delta_r G^0$ (64.7 and 89.3 kJ/mol respectively), meaning that the bromide and chloride perovskites are thermodynamically much more stable against O_2. Even under real operative conditions, the materials have a significantly lower tendency towards degradation than their iodide counterpart (see **§ 6.6**). There are, unfor-

tunately, no reported thermodynamic data for formamidinium- (FA) containing perovskites, even though $FAPbI_3$ or MA,FA mixtures appear to have a significantly higher environmental stability when compared with $MAPbI_3$.[63,89] In the following section (**§ 5.6**), we will discuss our experimental evidences concerning these other HOIHPs compositions.

Thermodynamics of O_2-induced degradation

O_2 expected to completely degrade $MAPbI_3$ to PbI_2, CH_3NH_2 and I_2.

5.6 DEGRADATION KINETICS

Thermodynamic considerations clearly show a strong tendency of O_2 to react with $MAPbI_3$ and to induce degradation. This can be experimentally verified by monitoring the decomposition of $MAPbI_3$ thin films with UV-Vis spectroscopy, performed as a function of time under degradation conditions. Interestingly, as shown in **Fig. 5.7a**, no degradation is observable in the dark when $MAPbI_3$ is exposed to O_2, even after long times and temperatures higher than room temperature. In contrast, under illumination the decomposition process is swift (**Fig. 5.7b**). Control experiments carried out under inert atmosphere and identical illumination conditions also show no signs of degradation (Appendix **§ 10.4.6**).

This glaring difference in the degradation behavior in the dark and under illumination is not surprising, even though, in both cases, full degradation is thermodynamically expected. Indeed, the kinetic hindrances observed in the dark during ^{18}O incorporation experiments (**§ 5.3**), that impede oxygen incorporation, can fully explain the samples' stability under these conditions. Nonetheless, even in the dark, we expect this thermodynamic driving force to be of relevance at least for the surface layer, where a transfer step to the bulk is unnecessary. This is in agreement with the previously observed surface effect causing modification of the electrical transport properties under equilibrium (**§ 5.4**).

These kinetic hindrances can be removed by light, and this results in the observed quick degradation. The rate of this process can be extracted from the UV-Vis spectra, and it is given in **Fig. 5.7c**. Here, we see that the initial degradation occurs with a constant rate, while at a later stage it significantly accelerates, suggesting the opening of a second degradation path, possibly involving water molecules that are generated *in-situ*.[46,47]

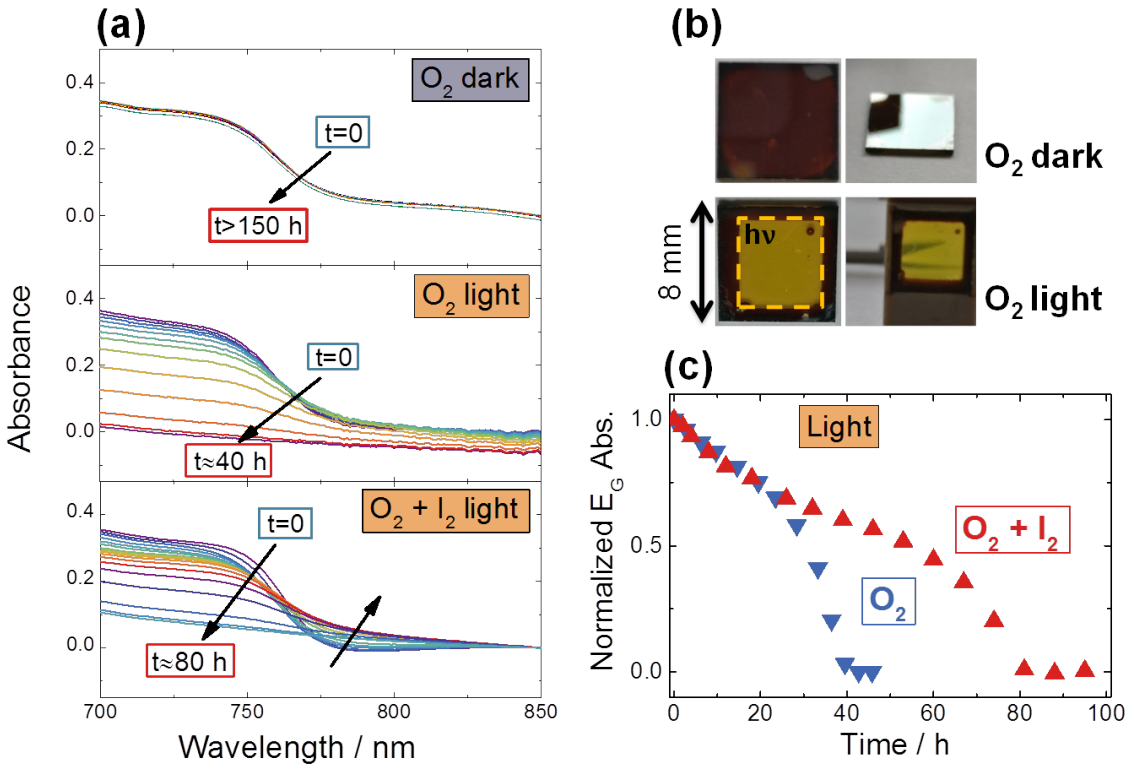

Figure 5.7. **(a)** Degradation study of $MAPbI_3$ thin films under O_2 exposure, monitored by UV-Vis spectroscopy at 333 K. Films are kept in the dark (top panel), under illumination (4.6 mW/cm^2, middle) and under illumination (4.6 mW/cm^2) with simultaneous I_2 exposure (bottom panel, $P(I_2) = 1.4 \cdot 10^{-5}$ bar). **(b)** Photos of the films after treatment in the dark (150 h) and under illumination (40 h). The sample holder protects from the light the border area of the film, which therefore does not degrade. **(c)** Degradation rate, taken as the normalized bandgap absorption, extracted from the spectra of panel (a).

Remarkably, the simultaneous application of iodine partial pressure during O_2 exposure slows down the decomposition process significantly (**Fig. 5.7c**). Note that this behavior is completely expected based on **(Eq. 5.4)**. Exposure of the samples to such low $P(I_2)$ values in an otherwise inert atmosphere (Ar) does not result in significant degradation (Appendix **§ 10.4.6**), even though decomposition of $MAPbI_3$ is reported under extremely high $P(I_2)$.[163]

We can gain further information on this process by monitoring the degradation using XRD. As shown in **Fig. 5.8**, we see once again decomposition taking place under O_2 and light (no degradation is observed in the dark, Appendix **Fig. 10.18**), that can be slowed down by simultaneous I_2 exposure. A striking difference is that, while under O_2 the films degrade yielding crystalline PbI_2, under simultaneous I_2 exposure the PbI_2 peaks are almost entirely missing, indicating formation of an amorphous phase. We note that the color change from black ($MAPbI_3$) to yellow (PbI_2) happens as expected, and no other phases are present after degradation (**Fig. 5.8d**).

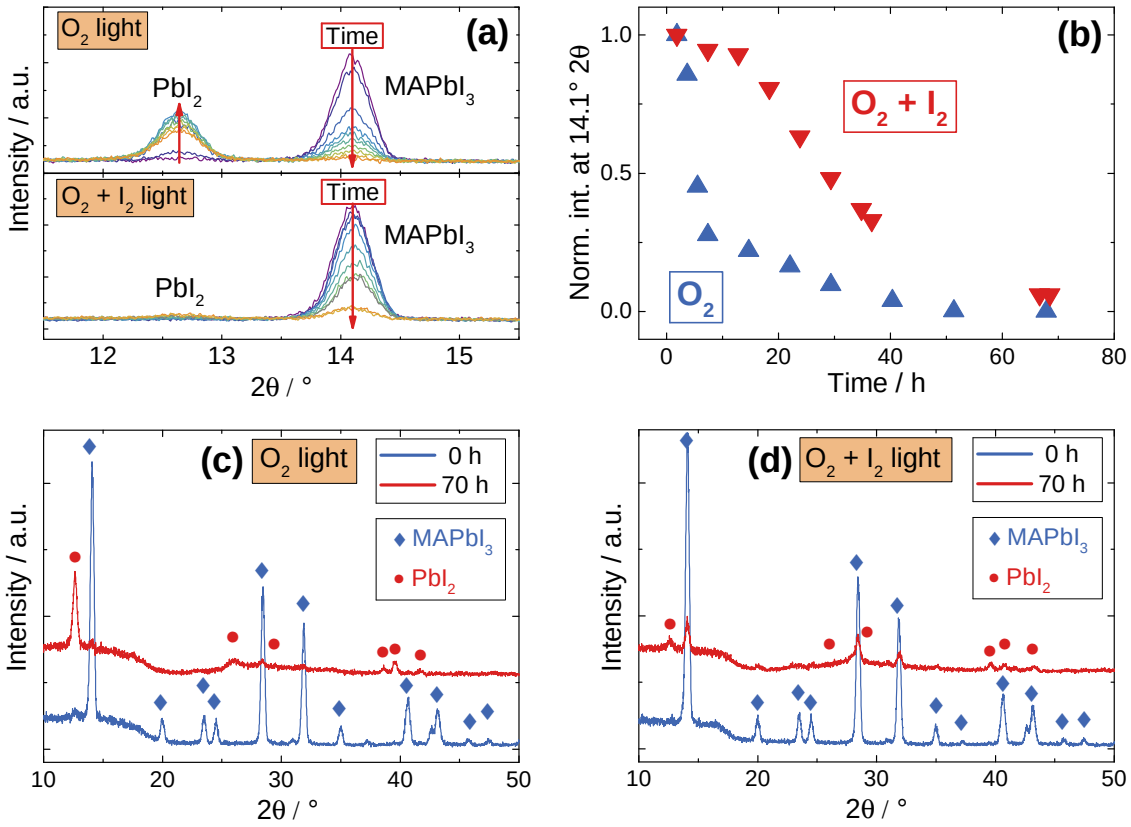

Figure 5.8. Degradation of $MAPbI_3$ thin films under O_2 and light (43 mW/cm^2), monitored by GIXRD at room temperature. **(a)** XRD patterns showing the progressive disappearance of the main $MAPbI_3$ peak, with and without simultaneous I_2 exposure ($P(I_2)= 4.5 \cdot 10^{-6}$ bar). **(b)** Degradation rate extracted from the intensity of the $MAPbI_3$ peak (14.1 2θ) of panel (a). **(c)** XRD patterns before and after degradation under O_2. **(d)** XRD patterns before and after degradation under O_2 and I_2 ($P(I_2)= 4.5 \cdot 10^{-6}$ bar).

In addition, indications of a loss of crystallinity of the perovskite phase are also present in the UV-Vis spectra under O_2 and I_2 exposure, where a tail in the absorption is visible at higher wavelengths. A similar effect, albeit much weaker, is observed for I_2 exposure under Ar atmosphere (Appendix **Fig. 10.17**). Unfortunately, at the moment we do not have sufficient evidences to clarify this finding, therefore we will not discuss it further here.

A great deal of information regarding the mechanism of O_2 degradation can also be extracted from the dependence of the degradation process on light intensity and spectral content. **Fig. 5.9a** shows the degradation process becoming, as expected, faster with increasing intensity. This is in agreement with the ^{18}O incorporation results, and conforms with our hypothesis that a higher concentration of electronic carriers can facilitate the O_2 reduction reaction and thus the subsequent incorporation.

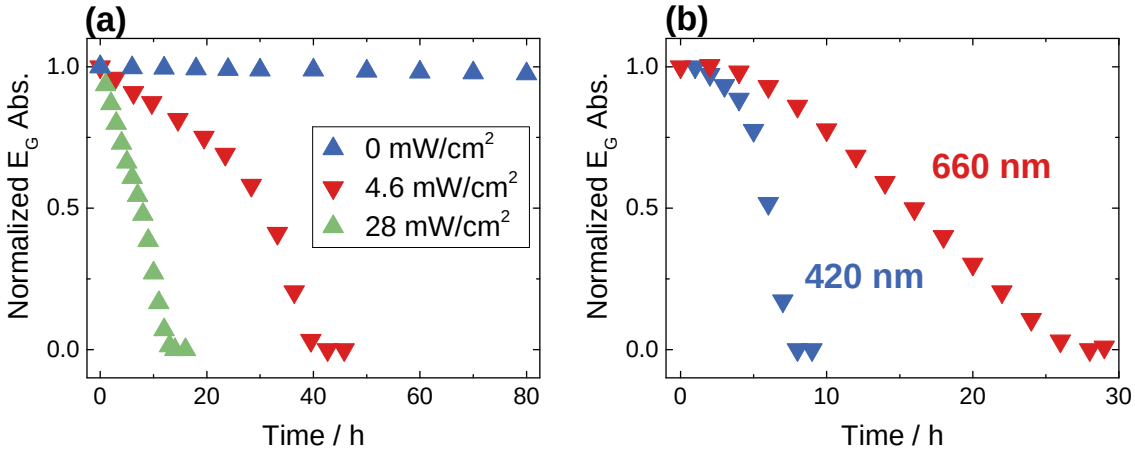

Figure 5.9. Degradation kinetics of $MAPbI_3$ thin films exposed to O_2, recorded using UV-Vis spectroscopy as a function of **(a)** light intensity and **(b)** spectral content (constant intensity = 4 mW/cm^2).

Regarding the light spectral content, **Fig. 5.9b** shows that degradation is much quicker under high energy radiation. Since we can rule out significant local heating as the cause of this discrepancy (the samples are already kept at 333 K), the most plausible hypothesis relies on a favored electron transfer from the photo-excited $MAPbI_3$ to molecular O_2, due to high-energy (hot) electrons. This process would also be facilitated by the remarkably slow cooling of hot electrons that takes place in HOIHPs.[16,164,165]

Lastly it is worth noting that, in all degradation experiments, the light intensity is well below 1 Sun (100 mW/cm^2) and does not contain UV radiation. Therefore we expect that under device operative conditions (1 Sun, including high energy UV light), the degradation process will be markedly more drastic, making the O_2-induced degradation most relevant for real solar cells.

Degradation kinetics

- **Dark**: kinetic hindrances make $MAPbI_3$ metastable.
- **Illumination**: kinetic hindrances removed, quick degradation observed.

5.7 INCORPORATED OXYGEN: SUPEROXIDE OR OXIDE IONS?

As mentioned in the introduction, several studies observed that the interaction of O_2 with $MAPbI_3$ results in the formation of superoxide (O_2^-) species.[53,58,61] The relevant degradation step, according to these reports, involves deprotonation of MA cations by the basic superoxide ions, forming water and volatile methylamine. In our defect chemical model, and throughout this chapter, we considered instead O_2 to be incorporated in the form of oxide (O^{2-}) ions, being

this the most thermodynamically stable form. We think that incorporation of O_2 in halide perovskites as superoxide ions is improbable for the following reasons:

- Atomic oxygen species (O^{2-}) are expected to show significantly higher solid-state diffusivity with respect to their molecular (O_2^-) counterparts, based on simple size and shape considerations. We note that such diffusion is necessary for bulk incorporation.
- Computational approaches show superoxide species to be stable when occupying an iodine vacancy.[61] If this was the case, a charge-neutral substitution would be achieved ($(O_2)_I^x$), yielding no doping effect, and this is in clear contrast with our experimental observations (**Fig. 5.4**).
- A degradation path involving deprotonation of MA cations relies on the basicity of the superoxide ion. However, oxide ions are more basic and could therefore undertake this endeavor more efficiently.
- ^{18}O incorporation experiments show O_2 present in the depth of a film after turning off the light (or even in a pellet kept in the dark), and after applying high vacuum on the sample for several hours (necessary before measuring ToF-SIMS). This provides a clear indication that the form in which O_2 is incorporated is stable, and does not require light to be maintained.

Based on this, we conclude that the formation of superoxide species is probably an intermediate step towards reduction of O_2 to O^{2-}, and that O_2^- ions are not likely present in perceptible concentrations in the halide perovskite lattice. This is also widely accepted to be the case for oxide perovskites.[166]

Superoxide ions or oxide ions?

O_2^- likely only an intermediate species in the process forming O^{2-}.

5.8 STABILITY OF MIXED-CATION AND MIXED-HALIDE COMPOSITIONS

The degradation processes experimentally observed for $MAPbI_3$ under O_2 are extremely severe (**§ 5.6**). In addition, thermodynamic considerations show that this material is fully unstable against oxygen (**§ 5.5**). However, this is not the case for $MAPbBr_3$ and $MAPbCl_3$, and possibly even for $FAPbI_3$ (**§ 5.5**). The state-of-the-art perovskite formulations used to fabricate high efficiency solar cell devices are based on a mixture of MA and FA cations (in certain cases with small quantities of Cs and Rb) on the A-site, and a mixture of I and Br on the

anion site.[24,71] We thus find it important to check stability against oxygen of these mixed cation, mixed anion compositions. In order to distinguish the effect of O_2 on the cationic or anionic site, we prepared two compositions, namely a mixed halide $MAPb(Br_{0.2}I_{0.8})_3$ and a mixed cation $(MA_{0.8}FA_{0.2})PbI_3$ perovskite.

We consider at first the mixed-halide composition. Since I and Br mixtures are known to undergo de-mixing under illumination,[167] a stable composition (20 % Br) has been chosen. As shown in **Fig. 5.10a**, the halide mixture does not show any significantly enhanced stability with respect to pure $MAPbI_3$, even though we would expect this thermodynamically, both from the higher stability of the $MAPbBr_3$ phase but also from the mixing entropy, albeit the latter is usually rather small. This behavior can be clarified by looking at the XRD analysis of the mixed-halide film after degradation (**Fig. 5.10b**). Here we see the presence of a cubic $MAPbBr_3$ phase, while the pristine sample only showed reflections belonging to tetragonal $MAPbI_3$. This indicates that the O_2-induced I_2 removal takes place in this system as well, and causes formation of pure $MAPbBr_3$ and of PbI_2. $MAPbBr_3$ is thermodynamically stable against O_2, as experimentally verified by the absence of any $PbBr_2$ peaks. We note that, after degradation, $MAPbI_3$ reflections are still visible, but this is due to the fact that the sample holder used protects the edges of the film from light, and this part therefore does not experience degradation (see photos of **Fig. 5.7b**).

We can consider now the mixed-cation formulation. Here, we select a composition (20 % FA) that forms a stable perovskite at room temperature, as pure $FAPbI_3$ crystallizes in a non-perovskite phase.[119] **Fig. 5.10c,d** shows how the degradation rate is significantly lowered in the mixture, even though it is not completely suppressed. XRD analyses show that no peaks belonging to PbI_2 are visible after degradation (Appendix **Fig. 10.19**), pointing towards the formation of an amorphous phase. Also, the clear absorption tail visible in the UV-Vis spectra (**Fig. 5.10c**) indicate loss of crystallinity in the perovskite phase during degradation. Based on the results on the mixed-anion formulation, we can rule out a significant contribution to the stability coming from the mixing entropy, therefore we rationalize the enhanced stability of the mixed-cation formulation as follows: (i) An increase in stability is thermodynamically expected due to the lower tendency towards deprotonation of the FA cation with respect to MA (formamidine is a stronger base than methylamine).[168] (ii) Mixing FA causes a lowering of the ion conductivity in the samples,[89] which we directly measured (Appendix **Fig. 10.20**).

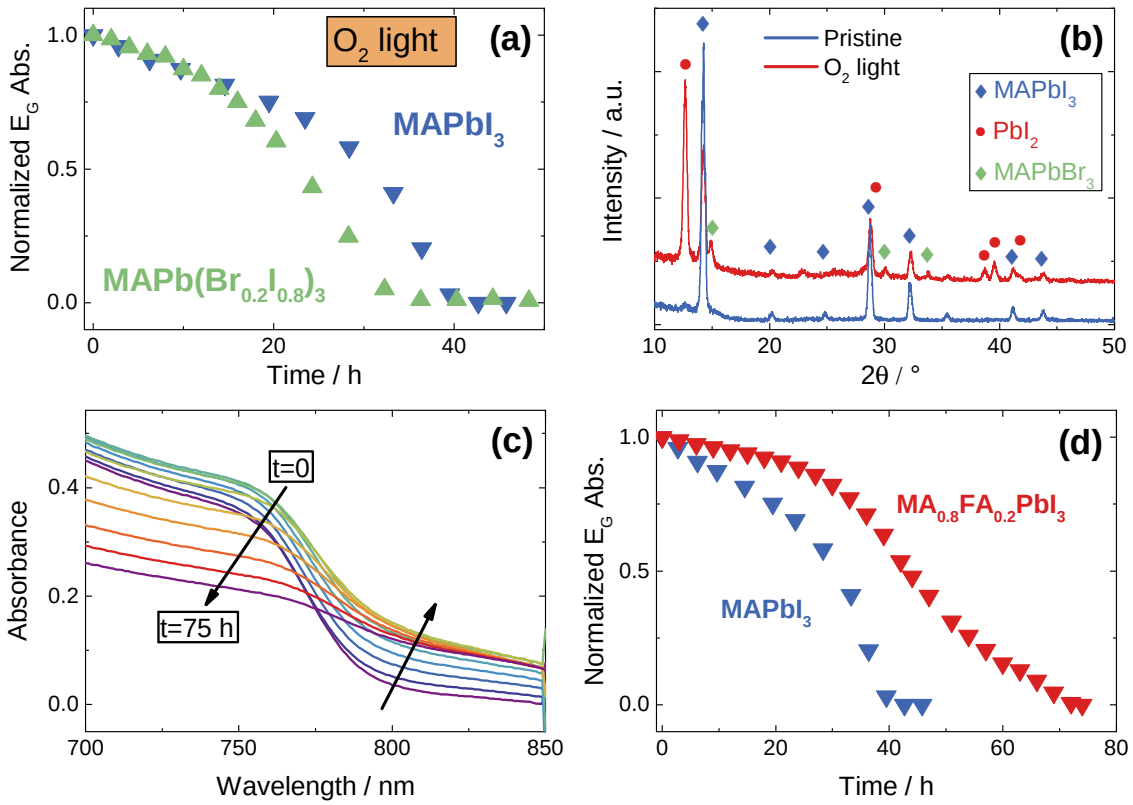

Figure 5.10. **(a)** Degradation rate of $MAPbI_3$ and $MAPb(Br_{0.2}I_{0.8})_3$ under O_2 exposure at 333 K with 4.6 mW/cm^2 illumination, extracted from UV-Vis spectroscopy data. **(b)** XRD analysis before and after degradation of panel (a). **(c)** Degradation of $(MA_{0.8}FA_{0.2})PbI_3$ under O_2 exposure at 333 K with 4.6 mW/cm^2 illumination, monitored with UV-Vis spectroscopy. **(d)** Comparison of the degradation rates of $MAPbI_3$ and $(MA_{0.8}FA_{0.2})PbI_3$ under O_2, 4.6 mW/cm^2 illumination and 333 K.

This yields a slower rate for the transport step that decelerates degradation. At last we note that, as shown in the Appendix **Fig. 10.21**, increasing FA content ($(MA_{0.2}FA_{0.8})PbI_3$) yields even more stable compounds, even though under these conditions we cannot ensure phase purity.[169] Thus, the enhanced stability of this latter formulation might not be due to the chemistry (as in the low FA content sample), but possibly to the two phase nature of the compound (details in Appendix § **10.4.7**).

Mixed-halide and mixed-cation compositions

- **$MAPb(Br_{0.2}I_{0.8})_3$**. No enhanced stability due to selective I_2-loss.
- **$(MA_{0.8}FA_{0.2})PbI_3$**. Degradation rate lower than in $MAPbI_3$.

5.9 CONCLUSIONS

This chapter showed that, concerning O_2 interaction with $MAPbI_3$, three different regimes have to be distinguished:

- **Dark.** Surface-to-bulk transfer is sluggish and the O_2-effect is limited to the surface ($2I^-_{(\text{lattice})} + O_{2\ (g)} \rightarrow I_{2\ (g)} + O^{2-}_{(\text{lattice})}$), causing only mild changes in the electrical properties. Thermodynamic considerations indicate $MAPbI_3$ to be unstable against O_2, but the sluggish kinetics makes it metastable. This regime can also be established under weak illumination and low $P(O_2)$.

- **Illumination I.** Under mild conditions (low temperature, low light intensity and/or short exposure times), the kinetic barrier is partially removed, yielding a substantial incorporation of O_2, provided $P(O_2)$ is sufficiently high. This results in reversible acceptor doping that greatly varies the ionic and electronic transport properties. The material still shows metastable behavior under these conditions.

- **Illumination II.** Under harsh conditions (high temperature, high light intensity and/or long exposure times), large quantities of O_2 can be rapidly incorporated, provided $P(O_2)$ is sufficiently high. This incorporated oxygen exceeds the solubility limit of the $MAPbI_3$ phase, resulting in severe degradation yielding H_2O, PbI_2 and I_2.

In addition, we have shown that, under degradation conditions, mixed halide (I, Br) compositions undergo selective iodine removal, with no effective improvement in stability. In contrast, mixed cation (MA, FA) compositions give an enhanced stability, albeit the degradation process is not entirely suppressed. We note that our main conclusion here is that many HOIHP compositions are, even without being in a device architecture, already highly unstable against oxygen exposure. Clearly, this means that photovoltaic devices based on these compositions will also show instability, provided that oxygen has access to the perovskite layer.

6

THERMODYNAMIC STABILITY OF HALIDE PEROVSKITES

Abstract. *In this chapter, we explore the stability of HOIHPs from the thermodynamic point of view. We have observed previously how, in certain situations, the halide perovskite phase is subject to distinct degradation phenomena (e.g. under oxygen and/or under illumination). With the help of literature thermodynamic data and a few selected experiments (heat capacity measurements and precursors reactivity studies), we discuss several different degradation mechanisms in HOIHPs (e.g. induced by temperature, illumination, oxygen exposure and water) and examine the underlying thermodynamics. These considerations, in agreement with experiments, show a severe tendency of HOIHPs towards degradation, which in certain conditions is especially critical for $MAPbI_3$.*
We acknowledge the important help of Gisela Siegle and Dr. Reinhard K. Kremer for the heat capacity measurements.

6.1 INTRODUCTION

We have already observed how severe degradation phenomena in HOIHPs can be induced under certain conditions, such as under oxygen (**§ 5.6**) and/or under illumination (**§ 4.6**). Furthermore, we mentioned previously that the stability of these materials is a most pressing issue to be solved before practical applications. We thus find it worth discussing the underlying thermodynamics of these compounds, and examining the different degradation mechanisms involved.

In the general case of a binary metal iodide MI, one can represent thermodynamic stability by drawing a phase diagram between the elemental components M and I. In this picture, as shown in **Fig. 6.1**, stability is represented by a window that widens with temperature, corresponding to the tolerable changes in stoichiometry that the material can undergo without phase degradation. Note that this window comprises the entire defect diagram describing the material (see **§ 3.2**), including changes of the nature of the majority species generating N-,

I- and P-regimes. As shown in previous chapters (§ 3.2 and § 5.2), even though these defect numbers are much smaller than the regular lattice sites, their variations have drastic effects on the electrical properties of a compound. In the present chapter, we will ignore such tolerable defect concentration changes (as they are expected to have a negligible impact on the phase energetics) and concentrate instead on the variations exceeding phase homogeneity.

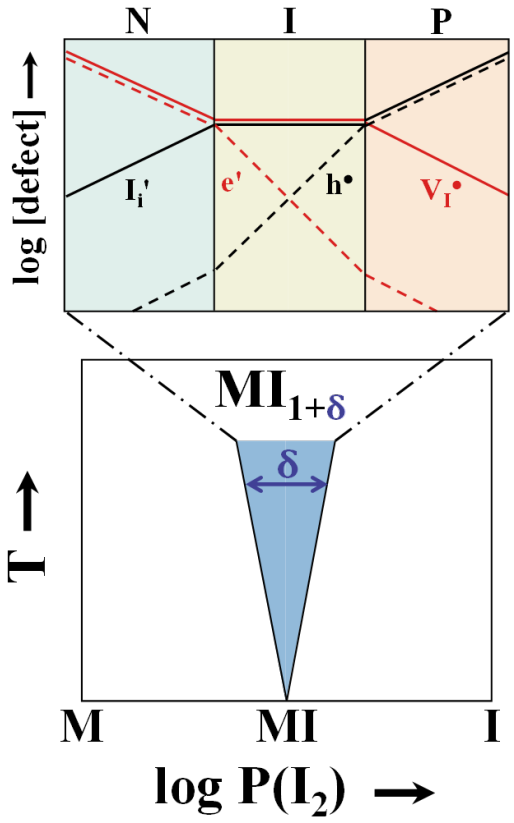

Figure 6.1. Phase diagram of a general binary iodide MI. Blue region represents the stability window in which stoichiometry (δ) can be freely varied without phase degradation. As shown in the top part of the diagram, drastic changes in the defect concentrations can take place within this window upon changing stoichiometry.

Coming back to the specific case of HOIHPs, we already mentioned that these materials suffer from significant degradation phenomena, which prevent their practical application in commercial photovoltaic devices. Such phenomena can be induced by temperature,[37–45] water or high humidity,[39,46–52] oxygen exposure[53–62] or even illumination.[45,63–68] We will discuss all these aspects in detail below.

Notably, the existing thermodynamic studies[43,170,171] report rather different values for the formation enthalpy of various MA-based halide perovskites. In the specific case of $MAPbI_3$, these values differ to the point of describing a thermodynamically stable[43,171] or unstable[170] compound with respect to its

precursors under standard conditions. Naturally, it is of utmost importance to give unambiguous answers to these questions, as they may determine whether it is worth proceeding with the studies of these materials (especially for practical application) or not. For this reason, we will start with the discussion on the standard formation enthalpies (**§ 6.2**), before moving on to the treatment of the various degradation processes involving HOIHPs (**§ 6.3-6.6**).

6.2 STANDARD ENTHALPIES OF FORMATION

As mentioned in the introduction, significantly different values for the formation enthalpies of various HOIHPs have been reported in the literature,[43,170,171] and are collected in **Table 6.1**. This discrepancy is particularly severe in the case of $MAPbI_3$, where a difference of more than 30 kJ/mol is recorded in the standard enthalpy of formation of the compound ($\Delta_f H^0_{298K}$). Notably, such a difference marks the separation between a material that can be stabilized by entropy contributions (at room temperature) or not, with respect to its halide precursors (PbI_2 and MAI). The relevant thermodynamic data describing the degradation into halide precursors are given below in **Table 6.2**.

Table 6.1. Standard thermodynamic data for the formation of HOIHPs with respect to their elemental components.

Compound	$\Delta_f H^0$ / kJ · mol^{-1}	$\Delta_f S^0$ / J · (mol · K)$^{-1}$	$\Delta_f G^0$ / kJ · mol^{-1}
$MAPbI_3$	-357.7[43]	-358.4*	-268.8
	-341.6[170]		-234.7
	-371.6[171]		-264.7
$MAPbBr_3$	-539.6[43]	-437.4*	-409.1
	-529.6[170]		-399.1
	-543.1[171]		-412.6
$MAPbCl_3$	-660.5[43]	-579.7*	-487.6
	-666.7[170]		-493.8
	-662.2[171]		-489.3

* S^0 values used to calculate $\Delta_f S^0$ are taken from Ref.[172].

Indeed, according to Nagabhushana *et al.*,[170] $MAPbI_3$ is intrinsically unstable under standard conditions. In contrast, according to Ivanov *et al.*[171] and Brunetti *et al.*[43], $MAPbI_3$ is a stable material under the same conditions. We note that the observations by Nagabhushana *et al.*[170] contradict various exper-

imental observations, such as: (i) It is well-known that $MAPbI_3$ can be synthesized mechano-chemically by mechanically mixing PbI_2 and MAI powders in a mortar.[119,173,174] Interestingly, we observe a similar behavior when preparing two dense pellets of MAI and PbI_2 and sliding their surfaces against one another (**Fig. 6.2a**), obtaining an instantaneous and significant perovskite phase formation. (ii) The reaction between PbI_2 and MAI takes place in the solid state even at room temperature simply by allowing them to come in contact. As shown in **Fig. 6.2b**, we contact two pellets of MAI and PbI_2 with a light spring force, carefully avoiding any scratching during the assembly. After waiting for several hours in inert atmosphere, we observe formation of black powders on top of the PbI_2 pellet when separating the stack (**Fig. 6.2b**). (iii) The main method of synthesis of $MAPbI_3$ powders simply consists in dissolving the precursors and subsequently removing the solvent.[2,3] Even at room temperature, such a procedure yields substantial amounts of the perovskite phase. These experimental evidences show that $MAPbI_3$ has a negative Gibbs energy of formation.

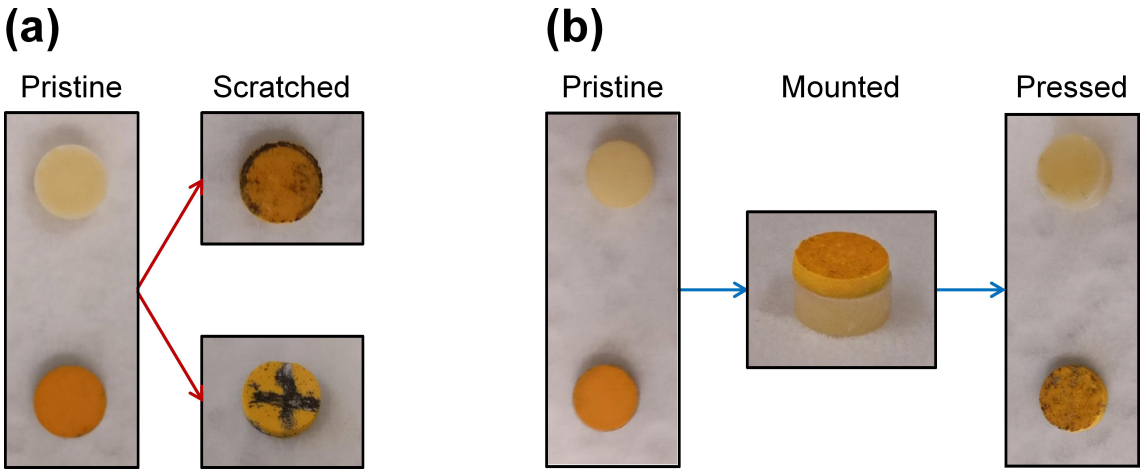

Figure 6.2. Pellets of MAI (white) and PbI_2 (orange/yellow) prepared by cold pressing the respective powders. (a) The MAI pellet is used to lightly scratch the PbI_2 pellet circularly (top) or used to write an X-shape (bottom). $MAPbI_3$ formation (black) is immediate and significant. (b) The pellets are stacked and lightly pressed by spring force under inert atmosphere. Upon separating the stack, the PbI_2 pellet shows black particles due to $MAPbI_3$ formation.

One reason for the reported discrepancy could lie in the method of choice for assessing the thermodynamic parameters, that is calorimetry.[170,171] These characterizations measure the heat of dissolution of the single precursors (e.g. PbI_2 and MAI) and of the final product (e.g. $MAPbI_3$) in order to extract the relevant thermodynamic data for the phase formation. However, this assumes that the same process takes place when dissolving the precursors alone or together. This is not the case for PbI_2 and MAI, for which an appreciable co-dissolution

process exists.[175] This indicates significant chemical interaction between the precursors, which is able to affect their solution thermodynamics. Possibly, this process is related to the formation of complex aggregates made of PbI_2 crystalline sheets coordinated around MA ions with the help of solvent molecules, as experimentally observed when using DMSO.[176,177] Such considerations reveal that calorimetric measurements cannot be properly applied to this system without taking into account the precursors' interactions in the used solvent. We thus conclude, based on the previous experimental evidences, that $MAPbI_3$ is thermodynamically stable under standard conditions with respect to its halide precursors, albeit probably only slightly.

As a last note, we have also performed heat capacity measurements on a series of halide perovskites, both hybrid and fully organic. The results are given in Appendix **§ 10.5.1**, **Fig. 10.22**. These plots allow us to obtain standard entropies of formation for the compounds, but since the values extracted from our experiment (in the 4-100 K range) conform rather nicely to the ones previously reported,[172] we will use the literature data instead in all the following calculations.

Standard enthalpies of formation

- $MAPbI_3$ is intrinsically stable under standard conditions.
- Precursor-solvent interactions can affect calorimetric measurements.

6.3 TEMPERATURE-INDUCED DEGRADATION

Degradation of HOIHPs upon heating has been heavily investigated, both in the standalone materials[37,38,41–43] as well as in photovoltaic devices.[39,40,44,45] When considering the temperature-induced degradation of these compounds, we can formulate three different decomposition pathways, the first being the degradation yielding the halide precursors:

$$CH_3NH_3PbX_3 \rightarrow CH_3NH_3X + PbX_2 \tag{6.1}$$

Gibbs energy values for this reaction are given in **Table 6.2** for different HOIHPs (note that in the table the values are of opposite sign since they represent formation). As discussed in the previous section (**§ 6.2**), in the case of $MAPbI_3$ the literature thermodynamic data strongly differ, with some reports indicating instability with respect to the precursors,[170] even though spontaneous de-mixing into the solid halides was never observed at room temperature.

Table 6.2. Standard thermodynamic data for the formation of HOIHPs with respect to their halide precursors.

Compound	$\Delta_f H^0$ / kJ · mol^{-1}	$\Delta_f S^0$ / J · (mol · K)$^{-1}$	$\Delta_f G^0$ / kJ · mol^{-1}
$MAPbI_3$	0.5[43]	39.5	−11.3
	34.6[170]		22.8
	4.6[171]		−7.2
	/		−15.4*
$MAPbBr_3$	−2.0[43]	(38.6)**	(−13.5)
	8.0[170]		(−3.5)
	−5.5[171]		(−17.0)
$MAPbCl_3$	−2.8[43]	38.8	−14.4
	−9.0[170]		−20.6
	−4.5[171]		−16.0

* Value obtained by DFT calculations.[42].

** Estimated assuming the S^0 of MABr to be between the values for MAI and MACl, as done in Ref.[171]. Values in parentheses are thus only an estimate.

We can thus calculate the temperature trend of the Gibbs energy of formation of **(Eq. 6.1)**. Here we chose to use the thermodynamic data of Ref.[171] to describe the various HOIHPs, since these are in good agreement with Ref.[43] and with experimental evidences. As shown in **Fig. 6.3a**, we observe that all halide perovskites are entropically stabilized with respect to their halide components, with $MAPbI_3$ expected to be more unstable than $MAPbCl_3$ and $MAPbBr_3$.

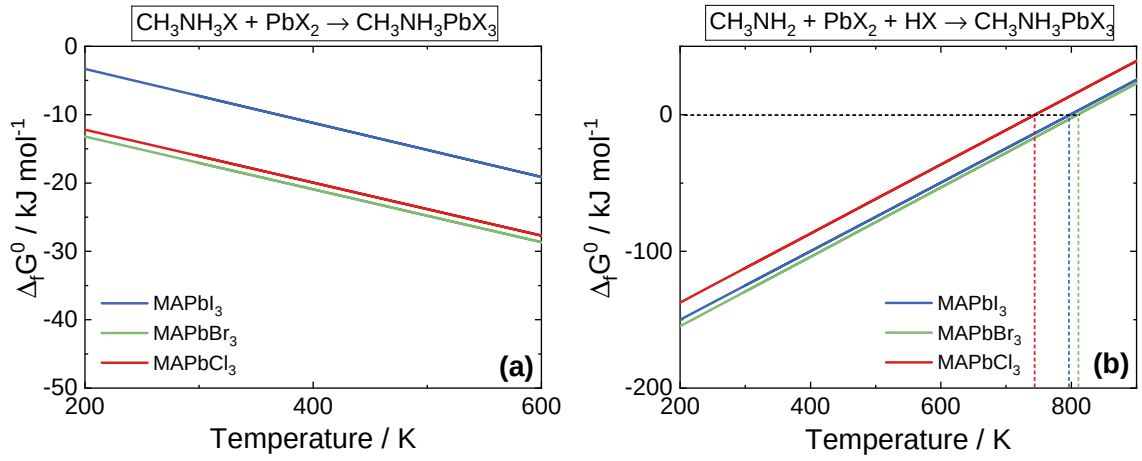

Figure 6.3. Gibbs free energy of formation for different HOIHPs with respect to **(a)** their halide precursors (**(Eq. 6.1)**) and **(b)** their hydrogen halides and lead halides (**(Eq. 6.2)**). Thermodynamic data of halide perovskites taken from Ref.[171]. *Author's note: This figure has been changed from the originally submitted version of the thesis due to a calculation error.*

Interestingly, decomposition into the solid halide precursors was never experimentally observed, even though sublimation of MAX during heating was suggested in Ref.[41]. The lack of observation of $MAPbX_3$ de-mixing into its halide precursors could also be due to kinetic reasons, or even more likely to the presence of more efficient degradation pathways.

This brings us to the second decomposition reaction, which represents the dissociation of MA cations into methylamine (CH_3NH_2) and hydrogen halides (HX). This reaction was proposed in Ref.[37] and experimentally verified for $MAPbI_3$, and in its general form reads as follows:

$$CH_3NH_3PbX_3 \rightarrow CH_3NH_2 + PbX_2 + HX \tag{6.2}$$

As reported in **Table 6.3**, the Gibbs energy for this degradation reaction is clearly positive for all HOIHPs (note that the table shows negative formation values), much more than the previous degradation pathway given in **(Eq. 6.1)**. Nevertheless, in reaction **(Eq. 6.2)** the products are mostly gaseous, providing a significant driving force for degradation under non-standard conditions (especially in a dynamic gas atmosphere). Note that lowering the partial pressure of any of the products by one order of magnitude give a Gibbs energy loss of -5.7 kJ/mol per gas molecule. Thus, this decomposition reaction could happen even at room temperature, for example if $P(CH_3NH_2) = P(HX) \leq 10^{-11}$ bar.

Table 6.3. Standard thermodynamic data for the formation of HOIHPs with respect to methylamine and hydrogen halides.

Compound	$\Delta_f H^0$ / kJ · mol^{-1}	$\Delta_f S^0$ / J · (mol · K)$^{-1}$	$\Delta_f G^0$ / kJ · mol^{-1}
$MAPbI_3$	-204.2 [43]	-178.4	-127.9
	-170.1 [170]		-95.4
	-200.1 [171]		-125.4
$MAPbBr_3$	-202.1 [43]	(-253.8)*	(-126.4)
	-192.1 [170]		(-116.4)
	-205.6 [171]		(-129.9)
$MAPbCl_3$	-186.3 [43]	-252.5	-111.0
	-192.5 [170]		-117.2
	-188.0 [171]		-112.7

* Estimated assuming the S^0 of MABr to be between the values for MAI and MACl, as done in Ref.[171]. Values in parentheses are thus only an estimate.

These values, albeit apparently low, are likely to be reached under real conditions, particularly in a dynamic gas flow. We also note that, in the specific case of $MAPbI_3$, hydrogen iodide (HI) is only marginally stable, so it can easily undergo further degradation into I_2 and H_2, with a minor energy gain towards decomposition (see Appendix **Table 10.4**). We can now discuss the temperature effect for the degradation pathway of **(Eq. 6.2)**, which again we calculate using the thermodynamic data of Ref.[171]. As shown in **Fig. 6.3b**, we can expect that under standard conditions $MAPbCl_3$ would be, thermodynamically, the first to degrade, followed by the iodide and the bromide. Again, this is mostly due to substantial entropy contributions.

We now discuss the third and last decomposition pathway, which involves the breaking of a C-N bond and the formation of methyl halides and ammonia:

$$CH_3NH_3PbX_3 \rightarrow CH_3X + NH_3 + PbX_2 \tag{6.3}$$

We note that some reports showed this reaction to be kinetically hindered and thus not relevant for room temperature,[178] while it was experimentally observed by others at higher temperatures.[44,179] The Gibbs energy of degradation for this reaction are given in **Table 6.4**. We observe that the values do not severely differ from the previous decomposition reaction (**(Eq. 6.2)**), and that here again the products are mostly gaseous. Thus, this degradation could take place at room temperature, e.g. by assuming $P(CH_3X) = P(NH_3) \leq 10^{-9}$ bar.

Table 6.4. Standard thermodynamic data for the formation of HOIHPs with respect to methyl halides and ammonia.

Compound	$\Delta_f H^0$ / kJ · mol^{-1}	$\Delta_f S^0$ / J · (mol · K)$^{-1}$	$\Delta_f G^0$ / kJ · mol^{-1}
$MAPbI_3$	-140.7[43]	-156.8	-94.0
	-106.6[170]		-59.9
	-136.6[171]		-89.9
$MAPbBr_3$	-179.6[43]	(-254.3)*	(-103.8)
	-169.6[170]		(-93.8)
	-183.1[171]		(-107.3)
$MAPbCl_3$	-173.3[43]	-250.1	-98.8
	-179.5[170]		-105.0
	-175.0[171]		-100.4

* Estimated assuming the S^0 of MABr to be between the values for MAI and MACl, as done in Ref.[171]. Values in parentheses are thus only an estimate.

Again here, these values are likely to be reached under real conditions, particularly in a dynamic gas flow. Interestingly, in the specific case of $MAPbI_3$, one of the products (CH_3I) is a liquid under standard conditions, meaning that degradation could theoretically only happen at room temperature under $P(NH_3) \leq 10^{-17}$ bar. The temperature dependence of the Gibbs energy of the reaction **(Eq. 6.3)**, calculated using data from Ref.[171], is given in **Fig. 6.4a**. Due to the different entropy contributions, for this pathway $MAPbI_3$ is expected to be slightly less stable than $MAPbBr_3$ and $MAPbCl_3$.

As a last point, we compare the 3 different degradation pathways for the various HOIHPs. In the case of $MAPbI_3$ (**Fig. 6.4b**), we see that reaction **(Eq. 6.3)** is thermodynamically expected to be more relevant than **(Eq. 6.2)** at room temperature. Nevertheless, the above-mentioned consideration shows CH_3I being a liquid at room temperature, thus we can conclude that **(Eq. 6.3)** is unlikely to be relevant at room temperature under real conditions. This is consistent with the previously discussed kinetic hindrances of the C-N bond breaking process.[178] The reaction is still expected to be relevant at higher temperatures, in agreement with experimental observations.[44,179]

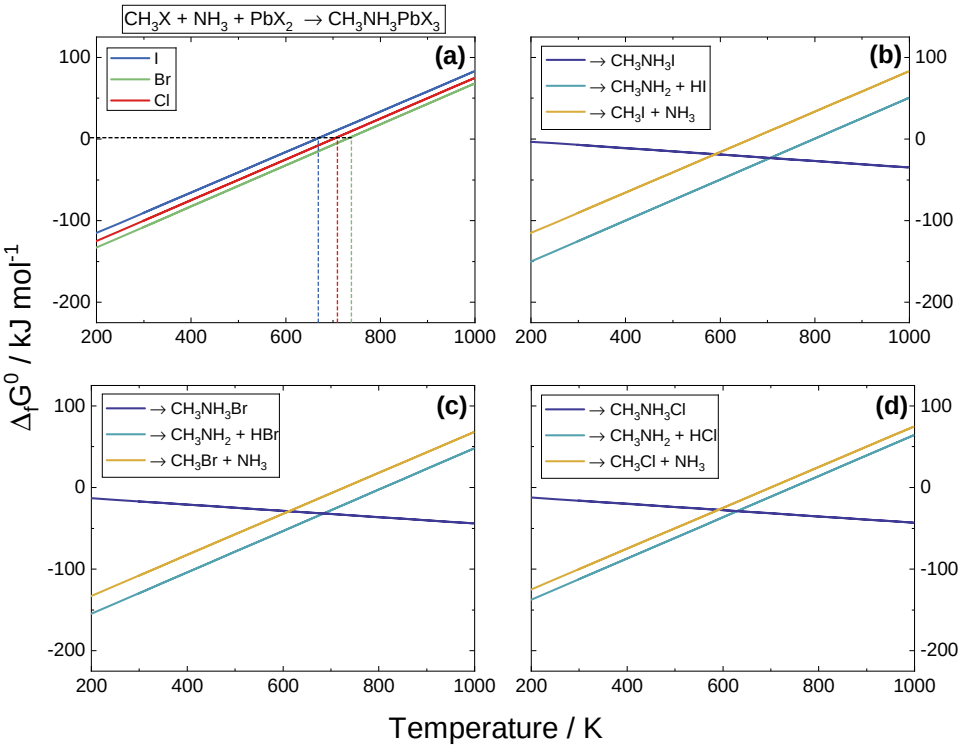

Figure 6.4. **(a)** Gibbs free energy of formation for different HOIHPs with respect to methyl halides and ammonia (as in **(Eq. 6.3)**). **(b-d)** Comparison between the temperature trends of the Gibbs free energy of formation of $MAPbX_3$, with X= I (b), Br (c) and Cl (d), obtained by considering different reactions (**(Eq. 6.1)**, **(Eq. 6.2)** and **(Eq. 6.3)**). *Author's note: This figure has been changed from the originally submitted version of the thesis due to a calculation error.*

We can draw similar conclusions for $MAPbBr_3$ and $MAPbCl_3$, as shown in **Fig. 6.4c,d**, even though in these cases reaction **(Eq. 6.3)** is only slightly energetically favorable over reaction **(Eq. 6.2)** even under standard conditions.

Temperature-induced degradation

Degradation path yielding CH_3NH_2 and HX is the most relevant under real conditions.

6.4 WATER-INDUCED DEGRADATION

Degradation of halide perovskites under water or humidity has been shown to be extremely severe, and it has been investigated both in the standalone materials[46–51] as well as in photovoltaic devices.[39,52] Most of the studies have focused on $MAPbI_3$, where the general consensus is that the process takes place through the formation of intermediates (hydrated species), as shown in **Fig. 6.5**. For low water partial pressures, the hydration is reversible, while for higher relative humidities the system undergoes an irreversible degradation.

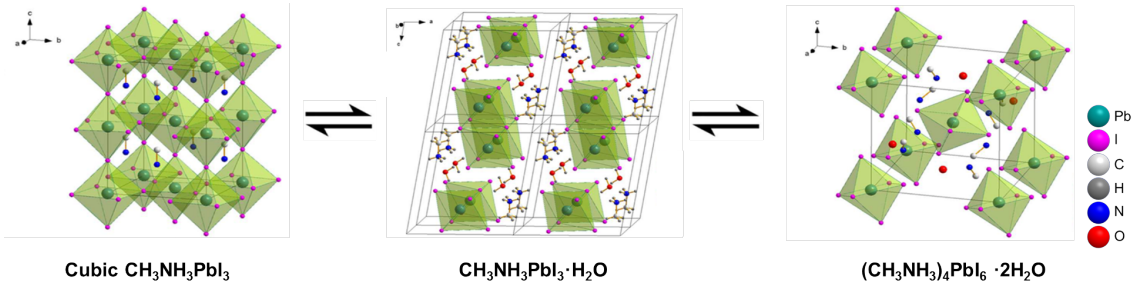

Figure 6.5. Reversible hydration of $MAPbI_3$ upon exposure to humidity. Figure adapted from Ref.[47].

This decomposition, both under high humidity and when exposing to liquid water, happens due to MAI leaching out of the structure.[46,47] MAI can also possibly decompose in gaseous CH_3NH_2 and HI, providing a further energy gain for degradation under dynamic gas flow. Unfortunately, we cannot apply a rigorous thermodynamic treatment for this process, because no thermodynamic data are available for the various intermediates.

Water-induced degradation

Extremely severe degradation of $MAPbX_3$ under water or high humidity.

6.5 PHOTO-INDUCED DEGRADATION

Photo-induced degradation of HOIHPs has also received a significant attention, and previous reports have studied both the materials[45,63,64,66,67] and the related photovoltaic devices.[65,68] Here, however, we propose a new mechanism, which appears as a direct consequence of the photo-induced ion transport described in § 4. Having collected data mostly on $MAPbI_3$, we will restrict here to the discussion of the mechanism on this compound, albeit this process could be of relevance also for other halide perovskites.

The light-induced increase of iodine vacancies discussed in **§ 4.6** has serious implications on decomposition, since the generation of a high number of neutral iodine atoms as a consequence of illumination is reversible only as long as these remain in the lattice. This is the situation taking place in our normal electrical experiments (see **§ 4.2**), where complete reversibility is commonly observed. However, if I_2 is extracted by a sink (e.g. toluene, vacuum, ambient gas phase, etc.), the homogeneity range of the $MAPbI_3$ phase may be exceeded and eventually decomposition will take place. A schematic of our proposed mechanism for the photo-induced degradation is given in **Fig. 6.6**, where we assume that an equilibrium is initially established between $MAPbI_3$ and the outer atmosphere in the dark (here labeled as "Sink").

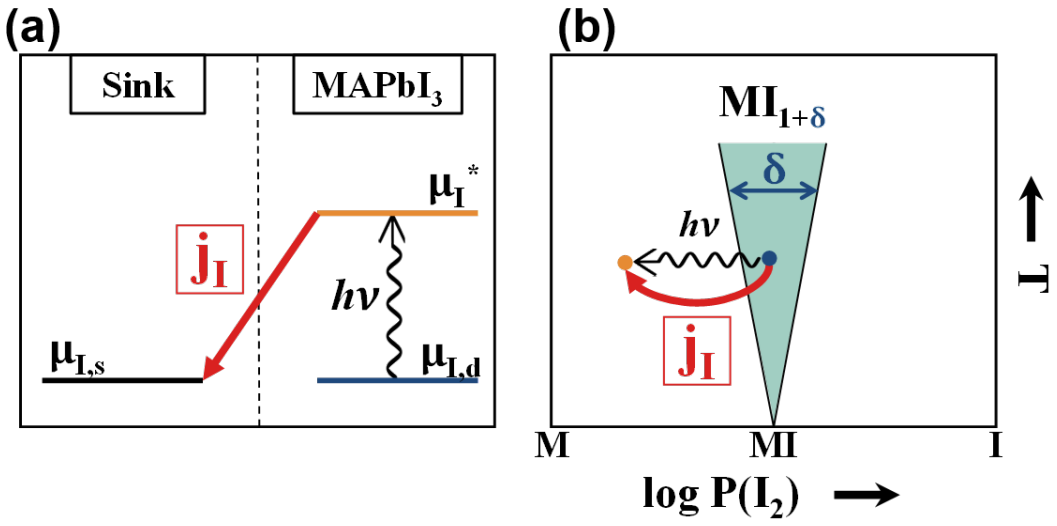

Figure 6.6. Schematic of the light-induced photo decomposition process. **(a)** Illumination enhances the iodine chemical potential in $MAPbI_3$, causing a difference with the equilibrium dark value previously established ($\mu_{I,d} = \mu_{I,s}$). This yields a driving force for an iodine flux ($j_I \propto -\sigma_I^{\delta} \Delta\mu_I$) to take place. **(b)** This photo-induced iodine flux can cause an iodine deficiency exceeding the homogeneity range of the $MAPbI_3$ phase, leading to decomposition. For simplicity, the diagram represents a binary iodide MI.

Upon illumination, the chemical potential of iodine (represented by the activity of the photo-generated neutral iodine atoms) is increased inside $MAPbI_3$, providing a driving force for the generation of an iodine flux (j_I) directed to the outer environment (**Fig. 6.6a**). The initiated iodine flux is driven by this chemical potential difference and is determined by the ambipolar conductivity (σ_I^δ) of iodine in $MAPbI_3$ ($j_I \propto -\sigma_I^\delta \Delta\mu_I$), notwithstanding possible contributions from mobile neutral defects. Assuming no interference coming from electrons, the non-stoichiometry level induced by light can exceed the homogeneity range and therefore surpass the equilibrium stability limit (**Fig. 6.6b**).

This mechanism will necessarily compete with other decomposition pathways, such as the one activated by O_2 or humidity exposure (see for example **§ 5**). As a last point, we note that this decomposition pathway is expected to yield metallic Pb upon substantial I_2 removal. This is indeed observed for $MAPbI_3$ thin film exposed to toluene (acting as an iodine sink) for long times, as reported in the Appendix (**§ 10.5.3**). Interestingly, Pb^0 formation has also been reported in the literature, in complete agreement with our proposed mechanism.[38,55,151] We note also that this process provides a pathway for electron trapping and can explain the *p*-type nature of the electronic conductivity of $MAPbI_3$ samples previously observed under light (**§ 4.5**). The recent experimental observation of partially reversible Pb^0 formation in HOIHPs under light also strongly supports our proposed photo-decomposition mechanism.[150]

Photo-induced degradation in $MAPbI_3$

Light can induce I_2 loss, resulting in intolerable stoichiometric changes.

6.6 OXYGEN-INDUCED DEGRADATION

The effect of oxygen exposure on the stability of HOIHPs was already introduced in a previous chapter (**§ 5.5** and **§ 5.6**), where it was experimentally observed that O_2 can cause severe degradation of HOIHPs and related devices, in agreement with literature.[53–62] The corresponding decomposition reaction is expected to take place whenever the incorporated oxygen content in the halide perovskite lattice exceeds the solubility limit of the phase. We note again that solubility effects have a negligible impact on the phase energetics, even though they are of great importance for transport phenomena (as demonstrated in **§ 5.4**). We can thus calculate the standard Gibbs energies of degradation for several HOIHPs combining tabulated data (given in **Table 6.1** and Appendix **Table 10.3**) together with standard formation enthalpy and entropy values for the perovskite phases

(§ **6.2**). We ignore here reactions that lead to the C-N bond breaking in the MA cation, since these are reported to be kinetically hindered[178] and thus not relevant at room temperature (see also discussion in § **6.3**).

The general degradation reaction of an HOIHP under O_2 can thus be written as follows:

$$CH_3NH_3PbX_3 + \frac{1}{4}O_2 \rightarrow \frac{1}{2}H_2O + CH_3NH_2 + PbX_2 + \frac{1}{2}X_2 \tag{6.4}$$

The calculated thermodynamic data for this reaction are given in **Table 6.5**. Compared with the degradation expected in the absence of oxygen (see **(Eq. 6.2)** and **Table 6.3**), this process shows a much larger tendency towards decomposition due to the large energy gain that comes from forming water instead of HX. This is particularly true in the case of $MAPbI_3$, where HI is only marginally stable with respect to H_2 and I_2. In addition, PbI_2 can also further react with O_2 to yield PbO (Appendix **Table 10.4**), but even though this reaction is slightly thermodynamically favorable, it was never experimentally observed probably due to kinetic reasons. Note that, instead, both $PbBr_2$ and $PbCl_2$ are thermodynamically stable against PbO formation.

Table 6.5. Standard thermodynamic data for HOIHPs degradation against oxygen.

Compound	$\Delta_r H^0$ / kJ · mol^{-1}	$\Delta_r S^0$ / J · (mol · K)$^{-1}$	$\Delta_r G^0$ / kJ · mol^{-1}
$MAPbI_3$	34.8[43]	85.6	9.3
	0.7[170]		−24.8
	30.7[171]		5.2
$MAPbBr_3$	95.5[43]	(115.1)*	(61.1)
	85.5[170]		(51.2)
	99.0[171]		(64.7)
$MAPbCl_3$	135.7[43]	161.0	87.7
	141.9[170]		93.9
	137.4[171]		89.3

* Estimated assuming the S^0 of MABr to be between the values for MAI and MACl, as done in Ref.[171]. Values in parentheses are thus only an estimate.

The apparent, albeit weak, stability of HOIHPs with respect to O_2 exposure is easily lost if the products of reaction **(Eq. 6.4)** are far from standard conditions. This refers particularly to the gaseous species, since we stress here again that lowering the partial pressure of any decomposition product by one order

of magnitude gives a ΔG^0 increase of 5.7 kJ/mol per gas molecule. This is especially critical in the case of $MAPbI_3$, where we expect this effect to easily overcompensate the slight stability under standard conditions and yield instead a strong tendency towards oxygen-induced degradation in real conditions. As an example, we can assume a very conservative estimate of the partial pressures of the various degradation products of $MAPbI_3$ in air, such as water partial pressure $P(H_2O) = 10^{-3}$ bar (3% RH at room temperature), iodine partial pressure $P(I_2) = 10^{-7}$ bar and methylamine partial pressure $P(CH_3NH_2) = 10^{-7}$ bar. By taking oxygen partial pressure at 0.1 bar, the overall $\Delta_f G^0$ of **(Eq. 6.4)** under these assumption is 47.9 kJ/mol, indicating full instability ($MAPbI_3$ values taken from Ref.[171]). Thermodynamic stability can be reached in the aforementioned conditions only by reducing the $P(O_2)$ to the value of 10^{-45} bar at room temperature, that is naturally impossible to reach. We can thus conclude that, without a far-reaching exclusion of oxygen, $MAPbI_3$ is expected to severely degrade upon O_2 exposure, producing PbI_2, CH_3NH_2 and I_2. This reaction was indeed experimentally observed and is discussed in detail in **§ 5.6**.

The degradation process is expected to be less critical for the other halides, due to their enhanced thermodynamic stability against O_2 (**Table 6.5**). Indeed, assuming analogous conditions as before ($P(H_2O) = 10^{-3}$ bar, $P(Br_2/Cl_2) = 10^{-7}$ bar, $P(CH_3NH_2) = 10^{-7}$ bar) we expect $MAPbBr_3$ and $MAPbCl_3$ to be thermodynamically stable under 0.1 bar of O_2, with $\Delta_f G^0_{Br} = -3.5$ kJ/mol and $\Delta_f G^0_{Cl} = -26.7$ kJ/mol. We note once again that such halide and methylamine partial pressures are a very conservative estimate, and are likely significantly lower in air (especially under a streaming gas flow), thus making the degradation likely much more severe. Just to provide an example, atmospheric iodine concentrations (which consider I_2, iodine monoxide IO, iodine dioxide IO_2, etc) are often found around a few ppt (10^{-12} bar) on the mainland, and around 10-100 ppt in coastal air.[180,181] As a last point, we note that albeit thermodynamic considerations clearly indicate a strong tendency for O_2 to degrade HOIHPs (especially $MAPbI_3$), kinetics plays a fundamental role in the interaction of these materials with oxygen, which can ultimately results in a metastable behavior (as discussed in detail in **§ 5.6**).

Oxygen-induced degradation

$MAPbI_3$ unstable against O_2, yielding PbI_2, CH_3NH_2, H_2O and I_2.

6.7 CONCLUSIONS

In conclusion, this chapter has discussed several degradation processes that affect HOIHPs, where possible through thermodynamic arguments. Main findings are:

- Despite some literature reports, formation of $MAPbI_3$ from its halide precursors is expected to be energetically favorable. The same is true for $MAPbBr_3$ and $MAPbCl_3$.
- Temperature can activate a severe decomposition in $MAPbX_3$, with the main degradation reaction expected to yield CH_3NH_2 and HX under real conditions.
- Water and humidity cause severe degradation, mainly caused by MAX leaching from the structure.
- Light can also induce degradation, as a consequence of the photo-enhanced ion transport discussed previously (**§ 4**).
- Oxygen exposure produces a great degradation tendency in $MAPbX_3$. This is particularly critical for $MAPbI_3$, that is expected under real conditions to completely degrade to H_2O, PbI_2, CH_3NH_2 and I_2.

7

SHORT-RANGE ION DYNAMICS IN $MAPbI_3$

Abstract. *In this chapter, we explore the short-range dynamics in* $MAPbI_3$ *using multinuclear NMR and* ^{127}I *NQR. The motion of the MA cation is resolved in a broad temperature range using* ^{1}H, ^{13}C, ^{14}N *and* ^{15}N *spectra, paired with DFT calculations and spectral simulations. We show that this motion can be well described by a bi-axial rotation, becoming isotropic above the cubic phase transition. At higher temperatures, such motion dominates the spin-lattice relaxation time of* ^{1}H, ^{13}C *and* ^{15}N *through a spin-rotational relaxation. These spectra also reveal that* CH_3 *and* NH_3 *groups composing the MA cation show similar interactions with the inorganic framework. Concerning the latter, we observe a strong internuclear coupling between Pb and I, that ultimately dominates both spin-spin and spin-lattice relaxation in* ^{207}Pb. *As for* ^{127}I, *NQR measurements clearly suggest a highly active I-dynamics in the form of planar-torsional oscillations about Pb nuclei.*
We acknowledge Dr. Igor Moudrakovski for having performed the simulations and part of the NMR and NQR experiments.

Publications. *This study has been published in Ref.*[182].

7.1 INTRODUCTION

The short-range ion dynamics in a given compound comprises the various rotational and torsional motions involving its atomic (or molecular) constituents. NMR spectroscopy is an extremely powerful tool to study such processes, particularly because of its unsurpassed sensitivity to short-range interactions.[99–102,183] In the specific case of $MAPbI_3$ (and of other HOIHPs), such dynamics refer to the rotational motion of the organic cation, to the interaction between the organic molecule and the inorganic framework and also to the motions taking place in the inorganic framework. In general, this study aims at the clarification of those dynamic processes that take place on a shorter length scale with respect to ion diffusion, involving local reorientation of the various atomic and molecular com-

ponents. Even more interestingly, the organic cation dynamics (especially in MA-based perovskites) has been linked to the long carrier lifetimes[184–186] and to optical and electronic properties in these materials.[187,188] In addition, the interaction between the organic cation and the inorganic framework through hydrogen bonding[189] has been related to the material structural stability,[190] making the thorough investigation of these dynamic processes extremely important.

First studies on the organic cation dynamics in MA perovskites date back to 1985,[191–195] and report on the rotation of MA in all crystalline phases of $MAPbI_3$, $MAPbBr_3$ and $MAPbCl_3$ using ^1H, ^2H and ^{14}N spin-lattice relaxation time (T_1) measurements. Interestingly, rotation around the C-N axis was observed down to 50 K, even though cooling naturally decreases the rotation rate. Cation dynamics has also been studied in more recent works, both in MA- and MA,FA-perovskites.[69,169,196] Furthermore, structural information can be obtained by NMR. In particular, the low temperature phase transition (orthorombic to tetragonal at 162 K)[195] was observed through ^1H T_1 measurements,[194] while it did not appear in ^2H and ^{14}N measurements.[193] The high-temperature phase transition (tetragonal-cubic at 327 K),[195] which has been investigated much more recently, is instead clearly visible in ^{14}N NMR spectra.[69,197] More generally, NMR spectroscopy has also been used on halide perovskites to study structural properties (crystal quality and presence of extended defects),[198] Pb-X environment,[199] material degradation[200] and phase segregation in multiple cation compositions.[201]

7.2 ^1H NMR

^1H NMR is characterized by such a high sensitivity that it is possible to collect noise-free stationary spectra even in $MAPbI_3$ thin films (**§ 4.4**). In the case of bulk powders, as shown in **Fig. 7.1a**, both stationary and MAS conditions can be applied, the latter yielding two well-resolved signals from CH_3 and NH_3 groups at 3.4 and 6.4 ppm respectively. The position of these signals upon changing temperature is virtually constant (Appendix **Fig. 10.25**). ^1H NMR spectra under MAS conditions can also be useful in assessing the presence of residual solvents from the synthetic step, albeit none were detected in the samples here under analysis. The phase purity of the powders used was also assessed by means of XRD (Appendix **Fig. 10.24**). The majority of our measurements was carried out under stationary conditions, despite the clear improvement in resolution given by MAS. Here, the reason is two-fold. First, it is practically very challenging

to provide a consistent spinning in a broad range of temperature such as the one we examined, especially considering that $MAPbI_3$ powders were sealed in a glass tube in order to guarantee long-time stability. Secondly, MAS conditions have been observed to affect our spin-lattice relaxation time measurements (see Appendix **Fig. 10.26** and **§ 10.6.4** for a more in-depth discussion). This behavior has also been reported in other organic and inorganic solids.[202,203]

Stationary ^{1}H NMR spectra show a broad ($\sim$ 8 kHz) signal, composed of both CH_3 and NH_3 contributions and with a lineshape well represented by a Gaussian function (**Fig. 7.1a**).

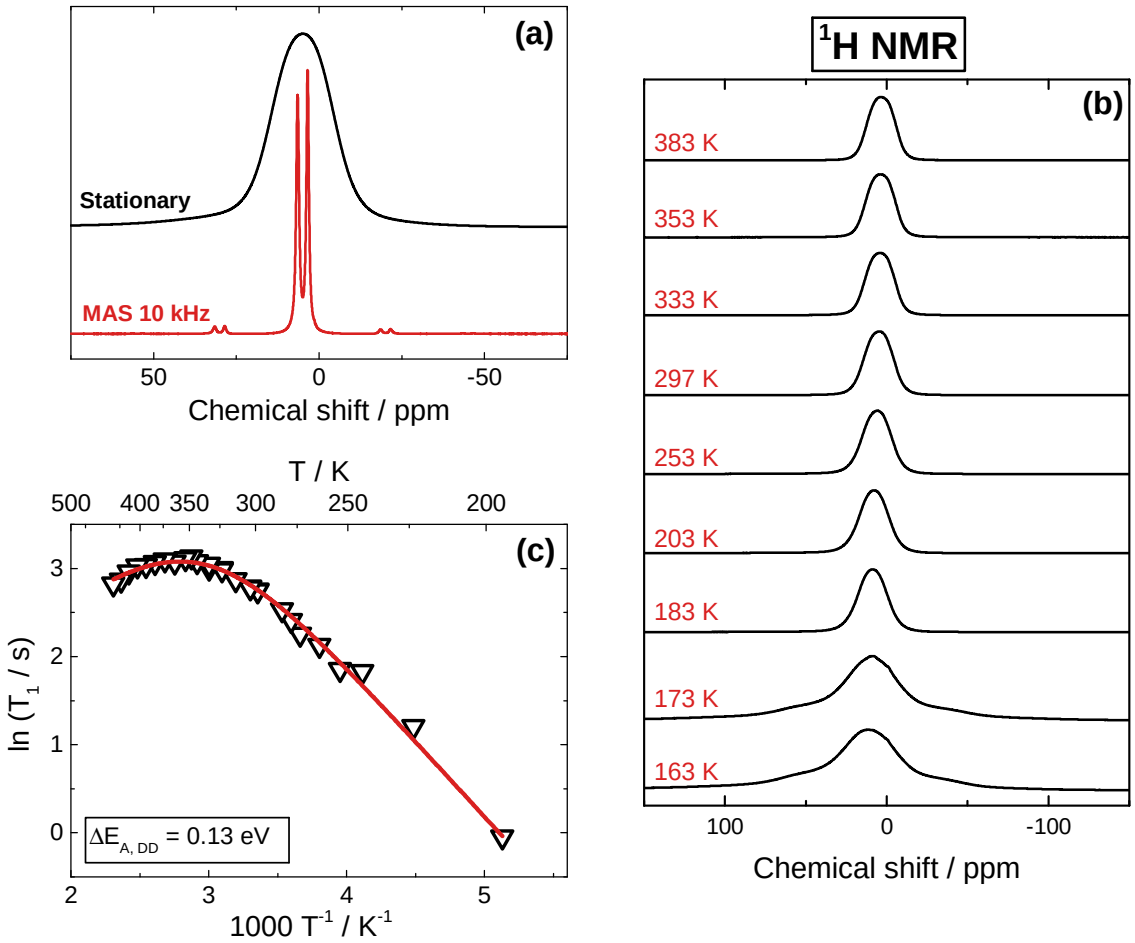

Figure 7.1. **(a)** Comparison between ^{1}H NMR spectra at room temperature collected in stationary and MAS conditions. **(b)** Stationary ^{1}H NMR spectra and **(c)** ^{1}H stationary spin-lattice relaxation time (T_1) as a function of temperature. The low temperature linear behavior was fitted to extract an activation energy for the dipole-dipole relaxation ($\Delta E_{A,\,DD} = 0.13$ eV). This value was then used to perform a fit of the entire curve, yielding an activation energy for the high temperature region (dominated by spin rotational relaxation) of $\Delta E_{A,\,SR} = -0.1$ eV. Due to the narrow range accessible at high temperatures, this latter energy value is only indicative.

As mentioned in **§ 2.4**, the shape and width of ^1H NMR signals in $MAPbI_3$ are defined by different factors, primarily homonuclear dipole-dipole (DD) interactions between protons in the MA cation. Additional contributions come from the heteronuclear interaction between protons and ^{14}N and also between protons and atoms in the inorganic lattice. In general, DD interactions in solids can be evaluated based on the second moment (M_2) of the spectrum, which can be extracted from the FWHM of the signal, making the experimental M_2 values highly sensitive to internal molecular motions. This approach was applied to solid methylammonium halides.[204–207] In parallel, M_2 values can be calculated, for example by assuming a static environment and knowing the geometry of the system. Considering an entirely rigid tetragonal $MAPbI_3$, we obtain M_2 values for CH_3 and NH_3 protons ($1.5 \cdot 10^{10}$ and $4.1 \cdot 10^{10}$ rad^2s^{-2}) that yield calculated static linewidths of 45.7 and 75.6 kHz, respectively (details are given in Ref.[182], particularly in the Supporting Information). In case of internal rotation around the C-N axis, M_2 will be reduced by a factor $F(\gamma) = \frac{1}{4}(3cos^2\gamma - 1)^2$ (with γ the angle between the internuclear axis and the axis of motion).[208] This occurrence (assuming the rotational axis to be normal to all internuclear vectors) yields a reduction of M_2 by a factor of 4. The second moment values obtained both in the static situation and considering only the internal rotation are in contrast with the much narrower experimental linewidth of about 8 kHz coming from the overlap of CH_3 and NH_3 signals ($M_2 = 4.8 \cdot 10^8$ rad^2s^{-2}). This significant discrepancy between calculated and experimental values indicate that both CH_3 and NH_3 groups, along with the aforementioned rotation around the C-N axis, are likely involved in another reorientation with a higher than 2-fold symmetry axis. As the methyl and amino groups composing MA have similar masses, such a reorientation could be a rotational oscillation about an axis passing near the center of the C-N bond and tilted relative to the bond at angle θ. This composite rotation is expected to reduce the second moment by a factor $= \frac{1}{16} \cdot (3cos^2\theta - 1)^2$.[192,209] Since 180°flips ($\theta = 180°$) are not the dominant motion decreasing M_2, we can speculate that a conical motion about the C-N bond at an angle $\theta \leq 60°$(schematics is given below in **Fig. 7.6c**) is likely responsible for the small experimental M_2. This hypothesis will be revisited and confirmed below when discussing ^{14}N NMR results (**§ 7.4**). Note that the absence of 180°flips is consistent with our observation of quadrupolar splitting in ^{14}N spectra (**§ 7.4**) and has also been directly measured by neutron scattering experiments.[210] We expect this situation to remain almost constant as long as the MA cation sustains a fast rotational motion without leaving the cage formed by PbI_6 octahedra at any time. In this respect, many evidences have already been

given to confirm the absence of translational MA diffusion in $MAPbI_3$ (see **§ 2.4**, **§ 4.4**, also Refs.[69,121]). We note that DD interactions remain not fully averaged, neither among the protons in the MA cation, nor with protons from neighboring cells, nor with the atoms of the inorganic lattice. As shown in **Fig. 7.1b**, this yields a ^{1}H NMR signal with an almost constant line shape and FWHM in a broad range of temperatures (see also **Fig. 2.3b**). The only significant change is observed at $T \leq 173$ K, when the signal transforms into a poorly resolved triplet (**Fig. 7.1b**), a signal shape that is commonly assigned to a system of three protons lying at the corners of an equilateral triangle.[208,211] A sudden broadening of the linewidth upon transition below the tetragonal phase has also been observed for $MAPbBr_3$ and $MAPbCl_3$.[192]

More information about dynamics and possible modes of motion involving MA is obtained from ^{1}H spin-lattice relaxation time (T_1) measurements. As presented in **Fig. 7.1c**, between 183 K and 310 K, ^{1}H T_1 shows a relaxation behavior characteristic of the fast motion limit of the Bloembergen-Purcell-Pound (BPP)[212] model. In this temperature range, the relaxation is dominated by DD interactions and assuming an Arrhenius dependence of the correlation time ($\tau_\rho \propto {T_1}^{-1}$) we can extract an activation energy of $\Delta E_{A,\,DD} = 0.13$ eV, that is well within expectations for the rotation of MA inside the Pb-I lattice, and also in good agreement with earlier reports.[194] Note that the T_1 values given here represent an average of the relaxation of CH_3 and NH_3 protons. An accurate analysis of the ^{1}H T_1, given in **Fig. 7.2**, also shows how the observed relaxation time is mono-exponential at every temperature above 173 K, indicating a single relevant contribution to the relaxation mechanism.

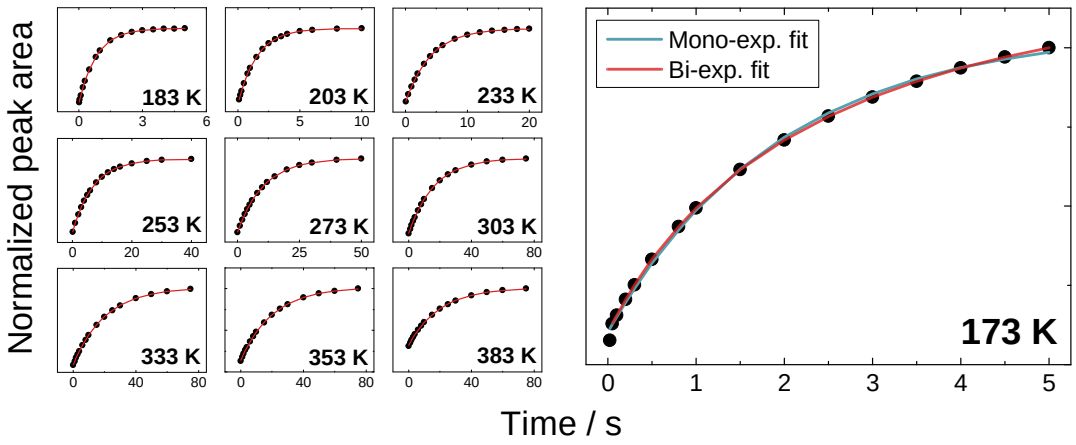

Figure 7.2. Fit of the ^{1}H spin-lattice relaxation time measurements, collected with the saturation recovery method. At all temperatures above 173 K, the trend is well fitted with a mono-exponential function, indicating a single contribution to the relaxation. Below 173 K, a bi-exponential function gives a slightly better fit, possibly suggesting the appearance of a minor second contribution to the relaxation mechanism.

This strongly suggests that the two contributions to the relaxation coming from CH_3 and NH_3 protons are, if not equal, at least very similar, and that there is no sign of a preferential interaction between the inorganic framework and CH_3 or NH_3 groups. We note that the latter statement is in contrast with a previous report where ^1H T_1 measurements under MAS conditions were applied to claim a preferential interaction of the NH_3 group with the Pb-I framework.[196] By repeating the same experiment (Appendix **Fig. 10.26**), we observe a very minor discrepancy between the relaxation times of the two groups, which falls within the error margin of the measurement. One should also note that in this experiment MAS conditions directly affect the T_1 relaxation time (Appendix **Fig. 10.26**). We believe that, for these reasons, the previous literature[196] claim was rather unwarranted. Interestingly, the ^1H T_1 trend makes an inversion above room temperature, as typical of spin-rotational (SR) interactions. As shown in the following sections, the same behavior is observed in ^{13}C and ^{15}N T_1 measurements; moreover, it is found in ^1H T_1 measurements on $MAPbBr_3$ (Appendix **Fig. 10.25**) and $MAPbCl_3$.[192] The relaxation time for ^1H in $MAPbI_3$ can thus be defined as the sum of two contributions, a dipole-dipole and a spin-rotational mechanism, the former dominating the low temperature regime and the latter becoming relevant at higher temperatures (full expressions describing the relaxation mechanisms are given in Ref.[182] Supporting Information). We can thus fit the T_1 relaxation time behavior of **Fig. 7.1c** as the combination of these two contributions, and extract activation energies for both relaxation processes. Unfortunately, while a good estimate of the DD relaxation can be reliably extracted (see above), the experimentally accessible narrow temperature range (due to sample degradation) in which the SR contribution dominates prevents an accurate estimate of the SR activation barrier (see caption of **Fig. 7.1**). We note that in $MAPbI_3$ the change in dominant mechanism takes place in the vicinity of the tetragonal to cubic phase transition, likely because of the increased free space in the PbI_6 cage that permits a less obstructed (and therefore faster) rotation of MA cations. In the case of $MAPbBr_3$ (Appendix **Fig. 10.25**, also Ref.[192]), as expected, the inversion behavior takes place at a lower temperature, albeit not as low as the cubic phase transition (237 K).[195] This occurrence is consistent with previous reports.[192]

^{1}H NMR

- MA rotates around C-N while reorienting with symmetry axis $>$ 2-fold.
- Similar interactions of CH_3 and NH_3 groups with Pb-I framework.

7.3 ^{13}C AND ^{15}N NMR

^{13}C NMR spectra give a good spectral resolution, but a rather low sensitivity due to the scarce natural abundance of the isotope (1.1 %). By using a ^{13}C-enriched $MAPbI_3$ sample (20 % abundance), low-noise spectra can be collected in a relatively short time. Cross-polarisation (CP) to protons, while potentially interesting (see Appendix **§ 10.6.3** and **Fig. 10.26**), is severely hindered in this system by the extremely long ^{1}H spin-lattice relaxation times. For this reason, spectra were recorded with direct excitation.

As shown in **Fig. 7.3a**, both stationary and MAS conditions can be successfully applied. In contrast to protons, MAS here gives only marginal improvements in the resolution of the already narrow signal. In addition, our preliminary experiments have also indicated a clear influence of the spinning conditions on the spin-lattice relaxation time (Appendix **§ 10.6.4** and **Fig. 10.28**). A similar behavior has been reported for other materials.[202,203,213] For these reasons, ^{13}C T_1 measurements have been performed in stationary conditions.

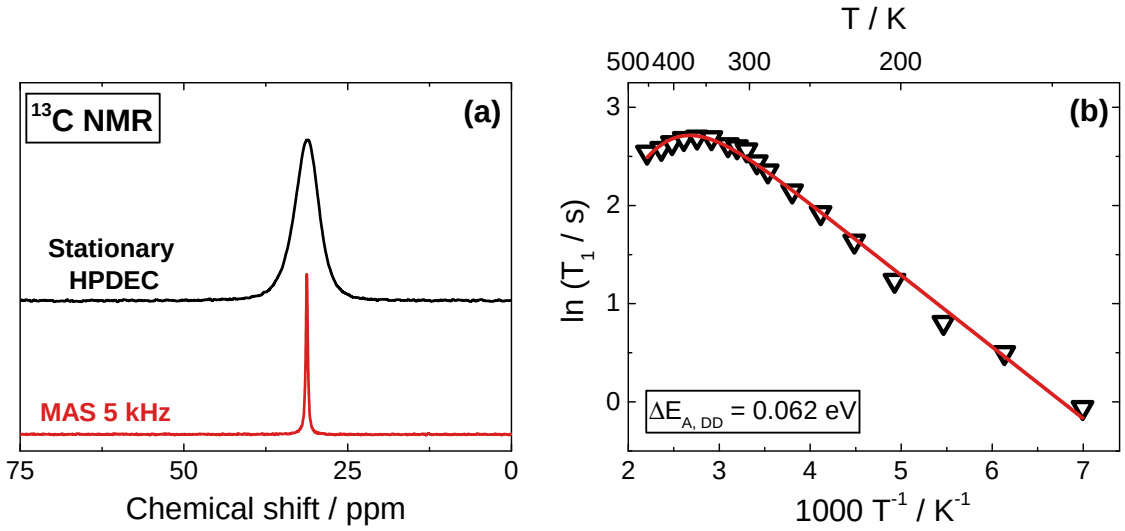

Figure 7.3. (a) ^{13}C NMR spectra at room temperature under stationary and MAS conditions. **(b)** ^{13}C stationary spin-lattice relaxation time as a function of temperature. The low temperature linear behavior was fitted to extract an activation energy for the DD relaxation ($\Delta E_{A,\,DD} = 0.062$ eV). This value was then used to fit the entire curve, yielding an activation energy for the high temperature region of $\Delta E_{A,\,SR} = -0.38$ eV. Due to the narrow range accessible at high temperatures, this latter value is highly inaccurate.

Generally, spin-lattice relaxation time for ^{13}C can be composed of three primary contributions from different relaxation mechanisms.[214–216] These are: i) heteronuclear DD interactions with protons, ii) relaxation due to chemical shift anisotropy (CSA) and iii) SR interactions. General expressions and full treatment of the relaxation time is found in Ref.[182] (Supporting Information). Notably,

we observe a nearly perfectly symmetrical ^{13}C signal lineshape, even at very low temperatures, indicating a negligible contribution of the CSA to the spectra. This is in agreement with *ab-initio* DFT calculations on the tetragonal phase of $MAPbI_3$ producing a very low value (38 ppm) for the shielding anisotropy (Appendix **§ 10.6.7**). Analogously to ^{1}H measurements, ^{13}C T_1 shows a linear trend (in Arrhenius coordinates) at low temperatures, that is attributed to a relaxation mechanism dominated by DD interactions ($\Delta E_{A,\,DD} = 0.062$ eV). At higher temperatures, this linear behavior undergoes a downward turn, corresponding to an increased contribution of the SR mechanism to the relaxation process. As for protons, the trend inverts across the tetragonal to cubic phase transition, indicating a less obstructed MA rotation as the cause for the change in dominant relaxation mechanism.

We can now discuss ^{15}N NMR spectra. As in the case of ^{13}C, the low natural abundance of the nitrogen isotope (0.4 %) gives a significant challenge in the signal acquisition, which however can be overcome by preparing a ^{15}N-enriched $MAPbI_3$ sample (20 % abundance). Analogously to the ^{13}C case, cross-polarisation to protons does not give any significant advantages here (Appendix **§ 10.6.3** and **Fig. 10.26**). As shown in **Fig. 7.4a**, both stationary and MAS conditions can be applied for ^{15}N, even though the spectra are clearly well resolved even in the stationary case. As for ^{1}H and ^{13}C, we also measure ^{15}N T_1 in stationary conditions as a function of temperature.

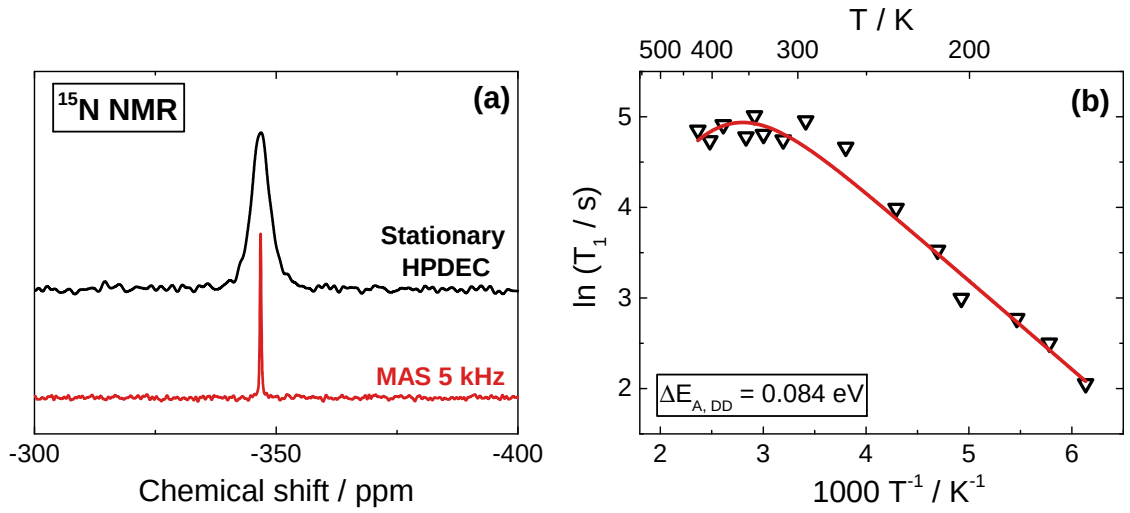

Figure 7.4. **(a)** ^{15}N NMR spectra at room temperature under stationary and MAS conditions. **(b)** ^{15}N stationary spin-lattice relaxation time (T_1) as a function of temperature. The low temperature linear behavior was fitted to extract an activation energy for the DD relaxation ($\Delta E_{A,\,DD} = 0.084$ eV). This value was then used to fit the entire curve, yielding an activation energy for the high temperature region of $\Delta E_{A,\,SR} = -0.17$ eV. Due to the short range accessible at high temperatures, this latter value is highly inaccurate.

The various contributions to the relaxation mechanism in the case of ^{15}N are expected to be the same as the ones discussed above for ^{13}C. Also here, no significant contribution of the CSA to the relaxation process is expected, based on *ab-initio* DFT calculations on the tetragonal phase of $MAPbI_3$ producing a very low value (10 ppm) for the shielding anisotropy (Appendix **§ 10.6.7**), which is by at least 2 orders of magnitude too small to generate significant contributions to the spin-lattice relaxation. As shown in **Fig. 7.4b**, ^{15}N T_1 presents again a linear behavior at low temperatures, characteristic of DD interactions ($\Delta E_{A,\,DD} = 0.084$ eV), while at higher temperatures (near the cubic phase transition), the trend inverts due to SR interactions starting to dominate the relaxation mechanism. Interestingly, the activation energy values obtained for the DD interactions in ^{13}C and ^{15}N are quite similar, indicating that the MA molecule is acting as an almost symmetrical rotor. Also, these energy values are comparable to the one extracted in the ^{1}H case, and this is expected since they refer to the same reorientation and to the same relaxation mechanism (DD interactions).

^{13}C, ^{15}N NMR

- MA behaves as an almost symmetrical rotor.
- Spin rotational interactions dominate relaxation at high T.

7.4 ^{14}N NMR

Due to the quadrupolar nature of ^{14}N nuclei (I = 1), ^{14}N NMR spectra contain a large amount of information regarding the dynamics of the MA cation. As shown in **Fig. 7.5a**, the spectrum demonstrates significant quadrupolar interactions in the tetragonal phase, resulting in a typical spin-1 powder pattern with axial symmetry of the electric field gradient (EFG). Above the cubic phase transition such interactions are averaged by the MA motion, and the quadrupolar splitting disappears (**Fig. 7.5a**, also **§ 2.4**). ^{14}N T_1 measurements, given in **Fig. 7.5b**, shows that the spin-lattice relaxation time becomes longer with temperature, as expected from a dominant quadrupolar relaxation mechanism that is in the fast motion limit of the BPP model.[212] The magnitude of ^{14}N T_1, along with its temperature dependence, indicate the presence of a rapid reorientation around the C-N axis, with a rotational correlation time $\tau_\rho(^{14}N)$ of of 1.0 ps at 303 K (tetragonal phase) and 0.53 ps at 333 K (cubic phase). Details on the calculations are given in the Appendix (**§ 10.6.5**). These extracted values are entirely in agreement with other reports.[191,193,197] In addition, the ^{14}N T_1 temperature dependence is linear in Arrhenius coordinates, with an activation energy in the

tetragonal phase (0.16 eV) that decreases above the cubic phase transition (0.1 eV). While these activation energies cannot be directly compared with the values obtained for the ^{15}N case, as different relaxation processes are involved, they are completely consistent with other reports.[197]

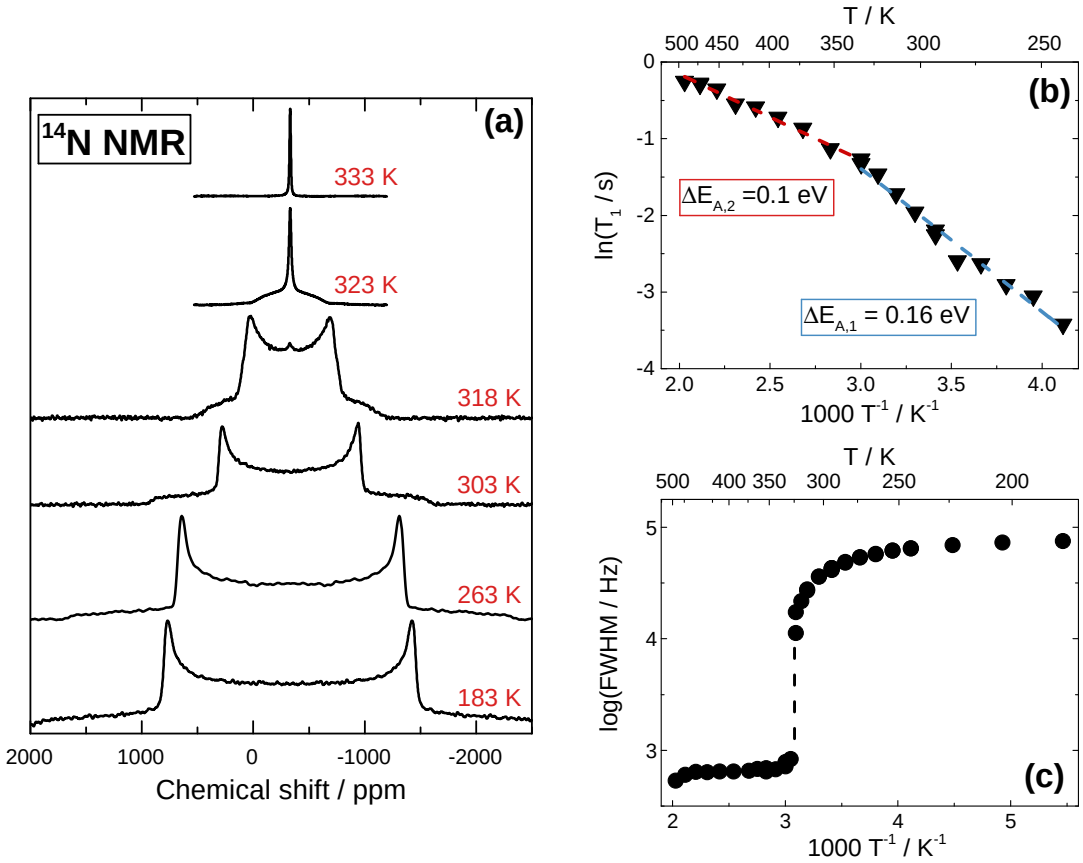

Figure 7.5. **(a)** ^{14}N NMR spectra as a function of temperature, collected in stationary conditions. The tetragonal phase shows a typical quadrupolar splitting ($\eta = 0$). No difference is visible comparing pure and ^{15}N-enriched $MAPbI_3$ samples. **(b)** ^{14}N spin-lattice relaxation time (T_1) and **(c)** ^{14}N FWHM obtained in stationary conditions as a function of temperature. For the signals below the cubic phase, showing a significant quadrupolar splitting, the value of the splitting has been used in lieu of the FWHM.

The drop in activation energy across the phase transition indicates, as expected, a less obstructed MA rotation in the cubic phase, where the signal transforms into a single, narrow Lorentzian peak (FWHM $\sim$ 710 Hz at 333 K) that keeps decreasing upon increasing temperature (**Fig. 7.5c**). This continuous narrowing of the signal is in agreement with a short-range MA motion that becomes faster, but without undergoing any long-range translational diffusion (absence of such motion is discussed in details in **§ 2.4**, **§ 4.4** and also Refs.[69,121]).

Both lineshape and linewidth of the ^{14}N NMR signals contain information on the modes of motion involving MA cations. Generally, lineshapes in ^{14}N NMR are defined by the interactions between the quadrupolar moment of the nucleus

with its surrounding EFG tensor. For a MA cation, this coupling is mainly of intramolecular origin, and is thus heavily influenced by both type and rate of the molecular motions involving MA. Notably, the experimental spectra (**Fig. 7.5a**) display a very broad frequency spread, meaning that we can investigate such motions in a very wide frequency range. As given in details in the Appendix (**§ 10.6.6**), we simulate ^{14}N spectra taking into account different possible MA motions. As shown in **Fig. 7.6**, such simulations yield strongly diverse spectra depending on the motion considered, allowing us to potentially discriminate between them.

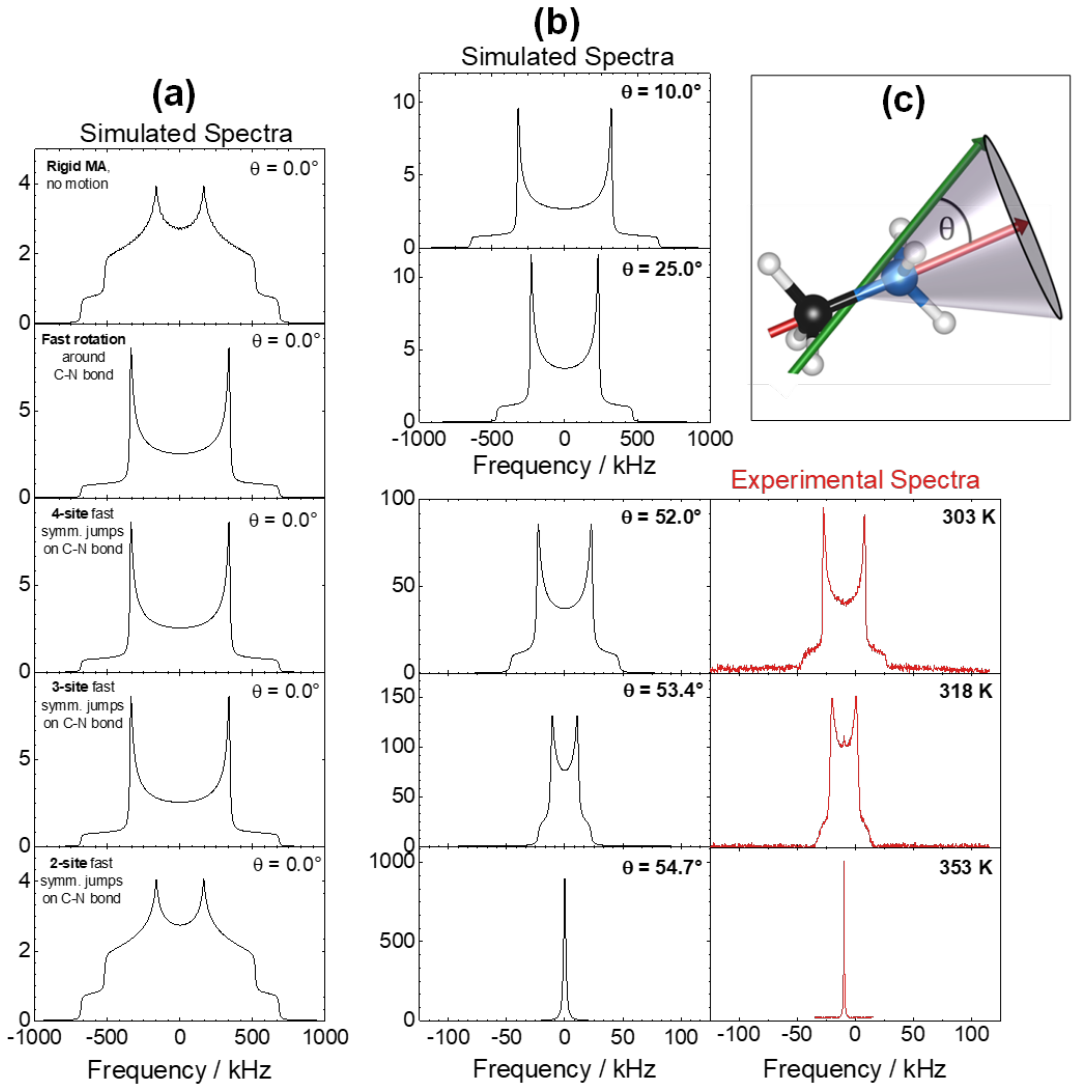

Figure 7.6. ^{14}N spectral simulations obtained considering several different modes of motion involving MA cations. **(a)** Simulations under different dynamic conditions (described on the figure). **(b)** Spectral simulations obtained by modeling a fast rotation of the MA cation around the C-N axis, with a simultaneous precessional motion around the C-N axis tilted at different angles θ. For comparison, experimental spectra across the tetragonal to cubic phase transition are given in red. **(c)** Schematics of the MA motion as resolved by NMR experiments.

It appears evident (**Fig. 7.6a**), that a relatively fast ($> 10^{-6}$ s) and continuous rotation around the C-N bond (or equally fast symmetrical jumps between ≥ 3 sites) is necessary to only qualitatively reproduce the experimental spectra of the tetragonal phase (**Fig. 7.5a**). Interestingly, these modes of motions are still not sufficient to quantitatively describe the situation, for which we must take into account another parallel process. Based on previous considerations (**§ 7.2**), we add to the fast rotation around the C-N bond an additional precessional motion (about the same axis), with increasing tilting angle θ (schematized in **Fig. 7.6c**). As shown in **Fig. 7.6b**, the quadrupolar splitting reduces continuously upon increasing θ up to 54.7°, when it completely disappears indicating that the quadrupolar interactions forming the lineshape have been fully averaged. This behavior describes very accurately the experimental situation across the tetragonal to cubic phase transition, as clear when comparing with the experimental ^{14}N spectra (**Fig. 7.6b**, also **Fig. 7.5a**). While a similar behavior could occur in the presence of 180° flips of the MA cations, or in the case of a sufficiently fast long-range MA diffusion, both of these motions have been clearly ruled out by previous experiments.[69,210] We can thus conclude that the above-mentioned bi-axial MA rotation is highly likely to be the dominant mode of motion involving the organic cation in $MAPbI_3$.

^{14}N NMR

MA motion resolved as bi-axial rotation, nearly isotropic in cubic phase.

7.5 ^{207}Pb NMR

Having fully resolved the MA motion, we can now turn our attention to the inorganic framework, where important information can be obtained using ^{207}Pb NMR. One of the challenges of acquiring ^{207}Pb spectra stems from the enormous range of chemical shifts that the nucleus can have depending on its environment and oxidation state. This yields, as shown previously (**Fig. 2.5**), a remarkably large difference ($\sim$ 1500 ppm) even between the chemical shift of $MAPbI_3$ and of PbI_2, which are expected to have similar Pb-environments. In order to rationalize this peculiar behavior we performed DFT calculations of the ^{207}Pb shielding on several Pb compounds of known environment (details in Appendix **§ 10.6.7**). The calculations capture the general trend between experimental chemical shifts and different Pb-environments, confirming the experimental results, albeit only semi-quantitatively (Appendix **Fig. 10.30**). Another challenge in the detection of ^{207}Pb spectra comes from the iodine surroundings, which cause a very short spin-spin

relaxation time T_2 ($\sim$ 20 μs) and consequently a remarkable broadening of the signals.

As shown in **Fig. 7.7a** (also **Fig. 2.5**), under stationary conditions the ^{207}Pb signal linewidth remains nearly constant in a broad temperature range (433 to 253 K), implying complete absence of translational diffusion of Pb ions. At temperatures below 253 K, a pronounced asymmetry starts appearing in the signals, indicating the presence of substantial chemical shift anisotropy. The signal significantly broadens close to the orthorombic phase transition (173 K, see **Fig. 7.7a**). An interesting temperature behavior is also demonstrated by the spin-spin relaxation time. As shown in **Fig. 7.7b**, ^{207}Pb T_2 increases upon decreasing temperature (up to a distinct 3-fold enhancement at 183 K), albeit the value drops back to 20 μs at 173 K, in agreement with previous reports.[198]

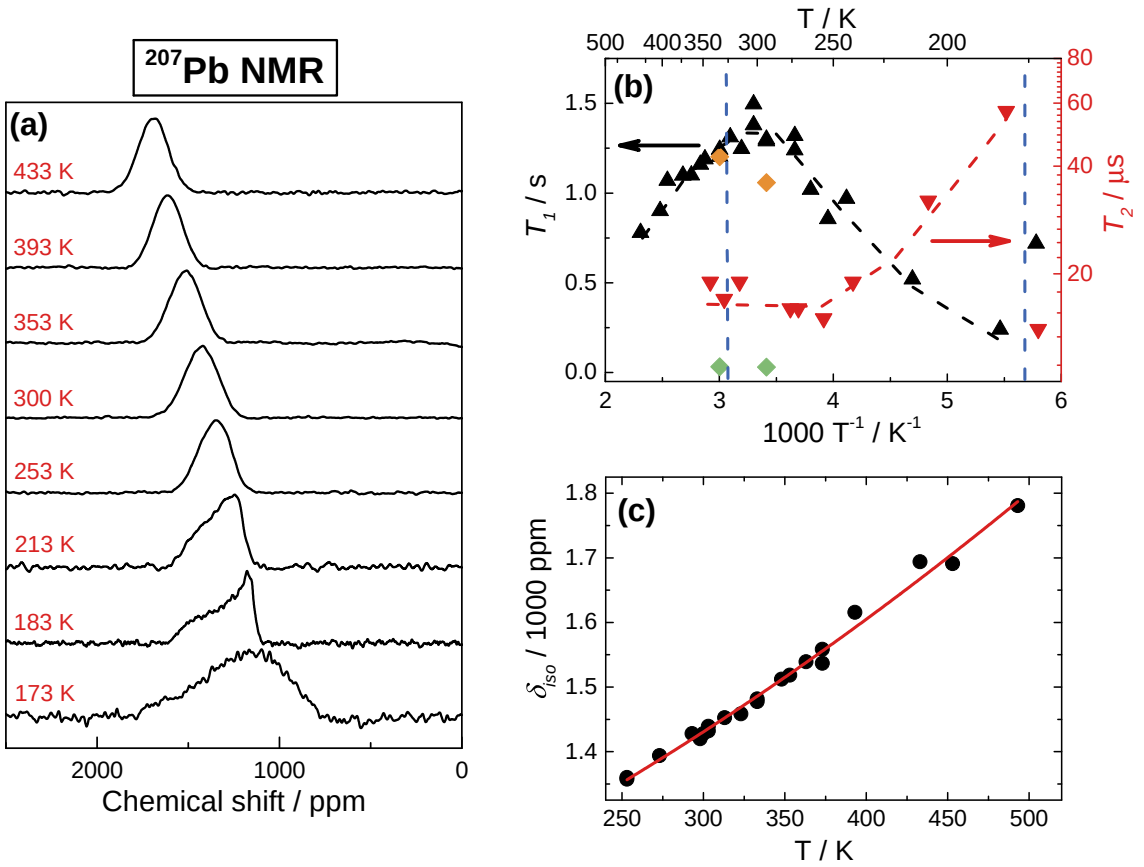

Figure 7.7. **(a)** ^{207}Pb NMR spectra and **(b)** ^{207}Pb spin-lattice (T_1) and spin-spin (T_2) relaxation times collected as a function of temperature in stationary conditions. Solid lines are only a guide to the eye. Vertical blue dashed lines are used to indicate the phase transition temperatures. Orange and green data points represents T_1 relaxation times collected at 21.1 T in stationary (♦) and 8 kHz MAS (♦) conditions respectively. While the higher field does not influence T_1 in stationary samples, a strong decrease of relaxation time is observed while spinning (down to 20-30 ms). **(c)** ^{207}Pb isotropic chemical shift (δ_{iso}) as a function of temperature. The line is a quadratic fit of the form $\delta_{iso} = 1.04 + 0.96(\mathrm{T/K}) + 0.001(\mathrm{T/K})^2$.

While we cannot describe this peculiar behavior through conventional relaxation mechanisms and spectral density functions, it can be easily explained it in terms of strong spin-spin interactions between the spin-$\frac{1}{2}$ ^{207}Pb nucleus and the quadupolar ^{127}I nucleus. In this picture, the ^{207}Pb T_2 is mainly defined by the cross-relaxation to ^{127}I that, as shown in the next section below, has very short T_2 relaxation times. As expected, reducing temperature slows down the cross-relaxation and results in longer ^{207}Pb T_2 relaxation times. Below the orthorombic phase transition the spin exchange dynamics appears to be altered, yielding again a shorter T_2. As this latter aspect needs more experimental evidences, we will presently refrain to discuss it further.

We can now look at the spin-lattice relaxation time T_1. As shown in **Fig. 7.7b**, the values of ^{207}Pb T_1 in $MAPbI_3$ are similar to those reported for PbI_2.[?] The weak temperature dependence and the similarity with ^{127}I T_1 measurements given below (**Fig. 7.8**) give another strong indication of the presence of a significant cross-relaxation between Pb and I. Additional proofs of such coupling are provided by the independence of the relaxation time on the magnetic field, and on the strong dependence on MAS, with spinning conditions able to decrease the ^{207}Pb T_1 by more than 1 order of magnitude (**Fig. 7.7b**, details in the caption). We note that the same behavior was recently discussed for Pb and Hg halides, and in the case of PbI_2 spinning conditions were required to produce effective level crossing between Pb and I.[217] As expected, in the case of $MAPbI_3$ spinning is less critical, as a sufficient crossing of the nuclear energy levels is already present even under stationary conditions, due to the much stronger quadrupolar interaction in this compound.

Finally, we can look at the temperature dependence of the ^{207}Pb isotropic chemical shift (δ_{iso}). As presented in **Fig. 7.7c**, δ_{iso} shows a clear temperature dependence such as the one reported for $MAPbCl_3$[218] and also normally observed in Pb compounds.[219–222] The experimental trend shows a small, albeit distinct, deviation from the usually reported linear temperature dependence (caption of **Fig. 7.7c**). We can fully ascribe this variation to changes in the lattice parameters,[198] as it is normally the case for Pb compounds.[219–222] The temperature dependence does not show any sign of the cubic phase transition, indicating absence of any abrupt change in the lattice parameters. This is in agreement with literature reports showing the high temperature phase of $MAPbI_3$ to be actually pseudo-cubic.[119,195]

^{207}Pb NMR

Strong coupling to quadrupolar ^{127}I, dominating relaxation processes.

7.6 ^{127}I NQR

While ^{127}I is in principle a nucleus that could allow for high sensitivity NMR, its considerable quadrupole moment[223] makes the acquisition of the spectra possible only in systems with relatively high symmetry.[224] Nevertheless, we have attempted to collect a ^{127}I NMR spectrum in $MAPbI_3$ (Appendix **Fig. 10.31**), even though the signal is so severely broadened as to make any information extracted highly unreliable, along with being practically extremely challenging and time consuming to acquire. Fortunately, in $MAPbI_3$ the presence of a substantial EFG at the iodine sites ($\chi_Q > 550$ MHz) makes it possible to study the iodine environment by means of Nuclear Quadrupolar Resonance (NQR) spectroscopy.

As reported in **Fig. 7.8a**, in the tetragonal phase of $MAPbI_3$ the presence of two distinct iodine sites yields two pairs of transitions in ^{127}I NQR. Upon transforming into the cubic phase, only one pair of transitions is visible, corresponding to the single remaining iodine site.

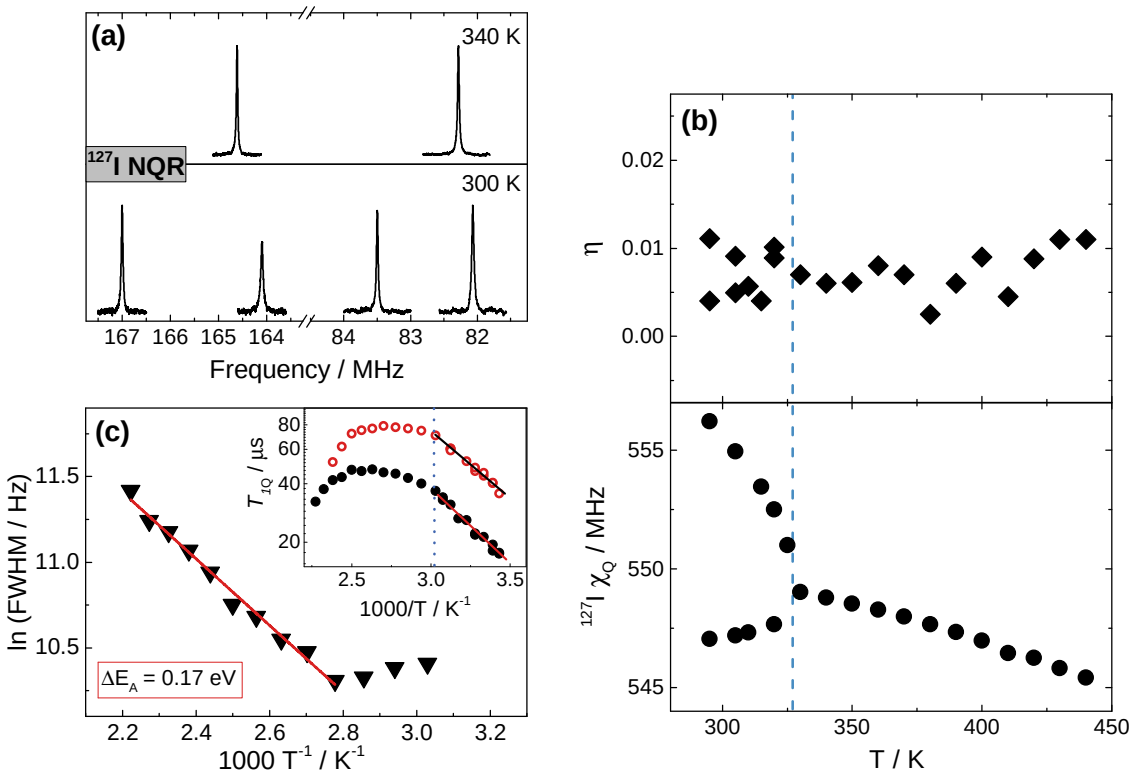

Figure 7.8. (a) ^{127}I NQR signals of $MAPbI_3$ in the tetragonal (300 K) and cubic (340 K) phase. **(b)** Temperature dependence of the ^{127}I quadrupolar coupling constant (χ_Q) and of the asymmetry parameter (η). Blue dashed line indicates the phase transition. **(c)** FWHM of a NQR transition ($\nu_{3/2\leftrightarrow5/2}$) as a function of temperature. Inset shows the temperature dependence of the quadrupolar spin-lattice relaxation time (T_{1Q}) for the two ^{127}I NQR transitions (● $\nu_{3/2\leftrightarrow5/2}$, ○ $\nu_{1/2\leftrightarrow3/2}$).

As shown in **Fig. 7.8b**, the phase transition is also visible in the temperature dependence of the quadrupolar coupling constant (see Appendix **Fig. 10.32** for the signal resonance frequencies). In addition, the appreciable temperature dependence that is visible above 327 K (**Fig. 7.8b**, also Appendix **Fig. 10.32**) can be attributed to a planar-torsional oscillation of a resonant nucleus (I) about another atom to which it is bonded (Pb). As detailed in Appendix **§ 10.6.9**, we can fit such temperature dependence to extract a torsional oscillation frequency $\nu_t \simeq 1.15$ THz (or 38 cm^{-1}). As a comparison, Raman frequencies around 20-50 cm^{-1} have been calculated for Pb-I contributions to the vibrational spectrum, albeit these are not purely inorganic but coupled with MA-modes.[225,226] Experimental works, instead, assign the Pb-I contribution to slightly higher frequencies (75-125 cm^{-1}), again stressing the coupling with the organic cation vibrations.[64]

As a last point and as shown in **Fig. 7.8c**, we also analyze the ^{127}I NQR FWHM as a function of temperature. The massive broadening of the signal upon increasing temperature strongly indicate highly active short-range iodine dynamics, which could happen as a pre-step of the substantial iodine translational diffusion reported in previous chapters (see **§ 2**, **§ 3**).

^{127}I NQR

Iodine atoms undergo planar-torsional oscillations about Pb atoms.

7.7 CONCLUSIONS

In this chapter, we studied the short-range ion dynamics in $MAPbI_3$ by means of many NMR and NQR experiments. Major findings are:

- MA motion can be described as a bi-axial rotation, which becomes almost fully isotropic above the cubic phase transition.
- MA cations behave as almost symmetrical rotors, with similar interactions of CH_3 or NH_3 groups with the inorganic framework.
- A very strong quadrupolar coupling between ^{207}Pb and ^{127}I is present, which entirely dominates the relaxation processes in the former nucleus.

CONCLUSIONS

8

CONCLUDING REMARKS

This thesis work has focused on the study of the defect chemistry and transport properties in hybrid halide perovskites, in particular in $MAPbI_3$. The main aspects investigated were:

- **Ionic and electronic charge transport,** where we aimed at elucidating the charge carrier chemistry in $MAPbI_3$, particularly in the dark.
- **The effect of light on ion transport,** where we investigated the remarkable finding of huge photo-enhanced ionic conduction in $MAPbI_3$.
- **The effect of oxygen on halide perovskites,** where we studied the stability and transport properties of various HOIHPs upon oxygen exposure.
- **Thermodynamic stability of halide perovskites,** where we explored the stability of HOIHPs from the thermodynamic point of view.
- **Short-range dynamics,** where we clarified the nature of the nuclear and molecular motions taking place in the $MAPbI_3$ structure.

Starting from the charge transport, we gave many unambiguous evidences that show $MAPbI_3$ to be a mixed-ionic electronic conductor under equilibrium conditions. Considering its charge carrier chemistry, we observed through various experimental methods that the situation in the dark does not strongly differ from the one often found in many oxide perovskites. Indeed, we recognized anion vacancies ($V_I^{\bullet}$) to be the dominant ionic charge carriers under equilibrium conditions, alongside electron holes ($h^{\bullet}$) for the electronic transport. Conduction electrons also come into play under very low iodine activities. NMR and tracer diffusion measurements also clearly showed no significant contribution of MA or Pb ions to the ionic transport. We note, nevertheless, that we observed a minor MA diffusion that could still be relevant for other processes such as cation exchange reactions or degradation. In addition to identifying the nature

of the dominant ionic and electronic charge carriers, we showed that stoichiometry variations and doping can be used to purposefully and greatly influence the ionic and electronic transport in $MAPbI_3$, offering a powerful tool to tune the material properties.

Having fully clarified the nature of the charge transport in the dark, we moved to characterize the situation under illumination. Under these conditions, surprisingly, $MAPbI_3$ is still a mixed ionic-electronic conductor, with a significant ionic conductivity. As for the situation in the dark, our experiments indicate the dominant ionic and electronic charge carriers to be $h^\bullet$ and $V_I^\bullet$. Remarkably, we observed that the reason for the still significant ionic conductivity under illumination lies in a large photo-induced enhancement of ion transport. We studied this striking effect through many techniques, ultimately attributing it to a light-induced generation of ionic charge carriers ($V_I^\bullet$). Based on the experimental data collected, we also proposed a straightforward mechanism for the photo-enhanced ion conductivity that relies on a quick interaction of electron holes and iodine lattice sites. While this process is reversible in the short time scale, we expect it will ultimately lead to a severe photodecomposition of $MAPbI_3$ (and possibly of other HOIHPs) due to irreversible halide loss.

The knowledge gained so far allowed us to study the charge transport properties of $MAPbI_3$ upon oxygen exposure, both in the dark and under illumination. In view of environmental stability being the most severe issue that presently impedes the further development of HOIHPs and related devices, we studied the degradation of several perovskite compositions under oxygen. Here, we observed how the O_2 interaction with $MAPbI_3$ takes place in three different regimes, which we described based on both thermodynamic and kinetic considerations. Thermodynamically, $MAPbI_3$ is expected to fully degrade upon oxygen exposure, and this is indeed observed under relatively intense light. Interestingly, we directly observed that illumination affects the kinetics of oxygen incorporation, so much so that in the dark the interaction is very sluggish, thus limiting the O_2-effect to a surface layer and making the material metastable. Under intermediate conditions (relatively low light intensity) the kinetics is partially accelerated, allowing for a substantial incorporation of O_2 that results in reversible acceptor doping of the material without undergoing degradation, thus greatly varying its electronic and ionic transport properties.

Recognizing the importance of stability issues in HOIHPs, we then investigated possible degradation pathways through thermodynamic considerations. We note that the underlying thermodynamics already captures the great tendency of halide perovskites towards decomposition. These considerations are in

full agreement with experimental literature reports showing significant degradation of HOIHPs upon exposure to water, temperature, oxygen and illumination. This decomposition is particularly critical for $MAPbI_3$, providing a severe intrinsic bottleneck for the future application of this material.

As a final aspect, having clarified the long-range diffusion of ions in $MAPbI_3$, both in the dark and under illuminations, we investigated the short-range ion dynamics by means of many NMR and NQR experiments. This study intended to clarify those dynamic processes that happen on a shorter length scale than solid state diffusion. Short-range processes concerning MA cations are known to directly affect the electronic charge transport. In this respect, we resolved the motion of the MA cation, ascribing it to a bi-axial rotation that becomes almost fully isotropic above the cubic phase transition. In addition, we observed that MA behaves as an almost symmetrical rotor, with similar interactions of CH_3 or NH_3 groups with the inorganic framework. Concerning the inorganic lattice, we observed a strong quadrupolar coupling between Pb and I nuclei, which entirely dominates relaxation processes in the former nucleus. Also, I atoms showed highly active short-range dynamics in the form of a torsional oscillation about Pb nuclei.

In a more general view, this research work contributed to the fundamental understanding of charge transport processes in HOIHPs, for which both ionic and electronic contributions must be considered. Also, the ionic transport was studied with respect to its influence on degradation kinetics of the materials and, even more importantly, to its interactions with light. Particularly concerning this latter topic, our investigations left many open questions, which deserve to be thoroughly investigated as they hold much potential both for fundamental insights and for practical applications.

As a closing remark, we find it important to underline again that hybrid halide perovskites truly show many exceptional photo-electrochemical properties, and even more interestingly, remarkable light effects on ion transport. Despite their present shortcomings, the fundamental understanding of their underlying properties will potentially lead to achievements that could result in important technological advances. For these reasons, we strongly encourage the continuation of these relevant -and potentially very fruitful- investigations.

APPENDIX

9

EXPERIMENTAL METHODS

SYNTHESIS

Methylammonium halides

MAI, MABr and MACl are synthetized by cooling in ice a solution of methylamine (CH_3NH_2, Sigma Aldrich) in ethanol (33 % wt.), and adding an excess amount of HX dropwise under constant stirring, to avoid increasing temperature. Then the solution is left to rest until crystallisation of the product. The MAX crystals are transferred into a Büchner funnel and washed several times with diethyl ether, to remove the excess HX. Finally, the crystals are dried at low temperature (333 K) and under rough vacuum for several hours before being stored in an Ar-filled glovebox and protected from the light. Formamidinium iodide can be synthetized in the same way from formamidine. In addition, ^{13}C- and ^{15}N-enriched MAI was also prepared, for NMR and tracer diffusion experiments. In this case, ^{13}C- and ^{15}N-enriched CH_3NH_2 (99% enrichment, Sigma Aldrich) gas was condensed and dissolved in ethanol, to be subsequently used in a normal MAI synthesis step.

$MAPbX_3$ *single crystals*

To achieve the necessary phase purity, halide perovskites are synthesized in single crystal form according to a modified reported procedure.[227] An equimolar mixture of MAX and PbX_2 (Alfa Aesar, 99.9995 %) of 1 M concentration is prepared by dissolving the compounds in γ-butyrolactone (X = I) or dimethylformamide (X = Br, Cl). This solution is filtered through a teflon (PTFE) filter with 2 μm pores and transferred in a vial that was previously cleaned with concentrated HNO_3. The closed vial is progressively heated in a oil bath up to 400 K, and left there until a significant amount of single crystals forms (3-5 hours).

Depending on the presence of nucleation centers (e.g. scratches on the vial or particles in solution) the growth yielded either many small crystallites or few large ones, and also affected the crystallisation time. The residual solution is then removed while still hot and the crystal quickly transferred on drying paper to remove the superficial solvent. Then, the crystals are dried using a Schlenk line at 333 K under mild vacuum for several hours. After this step, no solvent signals are visible in highly sensitive ^{1}H NMR spectra. No secondary phases are also detected by means of XRD. For Na-doped $MAPbI_3$ samples, the procedure is identical but the precursors mixture contains NaI and PbI_2 in the molar proportion 0.01 : 0.99. The syntheses are carried out in laboratory atmosphere, while the precursors are stored and weighted in an Ar-filled glovebox. Samples are also stored in the glovebox after the drying step, and protected from the light. For electrical measurements, the crystals are crushed and uniaxially pressed in 5 mm pellets, using carbon foil as electrodes. These procedures are carried out in the glovebox. The pressing step typically yielded $\sim$ 95 % dense samples.

XRD analysis

$MAPbI_3$ samples, after synthesis, are characterized by XRD analysis. For pellets, the characterization is carried out in Bragg-Brentano geometry, with a PANalytical Empyrean (Cu K_α, $\lambda = 0.154$ nm, 40 kV, 40 mA). For thin films, a PANalytical Empirean II (Cu K_α, $\lambda = 0.154$ nm, 40 kV, 40 mA) with a PIXcel^{3d} detector is used in Grazing Incidence (GI, $\omega = 2^\circ$).

Thin films preparation

Thin films are obtained by spin-coating on sapphire substrates an equimolar solution of MAX and PbX_2 in DMSO (1.5 M). During spinning, a drop of chlorobenzene (0.5-1 mL) is used to induce rapid crystallisation of the perovskite phase, being an effective antisolvent. The samples are then annealed at 373 K for 5 minutes. This entire procedure is carried out in an Ar-filled glovebox. Mixed-halide perovskites are obtained simply by mixing the respective methylammonium halides and lead halides in the appropriate amounts. For mixed-cation perovskites, formamidinium (FA) iodide is used as a precursor along with MAI. Typical films have a thickness of about 300 nm and are rather compact when observed with an optical microscope. Confirmation of the high film quality comes from the uniform dark color and mirror-like reflective surface typically obtained.

For electrical measurements, prior to spin-coating, Au electrodes are deposited by evaporation on the sapphire substrate in an interdigitated fashion (**Fig. 9.1a**).

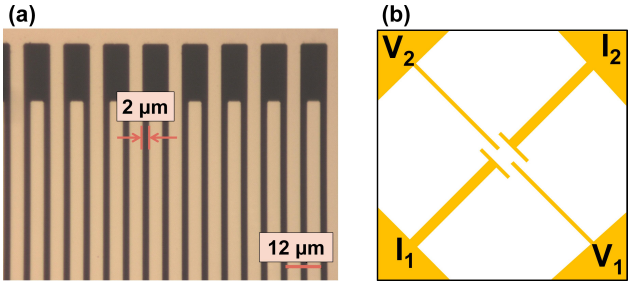

Figure 9.1. **(a)** Optical microscope image of interdigitated electrodes used for a.c. impedance and d.c. galvanostatic measurements. Bright parts are the gold electrodes. **(b)** Electrode geometry used for Hall effect measurements. The voltage side is spaced 5 μm, while the current side 20 μm.

ELECTRICAL MEASUREMENTS

Measurement cells and variable parameters

In-house built measurement cells are used for electrical measurements, in order to simultaneously control atmosphere, temperature and illumination over the samples. The cell is schematized in **Fig. 9.2**. For illumination, Xe-arc lamps (300 or 150 W) are used, and the intensity is cut with neutral density filters. A quartz rod is used as a light guide to bring the light to the thin-film samples. The electrical contact is achieved using Au-coated Cu pins, to avoid corrosion in I_2 atmosphere. For pellets, no illumination is required and therefore a simpler version of the cell is used, without a light guide.

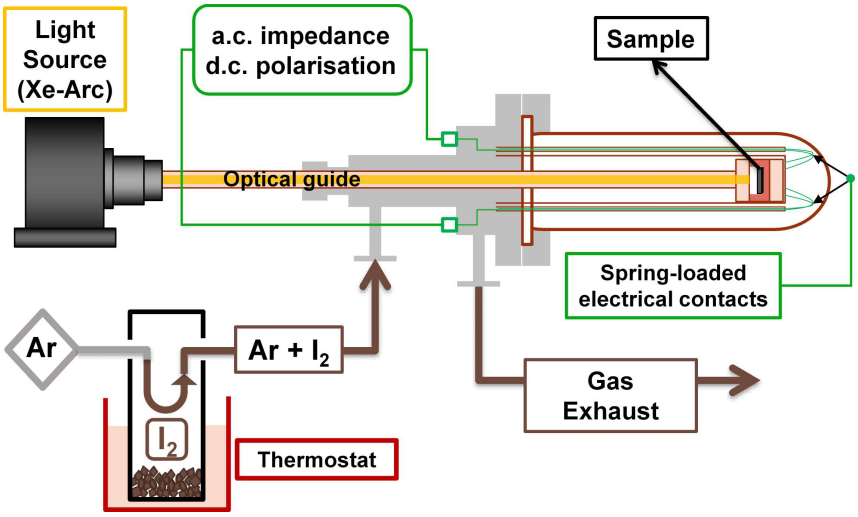

Figure 9.2. Schematics of the cell used for electrical measurements.

Atmosphere control

In almost all the experiments discussed, atmosphere control is of utmost importance. Oxygen partial pressure is controlled by mixing oxygen (99.9999 %) with argon (99.999 %) using mass flow controllers. When needed, 1000 ppm O_2/Ar is used instead of pure O_2. The oxygen concentration is always recorded at the exhaust of the measurement cell with a lambda sensor (Rapidox, Cambridge Sensotec). When needed, a humidity sensor (Hygrochip HYT, IST) is also used.

For iodine partial pressure control, the desired gas is flown through a container with solid I_2 chips, that is immersed in a thermostat (**Fig. 9.2**). By controlling the I_2 temperature, a known partial pressure of iodine is generated, that is equal to the equilibrium pressure. This can be calculated either from an empirical equation[228] or from simple thermodynamic considerations based on the Gibbs free energy of sublimation of solid I_2. The values obtained in the two cases are very similar, however for simplicity we used the empirical equation in all reported curves. Due to the lack of commercial iodine sensors, the effective I_2 pressure could not be directly measured.

We note that, in the interest of accurately measuring $P(I_2)$ values, we built a potentiostatic iodine sensor by assembling a cell of type Ag|AgI|Pb,PbI_2. Such a cell, exposed to I_2 on the Ag side, gives a $P(I_2)$-dependent voltage. Even though this cell could effectively capture $P(I_2)$ values above 10^{-5} bar, it was unable to accurately give a voltage response below that threshold, probably due to practical issues such as sealing and surface limited I_2-transfer. For this reason, we chose to evaluate $P(I_2)$ only based on the equilibrium pressure of crystalline iodine.

Galvanostatic polarisation and impedance spectroscopy

D.c. galvanostatic polarisation measurements were carried out with a high impedance current source (Keithley 220) and electrometer (Keithley 6514). Alternatively, a high impedance source meter was used (Keithley 2634B).

A.c. impedance spectroscopy data were acquired with Novocontrol Alpha A with electrochemical interface.

Hall effect

A in-house built setup was used to acquire Hall effect data, consisting of a Bruker B-E 15 magnet (up to 1.2 T) with a high impedance current source (Keithley 220) and electrometer (Keithley 6514). Thin films were measured, using sample cells

similar to the ones previously introduced (**Fig. 9.2**), with the notable differences of using 4 contacts and allowing a sample position normal to the magnetic field. For this measurements, the evaporated Au electrode were designed in a different fashion (**Fig. 9.1b**), in order to reduce as much as possible the resistance of the films. For illumination, a Xe-arc lamp was used.

ELECTROCHEMICAL EXPERIMENTS

Electromotive force experiments (emf)

This experiment is performed in two different fashions for pellets and thin films. In the former case, two glass tubes are used, and sealed on the two opposite faces of a pellet (previously equipped with electrodes). Sealing is provided by epoxy glue, which is also applied on the lateral surface of the pellet. Prior to the sealing step, coated Cu wires are connected to the electrodes with Ag-epoxy paste, in order to measure the emf voltage with a high impedance electrometer (Keithley 6514). Argon gas with two different $P(I_2)$ is flown in the tubes, while heating to the desired temperature. After an equilibration time, a voltage dependent to the difference between the two $P(I_2)$ values is established and recorded.

For thin films, the experimental schematic is given in **Fig. 4.2**. $P(I_2)$ values are here provided by mixtures of Ag, AgI and Pb, PbI_2 that are pressed in pellet form. The mixtures are prepared with excess metal in order to ensure good electrical contact ($R \sim 0$), and then applied on the surface of a $MAPbI_3$ thin film. The area around the contact with these pellets (and the rest of the film surface) are then sealed with polymethylmethacrylate in order to avoid exchange with the atmosphere. The emf voltage is measured with a Keithley 6514 after heating the cell and waiting for equilibration.

Reaction cell experiments

A typical reaction cell (**Fig. 2.1**) is assembled in the form $M|MAPbI_3|AgI|Ag|$, with M=Pb or Cu. AgI, $MAPbI_3$ and Pb are fabricated in pellet form (purity > 99.99 %) by pressing the corresponding powders. For Cu and Ag, a metal foil of similar purity is used. The cell is assembled and kept together by spring force, and a current ($25\ nA/cm^2$) is applied for 1 week under inert atmosphere and at T = 323 K. After this step, the cell is disassembled and the various surfaces probed by XRD, optical microscope and, when necessary, SEM and EDS. For the control experiments, identical conditions are used but without applying any current.

Permeation cell experiment

In a permeation experiment (schematic in **Fig. 4.2**), a Cu foil is used as substrate for depositing a $MAPbI_3$ thin film. The foil is initially cleaned with a citric acid solution to eliminate the surface oxide layer and then exposed to a very quick O_2 plasma cleaning step. A $MAPbI_3$ film is deposited and the sample is exposed to $P(I_2)$ (=$3.6 \cdot 10^{-6}$ bar), with half of the setup illuminated, while half kept in the dark. GIXRD analysis was later used to probe the growth of the CuI layer between Cu and $MAPbI_3$ caused by the iodine permeation flow. A control experiment without external $P(I_2)$ has also been carried out.

Toluene treatment and I-excorporation

For these experiments, a $MAPbI_3$ thin film on sapphire substrate is immersed in toluene, contained in a UV-Vis quartz cuvette. The rate of I_2 excorporation is monitored by recording *in-situ* the I_2 signal in UV-Vis spectroscopy as a function of time, with and without external illumination (schematic given in **Fig. 4.3**). The cuvette is closed in order to avoid solvent evaporation.

TRACER DIFFUSION EXPERIMENTS

^{13}C tracer

For this experiments, the source of isotope is a ^{13}C- and ^{15}N-labelled $MAPbI_3$ pellet or thin film. The two pellets (or two films), one pure and one enriched, are contacted from the surface by spring force, and kept under Ar. We note that, while in the pellet case the contact is expected to be satisfactory, we cannot guarantee an homogeneous contact in the film case. The pair of sample is loaded in a cell, which is kept under Ar flow and heated to the necessary temperature for the annealing to be carried out. In the case of films, light can also be applied during this step, and to achieve a better comparison between dark and illuminated conditions, two pairs of films are treated simultaneously (one with and one without light). After the annealing step, the samples are separated and transferred to a ToF-SIMS machine in order to measure the diffusion profiles. The minimum necessary amount of light is used during the transferring procedure, and also during vacuum pumping in the ToF-SIMS machine. The diffusion profiles are built by monitoring the ^{13}C signal, since the ^{15}N peak overlaps with many other fragments of similar mass/charge ratio.

^{18}O tracer

For this experiment, enriched O_2 gas (87 % abundance) is used as a source of ^{18}O. In a typical measurement, the sample (thin film or pellet) is loaded in a chamber that is evacuated to remove residual environmental atmosphere. The enriched $^{18}O_2$ is introduced, and then the sample chamber is heated to the desired temperature. When required, light is also applied using a Xe-arc lamp after reaching the annealing temperature. The annealing step is carried out for the desired amount of time and then the samples are cooled down, removed and quickly transferred in a ToF-SIMS machine. As for ^{13}C tracer experiments, the minimum amount of light is used during the transferring and vacuum pumping steps.

Time of Flight Secondary Ion Mass Spectroscopy

For all tracer experiment, the isotope ratio is obtained by measuring with a ToF-SIMS machine, model TOF.SIMS IV from IONTOF. In the case of pellets, typically a 500x500 μm^2 area is probed, using a Ga primary gun (25 keV) and a Cs sputter gun (1-2 keV). A Bruker Dektak profilometer is later used to assess the depth of the crater caused by sputtering. For thin films, a smaller area of 70x70 μm^2 is probed, using a Ga primary gun (15 keV) and a Cs sputter gun (250 eV). The sputtering depth is here assessed by knowing the thickness of the films and observing the rise of the Al signal from the sapphire substrate.

MATERIAL STABILITY TESTING

UV-Vis spectroscopy

In this experiment, a in-house built thin film holder is used, in order to keep the film vertical and to measure its UV-Vis absorption (**Fig. 9.3**). A modified cuvette is used to have a constant gas flow over the film, and it is placed directly in the UV-Vis spectrometer. Heating pads are applied on the aluminium cuvette holder and used to reach the desired temperature, that is measured directly in close proximity to the film. The absorption signal is monitored as a function of time after reaching the temperature and flowing the appropriate gas. When required, illumination is provided by a quartz-tungsten-halogen lamp (Thorlabs SLS201L) or, for wavelength dependent experiments, by a red (660 nm, Thorlab M660F1) or a violet (420 nm, Thorlab M420F2) LED.

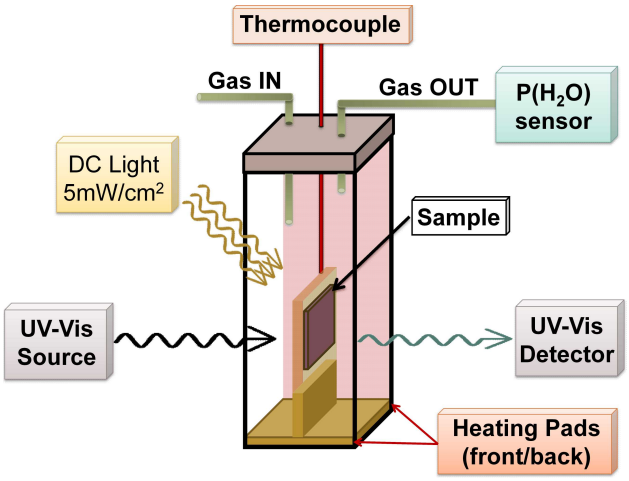

Figure 9.3. Schematics of the setup used for *in-situ* degradation measurements monitored by UV-Vis spectroscopy.

XRD analysis

In this experiment, a XRD thin film holder with polycarbonate dome (Anton Paar) is modified to equip the dome with gas tubes and with an optical fiber connector. This allows for GIXRD measurements to be carried out under constant illumination and controlled atmosphere, albeit only at room temperature. In this case, illumination was provided by a white LED light (6200 K, Thorlab MCWHF2).

NMR AND NQR MEASUREMENTS

Instrument details

^{1}H, ^{13}C, ^{14}N, ^{15}N, ^{22}Na and ^{207}Pb NMR measurements are performed on a Bruker Avance III 400 MHz instrument ($B_0 = 9.4$ T), using Bruker double resonance probes BL4 for MAS and PE5 for static. ^{127}I NQR spectra are collected on the same instrument with the BL4 probe set outside the magnet at a distance large enough to avoid stray magnetic fields. ^{127}I NMR spectra are instead acquired on a Bruker Avance II 900 MHz spectrometer ($B_0 = 21.1$ T), with a in-house built solenoid probe. ^{207}Pb spectra are also acquired at such higher field. All relaxation measurements are performed in static conditions. Temperature control is achieved using standard Bruker equipment, with the temperature value calibrated on the ^{207}Pb signal in $PbNO_3$.[229]

Pulse sequence details

^{1}H NMR spectra are acquired with standard single pulse excitation, and the same procedure is used for ^{23}Na. ^{13}C spectra are acquired both with single pulse excitation and with cross polarisation (CP) from protons. ^{15}N NMR spectra are collected exclusively in CP from protons. ^{14}N and ^{207}Pb NMR spectra are instead recorded using a $\frac{\pi}{2} - \tau - \frac{\pi}{2}$ solid echo pulse sequence.[99] ^{127}I NQR spectra are also acquired using a $\frac{\pi}{2} - \tau - \frac{\pi}{2}$ sequence, while ^{127}I NMR spectra with a $\frac{\pi}{4} - \tau - \frac{\pi}{4}$ solid echo pulse sequence (the signal is so severely broadened that more than 400000 scans are necessary to make it emerge from the noise level). All chemical shift are referenced to IUPAC standards,[230] with solid adamantane, NH_4Cl and $PbNO_3$ as secondary standards. Spin-lattice relaxation times are normally recorded with saturation recovery methods, while spin-spin relaxation times with the spin-echo sequence.[231] In the case of ^{127}I NQR, spin-lattice relaxation time is recorded using the inversion recovery technique with error-compensating composite pulses.[232]

Thin films under illumination

To measure NMR spectra of $MAPbI_3$ thin films under light, a very long quartz rod is used as an optical guide, and lowered inside the superconducting magnet. The light source is connected to the rod with an optical fiber and an in-house built connector, and can therefore remain at a safe distance from the magnet. The rod is fixed inside a teflon tube that inserts itself in the top part of the NMR probe, thus bringing the optical guide very close to the sample ($\sim$ 1 cm). Illumination was provided by a white LED light (6200 K, Thorlab MCWHF2). A simple schematics of this setup is given in **Fig. 4.5**. To effectively confirm that we were successful in bringing light to the samples *in-situ*, we use a commercial photochromic dye (TCI, B2629) and compare its color before and after exposure to UV-light (365 nm) directly inside the magnet. As shown in **Fig. 9.4**, the dye is initially white, while after even a short illumination inside the magnet it clearly changes to blue. Note that for short times the coil shape is imprinted in the dye, as expected, while the situation becomes more uniform at longer exposure times. This demonstrates the successful *in-situ* illumination of the samples.

During normal measurements, in order to improve the signal to noise ratio, 2 thin films (on double-polished quartz substrates) are placed face to face in the NMR coil. The coil itself is fabricated in-house in a square fashion using Ag-

coated Cu flat wire. Such coil has an inner space that can be almost entirely filled by the thin films.

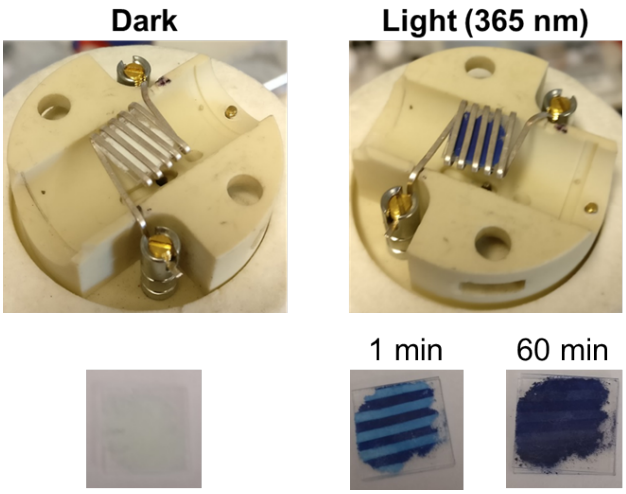

Figure 9.4. Photos of the in-house built flat coil loaded with a photochromic dye between 2 quartz substrates, to approach sample conditions. The probe is loaded in the magnet and the dye is illuminated in-situ with UV-light. After illuminating for 1-minute, a strong color change is visible in the dye.

In a typical experiments, enriched films are used, and thousands of scans are acquired in order to achieve a good signal, particularly in the case of ^{13}C ($>$ 6000 scans). Unfortunately, this process results in extremely long experimental times for a simple spectrum (3-4 h for ^{1}H, 12-15 h for ^{13}C), making relaxation time measurements as a function of temperature extremely time-consuming. Also, no ^{15}N signal is visible even after a very long acquisition ($>$ 50 h).

Spectral line referencing is carried out using butyl rubber slices, that were cut in different thicknesses to test possible influences on the chemical shift due to the coil being only partially filled. No effect of the thickness on the chemical shift is visible. To approach sample conditions, a thin film of silicon grease between two quartz substrates is also used as a reference. Adamantane pellets and adamantane thin crystals evaporated on quartz substrates are also used as a control, again giving no discernible differences in the chemical shift. All these secondary standards are later referenced to a normal round coil and to a primary standard, so to compare with normal powder measurements.

10

SUPPORTING MATERIAL

10.1 THE NATURE OF ION CONDUCTION IN $MAPbI_3$

10.1.1 *Defect Chemical Notation*

The notation used to write point defects throughout this thesis is the Kröger-Vink notation, where a general point defect D of C charge, which occupies a lattice site S is written as D_S^C. **Table 10.1** gives the symbols used to refer to the charge, to the defect involved or to the site occupied in Kröger-Vink notation, while **Table 10.2** lists various point defects represented with this convention.

Table 10.1. List of symbols used in Kröger-Vink notation.

Kröger-Vink notation	Charge	Defect specie/Site occupied
$\bullet$	excess positive	
$'$	excess negative	
x	zero excess charge	
Si, Al, etc.		Atom
V		Vacancy
i		Interstitial site
e/h		excess electrons/holes

Table 10.2. Examples of typical point defects in Kröger-Vink notation.

Kröger-Vink notation	Description
Fe'_{Ti}	Fe^{III} substituting Ti^{IV}, negative eff.charge.
$V_O^{\bullet\bullet}$	Oxygen vacancy, double positive eff. charge.
Cl_I^x	Homovalent substitution of Cl on I, eff. neutral.
$Na_i^{\bullet}$	Na in interstitial site, positive eff. charge.

10.1.2 *Chemical diffusion and d.c. galvanostatic polarization*

The term chemical diffusion refers to a process that involves simultaneous transport of at least 2 differently charged species, effectively resulting in the diffusion of a neutral component (mass transport) generating a stoichiometry variation in a material. An exhaustive treatment of chemical diffusion is given in the literature.[77,78,98,152] For simplicity, here we refer to the example of a mixed ionic-electronic conductor, where this process corresponds (in his simplest form) to an ambipolar transport of one ionic (ion) and one electronic (eon) species, that together form a neutral component. A driving force for such a diffusion can be a voltage difference or a chemical potential difference applied over the material. Intuitively, the corresponding diffusion coefficient (chemical diffusion coefficient, D^{δ}) will depend on the diffusion coefficients of the single species involved in the transport (in this example, to D_{eon} and D_{ion}). Therefore, measuring a chemical diffusion process allow us to disclose important information on the mixed ionic-electronic nature of the conductivity in a mixed conductor. One of the mostly used techniques to probe this process is d.c. galvanostatic polarization.[79,98] For this measurement, the mixed conductor is equipped with electrodes that are reversible only to one of the conductive species while being blocking for the other. For example, in $MAPbI_3$, carbon electrodes were used, that are conductive for electronic carriers but blocking for ions. By applying a current load, a mixed-conducting sample shows a voltage response analogous to the one given in **Fig. 10.1**. The initial IR drop (= voltage increase) corresponds to the total resistance (R_{tot}) of the sample, since at $t = 0$ both ionic and electronic carriers respond, analogously to high frequency in a.c. impedance. Then, a voltage transient builds up, corresponding to the progressive formation of a stoichiometric polarisation due to the chemical diffusion process.

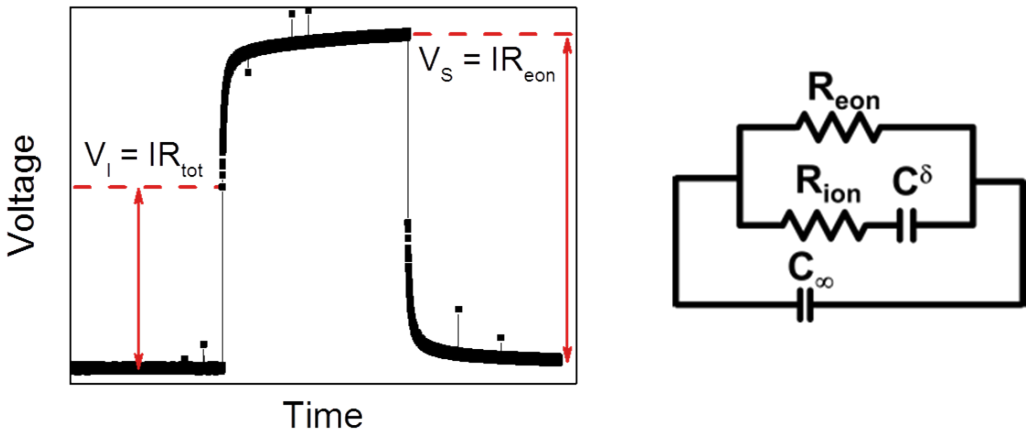

Figure 10.1. D.c. galvanostatic polarisation curve with a simplified model circuit.

This polarisation seizes the entire bulk of the material, and effectively generates a composition (stoichiometry) profile with respect to the position between the electrodes. After a certain time, the voltage reaches a steady-state value (V_S), i.e. a situation where only electronic carriers can flow (ionic carriers are fully blocked by selective electrodes in this example). Using the simplified circuit depicted in **Fig. 10.1** (full form is given in Ref.[233]), the ionic resistance (R_{ion}) can be extracted from R_{tot} and R_{eon}. The transient can also be analyzed, and it is expected to be linear with $t^{1/2}$ for short times, i.e., for $t < \tau^\delta$, where τ^δ is the time scale of the polarization transient. Instead, the voltage transient is exponential ($V = V_S[1 - \exp(-t/\tau^\delta)]$) for longer times ($t > \tau^\delta$). The time constant τ^δ is related to the the chemical capacitance through the formula $\tau^\delta = R^\delta C^\delta$, where R^δ is the chemical resistance ($R^\delta = R_{eon} + R_{ion}$). In addition, τ^δ is related to the chemical diffusion coefficient D^δ through the expression $D^\delta = L^2/\pi^2\tau^\delta$.

10.1.3 *Cu and Pb reaction cell*

As shown in **Fig. 10.2**, there is a distinct formation of a secondary phase, later identified by XRD analysis as CuI, on the Cu foil side (B) in contact with $MAPbI_3$. The other side (A) shows only the original morphology. In addition, performing the experiment without current load (**Fig. 10.3**) shows no formation of CuI, confirming the expected thermodynamic stability of Cu against $MAPbI_3$. Indeed, $MAPbI_3$ is expected to be more stable than PbI_2 (see discussion in **§ 6.2** and **§ 6.3**), and simple thermodynamic calculations based on tabulated data show how the relevant reaction ($2Cu + PbI_2 \rightarrow 2CuI + Pb$) has a distinctly positive Gibbs energy value (+ 34.6 kJ/mol). We note that the same holds for CuI_2.

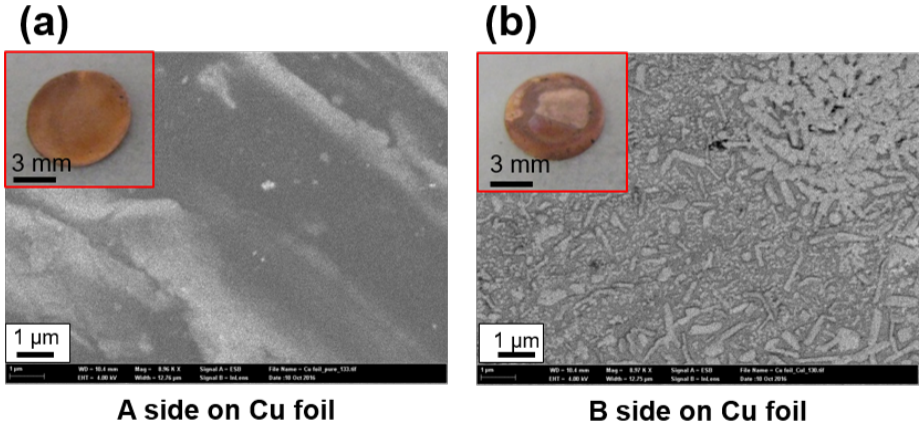

Figure 10.2. SEM pictures obtained on Cu foil after the reaction cell experiment presented in **Fig. 2.2**. **(a)** Surface of the A-side. The visible scratches were performed in order to remove the oxide layer present on the pristine Cu foil. **(b)** Surface of B-side, in contact with $MAPbI_3$, showing secondary phase (CuI) formation.

Even though these thermodynamics considerations are clear in showing the stability of Cu against PbI_2, we analyzed the $MAPbI_3$ side in contact with Cu, in order to unequivocally confirm the absence of degradation products such as PbI_2 or Pb at the interface (these could give an alternative path for CuI formation). As shown in **Fig. 10.3c**, no formation of secondary phases is detected.

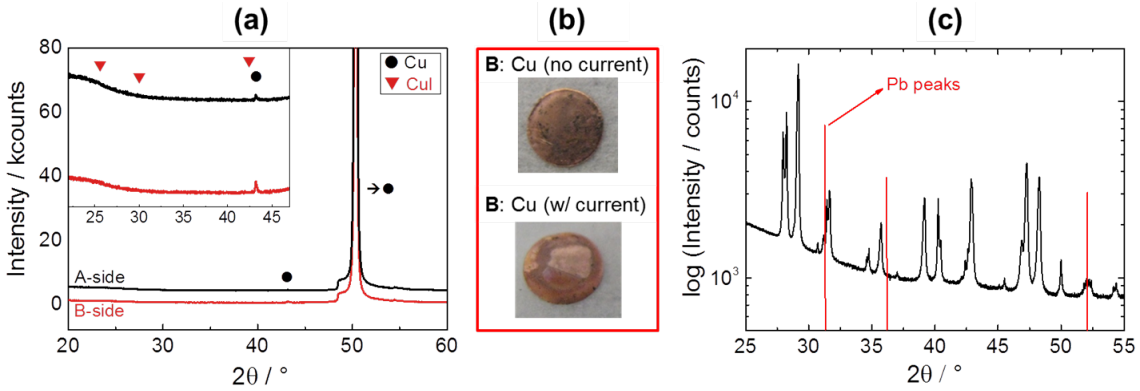

Figure 10.3. **(a)** XRD analysis of side A and B of the Cu foil used in a reaction cell experiment performed for 1 week at 323 K with no current flow. No CuI peaks (marked) are visible. **(b)** Photos comparing the B-side (in contact with $MAPbI_3$) of two reaction cell experiments, with and without current load. **(c)** XRD of $MAPbI_3$ in contact with Cu (B-side), after the experiment with current load (**Fig. 2.2**). No secondary phases visible.

Regarding the reaction cell experiment using a Pb electrode, this also shows substantial iodide mobility in the form of a secondary phase (PbI_2) generated on the Pb electrode at Pb-$MAPbI_3$ contact. To validate this results, we analyzed the $MAPbI_3$-AgI contact (C-side), in order to check that no formation of PbI_2 (from Pb motion) or MAI (from MA motion) is present on this side. We compare the XRD pattern obtained for the AgI C-side with the ones measured on the other side (D-side, AgI-Ag interface). As shown in **Fig. 10.4**, only reflections from the AgI phase are visible on the two sides, as previously reported.[31]

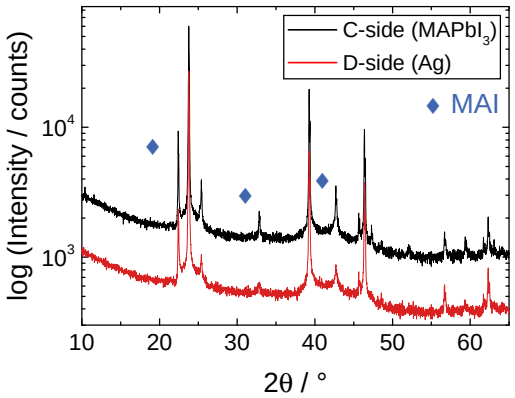

Figure 10.4. XRD of the AgI pellet used in the Pb reaction cell, comparing the $MAPbI_3$-AgI contact (C-side) and AgI-Ag contact (D-side), both with no secondary phases.

10.1.4 *Surface roughness role in ^{13}C tracer experiments*

To confirm that no role is played by the microstructural surface features of the samples during ^{13}C tracer experiments (**§ 2.4**, **Fig. 2.4**), we collected an AFM picture of the pellet after the treatment. As visible in **Fig. 10.5**, the surface appears rather flat, probably due to the spring force applied to achieve contact. The surface roughness is clearly in the 100 nm range, and thus is of little relevance for the depth scale probed in the experiments via ToF-SIMS (several μm).

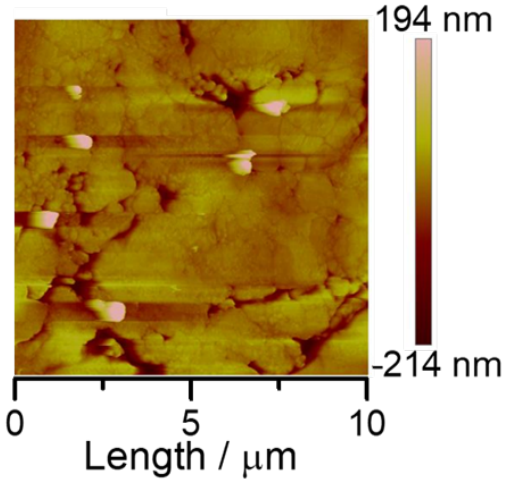

Figure 10.5. Surface roughness of a $MAPbI_3$ pellet after the ^{13}C tracer experiment.

10.2 DEFECT CHEMICAL STUDY OF $MAPbI_3$

10.2.1 *Quantification of Na content in doped samples*

Quantifying the Na content in a doped sample allows the extraction of mobility values from conductivity data. To achieve a reliable quantification, we used solid-state ^{23}Na NMR on the doped sample, and we calibrated the intensity of the signal by using a known amount of NaI. Note that NMR has been widely used for quantification of quadrupolar nuclei in the solid state.[234–236] As reported in **Fig. 10.6**, no Na signal is visible for pure $MAPbI_3$, while a clear peak appears in the doped sample. We note also that the signal linewidth is very narrow, indicating a simmetric environment for the ^{23}Na nuclei, that suggests successful incorporation of this nucleus in the lattice (as compared with a segregation of Na ions taking place on the surface or at the grain boundaries). The quantification yielded 0.5 % at. Na with respect to Pb. Nominal quantity used in the synthesis step was 1 % at.

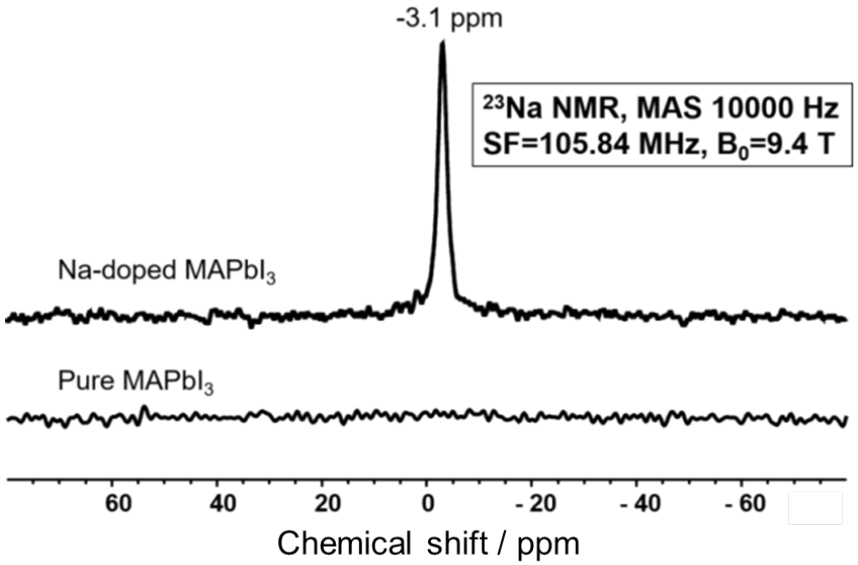

Figure 10.6. Stationary ^{23}Na NMR of pure and Na doped $MAPbI_3$.

10.2.2 *Na doping XRD analysis*

We collected XRD pattern on Na-doped $MAPbI_3$ powders, to verify the absence of secondary phases. As seen in **Fig. 10.7**, no peaks belonging to PbI_2 are visible. As expected, the doped sample shows identical reflections with respect to pure $MAPbI_3$.

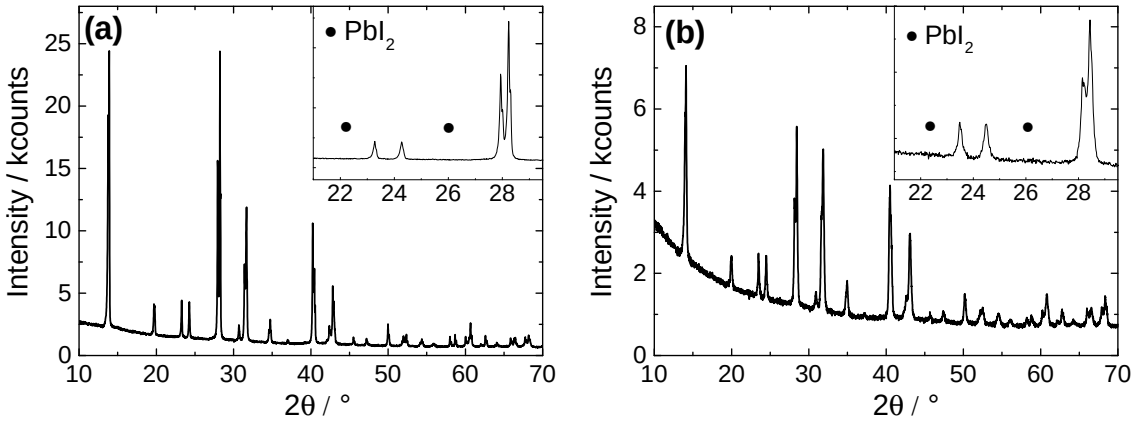

Figure 10.7. XRD analysis of **(a)** pure $MAPbI_3$ and **(b)** Na-doped $MAPbI_3$. The insets show a magnification of the region where the most intense PbI_2 peaks should appear.

10.3 LIGHT EFFECTS ON IONIC TRANSPORT

10.3.1 *D.c. galvanostatic polarization under light*

Thorough analysis of the voltage transient in d.c. polarisation experiments under illumination show that this well-represents a chemical diffusion process (see **§ 10.1.2**). As shown in **Fig. 10.8**, for short times both in the dark and under illumination the transient is linear with $t^{1/2}$. For long times, as expected, the transient is exponential.

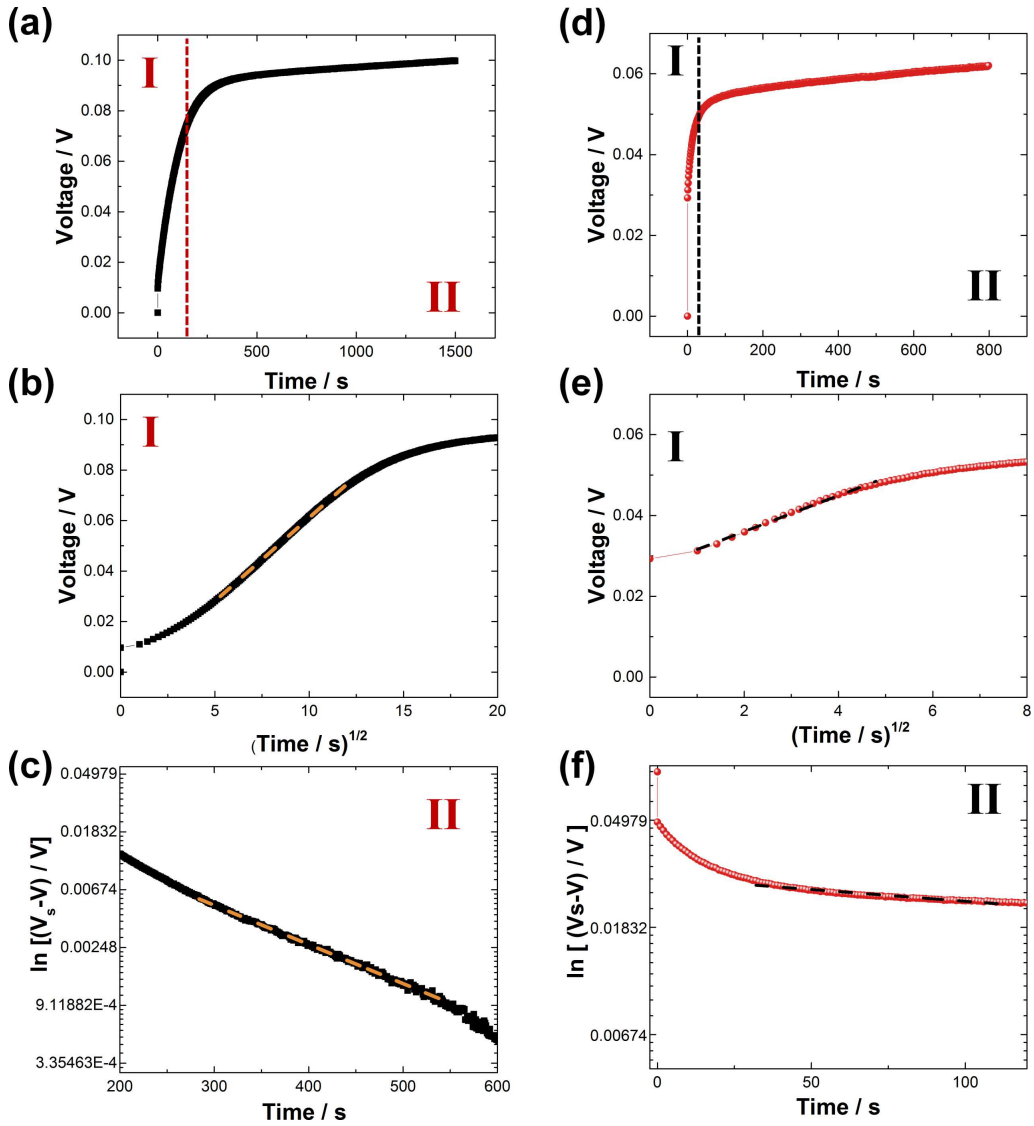

Figure 10.8. D.c. polarisation curves for $MAPbI_3$ thin film **(a)** in the dark and **(d)** under illumination (1 mW/cm^2). Short-time region of the voltage transient plotted as a function of $t^{1/2}$, for samples measured **(b)** in the dark and **(e)** under illumination. Long-time region of the voltage transient plotting lnV as a function of time, for samples measured **(c)** in the dark and **(f)** under illumination.

10.3.2 *Permeation cell experiment: calculations*

The permeation flux of I_2 (j_I) through $MAPbI_3$ is proportional to its ambipolar conductivity ($\sigma_I^\delta = \sigma_{ion}\sigma_{eon}/\sigma_{tot}$), when surface limitations are irrelevant.[237] Both ionic and electronic conductivity values in $MAPbI_3$ are dependent on the iodine activity, and can thus expressed as a power law of the form:

$$\log \sigma_{\text{ion}} = \log \alpha_{\text{ion}} + N_{\text{ion}} \log \mathrm{P}(\mathrm{I}_2) \tag{10.1a}$$

$$\log \sigma_{\text{eon}} = \log \alpha_{\text{eon}} + N_{\text{eon}} \log \mathrm{P}(\mathrm{I}_2) \tag{10.1b}$$

where N_{eon} and N_{ion} are the slopes of the $\log \sigma$ vs $\mathrm{P}(\mathrm{I}_2)$ dependences (**Fig. 4.6**). We note that, in the permeation cell experiment, the iodine activity is not a fixed value, but rather it ranges between a high value established by the I_2 gas on the surface (I-source) and a lower value established by the Cu interface (I-sink). We therefore need to integrate our conductivity values over this activity range.[98,237] By doing so, and by substituting this integral in the ambipolar conductivity formula we obtain:

$$j_{\mathrm{I}} \propto \int_{\mathrm{P}(\mathrm{I}_2)_{\text{interf.}}}^{\mathrm{P}(\mathrm{I}_2)_{\text{surf.}}} \frac{\alpha_{\text{eon}} P^{N_{\text{eon}}} \alpha_{\text{ion}} P^{N_{\text{ion}}}}{\alpha_{\text{eon}} P^{N_{\text{eon}}} + \alpha_{\text{ion}} P^{N_{\text{ion}}}} \frac{\mathrm{dP}(\mathrm{I}_2)}{\mathrm{P}(\mathrm{I}_2)} \tag{10.2}$$

By substituting our experimental values of σ vs $\mathrm{P}(\mathrm{I}_2)$ in the dark and under illumination, we obtain a ratio of the flux values between these two conditions of 1 order of magnitude. However, only taking into account an increase of electronic conductivity (with a constant σ_{ion}) upon illumination, we obtain a significantly different ratio between the fluxes (2-3 times). Note that the experimentally observed difference is at least 1 order of magnitude (**Fig. 4.2**).

10.3.3 *Iodine removal in toluene*

The rate of I_2-removal when immersing $MAPbI_3$ in toluene is determined by the I_2 chemical potential gradient between the sample and the solvent. This is qualitatively similar to the permeation cell experiment of the previous section, albeit in this characterization the chemical potential of I_2 in $MAPbI_3$ is non-stationary. Indeed, the higher excorporation from $MAPbI_3$ to toluene is achieved, the lower the residual I_2 chemical potential will be. The exact evaluation of this problem is rather complicated, since the interface between the sample and toluene sets time-dependent boundary conditions. Intuitively, one expects the interface

to be quickly depleted of I_2 (assuming surface transfer resistance is not large), while the concentration profiles develops later in the $MAPbI_3$ bulk, and are determined by the chemical diffusion coefficient (that does not vary significantly with light intensity, as reported in **§ 4.2**). The process is schematized in **Fig. 10.9**. By assuming an infinite diffusion coefficient of I_2 in toluene, we obtain a situation that is rate-limited by the diffusion in $MAPbI_3$. To simplify the problem of the time-dependent boundary condition at the $MAPbI_3$/toluene interface, we consider the I_2 concentration in toluene to be very small at any given time. This is likely a realistic assumption, since in our experiments a 300 nm thick $MAPbI_3$ film is in contact with a macroscopic quantity of solvent (3-5 mL). We can thus solve the problem in its initial state, i.e. when the I_2 concentration in toluene is 0, and the I_2 concentration in $MAPbI_3$ (or, more appropriately, its non-stoichiometry) still has the pristine value c_0.

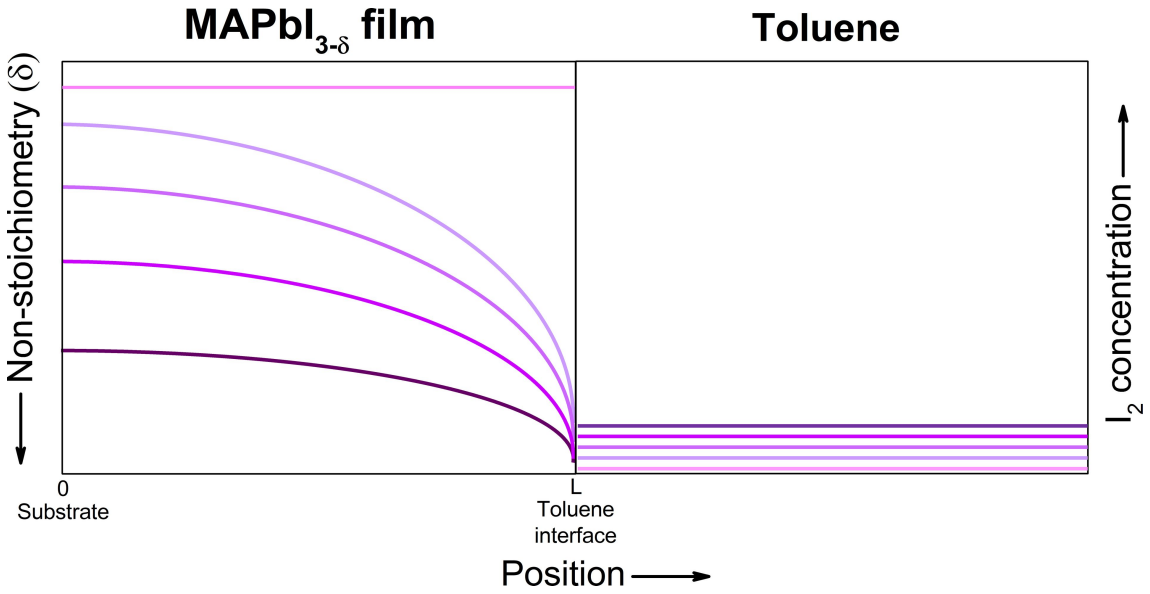

Figure 10.9. Concentration profiles of iodine non-stoichiometry (δ) in $MAPbI_3$ (left) and of iodine concentration in toluene (right) as a function of exposure time.

The solution to this problem is given, for example, in Ref.[238]. Using this approach we can calculate the concentration gradient established at the interface and, with it, the outflux of iodine in toluene that is proportional to the initial concentration c_0 and thus to the charge carrier concentration (iodine vacancies in our case) and hence to $MAPbI_3$ stoichiometry (δ). This yields an expected light-induced enhancement of the I_2-excorporation rate up to 2 orders of magnitude. Consistently, we measure a 1 order difference (**Fig. 4.3**).

10.3.4 ^{13}C *tracer diffusion under light: simulations*

In the case of ^{13}C diffusion profiles obtained in thin films under light, the analysis was carried out with the reported formula for diffusion in a finite medium, including surface limitations.[106] Since the profile is here composed by two different contributions, and due to the lack of an analytical solution for such a problem, we use a numerical simulation (based on the finite difference method) of two overlapping processes in order to simulate the experimental profile. The two diffusion processes were assumed to have the same surface rate constant but different diffusion coefficients, as it would be the case for a comparatively fast grain boundary (or other extended defects) diffusion happening alongside a more sluggish bulk diffusion (providing the distance between grain boundaries is sufficiently large). Presently we have no direct experimental evidences on the nature of these processes.

Fig. 10.10 shows different simulation obtained by varying the surface rate constant or alternatively one of the diffusion coefficients.

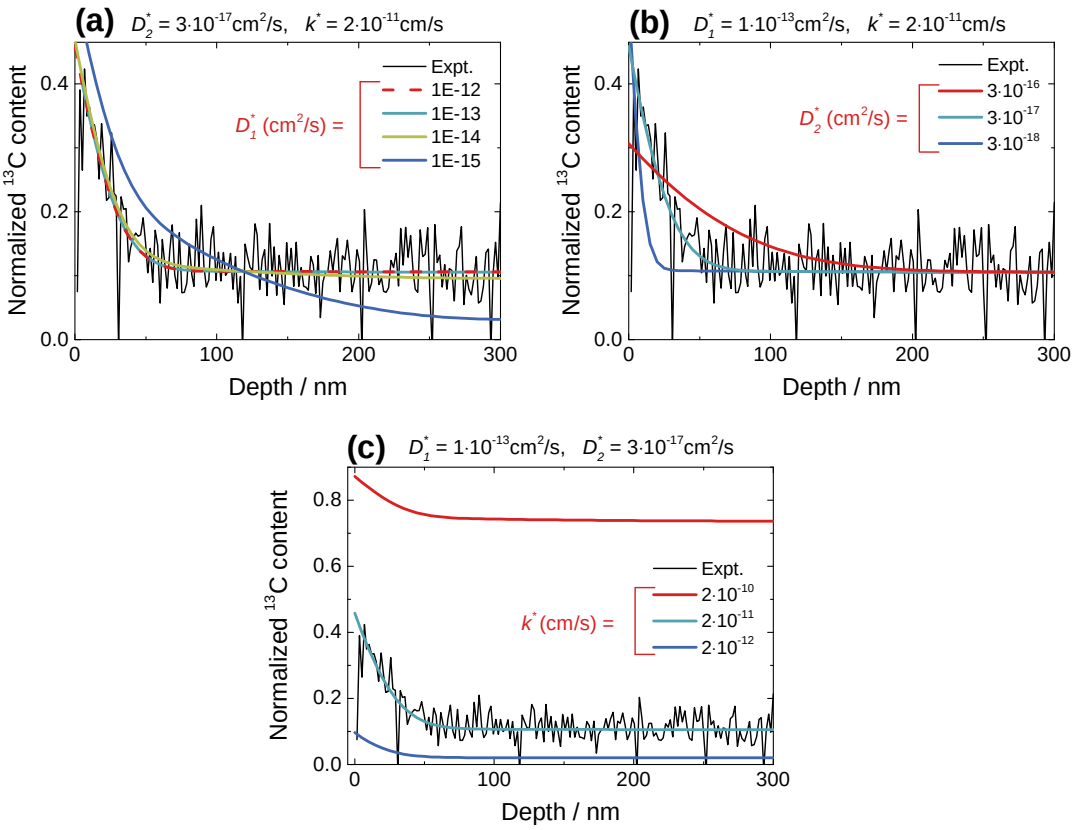

Figure 10.10. Simulation of ^{13}C tracer diffusion profiles in a finite medium in the presence of two distinct diffusion processes. The results are obtained by varying the **(a)** fast diffusion coefficient (D_1^*), **(b)** sluggish diffusion coefficient (D_2^*) and **(c)** surface rate constant (k^*).

Changes in the fast diffusion coefficient (D_1^*) affect the profiles only when this value becomes comparatively small. This is so because such a fast diffusion process is clearly surface-controlled, therefore an increase in the diffusion coefficient alone cannot enhance the final ^{13}C content. Therefore, the extracted value of D_1^* represents only a lower limit for the fast process. It follows that a potential increase of D_1^* upon illumination would not influence the final tracer profile. This lack of a precise estimate of D_1^*, however, does not change the main conclusions as this fast process likely does not represent bulk diffusion. On the other hand, as discussed in the main text, the slower diffusion process is in agreement with bulk diffusion. As shown in **Fig. 10.10**, changes in this sluggish diffusion coefficient (D_2^*) -or also in the surface rate constant (k^*)- result in entirely different profiles. This indicates that a proper evaluation of these parameters is possible. As a consequence, the experimental tracer diffusion profiles would necessarily reflect any influence of light on these two latter parameters. As this is clearly not the case, we can conclude that light does not affect bulk MA transport.

10.4 INTERACTION OF OXYGEN WITH HALIDE PEROVSKITES

10.4.1 *Interstitial oxygen incorporation*

We provide here, in **Fig. 10.11**, the comparison between the defect diagrams obtained from the defect chemical modeling presented in **§ 5.2**, when considering oxygen incorporation on a iodine vacancy site or in an empty interstitial site. As expected, the diagrams are qualitatively identical.

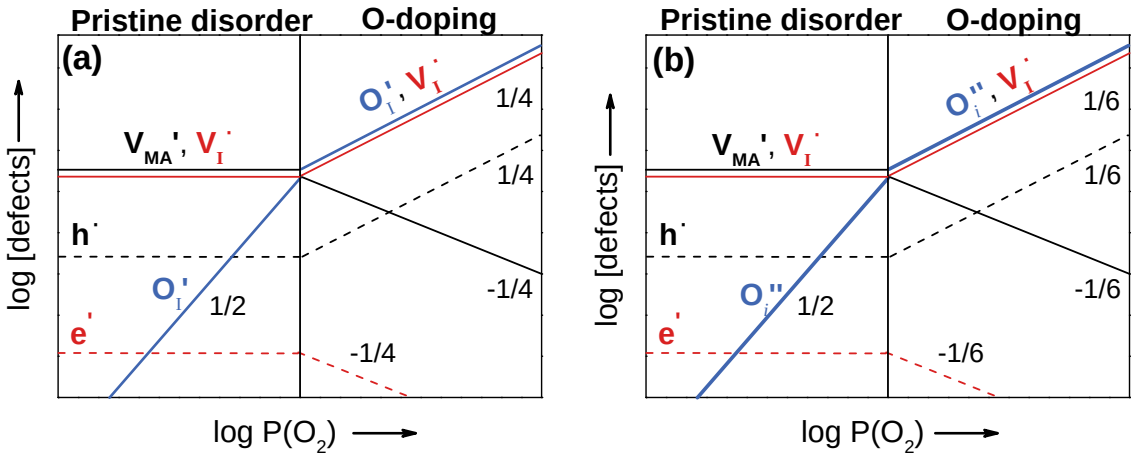

Figure 10.11. Defect diagrams of $MAPbI_3$ as a function of $P(O_2)$ in $MAPbI_3$, assuming oxygen **(a)** to occupy an iodine vacancy ($O_I^{'}$) or **(b)** to incorporate interstitially ($O_i^{''}$).

10.4.2 *XRD analysis of films after ^{18}O incorporation experiments*

Fig. 10.12 shows the structural analysis of $MAPbI_3$ films after performing the ^{18}O incorporation experiment.

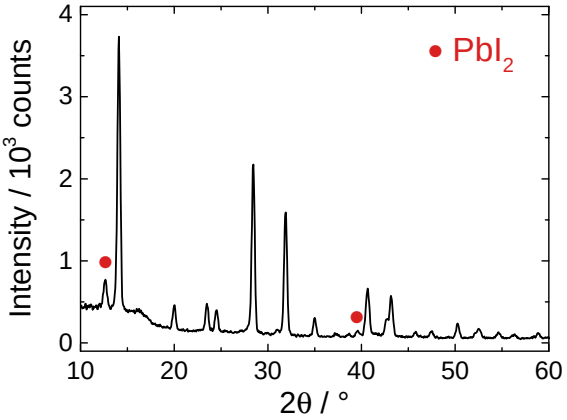

Figure 10.12. XRD of a $MAPbI_3$ thin film after the ^{18}O incorporation under 1 mW/cm^2 illumination.

It appears evident that the treatment was so mild that, even under the highest light intensity used (1 mW/cm^2), the perovskite phase is almost entirely preserved, with a minor appearance of PbI_2 peaks (**Fig. 10.12**) only in certain orientations. We note that such quantities of PbI_2 are often present in pristine films as well.

10.4.3 *Impurity motion of oxygen*

The following treatment, based on detailed kinetics, can be found in Ref.[239]. When O_2 is incorporated in $MAPbI_3$, an impurity defect is formed. Assuming occupation of a $V_I^{\bullet}$, the resulting defect is $O_I^{'}$. We show here that the motion of such defect is not necessarily dependent on the background bulk concentration of $V_I^{\bullet}$. Indeed, the impurity diffusion coefficient for oxygen, here represented by a chemical diffusion coefficient (D^{δ}), will be sensitive to the bulk $V_I^{\bullet}$ concentration only when the impurity moves independently from $V_I^{\bullet}$. In contrast, in the case of a coupled motion, D^{δ} is expected to be insensitive to $V_I^{\bullet}$ concentration. In the former case, the independent motion of the impurity (e.g. $O_I^{'}$) from x to $x^{\wr}$ can be written as:

$$O_I^{'}(x) + V_I^{\bullet}(\widehat{x}) \rightleftharpoons O_I^{'}(\widehat{x}) + V_I^{\bullet}(x) \tag{10.3}$$

The flux can be equated as:

$$j_{O_I^{'}} = j^* \propto \overrightarrow{k}\,[O_I^{'}][\widehat{V_I^{\bullet}}] - \overleftarrow{k}\,[\widehat{O_I^{'}}][V_I^{\bullet}] \tag{10.4}$$

where $\overrightarrow{k} \simeq \overleftarrow{k}$. Assuming a comparatively large background $V_I^{\bullet}$ concentration ($[V_I^{\bullet}] \simeq [\widehat{V_I^{\bullet}}]$), the flux simplifies to $j_{O_I^{'}} = [V_I^{\bullet}]\nabla c^*$, and the impurity diffusivity is proportional to $[V_I^{\bullet}]$. We note that the incorporation of O_2 also produces $V_I^{\bullet}$ according to **(Eq. 5.1)** (see also **Fig. 5.1**, both in **§ 5.2**), and that this complicates the picture significantly. Nevertheless, the result remains valid as long as we are in the above limit. In the case of an ambipolar motion involving $O_I^{'}$ and $V_I^{\bullet}$, D^{δ} is also expected to be $\propto u_{O_I^{'}}$ when both conductivity and concentration of $V_I^{\bullet}$ are large. This also yields $u_{O_I^{'}} \propto c_{O_I^{'}}$, since $V_I^{\bullet}$ is the jump partner for the impurity oxygen defect.

Let us focus now on the coupled motion of $V_I^{\bullet}$ and $O_I^{'}$, that is expected to take place when there is strong association between the two defects (e.g. at room temperature). In this case, the entire pair undergoes the diffusion process:

$$(O_I^{'} - V_I^{\bullet})(x) \rightleftharpoons (O_I^{'} - V_I^{\bullet})(\widehat{x}) \tag{10.5}$$

The flux is then given as:

$$j^* = j_{O_I'-V_I^\bullet} \simeq const.\nabla c^* \tag{10.6}$$

It is thus clear that the impurity diffusion coefficient is here independent of the $V_I^\bullet$ concentration. We note that, as shown in **Fig. 10.13**, the coupled motion is not an elementary reaction, therefore it is not possible to find a simple expression for the jump rate constant. Nevertheless, the conclusions given above are valid as long as the $V_I^\bullet$ concentration is not so large as to result in the involvement of an extra vacancy in the motion process. We also note that the possible occurrence of oxygen incorporation on interstitial sites (**§ 10.4.1**) is already expected to yield a diffusion process independent on $V_I^\bullet$ concentration.

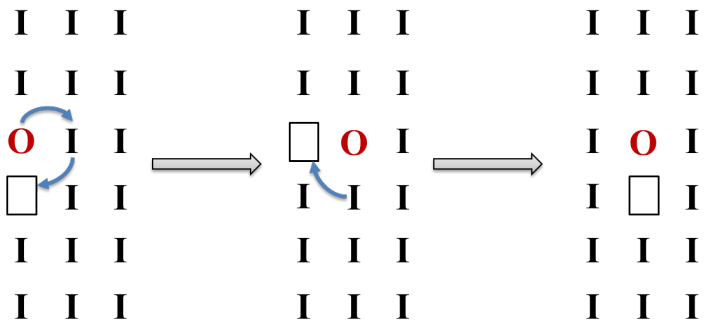

Figure 10.13. Schematics depicting a correlated pair motion of an oxygen defect with an iodine vacancy. Note that the vacancy is generated by oxygen incorporation, and no extra vacancies are needed for the motion to take place.

10.4.4 *Oxygen partial pressure at higher light intensity*

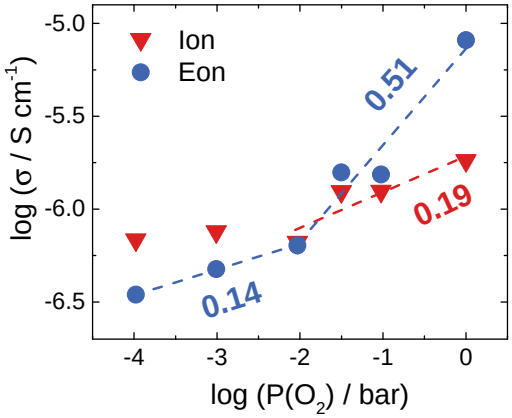

Figure 10.14. Conductivity as a function of $P(O_2)$ for a $MAPbI_3$ thin film at 333 K and under 1.75 mW/cm^2 illumination.

10.4.5 *Conductivity equilibration times upon* $P(O_2)$ *changes*

Information on the O_2 interaction and incorporation can also be obtained by analyzing the conductivity equilibration times upon switching $P(O_2)$ over a sample. In $MAPbI_3$ pellets in the dark, as shown in **Fig. 10.15**, the equilibration time upon switching $P(O_2)$ is much faster than upon switching $P(I_2)$. Considering the kinetically hindered O_2 incorporation that we observe with ^{18}O incorporation experiments (**§ 5.3**), this behavior is not surprising, since O_2 interaction in these conditions is limited to a surface layer. Curiously, upon reinstatement of the previous $P(O_2)$ value (**Fig. 10.15c**), the equilibration time lengthens, resembling more the one measured upon changes in $P(I_2)$. This provides further evidence for the O_2 affecting the I_2 activity (**§ 5.4**). Indeed, when O_2 induces I_2 release **[R. 5.4]**, this can be exchanged with the entire $MAPbI_3$ bulk, therefore to reverse the process it is not enough to remove O_2 from the surface, but it is also necessary to take out the incorporated I_2 from the bulk.

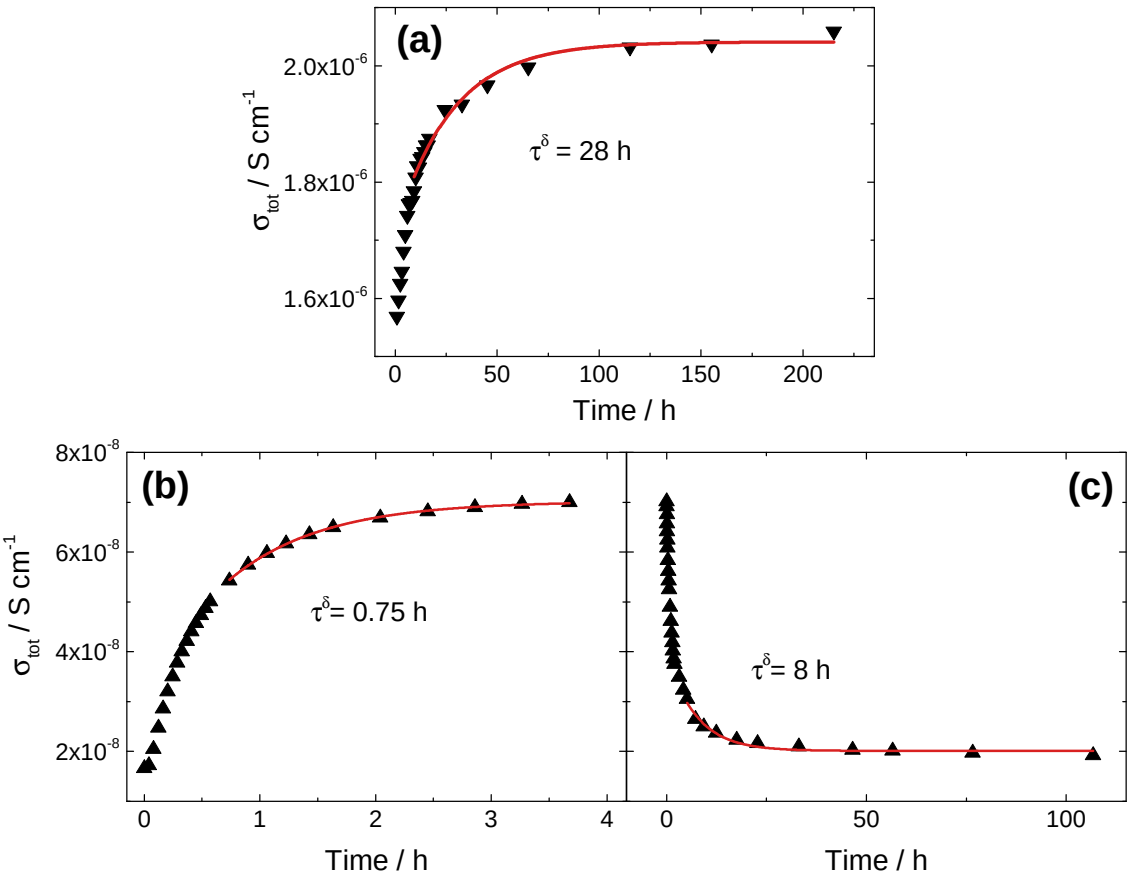

Figure 10.15. Conductivity equilibration recorded at 343 K for $MAPbI_3$ pellets upon changing **(a)** $P(I_2)$ from 10^{-7} to $7 \cdot 10^{-7}$ bar (carrier gas= Ar, $P(O_2)$=$3 \cdot 10^{-5}$), **(b)** $P(O_2)$ from 10^{-5} to 10^{-3} bar (carrier gas = Ar, $P(I_2)$= unknown) and **(c)** $P(O_2)$ in reverse from 10^{-3} to 10^{-5} bar (carrier gas = Ar, $P(I_2)$= unknown).

Performing the same analysis but on $MAPbI_3$ films (**Fig. 10.16**), we can gain information on the light effect on the O_2 interaction. As expected, equilibration times observed under dark are much slower than under illumination, and they become faster with increasing light intensity.

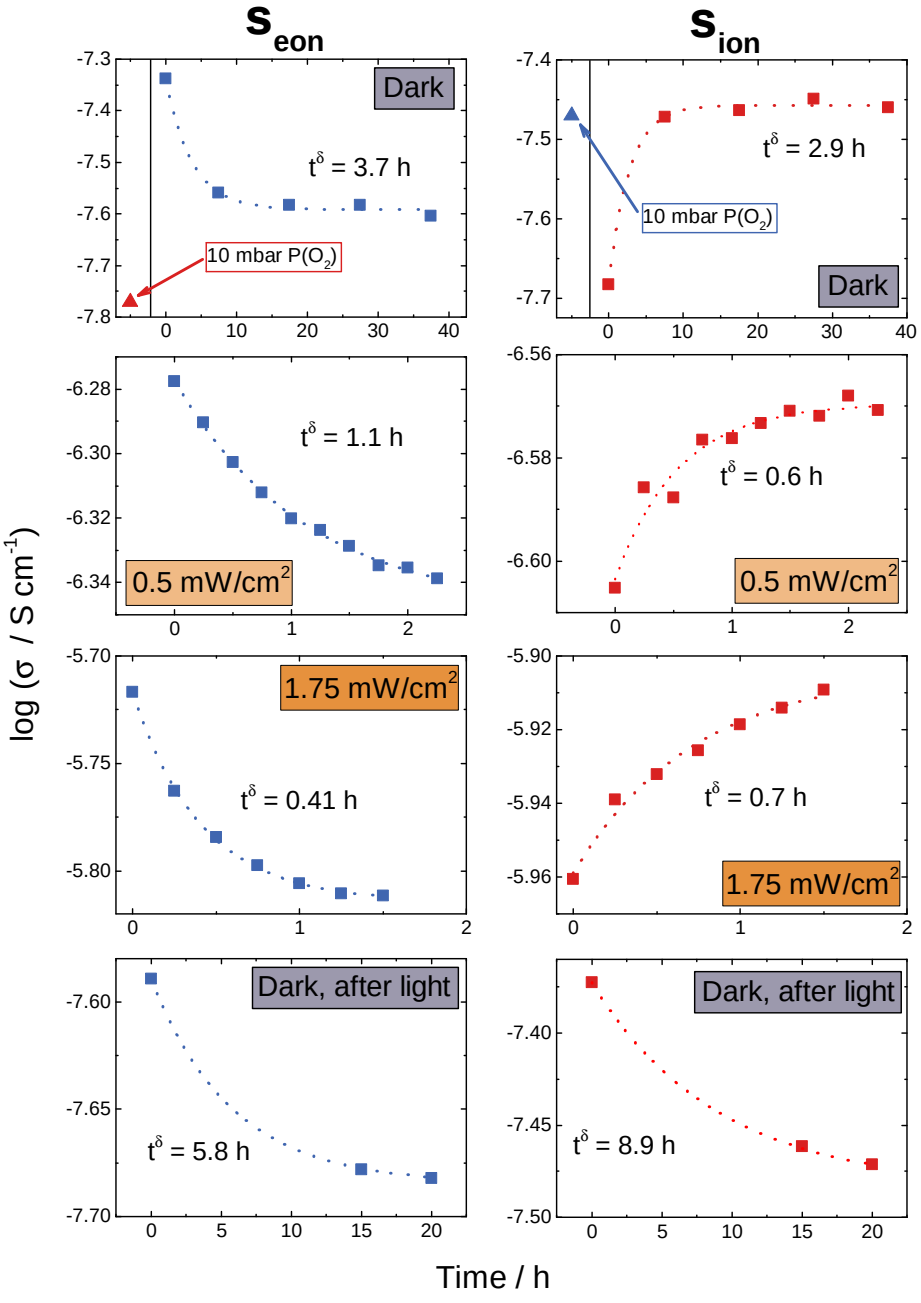

Figure 10.16. Equilibration of ionic and electronic conductivities of $MAPbI_3$ films at 333 K. The treatments were performed in the following sequence: (i) A sample at 10 mbar $P(O_2)$ was switched to 100 mbar, under dark conditions. (ii) After equilibration, light (0.5 mW/cm^2) is switched on. (iii) After equilibration, intensity is increased to 1.75 mW/cm^2. (iv) Light is switched off, still under 100 mbar $P(O_2)$. Analogous behavior was observed between any two subsequent points in $P(O_2)$. Time scales (τ^δ) extracted from the logarithmic behavior are given in the graphs.

Interestingly, a sample that is already fully equilibrated in the dark at a given $P(O_2)$ shows a further equilibration process upon illumination. This also happens when light intensity is increased. When switching off the light (after reaching equilibration at a given $P(O_2)$), the sample recovers its initial conductivity value, but with a slow time scale. This indicate that the high oxygen content that is incorporated under illumination can be "quenched" by removing the light. Notably, the equilibration under dark after increasing $P(O_2)$ (**Fig. 10.16**, top panel) shows a decrease of electronic (increase of ionic) conductivity as a function of time, while the opposite is expected. However, when we compare this with the conductivity values at lower $P(O_2)$ (given in the graph), we see that, as expected, upon increasing $P(O_2)$the absolute value of the electronic conductivity increases (and the ionic conductivity remains constant). The nature of this initial process causing an unexpected large increase of electronic (or decrease of ionic) conductivity is presently unclear.

10.4.6 *Oxygen degradation kinetics: UV-Vis and XRD reference data*

As shown in **Fig. 10.17**, no degradation is observed for $MAPbI_3$ under Argon and illumination, even after long times. In the same conditions but with O_2, degradation is complete in less than 40 h. Interestingly, when simultaneously using Ar and I_2, the samples are still stable, however a slight tail appears in the absorption at higher wavelengths, indicating a possible loss of crystallinity of the perovskite phase. This behavior is also observed when applying O_2 and I_2 simultaneously (**§ 5.6**).

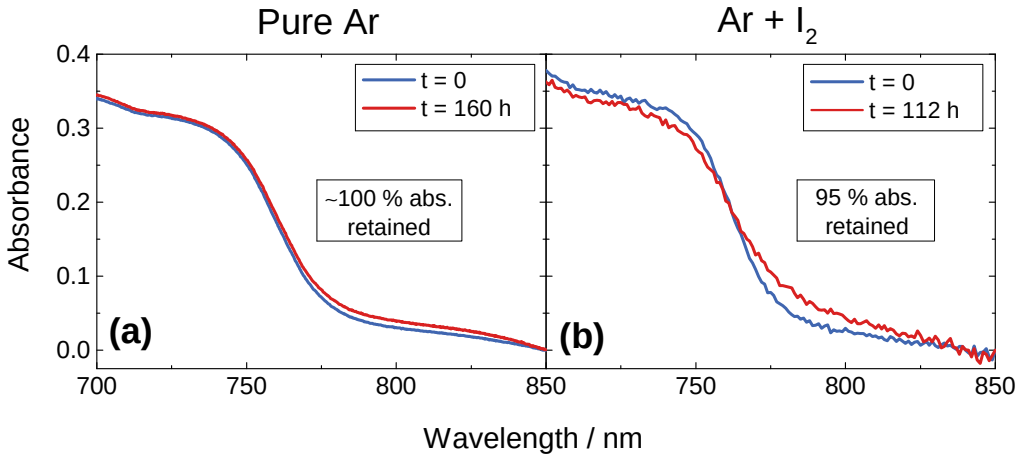

Figure 10.17. UV-Vis spectra of $MAPbI_3$ films under 4.6 mW/cm^2 illumination and 333 K before and after exposure to **(a)** pure Argon and **(b)** Ar with simultaneous $P(I_2)(= 1.4 \cdot 10^{-5}$ bar).

We also report the reference XRD pattern of a $MAPbI_3$ film exposed to O_2 in the dark (**Fig. 10.18**). The perovskite phase is almost entirely preserved after treatment, with a single, weak peak belonging to PbI_2 in a specific orientation.

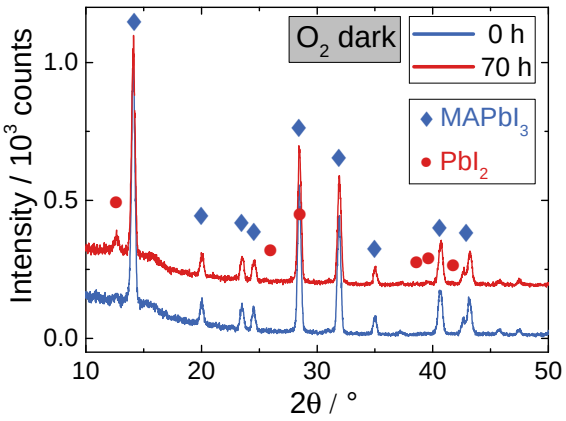

Figure 10.18. XRD of $MAPbI_3$ films before and after exposure to O_2 in the dark at room temperature for 70 h.

10.4.7 *Oxygen degradation in mixed-cation perovskites*

Mixed-cation formulations ($(MA_{0.8}FA_{0.2})PbI_3$) present a slower O_2-degradation rate, and this can be confirmed by XRD analysis. Interestingly, no reflections belonging to PbI_2 are visible after 70 h degradation, even though a significant reduction of peak intensity is present for the $MAPbI_3$ phase. Two plausible explanations for this finding are: (i) the formation of an amorphous PbI_2 phase and (ii) the formation of pure $FAPbI_3$, that at room temperature is stable in a δ-phase with weak XRD reflections.[119]

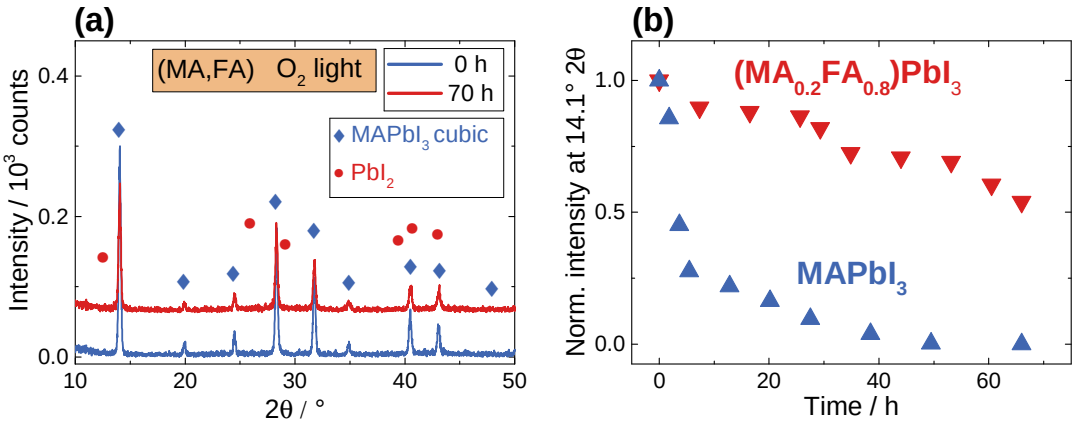

Figure 10.19. Degradation of $(MA_{0.8}FA_{0.2})PbI_3$ investigated by XRD under O_2 exposure at room temperature with 43 mW/cm^2 illumination. **(a)** Diffractograms before and after 70 h of treatment. **(b)** Degradation rate extracted from the XRD as a function of time.

In the intent of explaining the enhanced stability of $(MA_{0.8}FA_{0.2})PbI_3$ we measured its electrical transport properties. As seen in **Fig. 10.20**, FA admixing substantially reduces the ionic conductivity of $MAPbI_3$, yielding a lower transport rate. This occurrence can also provide an explanation for the observed enhanced stability of the cationic mixture.

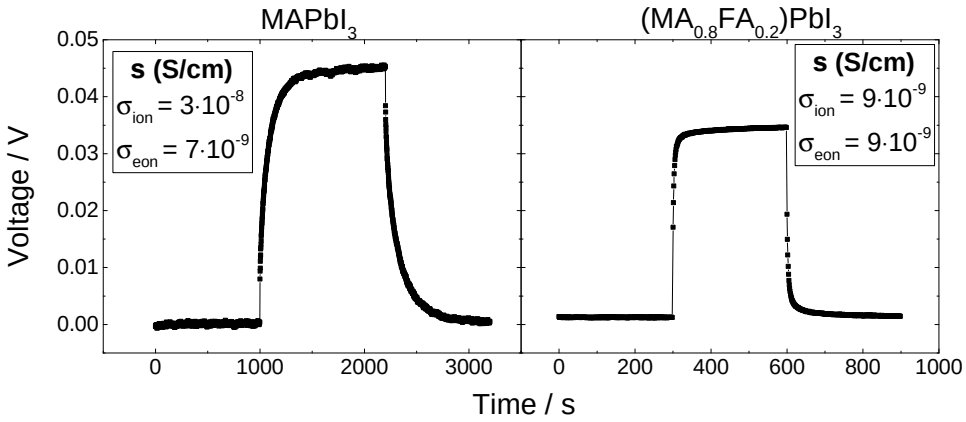

Figure 10.20. D.c polarisation of $MAPbI_3$ and $(MA_{0.8}FA_{0.2})PbI_3$ at 333 K under Ar.

In addition, we measured another composition, this time with a higher FA content $(MA_{0.2}FA_{0.8})PbI_3$. As expected and as shown in **Fig. 10.21a**, increasing FA contents further improves stability. However, it is known that high FA content mixtures can be two-phase,[169] possibly containing pure $FAPbI_3$, which is expected to be stable against oxygen. Therefore, we cannot unambiguously attribute this enhanced stability to the different FA and MA chemistry, as in the previous case, making this latter observation of limited relevance for the understanding of the oxygen interaction.

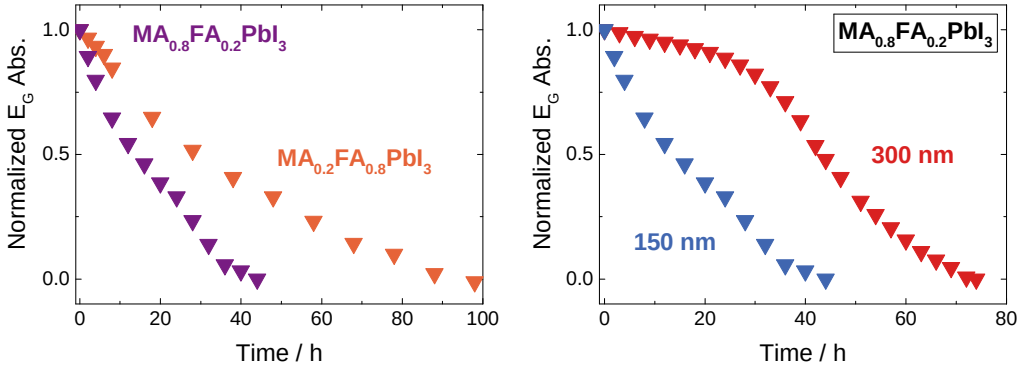

Figure 10.21. Degradation rate of mixed-cation formulations investigated by UV-Vis spectroscopy under O_2 exposure at 333 K with 4.6 mW/cm^2 illumination. **(a)** As a function of FA content (thickness = 150 nm). **(b)** As a function of thickness in $(MA_{0.8}FA_{0.2})PbI_3$.

Lastly, we compare the thickness dependence of the degradation, on two samples of equal composition ($(MA_{0.8}FA_{0.2})PbI_3$). As shown in **Fig. 10.21b**, thicker samples give a slower degradation rate, as expected. This underlines once more the bulk nature of the oxygen interaction with halide perovskites and of the related degradation.

10.5 THERMODYNAMIC STABILITY OF HALIDE PEROVSKITES

10.5.1 *Standard entropies of formation and heat capacity*

We performed heat capacity measurements on a series of halide perovskites, both hybrid and inorganic. As shown in **Fig. 10.22**, changing the halide in MA-based perovskites drastically changes the heat capacity. Firstly, the peak maximum in the C_p/T^3 plot is shifted to higher temperatures upon moving towards lighter halides. This is expected, as lighter atoms are involved in vibrational modes located at higher frequencies with respect to heavier atoms. Secondly, the overall heat capacity is decreased when going from I to Br to Cl, again consistently with the weight of the halide.

We can also extract standard entropies of formation for these low-temperature C_p plots. The values extracted from our measurements are very similar to the ones previously obtained by Onoda-Yamamuro.[172] Thus, we did not extend our measurements to higher temperatures but rather used these literature data whenever necessary.

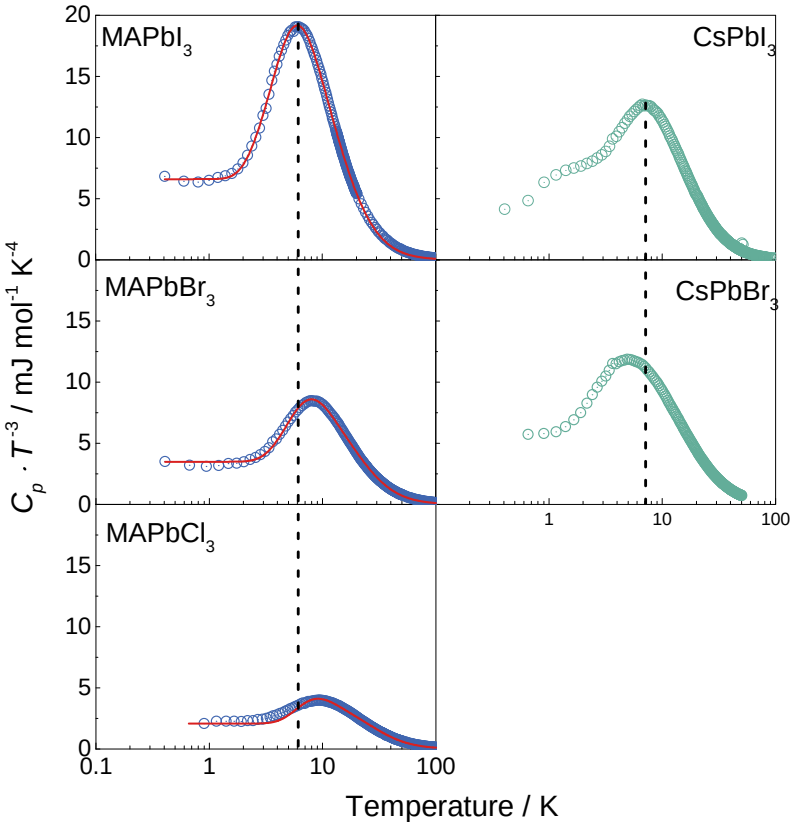

Figure 10.22. C_p/T^3 plot of the low temperature heat capacity of different MA- and Cs-based halide perovskites. Note that the MA-perovskite samples analyzed are single crystals while Cs-perovskites are in powder form.

10.5.2 *Tabulated thermodynamics data*

Table 10.3. Standard thermodynamic data for several substances, taken or calculated from the values in Ref.[240].

Compound	$\Delta_f H^0$ / kJ · mol^{-1}	$\Delta_f S^0$ / J · (mol · K)$^{-1}$	$\Delta_f G^0$ / kJ · mol^{-1}
I_2 (g)	62.4	144.6	19.3
I_2 (s)	0.0	0.0	0.0
Br_2 (g)	0.0	0.0	0.0
Cl_2 (g)	0.0	0.0	0.0
HI (g)	26.5	83.6	1.6
HBr (g)	−36.3	57.3	−53.4
HCl (g)	−92.3	10.0	−95.3
CH_3I (g)	14.4	−5.7	16.1
CH_3I (l)	−13.6	−96.6	15.2
CH_3Br (g)	−35.4	−28.6	−26.9
CH_3Cl (g)	−81.9	−78.7	−58.4
CH_3NH_3I (s)	−200.7	−392.0	−83.8
CH_3NH_3Br (s)	−258.9	(−420.6)	(−133.5)
CH_3NH_3Cl (s)	−298.3	−466.6	−159.2
PbI_2 (s)	−175.5	−6.0	−173.7
$PbBr_2$ (s)	−278.7	−55.5	−262.2
$PbCl_2$ (s)	−359.4	−151.9	−314.1
C (s)	0.0	0.0	0.0
Pb (s)	0.0	0.0	0.0
H_2 (g)	0.0	0.0	0.0
N_2 (g)	0.0	0.0	0.0
O_2 (g)	0.0	0.0	0.0
H_2O (g)	−241.8	−44.5	−228.6
H_2O (l)	−285.8	−163.3	−237.1
NH_3 (g)	−45.9	−99.1	−16.4
CH_3NH_2 (g)	−22.5	−185.4	32.8
PbO (s)	−217.3	−98.7	−187.9

10.5.3 *XPS measurements of partially degraded sample*

Upon long-time immersion in toluene, $MAPbI_3$ thin film samples start undergoing degradation. We expect that this process, when it takes place under illumination, would be accompanied by metallic lead formation. In order to confirm this hypotesis, we carried out XPS analysis of $MAPbI_3$ thin films immersed in toluene, both in the dark and under illumination. As shown in **Fig. 10.23a**, when performing the treatment under illumination a distinct Pb^0 signal is present in the spectra. The amount is clearly larger than what is obtained by treating the sample in toluene under dark. Even though we cannot exclude parallel decomposition pathways taking place during our experiments (e.g. during toluene immersion or during the vacuum exposure preceding XPS measurements), this observation is in good agreement with our proposed photo-decomposition model (§ **6.5**). In addition, **Fig. 10.23b** shows a much stronger decrease in the peak corresponding to the C-N bond, indicating a more severe loss of methylamine when immersing the film in toluene under light, again in agreement with the proposed mechanism (§ **6.5**). Note that the peak corresponding to C-C and C-H could also come from residual toluene.

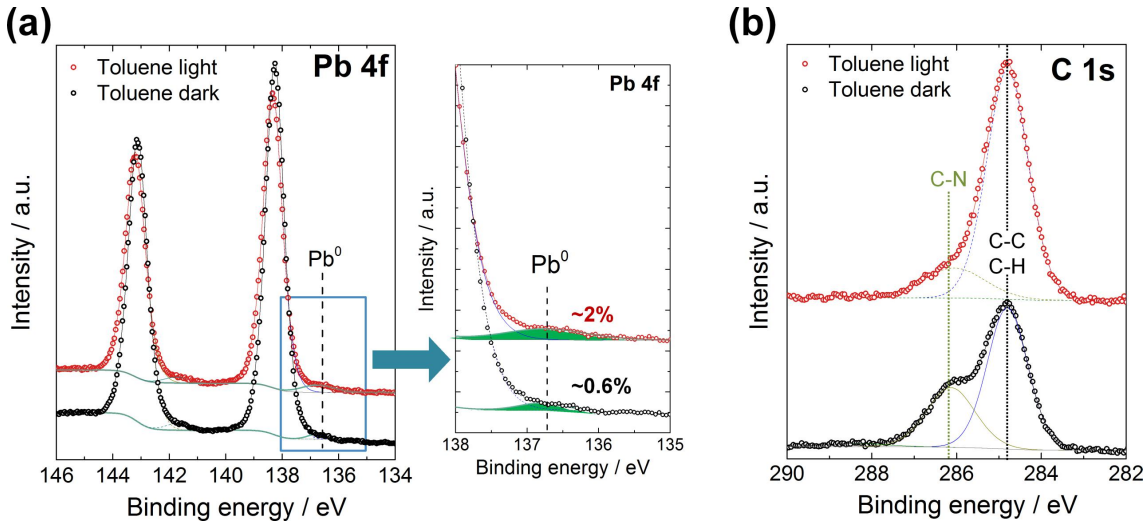

Figure 10.23. XPS measurements of $MAPbI_3$ films treated in toluene. The treatment was performed in the dark and under illumination at room temperature. **(a)** Pb 4f region, with magnification of the metallic lead peak at −136.7 eV. **(b)** C 1s region, showing a decrease in the peak located on the typical C-N binding energy (−286.1 eV).

10.5.4 *Summary of possible O_2-induced degradation reactions*

Table 10.4. Degradation reactions of several halide perovskites under oxygen, with their Gibbs free energies of decompositions. Thermodynamic data for halide perovskites were taken from Ref.[171].

Degradation reaction	$\mathbf{\Delta_r G^0_{298K}}$ **/ kJ mol^{-1}**
$CH_3NH_3PbI_3 \rightarrow CH_3NH_3I + PbI_2$	7.2
$CH_3NH_3PbI_3 \rightarrow CH_3NH_2 + PbI_2 + HI$	129.7
$CH_3NH_3PbI_3 \rightarrow CH_3NH_2 + PbI_2 + \frac{1}{2}H_2 + \frac{1}{2}I_2$	128.0
$CH_3NH_3PbI_3 + \frac{1}{4}O_2 \rightarrow \frac{1}{2}H_2O + CH_3NH_2 + PbI_2 + \frac{1}{2}I_2$	5.3
$CH_3NH_3PbI_3 + \frac{3}{4}O_2 \rightarrow \frac{1}{2}H_2O + CH_3NH_2 + PbO + \frac{3}{2}I_2$	−9.0
$CH_3NH_3PbBr_3 + \frac{1}{4}O_2 \rightarrow \frac{1}{2}H_2O + CH_3NH_2 + PbI_2 + \frac{1}{2}Br_2$	64.9
$CH_3NH_3PbCl_3 + \frac{1}{4}O_2 \rightarrow \frac{1}{2}H_2O + CH_3NH_2 + PbI_2 + \frac{1}{2}Cl_2$	89.4

10.6 SHORT-RANGE ION DYNAMICS IN $MAPbI_3$

10.6.1 *Structural characterization of the samples*

Fig. 10.24 shows that both pure and enriched $MAPbI_3$ used in the NMR measurements were entirely phase pure.

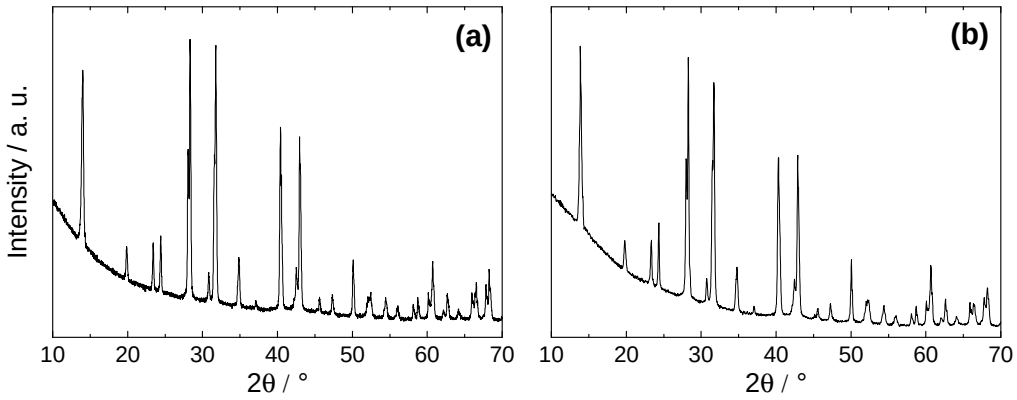

Figure 10.24. XRD analysis of **(a)** pure (i.e. natural abundance) and **(b)** (^{13}C,^{15}N)-enriched $MAPbI_3$ powders used for the NMR experiments.

10.6.2 ^1H *NMR additional spectra*

Fig. 10.25a shows the absence of any significant variation of the chemical shift in ^1H NMR under MAS conditions. Changes in the temperature $> 200K$ results in barely discernible shift (< 0.1 ppm)

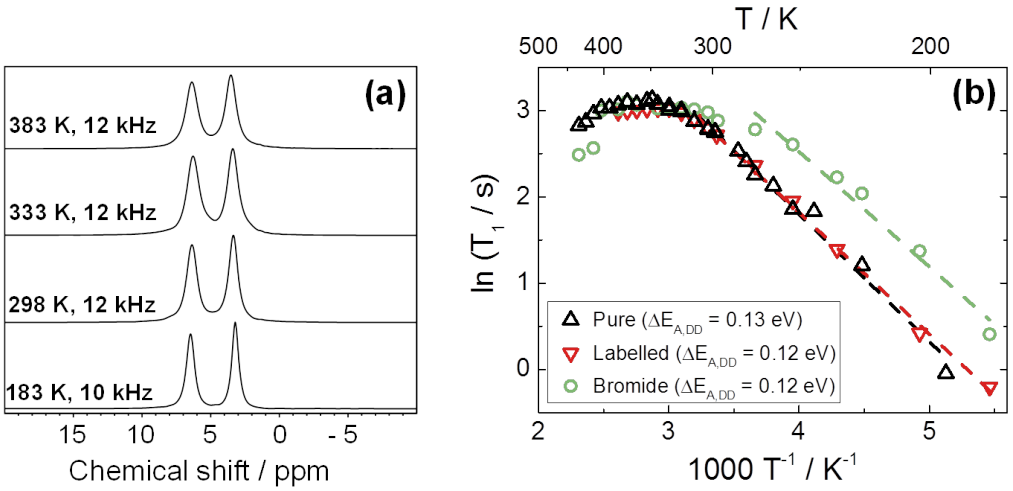

Figure 10.25. (a) ^1H MAS NMR spectra of $MAPbI_3$ at different temperatures. **(b)** Temperature dependence of ^1H T_1 in pure $MAPbBr_3$, compared with the values collected in pure and (^{13}C,^{15}N)-enriched $MAPbI_3$.

Fig. 10.25b compares the ^1H T_1 in $MAPbBr_3$ and $MAPbI_3$. While the behaviors are very similar, the inflection point at which spin-rotational interactions start to dominate the relaxation process is distinctly shifted at lower temperatures in $MAPbBr_3$, in agreement with previous observations.[192]

10.6.3 ^1H *relaxation times under MAS conditions*

Fig. 10.26a shows that, as expected, deconvoluting the contributions coming from CH_3 and NH_3 groups to the ^1H spin-lattice relaxation time yields very similar values. This occurrence is consistent with our hypothesis of MA cations behaving as symmetrical rotors, with similar interactions of the CH_3 and NH_3 groups with the inorganic lattice. In addition, **Fig. 10.26a** shows that MAS conditions induce a deviation from the monotonous behavior expected for ^1H T_1. For this reason, we collected the relaxation times measurements in stationary conditions. A similar effect is also visible for ^{13}C spectra (**Fig. 10.28**), and has been reported for other materials as well.[202,203,213]

Fig. 10.26b shows the ^1H T_1 in the rotating frame ($T_{1\rho}$), recorded at two different radio-frequency fields. The $T_{1\rho}$ values are on the order of tens of millisecond, suggesting that a cross-polarisation between ^1H and ^{13}C or ^{15}N could potentially improve the measurement time (by applying CP techniques). Unfortunately, as discussed in the main text, ^1H T_1 times in $MAPbI_3$ are too long to provide any advantage by using the CP method, thus we used the direct excitation.

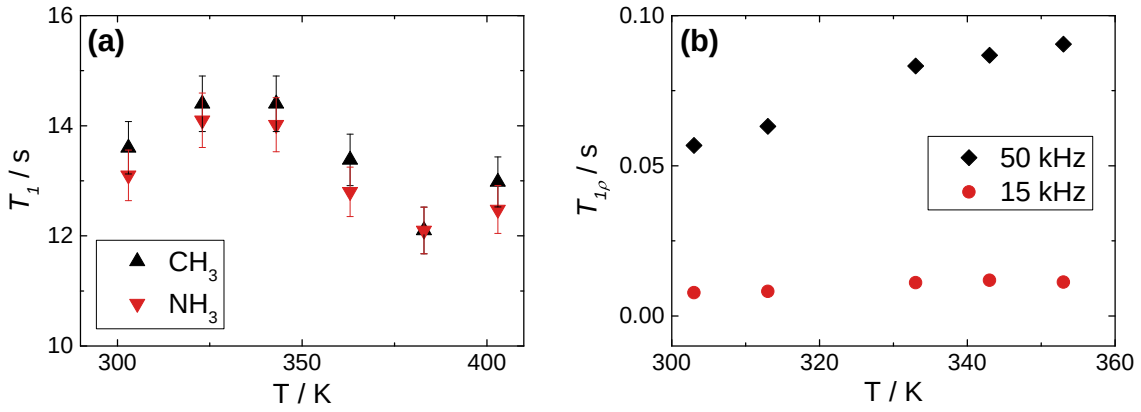

Figure 10.26. Temperature dependence of **(a)** ^1H T_1 under MAS conditions (10 kHz) and **(b)** ^1H $T_{1\rho}$ in $MAPbI_3$. The latter is measured in a spin-locking experiment by varying the time of the spin-lock. Spin-locking radio-frequencies are indicated on the figure.

10.6.4 ^{13}C *and* ^{15}N *MAS spectra and relaxation times*

Fig. 10.27 shows ^{13}C and ^{15}N MAS spectra as a function of temperature. The changes in chemical shift observed are consistent with the structural modifications induced by temperature variations.

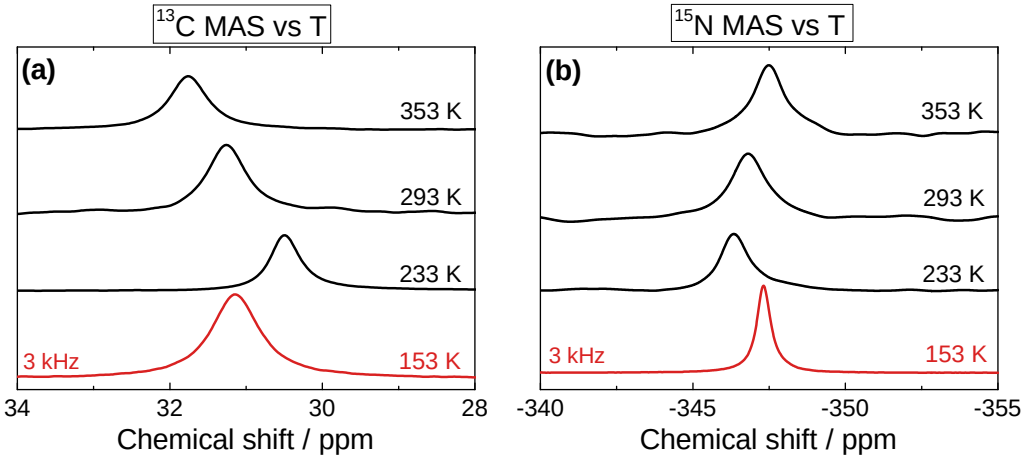

Figure 10.27. Temperature dependence of ^{13}C and ^{15}N NMR MAS spectra of (^{13}C,^{15}N)-enriched $MAPbI_3$. Spinning rate was 5 kHz unless specified. The chemical shift trend is expected above the orthorhombic phase transition, but shows a discontinuity below.

Interestingly, as shown in **Fig. 10.28**, MAS conditions affect the spin-lattice relaxation times, in a manner similar to what was reported for spin-lattice relaxation of ^{207}Pb in PbI_2 and $PbBr_2$.[217] In that case, the phenomenon was of higher magnitude and was attributed to a MAS-assisted cross-relaxation of a spin-$\frac{1}{2}$ nucleus (^{207}Pb) to a strongly quadrupolar nucleus (^{127}I). Note that such behavior has also been reported for other materials.[202,203,213]

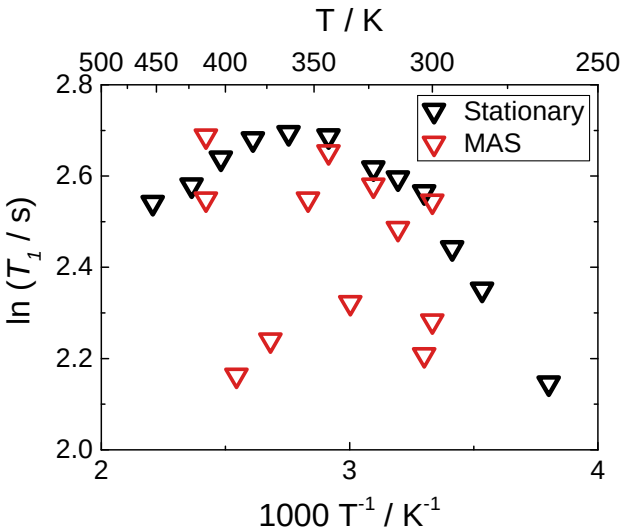

Figure 10.28. Temperature dependence of ^{13}C T_1 in $MAPbI_3$, stationary and 5 kHz MAS.

This effect is less pronounced in the case of protons (**Fig. 10.26b**) because of the large difference in the Larmor frequency between ^{127}I and ^{1}H, that is > 300 MHz at the used field of 9.4 T. However, in the case of ^{13}C, the difference is much smaller (~ 20 MHz) and given the massive quadrupolar constant of ^{127}I in $MAPbI_3$ (> 550 MHz),[194] we expect a significant crossing of the nuclear energy levels under MAS conditions and subsequently effective cross-relaxation. For this reason, we only performed T_1 measurements in stationary conditions.

10.6.5 ^{14}N *rotational correlation time*

In the case of ^{14}N (spin-1), the dominating mechanism of spin-lattice relaxation can be assigned to quadrupolar interactions. In the fast motion limit of the BPP model, such relaxation can be given as:[99,100]

$$\frac{1}{T_1^Q} = \frac{12\pi^2\chi_Q^2}{8}(1 + \frac{\eta_Q^2}{3})\tau_c \tag{10.7}$$

where χ_Q and η_Q are respectively the nuclear quadrupolar coupling constant and quadrupolar asymmetry parameter, and τ_c is the rotational correlation time. For ^{14}N relaxation in an axially symmetrical MA cation, τ_c described the spatial reorientation of the C-N axis. Due to the fast axial rotation of MA cations taking place in both tetragonal and cubic phases of $MAPbI_3$, the effective η_Q is reduced to 0 in both phases, further simplifying the equation. To evaluate τ_c we use the $\chi_Q(^{14}N)$ value we obtained from DFT MD simulations (Appendix **§ 10.6.7**) of 0.68 MHz, yielding correlation times of 1.0 ps at 303 K (tetragonal phase) and 0.53 ps at 333 K (cubic phase). These values underline the rapid reorientation of the C-N axis taking place in both phases, and are in full agreement with previous reports.[191,193,197] Note that a much higher correlation time of 108 ps has also been reported,[169] however this value was extracted using an entirely different method, thus not allowing for a direct comparison.

10.6.6 ^{14}N *spectral simulations*

Both the lineshape and linewidth of the ^{14}N NMR signals contain information on the modes of motion involving MA cations. Lineshapes in ^{14}N NMR are generally defined by the interactions between the quadrupolar moment of the nucleus with the surrounding EFG tensor. In the case of a MA cation, this coupling is mainly intramolecular, making it highly sensitive to both the type

and the rate of the molecular motions involving MA. We perform ^{14}N spectral simulations to investigate possible modes of motion for the MA cation, and compare these results with the experimental ^{14}N spectra. In the general case of non-axial EFG symmetry, the NMR frequencies (ω_Q) composing a ^{14}N NMR spectrum can be equated as:

$$\omega_Q(\theta,\varphi) - \omega_L = a\chi_Q F(\eta,\theta,\varphi), \qquad \text{with } \chi_Q = \frac{eQ}{4\hbar}V_{ZZ} \tag{10.8}$$

where ω_L is the Larmor frequency, a is a combination of constants, F is a function that defines the angular dependence of the EFG tensor, χ_Q is the quadrupolar constant and V_{ZZ} is the largest principal component of the EFG tensor. We note that, in a MA cation, V_{ZZ} is directed along the C-N bond. The deviation from axial symmetry is described by the asymmetry parameter (η), and the orientation of the EFG tensor with respect to the external magnetic field is given by the polar angles θ and φ. Note that if a second rank tensor undergoes fast axial motion about an axis involving 3 (or more) equivalent sites, this will yield an averaged axial symmetry ($\eta = 0$) for said tensor. Concerning the χ_Q, since the quadrupolar coupling in MA cations comes primarily from intramolecular origins, one could expect this value to not strongly differ from the one in MA halogenates (e.g. values of χ_Q of 1.1 MHz[241] and 0.9 MHz[242] have been reported for MACl). Curiously, our periodic *ab-initio* DFT MD simulations (see § **10.6.7**) yield a significantly different value ($\chi_Q = 0.68$ MHz, with $\eta = 0.52$) when averaging over all nitrogen sites, indicating a strong influence of the inorganic framework on the EFG. This aspect is discussed and reported in detail elsewhere (Ref.[182] and corresponding Supporting Information). The EFG parameters obtained in our calculations are in good agreement with recent reports,[198] and have therefore been used in all ^{14}N spectral simulations presented in the main text (**Fig. 7.6**).

10.6.7 *DFT calculations*

We have performed periodic lattice Molecular Dynamics DFT calculations for ^{14}N shielding and ^{207}Pb shielding on a 3x3x3 supercell of $MAPbI_3$. Here, the lattice parameters are constrained, while the MA cations are free to reorient (**Fig. 10.29**). Details and calculated values for these simulations are reported elsewhere (Ref.[182] and related Supporting Information).

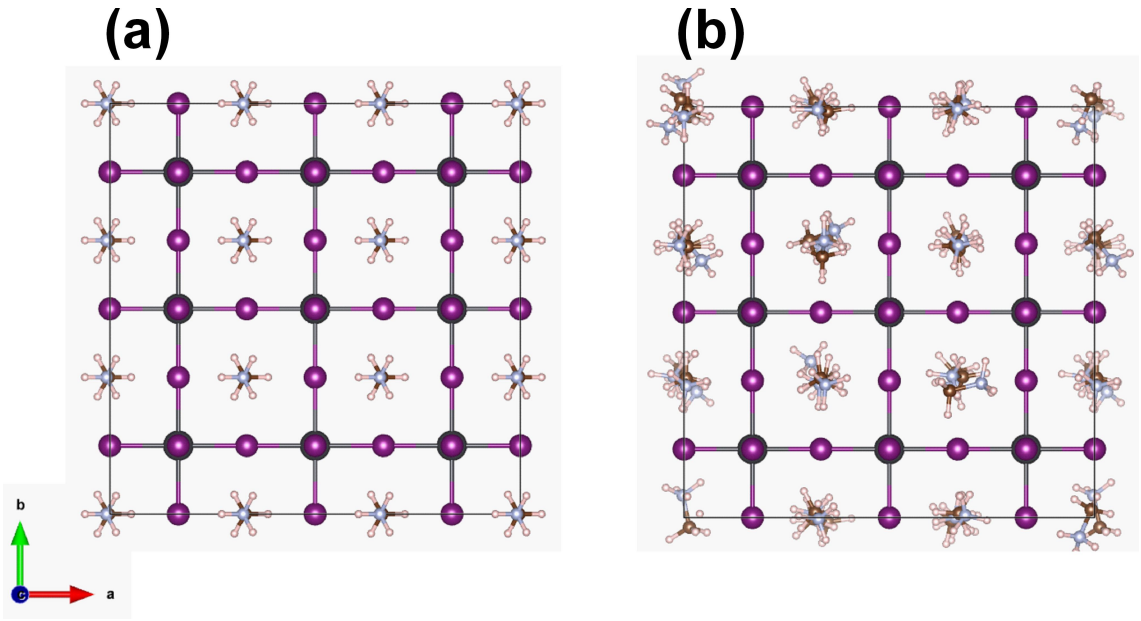

Figure 10.29. Structure of $MAPbI_3$ **(a)** before and **(b)** after DFT MD simulations. Note the reorientation of MA cations taking place within the constrained lattice.

In the case of ^{207}Pb, **Fig. 10.30** shows the qualitatively satisfactory agreement between calculated and experimental ^{207}Pb chemical shift in several Pb compounds of known environment. We note that the reason why the agreement is not entirely quantitative is because of the incomplete accounting of relativistic effects in the heavy Pb nuclei, resulting from using pseudopotentials instead of the full electron wave functions and to the lack of spin-orbit effects in the valence wavefunctions.

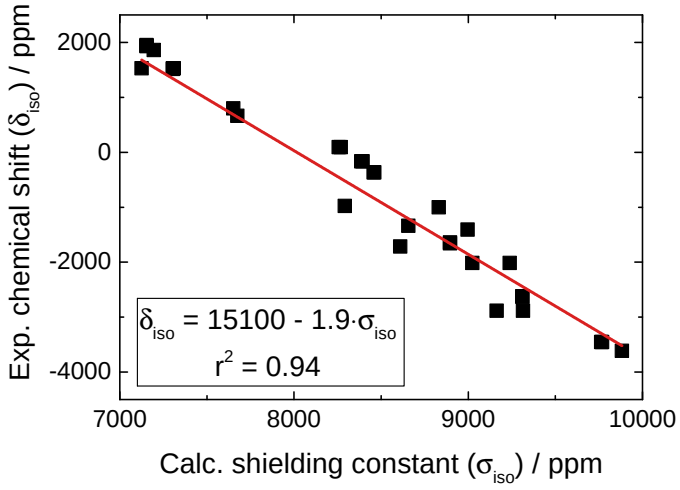

Figure 10.30. Correlation between calculated isotropic shielding and experimental ^{207}Pb isotropic chemical shifts in several diamagnetic Pb compounds (reference to lead tetramethyl at 0 ppm). All experimental data are taken from literature (See Ref. [182] for specific references.)

10.6.8 ^{127}I *NMR*

Fig. 10.31 shows the preliminary ^{127}I NMR spectra collected on $MAPbI_3$. Note that even small amounts of PbI_2 can easily give relatively narrower and stronger signals when compared to $MAPbI_3$. The actual signal of $MAPbI_3$ shows two outer singularities, centered at 4 and -8 MHz. The position of these signals correspond to a quadrupolar constant of about 550 MHz, with an asymmetry parameter close to 0, in good agreement with NQR data (**§ 7.6**). Due to very short T_2 relaxation time (15 μs) and a huge second-order quadrupolar broadening, we are able to record only these outer singularities of the signals, which span over 12 MHz. Remarkably, more than 22 hours of spectrometer time were required to collected such poorly resolved, noisy signals.

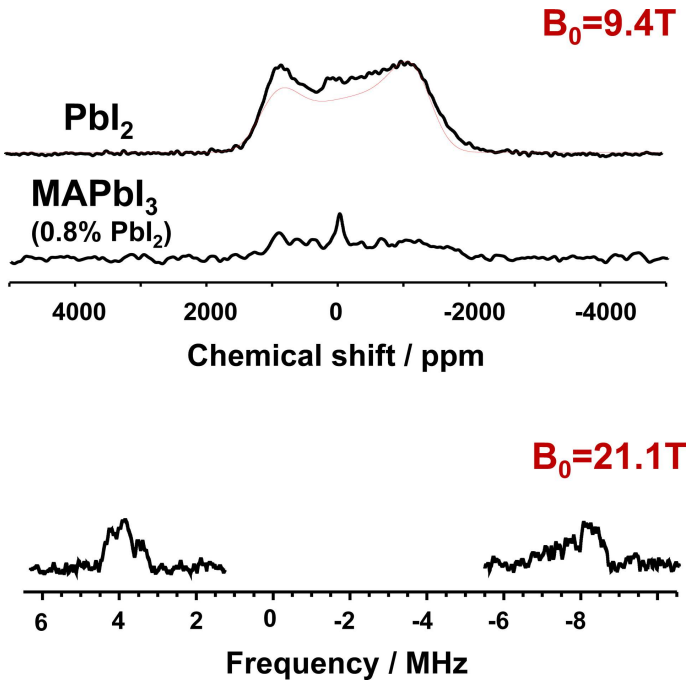

Figure 10.31. ^{127}I NMR spectra in $MAPbI_3$, collected using the solid-echo sequence. The upper part shows spectra collected at 9.4 T, comparing PbI_2 powders with $MAPbI_3$ powders which contains residual PbI_2 (responsible for the visible signal). The lower panel shows the ^{127}I NMR collected at 21.1 T.

10.6.9 ^{127}I *NQR torsional frequencies*

The temperature dependence of the resonant frequencies of the ^{127}I NQR signals can be modeled according to the Bayer theory[243] of torsional oscillation of atoms in a lattice[244] (for details see also Ref.[182] and Supporting Information). In this model, the nuclei are assumed to be agitated at a torsional rate that is very

fast compared to their NQR frequencies, making them affected by an averaged, temperature dependent EFG which differs from the stationary situation. This approach requires the assumption of an axially symmetric situation, i.e. with an asymmetry parameter close to 0, that is entirely valid for $MAPbI_3$ (see **Fig. 7.8b**). The fit of the temperature dependence yields a torsional frequency of 1.15 THz.

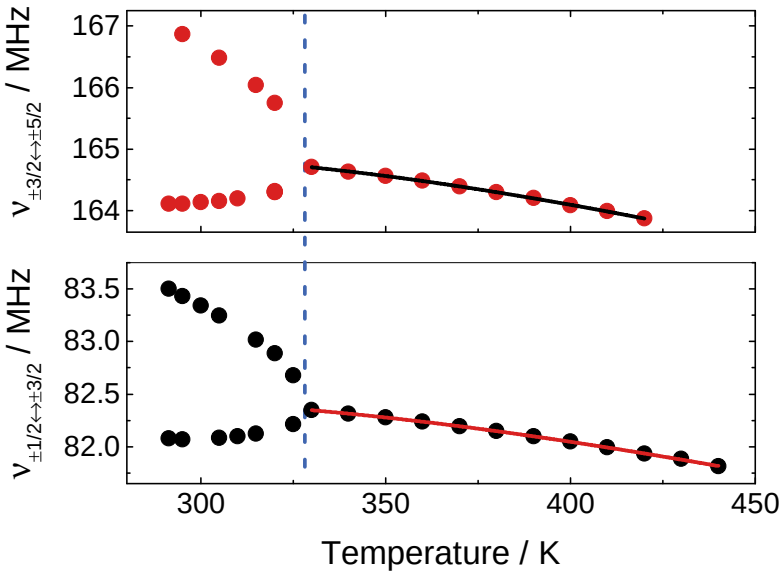

Figure 10.32. Temperature dependence of the ^{127}I NQR frequencies in $MAPbI_3$. Phase transition is marked with a blue line. Note that the temperature dependence is still significant after transformation into the cubic phase.

BIBLIOGRAPHY

[1] A. Kojima, K. Teshima, Y. Shirai, and T. Miyasaka, "Organometal Halide Perovskites as Visible-Light Sensitizers for Photovoltaic Cells," *Journal of the American Chemical Society*, vol. 131, pp. 6050–6051, may 2009.

[2] M. M. Lee, J. Teuscher, T. Miyasaka, T. N. Murakami, and H. J. Snaith, "Efficient Hybrid Solar Cells Based on Meso-Superstructured Organometal Halide Perovskites," *Science*, vol. 338, no. 6107, pp. 643–647, 2012.

[3] H.-S. Kim, C.-R. Lee, J.-H. Im, K.-B. Lee, T. Moehl, A. Marchioro, S.-J. Moon, R. Humphry-Baker, J.-H. Yum, J. E. Moser, M. Grätzel, and N.-G. Park, "Lead Iodide Perovskite Sensitized All-Solid-State Submicron Thin Film Mesoscopic Solar Cell with Efficiency Exceeding 9%," *Scientific Reports*, vol. 2, p. 591, dec 2012.

[4] Z.-K. Tan, R. S. Moghaddam, M. L. Lai, P. Docampo, R. Higler, F. Deschler, M. Price, A. Sadhanala, L. M. Pazos, D. Credgington, F. Hanusch, T. Bein, H. J. Snaith, and R. H. Friend, "Bright light-emitting diodes based on organometal halide perovskite," *Nature Nanotechnology*, vol. 9, p. 687, aug 2014.

[5] L. Protesescu, S. Yakunin, M. I. Bodnarchuk, F. Krieg, R. Caputo, C. H. Hendon, R. X. Yang, A. Walsh, and M. V. Kovalenko, "Nanocrystals of Cesium Lead Halide Perovskites (CsPbX3, X = Cl, Br, and I): Novel Optoelectronic Materials Showing Bright Emission with Wide Color Gamut," *Nano Letters*, 2015.

[6] C. R. Kagan, D. B. Mitzi, and C. D. Dimitrakopoulos, "Organic-Inorganic Hybrid Materials as Semiconducting Channels in Thin-Film Field-Effect Transistors," *Science*, vol. 286, no. 5441, pp. 945–947, 1999.

[7] X. Y. Chin, D. Cortecchia, J. Yin, A. Bruno, and C. Soci, "Lead iodide perovskite light-emitting field-effect transistor," *Nature Communications*, vol. 6, p. 7383, jun 2015.

[8] F. Deschler, M. Price, S. Pathak, L. E. Klintberg, D.-D. Jarausch, R. Higler, S. Hüttner, T. Leijtens, S. D. Stranks, H. J. Snaith, M. Atatüre, R. T.

Phillips, and R. H. Friend, "High Photoluminescence Efficiency and Optically Pumped Lasing in Solution-Processed Mixed Halide Perovskite Semiconductors," *The Journal of Physical Chemistry Letters*, vol. 5, pp. 1421–1426, apr 2014.

[9] G. Xing, N. Mathews, S. S. Lim, N. Yantara, X. Liu, D. Sabba, M. Grätzel, S. Mhaisalkar, and T. C. Sum, "Low-temperature solution-processed wavelength-tunable perovskites for lasing," *Nature Materials*, vol. 13, p. 476, mar 2014.

[10] S. Yakunin, M. Sytnyk, D. Kriegner, S. Shrestha, M. Richter, G. J. Matt, H. Azimi, C. J. Brabec, J. Stangl, M. V. Kovalenko, and W. Heiss, "Detection of X-ray photons by solution-processed lead halide perovskites," *Nature Photonics*, vol. 9, p. 444, may 2015.

[11] D. Weber, "CH3NH3PbX3, ein Pb(II)-System mit kubischer Perowskitstruktur / CH3NH3PbX3, a Pb(II)-System with Cubic Perovskite Structure," *Zeitschrift für Naturforschung B*, vol. 33, pp. 1443–1445, jan 1978.

[12] A. M. Soufiani, F. Huang, P. Reece, R. Sheng, A. Ho-Baillie, and M. A. Green, "Polaronic exciton binding energy in iodide and bromide organic-inorganic lead halide perovskites," *Applied Physics Letters*, vol. 107, p. 231902, dec 2015.

[13] K. Galkowski, A. Mitioglu, A. Miyata, P. Plochocka, O. Portugall, G. E. Eperon, J. T.-W. Wang, T. Stergiopoulos, S. D. Stranks, H. J. Snaith, and R. J. Nicholas, "Determination of the exciton binding energy and effective masses for methylammonium and formamidinium lead tri-halide perovskite semiconductors," *Energy Environmental Science*, vol. 9, no. 3, pp. 962–970, 2016.

[14] S. D. Stranks, G. E. Eperon, G. Grancini, C. Menelaou, M. J. P. Alcocer, T. Leijtens, L. M. Herz, A. Petrozza, and H. J. Snaith, "Electron-Hole Diffusion Lengths Exceeding 1 Micrometer in an Organometal Trihalide Perovskite Absorber," *Science*, vol. 342, pp. 341–344, oct 2013.

[15] Q. Dong, Y. Fang, Y. Shao, P. Mulligan, J. Qiu, L. Cao, and J. Huang, "Electron-hole diffusion lengths $>$ 175 m in solution-grown CH3NH3PbI3 single crystals," *Science*, vol. 347, pp. 967–970, feb 2015.

[16] Y. Yang, D. P. Ostrowski, R. M. France, K. Zhu, J. van de Lagemaat, J. M. Luther, and M. C. Beard, "Observation of a hot-phonon bottleneck in lead-iodide perovskites," *Nature Photonics*, vol. 10, no. 1, pp. 53–59, 2015.

[17] Z. Guo, Y. Wan, M. Yang, J. Snaider, K. Zhu, and L. Huang, "Long-range hot-carrier transport in hybrid perovskites visualized by ultrafast microscopy," *Science*, vol. 356, no. 6333, pp. 59–62, 2017.

[18] J. Fu, Q. Xu, G. Han, B. Wu, C. H. A. Huan, M. L. Leek, and T. C. Sum, "Hot carrier cooling mechanisms in halide perovskites," *Nature Communications*, vol. 8, no. 1, p. 1300, 2017.

[19] National Center for Photovoltaics at the National Renewable Energy Laboratory, "Research cell efficiency records."

[20] B. O'Regan and M. Grätzel, "A low-cost, high-efficiency solar cell based on dye-sensitized colloidal TiO2 films," *Nature*, vol. 353, pp. 737–740, oct 1991.

[21] G. A. Sepalage, S. Meyer, A. Pascoe, A. D. Scully, F. Huang, U. Bach, Y.-B. Cheng, and L. Spiccia, "Copper(I) Iodide as Hole-Conductor in Planar Perovskite Solar Cells: Probing the Origin of J-V Hysteresis," *Advanced Functional Materials*, vol. 25, no. 35, pp. 5650–5661, 2015.

[22] N. Arora, M. I. Dar, A. Hinderhofer, N. Pellet, F. Schreiber, S. M. Zakeeruddin, and M. Grätzel, "Perovskite solar cells with CuSCN hole extraction layers yield stabilized efficiencies greater than 20%," *Science*, vol. 358, pp. 768–771, nov 2017.

[23] K. Momma and F. Izumi, "VESTA 3 for three-dimensional visualization of crystal, volumetric and morphology data," *Journal of Applied Crystallography*, vol. 44, pp. 1272–1276, dec 2011.

[24] M. Saliba, T. Matsui, K. Domanski, J.-Y. Seo, A. Ummadisingu, S. M. Zakeeruddin, J.-P. Correa-Baena, W. R. Tress, A. Abate, A. Hagfeldt, and M. Gratzel, "Incorporation of rubidium cations into perovskite solar cells improves photovoltaic performance," *Science*, vol. 354, pp. 206–209, oct 2016.

[25] N. D. Marco, H. Zhou, Q. Chen, P. Sun, Z. Liu, L. Meng, E.-P. Yao, Y. Liu, A. Schiffer, and Y. Yang, "Guanidinium: A Route to Enhanced Carrier Lifetime and Open-Circuit Voltage in Hybrid Perovskite Solar Cells," *Nano Letters*, vol. 16, pp. 1009–1016, feb 2016.

[26] G. Kieslich, S. Sun, and T. Cheetham, "An Extended Tolerance Factor Approach for Organic-Inorganic Perovskites," *Chemical Science*, vol. 6, pp. 3430–3433, may 2015.

[27] Z. Shi, J. Guo, Y. Chen, Q. Li, Y. Pan, H. Zhang, Y. Xia, and W. Huang, "Lead-Free Organic-Inorganic Hybrid Perovskites for Photovoltaic Applications: Recent Advances and Perspectives," *Advanced Materials*, vol. 29, p. 1605005, apr 2017.

[28] H. Tsai, W. Nie, J.-C. Blancon, C. C. Stoumpos, R. Asadpour, B. Harutyunyan, A. J. Neukirch, R. Verduzco, J. J. Crochet, S. Tretiak, L. Pedesseau, J. Even, M. A. Alam, G. Gupta, J. Lou, P. M. Ajayan, M. J. Bedzyk, M. G. Kanatzidis, and A. D. Mohite, "High-efficiency two-dimensional Ruddlesden-Popper perovskite solar cells," *Nature*, vol. 536, pp. 312–316, aug 2016.

[29] J.-C. Blancon, H. Tsai, W. Nie, C. C. Stoumpos, L. Pedesseau, C. Katan, M. Kepenekian, C. M. M. Soe, K. Appavoo, M. Y. Sfeir, S. Tretiak, P. M. Ajayan, M. G. Kanatzidis, J. Even, J. J. Crochet, and A. D. Mohite, "Extremely efficient internal exciton dissociation through edge states in layered 2D perovskites," *Science*, vol. 355, no. 6331, pp. 1288–1292, 2017.

[30] J. Mizusaki, K. Arai, and K. Fueki, "Ionic conduction of the perovskite-type halides," *Solid State Ionics*, vol. 11, pp. 203–211, nov 1983.

[31] T.-Y. Yang, G. Gregori, N. Pellet, M. Grätzel, and J. Maier, "The Significance of Ion Conduction in a Hybrid Organic-Inorganic Lead-Iodide-Based Perovskite Photosensitizer," *Angewandte Chemie International Edition*, vol. 54, no. 27, pp. 7905–7910, 2015.

[32] Y. Cheng, H.-W. Li, J. Qing, Q.-D. Yang, Z. Guan, C. Liu, S. H. Cheung, S. K. So, C.-S. Lee, and S.-W. Tsang, "The detrimental effect of excess mobile ions in planar CH3NH3PbI3 perovskite solar cells," *Journal of Materials Chemistry A*, vol. 4, no. 33, pp. 12748–12755, 2016.

[33] M. Bag, L. A. Renna, R. Y. Adhikari, S. Karak, F. Liu, P. M. Lahti, T. P. Russell, M. T. Tuominen, and D. Venkataraman, "Kinetics of Ion Transport in Perovskite Active Layers and Its Implications for Active Layer Stability," *Journal of the American Chemical Society*, vol. 137, no. 40, pp. 13130–13137, 2015.

[34] J. Carrillo, A. Guerrero, S. Rahimnejad, O. Almora, I. Zarazua, E. Mas-Marza, J. Bisquert, and G. Garcia-Belmonte, "Ionic Reactivity at Contacts and Aging of Methylammonium Lead Triiodide Perovskite Solar Cells," *Advanced Energy Materials*, vol. 6, p. 1502246, may 2016.

[35] H. J. Snaith, A. Abate, J. M. Ball, G. E. Eperon, T. Leijtens, N. K. Noel, S. D. Stranks, J. T.-W. Wang, K. Wojciechowski, and W. Zhang, "Anomalous Hysteresis in Perovskite Solar Cells," *The Journal of Physical Chemistry Letters*, vol. 5, no. 9, pp. 1511–1515, 2014.

[36] E. J. Juarez-Perez, R. S. Sanchez, L. Badia, G. Garcia-Belmonte, Y. S. Kang, I. Mora-Sero, and J. Bisquert, "Photoinduced Giant Dielectric Constant in Lead Halide Perovskite Solar Cells," *The Journal of Physical Chemistry Letters*, vol. 5, no. 13, pp. 2390–2394, 2014.

[37] A. Dualeh, P. Gao, S. I. Seok, M. K. Nazeeruddin, and M. Grätzel, "Thermal behavior of methylammonium lead-trihalide perovskite photovoltaic light harvesters," *Chemistry of Materials*, vol. 26, no. 21, pp. 6160–6164, 2014.

[38] B. Conings, J. Drijkoningen, N. Gauquelin, A. Babayigit, J. D'Haen, L. D'Olieslaeger, A. Ethirajan, J. Verbeeck, J. Manca, E. Mosconi, F. De Angelis, and H. G. Boyen, "Intrinsic Thermal Instability of Methylammonium Lead Trihalide Perovskite," *Advanced Energy Materials*, vol. 5, p. 1500477, aug 2015.

[39] Y. Han, S. Meyer, Y. Dkhissi, K. Weber, J. M. Pringle, U. Bach, L. Spiccia, and Y.-B. Cheng, "Degradation observations of encapsulated planar $CH_3NH_3PbI_3$ perovskite solar cells at high temperatures and humidity," *Journal of Materials Chemistry A*, vol. 3, no. 15, pp. 8139–8147, 2015.

[40] G. Divitini, S. Cacovich, F. Matteocci, L. Cinà, A. Di Carlo, and C. Ducati, "In situ observation of heat-induced degradation of perovskite solar cells," *Nature Energy*, vol. 1, p. 15012, jan 2016.

[41] D. P. Nenon, J. A. Christians, L. M. Wheeler, J. L. Blackburn, E. M. Sanehira, B. Dou, M. L. Olsen, K. Zhu, J. J. Berry, and J. M. Luther, "Structural and chemical evolution of methylammonium lead halide perovskites during thermal processing from solution," *Energy & Environmental Science*, vol. 9, no. 6, pp. 2072–2082, 2016.

[42] E. Tenuta, C. Zheng, and O. Rubel, "Thermodynamic origin of instability in hybrid halide perovskites," *Scientific Reports*, vol. 6, p. 37654, dec 2016.

[43] B. Brunetti, C. Cavallo, A. Ciccioli, G. Gigli, and A. Latini, "On the Thermal and Thermodynamic (In)Stability of Methylammonium Lead Halide Perovskites," *Scientific Reports*, vol. 6, p. 31896, aug 2016.

[44] N.-K. Kim, Y. H. Min, S. Noh, E. Cho, G. Jeong, M. Joo, S.-W. Ahn, J. S. Lee, S. Kim, K. Ihm, H. Ahn, Y. Kang, H.-S. Lee, and D. Kim, "Investigation of Thermally Induced Degradation in CH3NH3PbI3 Perovskite Solar Cells using In-situ Synchrotron Radiation Analysis," *Scientific Reports*, vol. 7, p. 4645, dec 2017.

[45] G. Abdelmageed, C. Mackeen, K. Hellier, L. Jewell, L. Seymour, M. Tingwald, F. Bridges, J. Z. Zhang, and S. Carter, "Effect of temperature on light induced degradation in methylammonium lead iodide perovskite thin films and solar cells," *Solar Energy Materials and Solar Cells*, vol. 174, no. October 2017, pp. 566–571, 2018.

[46] G. Niu, W. Li, F. Meng, L. Wang, H. Dong, and Y. Qiu, "Study on the stability of CH3NH3PbI3 films and the effect of post-modification by aluminum oxide in all-solid-state hybrid solar cells," *J. Mater. Chem. A*, vol. 2, no. 3, pp. 705–710, 2014.

[47] A. M. A. Leguy, Y. Hu, M. Campoy-Quiles, M. I. Alonso, O. J. Weber, P. Azarhoosh, M. van Schilfgaarde, M. T. Weller, T. Bein, J. Nelson, P. Docampo, and P. R. F. Barnes, "Reversible Hydration of CH3NH3PbI3 in Films, Single Crystals, and Solar Cells," *Chemistry of Materials*, vol. 27, pp. 3397–3407, may 2015.

[48] J. A. Christians, P. A. Miranda Herrera, and P. V. Kamat, "Transformation of the excited state and photovoltaic efficiency of CH3NH3PbI3 perovskite upon controlled exposure to humidified air," *Journal of the American Chemical Society*, vol. 137, no. 4, pp. 1530–1538, 2015.

[49] J. Yang, B. D. Siempelkamp, D. Liu, and T. L. Kelly, "Investigation of CH3NH3PbI3 Degradation Rates and Mechanisms in Controlled Humidity Environments Using in Situ Techniques," *ACS Nano*, vol. 9, pp. 1955–1963, feb 2015.

[50] M. Shirayama, M. Kato, T. Miyadera, T. Sugita, T. Fujiseki, S. Hara, H. Kadowaki, D. Murata, M. Chikamatsu, and H. Fujiwara, "Degradation mechanism of CH3NH3PbI3 perovskite materials upon exposure to humid air," *Journal of Applied Physics*, vol. 119, p. 115501, mar 2016.

[51] W. C. Lin, H. Y. Chang, K. Abbasi, J. J. Shyue, and C. Burda, "3D In Situ ToF-SIMS Imaging of Perovskite Films under Controlled Humidity Environmental Conditions," *Advanced Materials Interfaces*, vol. 4, p. 1600673, jan 2017.

[52] M. Salado, L. Contreras, L. Calio, A. Todinova, C. Lopez-santos, S. Ahmad, A. Borras, J. A. Idígoras, and J. A. Anta, "Impact of Moisture on Efficiency-Determining Electronic Processes in Perovskite Solar Cells," *J. Mater. Chem. A*, vol. 5, pp. 10917–10927, jun 2017.

[53] N. Aristidou, I. Sanchez-Molina, T. Chotchuangchutchaval, M. Brown, L. Martinez, T. Rath, and S. A. Haque, "The Role of Oxygen in the Degradation of Methylammonium Lead Trihalide Perovskite Photoactive Layers," *Angewandte Chemie - International Edition*, vol. 54, pp. 8208–8212, jul 2015.

[54] F. T. F. O'Mahony, Y. H. Lee, C. Jellett, S. Dmitrov, D. T. J. Bryant, J. R. Durrant, B. C. O'Regan, M. Graetzel, M. K. Nazeeruddin, and S. A. Haque, "Improved environmental stability of organic lead trihalide perovskite-based photoactive-layers in the presence of mesoporous TiO 2," *J. Mater. Chem. A*, vol. 3, no. 14, pp. 7219–7223, 2015.

[55] X. Tang, M. Brandl, B. May, I. Levchuk, Y. Hou, M. Richter, H. Chen, S. Chen, S. Kahmann, A. Osvet, F. Maier, H.-P. Steinruck, R. Hock, G. J. Matt, and C. J. Brabec, "Photoinduced degradation of methylammonium lead triiodide perovskite semiconductors," *Journal of Materials Chemistry A*, vol. 4, no. 41, pp. 15896–15903, 2016.

[56] D. Bryant, N. Aristidou, S. Pont, I. Sanchez-Molina, T. Chotchunangatchaval, S. Wheeler, J. R. Durrant, and S. A. Haque, "Light and oxygen induced degradation limits the operational stability of methylammonium lead triiodide perovskite solar cells," *Energy Environmental Science*, vol. 9, no. 5, pp. 1655–1660, 2016.

[57] A. J. Pearson, G. E. Eperon, P. E. Hopkinson, S. N. Habisreutinger, J. T.-W. Wang, H. J. Snaith, and N. C. Greenham, "Oxygen Degradation in Mesoporous Al2O3/CH3NH3PbI3- xClx Perovskite Solar Cells: Kinetics and Mechanisms," *Advanced Energy Materials*, vol. 6, p. 1600014, jul 2016.

[58] S. Pont, D. Bryant, C.-T. Lin, N. Aristidou, S. Wheeler, X. Ma, R. Godin, S. A. Haque, and J. R. Durrant, "Tuning CH3NH3Pb(I1xBrx)3 perovskite oxygen stability in thin films and solar cells," *Journal of Materials Chemistry A*, vol. 5, no. 20, pp. 9553–9560, 2017.

[59] L. Zhang and P. H.-L. Sit, "Ab initio study of the role of oxygen and excess electrons in the degradation of CH3NH3PbI3," *Journal of Materials Chemistry A*, vol. 5, no. 19, pp. 9042–9049, 2017.

[60] Q. Sun, P. Fassl, D. Becker-Koch, A. Bausch, B. Rivkin, S. Bai, P. E. Hopkinson, H. J. Snaith, and Y. Vaynzof, "Role of Microstructure in Oxygen Induced Photodegradation of Methylammonium Lead Triiodide Perovskite Films," *Advanced Energy Materials*, vol. 7, p. 1700977, oct 2017.

[61] N. Aristidou, C. Eames, I. Sanchez-Molina, X. Bu, J. Kosco, M. S. Islam, and S. A. Haque, "Fast oxygen diffusion and iodide defects mediate oxygen-induced degradation of perovskite solar cells," *Nature Communications*, vol. 8, p. 15218, may 2017.

[62] N. Aristidou, C. Eames, M. S. Islam, and S. A. Haque, "Insights into the increased degradation rate of CH3NH3PbI3 solar cells in combined water and O2 environments," *Journal of Materials Chemistry A*, vol. 5, no. 48, pp. 25469–25475, 2017.

[63] G. Murugadoss, S. Tanaka, G. Mizuta, S. Kanaya, H. Nishino, T. Umeyama, H. Imahori, and S. Ito, "Light stability tests of methylammonium and formamidinium Pb-halide perovskites for solar cell applications," *Japanese Journal of Applied Physics*, vol. 54, p. 08KF08, aug 2015.

[64] P. Pistor, A. Ruiz, A. Cabot, and V. Izquierdo-Roca, "Advanced Raman Spectroscopy of Methylammonium Lead Iodide: Development of a Non-destructive Characterisation Methodology," *Scientific Reports*, vol. 6, p. 35973, oct 2016.

[65] D. Wei, T. Wang, J. Ji, M. Li, P. Cui, Y. Li, G. Li, J. M. Mbengue, and D. Song, "Photo-induced degradation of lead halide perovskite solar cells caused by the hole transport layer/metal electrode interface," *Journal of Materials Chemistry A*, vol. 4, no. 5, pp. 1991–1998, 2016.

[66] N. H. Nickel, F. Lang, V. V. Brus, O. Shargaieva, and J. Rappich, "Unraveling the Light-Induced Degradation Mechanisms of CH3NH3PbI3 Perovskite Films," *Advanced Electronic Materials*, vol. 3, p. 1700158, dec 2017.

[67] Y. Li, X. Xu, C. Wang, B. Ecker, J. Yang, J. Huang, and Y. Gao, "Light-Induced Degradation of CH3NH3PbI3 Hybrid Perovskite Thin Film," *The Journal of Physical Chemistry C*, vol. 121, pp. 3904–3910, feb 2017.

[68] Q.-D. Dao, R. Tsuji, A. Fujii, and M. Ozaki, "Study on degradation mechanism of perovskite solar cell and their recovering effects by introducing CH3NH3I layers," *Organic Electronics*, vol. 43, pp. 229–234, apr 2017.

[69] A. Senocrate, I. Moudrakovski, G. Y. Kim, T.-Y. Yang, G. Gregori, M. Grätzel, and J. Maier, "The Nature of Ion Conduction in Methylammonium Lead Iodide: A Multimethod Approach," *Angewandte Chemie International Edition*, vol. 56, pp. 7755–7759, jun 2017.

[70] D. Shi, V. Adinolfi, R. Comin, M. Yuan, E. Alarousu, A. Buin, Y. Chen, S. Hoogland, A. Rothenberger, K. Katsiev, Y. Losovyj, X. Zhang, P. A. Dowben, O. F. Mohammed, E. H. Sargent, and O. M. Bakr, "Low trap-state density and long carrier diffusion in organolead trihalide perovskite single crystals," *Science*, vol. 347, no. 6221, pp. 519–522, 2015.

[71] W. S. Yang, B.-W. Park, E. H. Jung, N. J. Jeon, Y. C. Kim, D. U. Lee, S. S. Shin, J. Seo, E. K. Kim, J. H. Noh, and S. I. Seok, "Iodide management in formamidinium-lead-halide-based perovskite layers for efficient solar cells," *Science*, vol. 356, no. 6345, pp. 1376–1379, 2017.

[72] Z. Xiao, Y. Yuan, Y. Shao, Q. Wang, Q. Dong, C. Bi, P. Sharma, A. Gruverman, and J. Huang, "Giant switchable photovoltaic effect in organometal trihalide perovskite devices," *Nature Materials*, vol. 14, pp. 193–198, feb 2015.

[73] K. Yamada, "Chloride ion conductor CH3NH3GeCl3 studied by Rietveld analysis of X-ray diffraction and 35Cl NMR," *Solid State Ionics*, vol. 79, pp. 152–157, jul 1995.

[74] K. Yamada, T. Matsui, T. Tsuritani, T. Okuda, and S. Ichiba, "127I-NQR, 119 Sn Mössbauer Effect, and Electrical Conductivity of MSnI3 (M = K, NH4 , Rb, Cs, and CH3NH3)," *Zeitschrift für Naturforschung A*, vol. 45, pp. 307–312, jan 1990.

[75] K. Yamada, K. Isobe, T. Okuda, and Y. Furukawa, "Successive Phase Transitions and High Ionic Conductivity of Trichlorogermanate (II) Salts as Studied by 35Cl NQR and Powder X-Ray Diffraction," *Zeitschrift für Naturforschung A*, vol. 49, pp. 258–266, jan 1994.

[76] K. Yamada, Y. Kuranaga, K. Ueda, S. Goto, T. Okuda, and Y. Furukawa, "Phase Transition and Electric Conductivity of ASnCl3 (A = Cs and CH3NH3)," *Bulletin of the Chemical Society of Japan*, vol. 71, pp. 127–134, jan 1998.

[77] C. Wagner, "Galvanische Zellen mit festen Elektrolyten mit gemischter Stromleitung," *Zeitschrift für Elektrochemie, Berichte der Bunsengesellschaft für physikalische Chemie*, vol. 60, no. 1, pp. 4–7, 1956.

[78] M. H. Hebb, "Electrical Conductivity of Silver Sulfide," *The Journal of Chemical Physics*, vol. 20, pp. 185–190, jan 1952.

[79] I. Yokota, "On the Theory of Mixed Conduction with Special Reference to Conduction in Silver Sulfide Group Semiconductors," *Journal of the Physical Society of Japan*, vol. 16, no. 11, pp. 2213–2223, 1961.

[80] J. Jamnik and J. Maier, "Transport across Boundary Layers in Ionic Crystals Part I: General Formalism and Conception," *Berichte der Bunsengesellschaft für physikalische Chemie*, vol. 101, no. 1, pp. 23–40, 1997.

[81] I. Riess and A. Leshem, "Odd rectification, hysteresis and quasi switching in solid state devices based on mixed ionic electronic conductors," *Solid State Ionics*, vol. 225, pp. 161–165, 2012.

[82] J. Maier, "Ionic conduction in space charge regions," *Progress in Solid State Chemistry*, vol. 23, no. 3, pp. 171–263, 1995.

[83] C. Eames, J. M. Frost, P. R. F. Barnes, B. C. O'Regan, A. Walsh, and M. S. Islam, "Ionic transport in hybrid lead iodide perovskite solar cells," *Nature Communications*, vol. 6, p. 7497, dec 2015.

[84] J. Haruyama, K. Sodeyama, L. Han, and Y. Tateyama, "First-Principles Study of Ion Diffusion in Perovskite Solar Cell Sensitizers," *Journal of the American Chemical Society*, vol. 137, no. 32, pp. 10048–10051, 2015.

[85] C. Li, S. Tscheuschner, F. Paulus, P. E. Hopkinson, J. Kießling, A. Köhler, Y. Vaynzof, and S. Huettner, "Iodine Migration and its Effect on Hysteresis in Perovskite Solar Cells," *Advanced Materials*, vol. 28, pp. 2446–2454, jan 2016.

[86] C. Besleaga, L. E. Abramiuc, V. Stancu, A. G. Tomulescu, M. Sima, L. Trinca, N. Plugaru, L. Pintilie, G. A. Nemnes, M. Iliescu, H. G. Svavarsson, A. Manolescu, and I. Pintilie, "Iodine Migration and Degradation of Perovskite Solar Cells Enhanced by Metallic Electrodes," *The Journal of Physical Chemistry Letters*, vol. 7, pp. 5168–5175, dec 2016.

[87] M. De Bastiani, G. Dell'Erba, M. Gandini, V. D'Innocenzo, S. Neutzner, A. R. S. Kandada, G. Grancini, M. Binda, M. Prato, J. M. Ball, M. Caironi, and A. Petrozza, "Ion Migration and the Role of Preconditioning Cycles in the Stabilization of the J - V Characteristics of Inverted Hybrid Perovskite Solar Cells," *Advanced Energy Materials*, vol. 6, p. 1501453, jan 2016.

[88] Z. Li, C. Xiao, Y. Yang, S. P. Harvey, D. H. Kim, J. A. Christians, M. Yang, P. Schulz, S. U. Nanayakkara, C.-S. Jiang, J. M. Luther, J. J. Berry, M. C. Beard, M. M. Al-Jassim, and K. Zhu, "Extrinsic ion migration in perovskite solar cells," *Energy & Environmental Science*, vol. 10, no. 5, pp. 1234–1242, 2017.

[89] T. Zhang, X. Meng, Y. Bai, S. Xiao, C. Hu, Y. Yang, H. Chen, S. Yang, D. S. Ginger, S. D. Stranks, F. Huang, K. S. Wong, H. L. Yip, S. Yang, and A. N. Tiwari, "Profiling the organic cation-dependent degradation of organolead halide perovskite solar cells," *J. Mater. Chem. A*, vol. 5, no. 3, pp. 1103–1111, 2017.

[90] K. Domanski, B. Roose, T. Matsui, M. Saliba, S.-H. Turren-Cruz, J.-P. Correa-Baena, C. R. Carmona, G. Richardson, J. M. Foster, F. De Angelis, J. M. Ball, A. Petrozza, N. Mine, M. K. Nazeeruddin, W. Tress, M. Grätzel, U. Steiner, A. Hagfeldt, and A. Abate, "Migration of cations induces reversible performance losses over day/night cycling in perovskite solar cells," *Energy & Environmental Science*, vol. 10, no. 2, pp. 604–613, 2017.

[91] Y. Yuan, Q. Wang, Y. Shao, H. Lu, T. Li, A. Gruverman, and J. Huang, "Electric-Field-Driven Reversible Conversion Between Methylammonium Lead Triiodide Perovskites and Lead Iodide at Elevated Temperatures," *Advanced Energy Materials*, vol. 6, p. 1501803, jan 2016.

[92] Y. Yuan, J. Chae, Y. Shao, Q. Wang, Z. Xiao, A. Centrone, and J. Huang, "Photovoltaic Switching Mechanism in Lateral Structure Hybrid Perovskite Solar Cells," *Advanced Energy Materials*, vol. 5, p. 1500615, aug 2015.

[93] T. Leijtens, E. T. Hoke, G. Grancini, D. J. Slotcavage, G. E. Eperon, J. M. Ball, M. De Bastiani, A. R. Bowring, N. Martino, K. Wojciechowski, M. D. McGehee, H. J. Snaith, and A. Petrozza, "Mapping Electric Field-Induced Switchable Poling and Structural Degradation in Hybrid Lead Halide Perovskite Thin Films," *Advanced Energy Materials*, vol. 5, p. 1500962, oct 2015.

[94] D. A. Jacobs, Y. Wu, H. Shen, C. Barugkin, F. J. Beck, T. P. White, K. Weber, K. R. Catchpole, H. J. Snaith, G. Hodes, D. Cahen, and S. V. Reenen, "Hysteresis phenomena in perovskite solar cells: the many and varied effects of ionic accumulation," *Phys. Chem. Chem. Phys.*, vol. 19, no. 4, pp. 3094–3103, 2017.

[95] L. Contreras, J. A. Idígoras, A. Todinova, M. Salado, S. Kazim, S. Ahmad, and J. Anta, "Specific Cation Interactions as the Cause of Slow Dynamics

and Hysteresis in Dye and Perovskite Solar Cells: a Small-Perturbation Study," *Phys. Chem. Chem. Phys.*, vol. 18, pp. 31033–31042, 2016.

[96] G. Gregori, T.-Y. Yang, A. Senocrate, M. Grätzel, and J. Maier, "Ionic Conductivity of OrganicInorganic Perovskites: Relevance for Long-Time and Low Frequency Behavior," in *Organic-Inorganic Halide Perovskite Photovoltaics* (N.-G. Park, M. Grätzel, and T. Miyasaka, eds.), ch. 5, pp. 107–135, Springer International Publishing, 2016.

[97] J. Berry, T. Buonassisi, D. A. Egger, G. Hodes, L. Kronik, Y.-L. Loo, I. Lubomirsky, S. R. Marder, Y. Mastai, J. S. Miller, D. B. Mitzi, Y. Paz, A. M. Rappe, I. Riess, B. Rybtchinski, O. Stafsudd, V. Stevanovic, M. F. Toney, D. Zitoun, A. Kahn, D. Ginley, and D. Cahen, "Hybrid Organic-Inorganic Perovskites (HOIPs): Opportunities and Challenges," *Advanced Materials*, vol. 27, pp. 5102–5112, sep 2015.

[98] J. Maier, *Physical Chemistry of Ionic Materials*. Chichester, UK: John Wiley & Sons, Ltd, apr 2004.

[99] C. P. Slichter, *Principles of Magnetic Resonance*. Springer-Verlag Berlin Heidelberg, 1990.

[100] A. Abragam, *The principles of nuclear magnetism*. Oxford University Press, 1961.

[101] V. I. Bakhmutov, *Solid State NMR in Materials Science*. CRC Press, 2011.

[102] K. J. MacKenzie and M. E. Smith, "Multinuclear Solid-State NMR of Inorganic Materials," in *Multinuclear Solid-State NMR of Inorganic Materials* (K. J. D. MacKenzie and M. E. Smith, eds.), vol. 6 of *Pergamon Materials Series*, Pergamon, 2002.

[103] A. J. Vega, "Quadrupolar Nuclei in Solids," in *Encyclopedia of Magnetic Resonance*, Chichester, UK: John Wiley & Sons, Ltd, mar 2010.

[104] L. A. O'Dell and C. I. Ratcliffe, "Quadrupolar NMR to Investigate Dynamics in Solid Materials," in *eMagRes* (R. K. Harris and R. L. Wasylishen, eds.), pp. 1–16, Chichester, UK: John Wiley & Sons, Ltd, mar 1996.

[105] J. S. Waugh and E. I. Fedin, "Determination of the hindered-rotation barriers in solids," *Sov. Phys. Solid State*, vol. 4, p. 1633, 1963.

[106] J. Crank, *The Mathematics of Diffusion*. Oxford University Press, 1975.

[107] G. E. Eperon, C. E. Beck, and H. J. Snaith, "Cation exchange for thin film lead iodide perovskite interconversion," *Materials Horizons*, vol. 3, no. 1, pp. 63–71, 2016.

[108] A. P. Lingras and G. Simkovich, "Electrochemical studies on lead iodide," *Solid State Communications*, vol. 27, no. 4, pp. iii–iv, 1978.

[109] B. Dunn, R. Ostrom, R. Seevers, and G. Farrington, "Divalent cation conductivity in beta alumina," *Solid State Ionics*, vol. 5, pp. 203–204, oct 1981.

[110] J. M. Azpiroz, E. Mosconi, J. Bisquert, and F. De Angelis, "Defect migration in methylammonium lead iodide and its role in perovskite solar cell operation," *Energy Environmental Science*, vol. 8, no. 7, pp. 2118–2127, 2015.

[111] W.-J. Yin, T. Shi, and Y. Yan, "Unusual defect physics in CH3NH3PbI3 perovskite solar cell absorber," *Applied Physics Letters*, vol. 104, p. 063903, feb 2014.

[112] J. Kim, S.-H. Lee, J. H. Lee, and K.-H. Hong, "The Role of Intrinsic Defects in Methylammonium Lead Iodide Perovskite," *The Journal of Physical Chemistry Letters*, vol. 5, no. 8, pp. 1312–1317, 2014.

[113] A. Senocrate, T.-Y. Yang, G. Gregori, G. Y. Kim, M. Grätzel, and J. Maier, "Charge carrier chemistry in methylammonium lead iodide," *Solid State Ionics*, vol. 321, pp. 69–74, aug 2018.

[114] F. A. Kröger, *The Chemistry of Imperfect Crystals*. Amsterdam: North-Holland Publishing Company, 1964.

[115] P. Kofstad, *Nonstoichiometry, diffusion, and electrical conductivity in binary metal oxides*. WILEY-VCH Verlag, 1972.

[116] A. Buin, P. Pietsch, J. Xu, O. Voznyy, A. H. Ip, R. Comin, and E. H. Sargent, "Materials Processing Routes to Trap-Free Halide Perovskites," *Nano Letters*, vol. 14, no. 11, pp. 6281–6286, 2014.

[117] A. Walsh, D. O. Scanlon, S. Chen, X. G. Gong, and S.-H. Wei, "Self-Regulation Mechanism for Charged Point Defects in Hybrid Halide Perovskites," *Angewandte Chemie International Edition*, vol. 54, no. 6, pp. 1791–1794, 2015.

[118] J. Maier, "Mass Transport in the Presence of Internal Defect Reactions-Concept of Conservative Ensembles: III, Trapping Effect of Dopants

on Chemical Diffusion," *Journal of the American Ceramic Society*, vol. 76, pp. 1223–1227, may 1993.

[119] C. C. Stoumpos, C. D. Malliakas, and M. G. Kanatzidis, "Semiconducting Tin and Lead Iodide Perovskites with Organic Cations: Phase Transitions, High Mobilities, and Near-Infrared Photoluminescent Properties," *Inorganic Chemistry*, vol. 52, no. 15, pp. 9019–9038, 2013.

[120] R. D. Shannon, "Revised effective ionic radii and systematic studies of interatomic distances in halides and chalcogenides," *Acta Crystallographica Section A*, vol. 32, pp. 751–767, sep 1976.

[121] G. Y. Kim, A. Senocrate, T.-Y. Yang, G. Gregori, M. Grätzel, and J. Maier, "Large tunable photoeffect on ion conduction in halide perovskites and implications for photo-decomposition," *Nature Materials - in press*, 2018.

[122] A. Senocrate, I. Moudrakovski, T. Acartürk, R. Merkle, G. Y. Kim, U. Starke, M. Grätzel, and J. Maier, "Slow CH 3 NH 3 + Diffusion in CH 3 NH 3 PbI 3 under Light Measured by Solid-State NMR and Tracer Diffusion," *The Journal of Physical Chemistry C*, vol. 122, pp. 21803–21806, sep 2018.

[123] E. L. Unger, E. T. Hoke, C. D. Bailie, W. H. Nguyen, A. R. Bowring, T. Heumüller, M. G. Christoforo, and M. D. McGehee, "Hysteresis and transient behavior in currentvoltage measurements of hybrid-perovskite absorber solar cells," *Energy Environmental Science*, vol. 7, no. 11, pp. 3690–3698, 2014.

[124] Y. Zhang, M. Liu, G. E. Eperon, T. C. Leijtens, D. McMeekin, M. Saliba, W. Zhang, M. de Bastiani, A. Petrozza, L. M. Herz, M. B. Johnston, H. Lin, and H. J. Snaith, "Charge selective contacts, mobile ions and anomalous hysteresis in organic-inorganic perovskite solar cells," *Mater. Horiz.*, vol. 2, no. 3, pp. 315–322, 2015.

[125] R. S. Sanchez, V. Gonzalez-Pedro, J.-W. Lee, N.-G. Park, Y. S. Kang, I. Mora-Sero, and J. Bisquert, "Slow Dynamic Processes in Lead Halide Perovskite Solar Cells. Characteristic Times and Hysteresis," *The Journal of Physical Chemistry Letters*, vol. 5, pp. 2357–2363, jul 2014.

[126] Y. Zhao, C. Liang, H. min Zhang, D. Li, D. Tian, G. Li, X. Jing, W. Zhang, W. Xiao, Q. Liu, F. Zhang, and Z. He, "Anomalously large interface charge in polarity-switchable photovoltaic devices: an indication of mobile ions in

organic-inorganic halide perovskites," *Energy Environmental Science*, vol. 8, no. 4, pp. 1256–1260, 2015.

[127] P. Calado, A. M. Telford, D. Bryant, X. Li, J. Nelson, B. C. O'Regan, and P. R. Barnes, "Evidence for ion migration in hybrid perovskite solar cells with minimal hysteresis," *Nature Communications*, vol. 7, p. 13831, dec 2016.

[128] Y. Zhao, W. Zhou, W. Ma, S. Meng, H. Li, J. Wei, R. Fu, K. Liu, D. Yu, and Q. Zhao, "Correlations between Immobilizing Ions and Suppressing Hysteresis in Perovskite Solar Cells," *ACS Energy Letters*, vol. 1, pp. 266–272, jul 2016.

[129] G. Richardson, S. O'Kane, R. G. Niemann, T. Peltola, J. M. Foster, P. J. Cameron, and A. Walker, "Can slow-moving ions explain hysteresis in the current-voltage curves of perovskite solar cells?," *Energy Environmental Science*, feb 2016.

[130] F. Sabeth, T. Iimori, and N. Ohta, "Gigantic Photoresponse and Reversible Photoswitching in Ionic Conductivity of Polycrystalline β-AgI," *The Journal of Physical Chemistry C*, vol. 116, no. 16, pp. 9209–9213, 2012.

[131] J. Xing, Q. Wang, Q. Dong, Y. Yuan, Y. Fang, and J. Huang, "Ultrafast ion migration in hybrid perovskite polycrystalline thin films under light and suppression in single crystals," *Physical Chemistry Chemical Physics*, vol. 18, no. 44, pp. 30484–30490, 2016.

[132] Y.-C. Zhao, W.-K. Zhou, X. Zhou, K. Liu, D. Yu, and Q. Zhao, "Quantification of light-enhanced ionic transport in lead iodide perovskite thin films and its solar cell applications," *Light: Science & Applications*, vol. 6, p. e16243, oct 2016.

[133] H. Rickert, *Electrochemistry of Solids*, vol. 7 of *Inorganic Chemistry Concepts*. Berlin, Heidelberg: Springer Berlin Heidelberg, 1982.

[134] M. Kubicek, G. M. Rupp, S. Huber, A. Penn, A. K. Opitz, J. Bernardi, M. Stöger-Pollach, H. Hutter, and J. Fleig, "Cation diffusion in Lao.6Sro.4CoO3δ below 800 C and its relevance for Sr segregation," *Physical Chemistry Chemical Physics*, vol. 16, no. 6, p. 2715, 2014.

[135] N. Čebašek, R. Haugsrud, Z. Li, and T. Norby, "Determination of Chemical Tracer Diffusion Coefficients for the La- and Ni-site in La2NiO4+δ Studied by SIMS," *Journal of the American Ceramic Society*, vol. 96, pp. 598–605, dec 2013.

[136] N. Čebašek, R. Haugsrud, and T. Norby, "Determination of inter-diffusion coefficients for the A- and B-site in the A2BO4+δ (A = La, Nd and B = Ni, Cu) system," *Solid State Ionics*, vol. 231, pp. 74–80, 2013.

[137] R. Sažinas, I. Sakaguchi, M.-A. Einarsrud, and T. Grande, "134Ba diffusion in polycrystalline BaMO3(M = Ti, Zr, Ce)," *AIP Advances*, vol. 7, no. 11, 2017.

[138] R. Sažinas, I. Sakaguchi, M.-a. Einarsrud, and T. Grande, "96Zr Tracer Diffusion in AZrO3 (A = Ca, Sr, Ba)," *Inorganics*, vol. 6, p. 14, jan 2018.

[139] W. Geng, L. Zhang, Y. N. Zhang, W. M. Lau, and L. M. Liu, "First-principles study of lead iodide perovskite tetragonal and orthorhombic phases for photovoltaics," *Journal of Physical Chemistry C*, vol. 118, no. 34, pp. 19565–19571, 2014.

[140] W. J. Yin, T. Shi, and Y. Yan, "Unique properties of halide perovskites as possible origins of the superior solar cell performance," *Advanced Materials*, vol. 26, no. 27, pp. 4653–4658, 2014.

[141] R. B. Murray and F. J. Keller, "Vk Centers and Recombination Luminescence in Rubidium Iodide and Sodium Iodide," *Physical Review*, vol. 153, pp. 993–1000, jan 1967.

[142] D. J. Wilson, A. A. Sokol, S. A. French, and C. R. A. Catlow, "Defect structures in the silver halides," *Physical Review B*, vol. 77, p. 064115, feb 2008.

[143] T. Brudevoll and E. Kotomin, "Interstitial-oxygen-atom diffusion in MgO," *Physical Review B - Condensed Matter and Materials Physics*, vol. 53, no. 12, pp. 7731–7735, 1996.

[144] A. I. Popov, E. A. Kotomin, and J. Maier, "Analysis of self-trapped hole mobility in alkali halides and metal halides," *Solid State Ionics*, vol. 302, pp. 3–6, apr 2017.

[145] S. Loftager, P. García-Fernández, J. A. Aramburu, M. Moreno, and J. M. Garcia-Lastra, "Stability and Polaronic Motion of Self-Trapped Holes in Silver Halides: Insight through DFT+U Calculations," *The Journal of Physical Chemistry C*, vol. 120, pp. 8509–8524, apr 2016.

[146] M. H. Du, "Efficient carrier transport in halide perovskites: theoretical perspectives," *J. Mater. Chem. A*, vol. 2, no. 24, pp. 9091–9098, 2014.

[147] L. D. Whalley, R. Crespo-Otero, and A. Walsh, "H-Center and V-Center Defects in Hybrid Halide Perovskites," *ACS Energy Letters*, pp. 2713–2714, 2017.

[148] W. Li, J. Liu, F. Q. Bai, H. X. Zhang, and O. V. Prezhdo, "Hole Trapping by Iodine Interstitial Defects Decreases Free Carrier Losses in Perovskite Solar Cells: A Time-Domain Ab Initio Study," *ACS Energy Letters*, vol. 2, no. 6, pp. 1270–1278, 2017.

[149] J. L. Minns, P. Zajdel, D. Chernyshov, W. van Beek, and M. A. Green, "Structure and interstitial iodide migration in hybrid perovskite methylammonium lead iodide," *Nature Communications*, vol. 8, p. 15152, may 2017.

[150] U. B. Cappel, S. Svanström, V. Lanzilotto, F. O. L. Johansson, K. Aitola, B. Philippe, E. Giangrisostomi, R. Ovsyannikov, T. Leitner, A. Föhlisch, S. Svensson, N. Mårtensson, G. Boschloo, A. Lindblad, and H. Rensmo, "Partially Reversible Photoinduced Chemical Changes in a Mixed-Ion Perovskite Material for Solar Cells," *ACS Applied Materials & Interfaces*, vol. 9, pp. 34970–34978, oct 2017.

[151] E. J. Juarez-Perez, L. K. Ono, M. Maeda, Y. Jiang, Z. Hawash, and Y. Qi, "Photodecomposition and thermal decomposition in methylammonium halide lead perovskites and inferred design principles to increase photovoltaic device stability," *Journal of Materials Chemistry A*, vol. 6, no. 20, pp. 9604–9612, 2018.

[152] J. Maier, "Mass Transport in the Presence of Internal Defect Reactions-Concept of Conservative Ensembles: I, Chemical Diffusion in Pure Compounds," *Journal of the American Ceramic Society*, vol. 76, pp. 1212–1217, may 1993.

[153] A. Senocrate, T. Acartürk, G. Y. Kim, R. Merkle, U. Starke, M. Grätzel, and J. Maier, "Interaction of oxygen with halide perovskites," *Journal of Materials Chemistry A*, vol. 6, no. 23, pp. 10847–10855, 2018.

[154] Y. Tian, M. Peter, E. Unger, M. A. Abdellah, K. Zheng, T. Pullerits, A. P. Yartsev, V. Sundström, and I. G. Scheblykin, "Mechanistic insights into perovskite photoluminescence enhancement: light curing with oxygen can boost yield thousandfold," *Physical Chemistry Chemical Physics*, vol. 17, no. 38, pp. 24978–24987, 2015.

[155] J. F. Galisteo-López, Y. Li, and H. Míguez, "Three-Dimensional Optical Tomography and Correlated Elemental Analysis of Hybrid Perovskite Microstructures: An Insight into Defect-Related Lattice Distortion and Photoinduced Ion Migration," *Journal of Physical Chemistry Letters*, vol. 7, pp. 5227–5234, dec 2016.

[156] R. Brenes, D. Guo, A. Osherov, N. K. Noel, C. Eames, E. M. Hutter, S. K. Pathak, F. Niroui, R. H. Friend, M. S. Islam, H. J. Snaith, V. Bulović, T. J. Savenije, and S. D. Stranks, "Metal Halide Perovskite Polycrystalline Films Exhibiting Properties of Single Crystals," *Joule*, vol. 1, no. 1, pp. 155–167, 2017.

[157] M. Manceau, S. Chambon, A. Rivaton, J.-L. Gardette, S. Guillerez, and N. Lemaître, "Effects of long-term UVvisible light irradiation in the absence of oxygen on P3HT and P3HT:PCBM blend," *Solar Energy Materials and Solar Cells*, vol. 94, pp. 1572–1577, oct 2010.

[158] M. Hermenau, M. Riede, K. Leo, S. A. Gevorgyan, F. C. Krebs, and K. Norrman, "Water and oxygen induced degradation of small molecule organic solar cells," *Solar Energy Materials and Solar Cells*, vol. 95, no. 5, pp. 1268–1277, 2011.

[159] F. C. Krebs and K. Norrman, "Analysis of the failure mechanism for a stable organic photovoltaic during 10 000 h of testing," *Progress in Photovoltaics: Research and Applications*, vol. 15, pp. 697–712, dec 2007.

[160] M. O. Reese, A. M. Nardes, B. L. Rupert, R. E. Larsen, D. C. Olson, M. T. Lloyd, S. E. Shaheen, D. S. Ginley, G. Rumbles, and N. Kopidakis, "Photoinduced degradation of polymer and polymer-fullerene active layers: Experiment and theory," *Advanced Functional Materials*, vol. 20, pp. 3476–3483, oct 2010.

[161] A. Seemann, H. J. Egelhaaf, C. J. Brabec, and J. A. Hauch, "Influence of oxygen on semi-transparent organic solar cells with gas permeable electrodes," *Organic Electronics: physics, materials, applications*, vol. 10, no. 8, pp. 1424–1428, 2009.

[162] R. Merkle, R. A. De Souza, and J. Maier, "Optically Tuning the Rate of Stoichiometry Changes: Surface-Controlled Oxygen Incorporation into Oxides under UV Irradiation," *Angewandte Chemie International Edition*, vol. 40, pp. 2126–2129, jun 2001.

[163] S. Wang, Y. Jiang, E. J. Juarez-Perez, L. K. Ono, and Y. Qi, "Accelerated degradation of methylammonium lead iodide perovskites induced by exposure to iodine vapour," *Nature Energy*, vol. 2, p. 16195, dec 2016.

[164] H. Zhu, K. Miyata, Y. Fu, J. Wang, P. P. Joshi, D. Niesner, K. W. Williams, S. Jin, and X.-Y. Zhu, "Screening in crystalline liquids protects energetic carriers in hybrid perovskites," *Science*, vol. 353, no. 6306, pp. 1409–1413, 2016.

[165] D. Niesner, H. Zhu, K. Miyata, P. P. Joshi, T. J. Evans, B. J. Kudisch, M. T. Trinh, M. Marks, and X. Y. Zhu, "Persistent Energetic Electrons in Methylammonium Lead Iodide Perovskite Thin Films," *Journal of the American Chemical Society*, vol. 138, no. 48, pp. 15717–15726, 2016.

[166] R. Merkle and J. Maier, "How Is Oxygen Incorporated into Oxides? A Comprehensive Kinetic Study of a Simple Solid-State Reaction with SrTiO3 as a Model Material," *Angewandte Chemie International Edition*, vol. 47, pp. 3874–3894, may 2008.

[167] E. T. Hoke, D. J. Slotcavage, E. R. Dohner, A. R. Bowring, H. I. Karunadasa, and M. D. McGehee, "Reversible photo-induced trap formation in mixed-halide hybrid perovskites for photovoltaics," *Chemical Science*, vol. 6, no. 1, pp. 613–617, 2015.

[168] CAS-SciFinder, "pKb value for Methylamine and Formamidine."

[169] D. J. Kubicki, D. Prochowicz, A. Hofstetter, P. Péchy, S. M. Zakeeruddin, M. Grätzel, and L. Emsley, "Cation Dynamics in Mixed-Cation (MA)x(FA)1xPbI3 Hybrid Perovskites from Solid-State NMR," *Journal of the American Chemical Society*, vol. 139, pp. 10055–10061, jun 2017.

[170] G. P. Nagabhushana, R. Shivaramaiah, and A. Navrotsky, "Direct calorimetric verification of thermodynamic instability of lead halide hybrid perovskites.," *Proceedings of the National Academy of Sciences of the United States of America*, vol. 113, pp. 7717–7721, jul 2016.

[171] I. Ivanov, A. Steparuk, M. Bolyachkina, D. Tsvetkov, A. Safronov, and A. Zuev, "Thermodynamics of formation of hybrid perovskite-type methylammonium lead halides," *The Journal of Chemical Thermodynamics*, vol. 116, pp. 253–258, jan 2018.

[172] N. Onoda-Yamamuro, T. Matsuo, and H. Suga, "Calorimetric and IR spectroscopic studies of phase transitions in methylammonium trihalogenoplumbates (II)," *Journal of Physics and Chemistry of Solids*, vol. 51, no. 12, pp. 1383–1395, 1990.

[173] D. Prochowicz, M. Franckevičius, A. M. Cieślak, S. M. Zakeeruddin, M. Grätzel, and J. Lewiński, "Mechanosynthesis of the hybrid perovskite $CH_3NH_3PbI_3$: characterization and the corresponding solar cell efficiency," *J. Mater. Chem. A*, vol. 3, no. 41, pp. 20772–20777, 2015.

[174] K. V. Manukyan, A. V. Yeghishyan, D. O. Moskovskikh, J. Kapaldo, A. Mintairov, and A. S. Mukasyan, "Mechanochemical synthesis of methylammonium lead iodide perovskite," *Journal of Materials Science*, vol. 51, no. 19, pp. 9123–9130, 2016.

[175] S. Yang, Y. C. Zheng, Y. Hou, X. Chen, Y. Chen, Y. Wang, H. Zhao, and H. G. Yang, "Formation mechanism of freestanding $CH_3NH_3PbI_3$ functional crystals: In situ transformation vs dissolution-crystallization," *Chemistry of Materials*, vol. 26, no. 23, pp. 6705–6710, 2014.

[176] N. J. Jeon, J. H. Noh, Y. C. Kim, W. S. Yang, S. Ryu, and S. I. Seok, "Solvent engineering for high-performance inorganic-organic hybrid perovskite solar cells," *Nature Materials*, vol. 13, no. 9, pp. 897–903, 2014.

[177] N. Ahn, D. Y. Son, I. H. Jang, S. M. Kang, M. Choi, and N. G. Park, "Highly Reproducible Perovskite Solar Cells with Average Efficiency of 18.3% and Best Efficiency of 19.7% Fabricated via Lewis Base Adduct of Lead(II) Iodide," *Journal of the American Chemical Society*, vol. 137, no. 27, pp. 8696–8699, 2015.

[178] A. Latini, G. Gigli, and A. Ciccioli, "A study on the nature of the thermal decomposition of methylammonium lead iodide perovskite, $CH_3NH_3PbI_3$: an attempt to rationalise contradictory experimental results," *Sustainable Energy & Fuels*, vol. 1, no. 6, pp. 1351–1357, 2017.

[179] E. J. Juarez-Perez, Z. Hawash, S. R. Raga, L. K. Ono, and Y. Qi, "Thermal degradation of $CH_3NH_3PbI_3$ perovskite into NH_3 and CH_3I gases observed by coupled thermogravimetrymass spectrometry analysis," *Energy & Environmental Science*, vol. 9, no. 11, pp. 3406–3410, 2016.

[180] R. J. Huang, K. Seitz, T. Neary, C. D. O'Dowd, U. Platt, and T. Hoffmann, "Observations of high concentrations of I_2 and IO in coastal air supporting

iodine-oxide driven coastal new particle formation," *Geophysical Research Letters*, vol. 37, no. 3, pp. 1–5, 2010.

[181] A. Saiz-Lopez, J. M. Plane, A. R. Baker, L. J. Carpenter, R. Von Glasow, J. C. Gómez Martín, G. McFiggans, and R. W. Saunders, "Atmospheric chemistry of iodine," *Chemical Reviews*, vol. 112, no. 3, pp. 1773–1804, 2012.

[182] A. Senocrate, I. Moudrakovski, and J. Maier, "Short-range ion dynamics in methylammonium lead iodide by multinuclear solid state NMR and 127 I NQR," *Physical Chemistry Chemical Physics*, vol. 20, no. 30, pp. 20043–20055, 2018.

[183] M. J. Duer, *Introduction to Solid-State NMR Spectroscopy*. Oxford: Blackweell Publishing, 2004.

[184] J. Ma and L.-W. Wang, "The Nature of Electron Mobility in Hybrid Perovskite CH3NH3PbI3," *Nano Letters*, vol. 17, pp. 3646–3654, jun 2017.

[185] C. Motta, F. El-Mellouhi, S. Kais, N. Tabet, F. Alharbi, and S. Sanvito, "Revealing the role of organic cations in hybrid halide perovskite CH3NH3PbI3," *Nature Communications*, vol. 6, p. 7026, dec 2015.

[186] J. Gong, M. Yang, X. Ma, R. D. Schaller, G. Liu, L. Kong, Y. Yang, M. C. Beard, M. Lesslie, Y. Dai, B. Huang, K. Zhu, and T. Xu, "Electron-Rotor Interaction in Organic-Inorganic Lead Iodide Perovskites Discovered by Isotope Effects," *The Journal of Physical Chemistry Letters*, vol. 7, pp. 2879–2887, aug 2016.

[187] A. Amat, E. Mosconi, E. Ronca, C. Quarti, P. Umari, M. K. Nazeeruddin, M. Grätzel, and F. De Angelis, "Cation-Induced Band-Gap Tuning in Organohalide Perovskites: Interplay of Spin-Orbit Coupling and Octahedra Tilting," *Nano Letters*, vol. 14, no. 6, pp. 3608–3616, 2014.

[188] C. Quarti, G. Grancini, E. Mosconi, P. Bruno, J. M. Ball, M. M. Lee, H. J. Snaith, A. Petrozza, and F. De Angelis, "The Raman Spectrum of the CH3NH3PbI3 Hybrid Perovskite: Interplay of Theory and Experiment," *The Journal of Physical Chemistry Letters*, vol. 5, pp. 279–284, jan 2014.

[189] J. H. Lee, J.-H. Lee, E.-H. Kong, and H. M. Jang, "The nature of hydrogen-bonding interaction in the prototypic hybrid halide perovskite, tetragonal CH3NH3PbI3," *Scientific Reports*, vol. 6, p. 21687, apr 2016.

[190] E. Mosconi, A. Amat, M. K. Nazeeruddin, M. Grätzel, and F. De Angelis, "First-Principles Modeling of Mixed Halide Organometal Perovskites for Photovoltaic Applications," *The Journal of Physical Chemistry C*, vol. 117, pp. 13902–13913, jul 2013.

[191] R. E. Wasylishen, O. Knop, and J. B. Macdonald, "Cation rotation in methylammonium lead halides," *Solid State Communications*, vol. 56, pp. 581–582, nov 1985.

[192] Y. Furukawa and D. Nakamura, "Cation Dynamics in the Crystalline Phases of (CH3NH3)PbX3 (X: Cl, Br) as Studied by Proton Magnetic Resonance Techniques," *Z. Naturforsch*, vol. 44a, no. 1989, pp. 1122–1126, 1989.

[193] O. Knop, R. E. Wasylishen, M. A. White, T. S. Cameron, and M. J. M. Van Oort, "Alkylammonium lead halides. Part 2. CH3NH3PbX3 (X = Cl, Br, I) perovskites: cuboctahedral halide cages with isotropic cation reorientation," *Canadian Journal of Chemistry*, vol. 68, pp. 412–422, mar 1990.

[194] Q. Xu, T. Eguchi, H. Nakayama, N. Nakamura, and M. Kishita, "Molecular Motions and Phase Transitions in Solid CH3NH3PbX3 (X = Cl, Br, I) as Studied by NMR and NQR," *Zeitschrift für Naturforschung A*, vol. 46, pp. 240–246, jan 1991.

[195] A. Poglitsch and D. Weber, "Dynamic disorder in methylammoniumtrihalogenoplumbates (II) observed by millimeterwave spectroscopy," *The Journal of Chemical Physics*, vol. 87, no. 11, 1987.

[196] T. Baikie, N. S. Barrow, Y. Fang, P. J. Keenan, P. R. Slater, R. O. Piltz, M. Gutmann, S. G. Mhaisalkar, and T. J. White, "A combined single crystal neutron/X-ray diffraction and solid-state nuclear magnetic resonance study of the hybrid perovskites CH3NH3PbX3 (X = I, Br and Cl)," *Journal of Materials Chemistry A*, vol. 3, no. 17, pp. 9298–9307, 2015.

[197] G. M. Bernard, R. E. Wasylishen, C. I. Ratcliffe, V. Terskikh, Q. Wu, J. M. Buriak, and T. Hauger, "Methylammonium Cation Dynamics in Methylammonium Lead Halide Perovskites: A Solid-State NMR Perspective," *The Journal of Physical Chemistry A*, vol. 122, no. 6, pp. 1560–1573, 2018.

[198] W. M. J. Franssen, S. G. D. van Es, R. Derviolu, G. A. de Wijs, and A. P. M. Kentgens, "Symmetry, Dynamics, and Defects in Methylammonium Lead Halide Perovskites," *The Journal of Physical Chemistry Letters*, vol. 8, pp. 61–66, jan 2017.

[199] C. Roiland, G. Trippé-Allard, K. Jemli, B. Alonso, J.-C. Ameline, R. Gautier, T. Bataille, L. Le Pollès, E. Deleporte, J. Even, and C. Katan, "Multinuclear NMR as a tool for studying local order and dynamics in CH3NH3PbX3 (X = Cl, Br, I) hybrid perovskites," *Physical Chemistry Chemical Physics*, vol. 18, no. 39, pp. 27133–27142, 2016.

[200] A. M. Askar, G. M. Bernard, B. Wiltshire, K. Shankar, and V. K. Michaelis, "Multinuclear Magnetic Resonance Tracking of Hydro, Thermal, and Hydrothermal Decomposition of CH3NH3PbI3," *The Journal of Physical Chemistry C*, vol. 121, pp. 1013–1024, jan 2017.

[201] D. J. Kubicki, D. Prochowicz, A. Hofstetter, S. M. Zakeeruddin, M. Grätzel, and L. Emsley, "Phase Segregation in Cs-, Rb- and K-Doped Mixed-Cation (MA)x(FA)1-xPbI3 Hybrid Perovskites from Solid-State NMR," *Journal of the American Chemical Society*, vol. 139, no. 40, pp. 14173–14180, 2017.

[202] A. M. Gil and E. Alberti, "The effect of Magic Angle Spinning on proton spin-lattice relaxation times in some organic solids," *Solid State Nuclear Magnetic Resonance*, vol. 11, pp. 203–209, jun 1998.

[203] S. Hayashi, "Effects of magic-angle spinning on spin-lattice relaxations in talc," *Solid State Nuclear Magnetic Resonance*, vol. 3, pp. 323–330, nov 1994.

[204] J. Tsau and D. F. R. Gilson, "Nuclear magnetic resonance studies of solid methylammonium halides," *Canadian Journal of Chemistry*, vol. 48, no. 5, pp. 717–722, 1970.

[205] E. R. Andrew and P. C. Canepa, "A proton magnetic resonance investigation of solid mono-, di-, tri- and tetra-methylammonium chlorides," *Journal of Magnetic Resonance (1969)*, vol. 7, no. 4, pp. 429–441, 1972.

[206] E. R. Andrew and J. Lipofsky, "The Second Moment of the Motionally Narrowed NMR Spectrum of a Solid," *J. Magn. Reson.*, vol. 8, pp. 217–221, 1972.

[207] S. Albert and J. A. Ripmeester, "Resolution of motions in the three solid phases of methylammonium chloride (CH3NH3Cl) by NMR," *The Journal of Chemical Physics*, vol. 58, pp. 541–548, jan 1973.

[208] H. S. Gutowsky and G. E. Pake, "Structural Investigations by Means of Nuclear Magnetism. II. Hindered Rotation in Solids," *The Journal of Chemical Physics*, vol. 18, no. 2, pp. 162–170, 1950.

[209] J. G. Powles and H. S. Gutowsky, "Proton Magnetic Resonance of the CH_3 Group. II. Solid Solutions of t-Butyl Chloride in Carbon Tetrachloride," *The Journal of Chemical Physics*, vol. 21, pp. 1704–1709, oct 1953.

[210] A. M. A. Leguy, J. M. Frost, A. P. McMahon, V. G. Sakai, W. Kochelmann, C. Law, X. Li, F. Foglia, A. Walsh, B. C. O'Regan, J. Nelson, J. T. Cabral, and P. R. F. Barnes, "The dynamics of methylammonium ions in hybrid organic-inorganic perovskite solar cells," *Nature Communications*, vol. 6, no. May, p. 7124, 2015.

[211] E. R. Andrew and R. Bersohn, "Nuclear Magnetic Resonance Line Shape for a Triangular Configuration of Nuclei," *The Journal of Chemical Physics*, vol. 18, no. 2, pp. 159–161, 1950.

[212] N. Bloembergen, E. M. Purcell, and R. V. Pound, "Relaxation effects in nuclear magnetic resonance absorption," *Physical Review*, vol. 73, pp. 679–712, apr 1948.

[213] A. M. Panich, N. A. Sergeev, and M. Olszewski, "Effect of magic angle spinning on 13C spin-lattice and spin-spin relaxation in nanodiamonds," *Journal of Physics: Condensed Matter*, vol. 27, no. 36, p. 365302, 2015.

[214] R. Ikeda and C. A. McDowell, "Spin-rotational relaxation for protons in solid, NH_4 ClO_4," *Chemical Physics Letters*, vol. 14, no. 4, pp. 389–392, 1972.

[215] V. I. Bakhmutov, *Practical NMR Relaxation for Chemists*. Chichester, UK: John Wiley & Sons, Ltd, nov 2004.

[216] J. L. Sudmeier, S. E. Anderson, and J. S. Frye, "Calculation of Nuclear Spin Relaxation Times," *Concepts in Magnetic Resonance*, vol. 2, pp. 197–212, oct 1990.

[217] A. A. Shmyreva, M. Safdari, I. Furó, and S. V. Dvinskikh, "NMR longitudinal relaxation enhancement in metal halides by heteronuclear polarization exchange during magic-angle spinning," *Journal of Chemical Physics*, vol. 144, p. 224201, jun 2016.

[218] G. M. Bernard, A. Goyal, M. Miskolzie, R. McKay, Q. Wu, R. E. Wasylishen, and V. K. Michaelis, "Methylammonium lead chloride: A sensitive sample for an accurate NMR thermometer," *Journal of Magnetic Resonance*, vol. 283, pp. 14–21, 2017.

[219] T. Mildner, H. Ernst, and D. Freude, "207Pb NMR detection of spinning-induced temperature gradients in MAS rotors," *Solid State Nuclear Magnetic Resonance*, vol. 5, no. 3, pp. 269–271, 1995.

[220] L. C. M. van Gorkom, J. M. Hook, M. B. Logan, J. V. Hanna, and R. E. Wasylishen, "Solid-state lead-207 NMR of lead(II) nitrate: Localized heating effects at high magic angle spinning speeds," *Magnetic Resonance in Chemistry*, vol. 33, no. 10, pp. 791–795, 1995.

[221] T. Takahashi, H. Kawashima, H. Sugisawa, and T. Baba, "207Pb chemical shift thermometer at high temperature for magic angle spinning experiments," *Solid State Nuclear Magnetic Resonance*, vol. 15, no. 2, pp. 119–123, 1999.

[222] P. A. Beckmann and C. Dybowski, "A Thermometer for Nonspinning Solid-State NMR Spectroscopy," *Journal of Magnetic Resonance*, vol. 146, no. 2, pp. 379–380, 2000.

[223] P. Pyykko, "Year-2008 nuclear quadrupole moments," *Molecular Physics*, vol. 106, no. 16-18, pp. 1965–1974, 2008.

[224] D. L. Bryce, C. M. Widdifield, R. P. Chapman, and R. J. Attrell, "Chlorine, Bromine, and Iodine Solid-State NMR," in *eMagRes*, John Wiley & Sons, Ltd, 2007.

[225] F. Brivio, J. M. Frost, J. M. Skelton, A. J. Jackson, O. J. Weber, M. T. Weller, A. R. Goñi, A. M. A. Leguy, P. R. F. Barnes, and A. Walsh, "Lattice dynamics and vibrational spectra of the orthorhombic, tetragonal, and cubic phases of methylammonium lead iodide," *Physical Review B*, vol. 92, p. 144308, oct 2015.

[226] T. Hata, G. Giorgi, and K. Yamashita, "The Effects of the Organic-Inorganic Interactions on the Thermal Transport Properties of CH3NH3PbI3," *Nano Letters*, vol. 16, no. 4, pp. 2749–2753, 2016.

[227] M. I. Saidaminov, A. L. Abdelhady, B. Murali, E. Alarousu, V. M. Burlakov, W. Peng, I. Dursun, L. Wang, Y. He, G. Maculan, A. Goriely, T. Wu, O. F. Mohammed, and O. M. Bakr, "High-quality bulk hybrid perovskite single crystals within minutes by inverse temperature crystallization," *Nature Communications*, vol. 6, no. May, p. 7586, 2015.

[228] L. J. Gillespie and L. H. D. Fraser, "The Normal Vapor Pressure of Crystalline Iodine 1," *Journal of the American Chemical Society*, vol. 58, pp. 2260–2263, nov 1936.

[229] A. Bielecki and D. P. Burum, "Temperature Dependence of 207Pb MAS Spectra of Solid Lead Nitrate. An Accurate, Sensitive Thermometer for Variable-Temperature MAS," *Journal of Magnetic Resonance, Series A*, vol. 116, pp. 215–220, oct 1995.

[230] R. K. Harris, E. D. Becker, S. M. C. De Menezes, P. Granger, R. E. Hoffman, and K. W. Zilm, "Further conventions for NMR shielding and chemical shifts IUPAC recommendations 2008," *Solid State Nuclear Magnetic Resonance*, vol. 33, no. 3, pp. 41–56, 2008.

[231] E. Fukushima and S. B. W. Roeder, *Experimental Pulse NMR: A nuts and bolts approach*. Addison-Wesley, 1981.

[232] S. Z. Ageev, D. J. Isbister, and B. C. Sanctuary, "Composite pulses in nuclear quadrupole resonance," *Molecular Physics*, vol. 83, no. 2, pp. 193–210, 1994.

[233] J. Jamnik and J. Maier, "Generalised equivalent circuits for mass and charge transport: chemical capacitance and its implications," *Physical Chemistry Chemical Physics*, vol. 3, pp. 1668–1678, jan 2001.

[234] D. Massiot, C. Bessada, J. Coutures, and F. Taulelle, "A quantitative study of 27Al MAS NMR in crystalline YAG," *Journal of Magnetic Resonance (1969)*, vol. 90, pp. 231–242, nov 1990.

[235] D. Freude and J. Haase, "Quadrupole Effects in Solid-State Nuclear Magnetic Resonance," *NMR Basic Principles and Progress*, vol. 29, pp. 1–90, 1993.

[236] D. L. Bryce, G. M. Bernard, M. Gee, M. D. Lumsden, K. Eichele, and R. E. Wasylishen, "Practical aspects of modern routine solid-state multinuclear magnetic resonance spectroscopy: one-dimensional experiments," *Canadian journal of analytical sciences and spectroscopy*, vol. 46, no. 2, pp. 46–81, 2001.

[237] V. V. Kharton, A. A. Yaremchenko, A. P. Viskup, M. V. Patrakeev, I. A. Leonidov, V. L. Kozhevnikov, F. M. Figueiredo, A. L. Shaulo, E. N. Naumovich, and F. M. B. Marques, "Oxygen Permeability and Ionic Conductivity of Perovskite-Related Lao.3Sro.7Fe(Ga)O3δ," *Journal of The Electrochemical Society*, vol. 149, p. E125, apr 2002.

[238] H. Mehrer, *Diffusion in Solids*, vol. 155 of *Springer Series in Solid-State Sciences*. Berlin, Heidelberg: Springer Berlin Heidelberg, 2007.

[239] J. Maier, "On the correlation of macroscopic and microscopic rate constants in solid state chemistry," *Solid State Ionics*, vol. 112, no. 3-4, pp. 197–228, 1998.

[240] "Standard Thermodynamic Properties of Chemical Substances," in *CRC Handbook of Chemistry and Physics* (D. R. Lide, ed.), CRC Press, 81 ed., 2000.

[241] P. Polatin, T. Barbara, and B. P. Dailey, "The determination of the 14N nuclear quadrupole coupling constant for the methylammonium ion in a liquid-crystal solution," *Journal of Magnetic Resonance (1969)*, vol. 47, no. 1, pp. 148–150, 1982.

[242] D. T. Edmonds, M. J. Hunt, and A. L. Mackay, "Pure quadrupole resonance of 14N in a tetrahedral environment," *Journal of Magnetic Resonance (1969)*, vol. 9, no. 1, pp. 66–74, 1973.

[243] H. Bayer, "Zur Theorie der Spin-Gitterrelaxation in Molekülkristallen," *Zeitschrift für Physik*, vol. 130, no. 2, pp. 227–238, 1951.

[244] J. Ramakrishna, "Temperature Dependence of the Iodine Pure Quadrupole Resonance Frequency in Methyl Iodide," *Proceedings of the Physical Society*, vol. 79, no. 5, p. 1069, 1962.

GLOSSARY

AFM	Atomic Force Microscopy
BPP	Bloembergen-Purcell-Pound
C^{δ}	Chemical capacitance
CP	Cross Polarisation
CSA	Chemical Shift Anisotropy
δ_{iso}	Isotropic chemical shift
ΔG_f^0	Standard Gibbs energy of formation
ΔG_r^0	Standard Gibbs energy of reaction (degradation)
D^*	Tracer diffusion coefficient
D^{δ}	Chemical diffusion coefficient
DD	Dipole-dipole
DFT	Density Functional Theory
DMF	Dimethylformamide
DMSO	Dimethylsulfoxide
$e^{'}$	Conduction electron (see also § **10.1.1**)
EDS	Energy Dispersive X-ray Spectrometry
EFG	Electric Field Gradient
ETM	Electron Transport Material
FA	Formamidinium cation ($CH(NH_2)_2^+$)
FWHM	Full Width Half Maximum
GBL	γ-butyrolactone
(GI) XRD	(Grazing Incidence) X-Ray Diffraction
$h^{\bullet}$	Electron hole (see also § **10.1.1**)
HOIHP	Hybrid Organic Inorganic Halide Perovskite
HTM	Hole Transport Material
k^*	Surface rate constant
M_2	Second moment
MA	Methylammonium cation ($CH_3NH_3{}^+$)
MAS	Magic Angle Spinning
MD	Molecular Dynamics
NMR	Nuclear Magnetic Resonance
NQR	Nuclear Quadrupolar Resonance

$\mathbf{P(I_2)}$	Iodine partial pressure
$\mathbf{P(O_2)}$	Oxygen partial pressure
PCBM	Phenyl-C61-butyric acid methyl ester
PSC	Perovskite Solar Cell
PTAA	Poly[bis(4-phenyl)(2,4,6-trimethylphenyl)amine
$\mathbf{R}^{\delta}$	Chemical resistance
σ	Conductivity
$\sigma_{\mathbf{ion/eon}}$	Ionic/electronic conductivity
SEM	Secondary Electron Microscopy
Spiro-OMeTAD	N^2,N^2,$N^{2'}$,$N^{2'}$,N^7,N^7,$N^{7'}$,$N^{7'}$-octakis(4-methoxyphenyl)- -9,9′-spirobi[9H-fluorene]-2,2′,7,7′-tetramine
SR	Spin-rotation
$\mathbf{T_1}$	Spin-lattice relaxation time
$\mathbf{T_2}$	Spin-spin relaxation time
ToF-SIMS	Time of Flight - Secondary Ions Mass Spectroscopy
μ	Chemical potential
UV-Vis	UltraViolet-Visible (spectroscopy)
$\mathbf{V_I^{\bullet}}$	Iodine vacancy (see also § **10.1.1**)
$\mathbf{V_{MA}^{'}}$	Methylammonium vacancy (see also § **10.1.1**)
$\chi_{\mathbf{Q}}$	Quadrupolar constant
XPS	X-ray Photoelectron Spectroscopy

LIST OF PUBLICATIONS

[1] G. Gregori, T.-Y. Yang, **A. Senocrate**, J. Maier, M. Grätzel, J. Maier, in *Organic-Inorganic Halide Perovskite Photovoltaics*, eds. N.-G. Park, M. Grätzel and T. Miyasaka, Springer International Publishing, **2016**, pp. 107-135.

[2] **A. Senocrate**, I. Moudrakovski, G. Y. Kim, T.-Y. Yang, G. Gregori, M. Grätzel, J. Maier, The Nature of Ion Conduction in Methylammonium Lead Iodide: A Multimethod Approach, *Angew. Chemie Int. Ed.*, **2017**, 56, 7755.

[3] G. Y. Kim, **A. Senocrate**, T.-Y. Yang, G. Gregori, M. Grätzel, J. Maier, Large tunable photoeffect on ion conduction in halide perovskites and implications for photodecomposition, *Nat. Mater.*, **2018**, 17, 445.

[4] **A. Senocrate**, T.-Y. Yang, G. Gregori, G. Y. Kim, M. Grätzel, J. Maier, Charge carrier chemistry in methylammonium lead iodide, *Solid State Ion.*, **2018**, 321, 69.

[5] **A. Senocrate**, T. Acartürk, G. Y. Kim, R. Merkle, U. Starke, M. Grätzel, J. Maier, Interaction of oxygen with halide perovskites, *J. Mater. Chem. A*, **2018**, 6, 10847.

[6] **A. Senocrate**, I. Moudrakovski, J. Maier, Short-range ion dynamics in methylammonium lead iodide by multinuclear solid state NMR and ^{127}I NQR, *Phys. Chem. Chem. Phys.*, **2018**, 20, 20043.

[7] **A. Senocrate**, I. Moudrakovski, T. Acartürk, R. Merkle, G. Y. Kim, U. Starke, M. Grätzel, J. Maier, Slow $CH_3NH_3^+$ diffusion in $CH_3NH_3PbI_3$ under light measured by solid-state NMR and tracer diffusion, *J. Phys. Chem. C.*, **2018**, 122, 21803.

[8] C. Lermer, **A. Senocrate**, I. Moudrakovski, T. Seewald, A.-K. Hatz, P. Mayer, F. Pielnhofer, J. A. Jaser, L. Schmidt-Mende, J. Maier, B. V. Lotsch, Completing the picture of 2-(aminomethylpyridinium) lead hybrid perovskites - Insights into structure, conductivity behavior and optical properties, *Chem. Mater.*, **2018**, 30, 6289.

[9] **A. Senocrate** and J. Maier, Solid state ionics of halide perovskites, *In preparation (Invited Perspective on J. Am. Chem. Soc.)*.

Alessandro Senocrate

Stoβäckerstr. 15, 70563, Stuttgart (DE)
+4915731702649
a.senocrate@fkf.mpg.de
https://www.fkf.mpg.de/5358578/Senocrate

Info

Birth	27 November 1987, Alzano Lombardo (BG), IT.
Citizenship	Italian
LinkedIn	`http://it.linkedin.com/pub/alessandro-senocrate/59/a4b/638`
Skype	alessandro.senocrate

Education

2012 **B. Sc. Chemistry**, Univ. degli Studi di Pavia (IT). Grade: 102/110.
Thesis title: *Inorganic aluminosilicate polymers: Eco-friendly ceramic materials.*

2014 **M. Sc. Chemistry**, Univ. degli Studi di Pavia (IT). Grade: 110/110 *Cum Laude*.
Thesis title: *Low temperature proton conductivity in porous TiO_2.*

March 2015-Oct 2018 **Ph.D. Chemistry**, Max Planck Institute for Solid State Research (DE) & École polytechnique fédérale de Lausanne (CH).
Thesis title: *Defect chemistry of methylammonium lead iodide.*

Publications

2016 **Ionic Conductivity of Organic-Inorganic Perovskites: Relevance of Long-Time and Low Frequency Behavior**, Gregori, Yang, Senocrate, Maier, In *Organic-Inorganic Halide Perovskite Photovoltaics*, Springer.

2017 **The nature of ion conduction in methylammonium lead iodide: A multi-method approach**, Senocrate, Moudrakovski, Kim, Yang, Gregori, Grätzel, Maier, *Angew. Chemie Int. Ed.*, 56, 7755.

2018 **Large tunable photoeffect on ion conduction in halide perovskites and implications for photo-decomposition**, Kim, Senocrate, Yang, Gregori, Grätzel, Maier, *Nature Mater.*, 17, 445.

2018 **Charge carrier chemistry in methylammonium lead iodide**, Senocrate, Yang, Gregori, Kim, Grätzel, Maier, *Solid State Ion.*, 321, 69.

2018 **The interaction of oxygen with halide perovskites**, Senocrate, Acartürk, Kim, Merkle, Starke, Grätzel, Maier, *J. Mater. Chem. A*, 6, 10847.

2018 **Short-range ion dynamics in methylammonium lead iodide by multinuclear solid state NMR and ^{127}I NQR**, Senocrate, Moudrakovski, Maier, *Phys. Chem. Chem. Phys*, 20, 20043.

2018 **Slow $CH_3NH_3^+$ diffusion in $CH_3NH_3PbI_3$ under light measured by solid-state NMR and tracer diffusion**, *Senocrate, Moudrakovski, Acartürk, Merkle, Kim, Starke, Grätzel, Maier, J. Phys. Chem. C*, 122, 21803.

2018 **Completing the picture of 2-(aminomethylpyridinium) lead hybrid perovskites**, Lermer, Senocrate, Moudrakovski, Seewald, Hatz, Mayer, Pielnhofer, Jaser, Schmidt-Mende, Maier, Lotsch, *Chem. Mater.*, 30, 6289.

Awards

2014 **Best Master Thesis**, from the Italian Chemical Society, Electrochemistry section.

2017 **Best Oral Contribution**, Conf. on Molecular Nanostructures, Ascona (CH).

2017 **Poster Prize**, Int. Conf. on Hybrid and Organic Photovoltaics, Lausanne (CH).

2017 **Poster Prize**, Int. Conf. on Materials Chemistry, Liverpool (UK).

2018 **Graduate student award**, E-MRS Spring, Strasbourg (FR).

2018 **Poster Prize**, Solid State Chemistry & Ionics Workshop, Fukuoka (JP).

Scientific contributions

2014 **Talk** National Meeting of the Italian Chemical Society, Rende (IT).

2016 **Talk** 115th Bunsentagung, Rostock (DE).

2016 **Talk** Workshop on Bio-inspired Nanosystems for Energy Conversion, Berlin (DE).

2016 **Talk** Non-Stoichiometric Compounds VI, Santa Fe (NM).

2016 **Talk** Perovskite Solar Cells and Optoelectronics Conf., Genova (IT).

2017 **Talk** Conf. on Molecular Nanostructure, Ascona (CH).

2017 **Talk** Int. Conf. on Materials for Advanced Technologies, Singapore (SGP).

2017 **Talk + Poster** Perovskite Solar Cells and Optoelectronics Conf., Oxford (UK).

2018 **Talk + Poster** Int. Conf. on Hybrid and Organic Photovoltaics, Benidorm (ES).

2018 **Invited Talk + Talk** E-MRS Spring, Strasbourg (FR).

Employment

2014 **Research scholarship**, at Università degli Studi di Pavia, Italy.

Languages

Self-assessment European level CEFR (C2 maximum evaluation)

		Understanding		**Speaking**		**Writing**
		Listening	Reading	Interaction	Production	
English		*C2*	*C2*	*C2*	*C2*	*C2*
German		*B1*	*B1*	*A2*	*A2*	*A2*
Italian	Native					

Certification <**English - IELTS Academic**>, 24.08.2013, overall band score of 8.0/9.0.

November 6, 2018